CHARACTERIZATION AND APPLICATION OF ISOLATED ATTOSECOND PULSES

by

MICHAEL CHINI
B.S. McGill University, 2007

A dissertation submitted in partial fulfillment of the requirements
for the degree of Doctor of Philosophy
in the Department of Physics
in the College of Sciences
at the University of Central Florida
Orlando, Florida

Fall Term
2012

Major Professor: Zenghu Chang

ABSTRACT

Tracking and controlling the dynamic evolution of matter under the influence of external fields is among the most fundamental goals of physics. In the microcosm, the motion of electrons follows the laws of quantum mechanics and evolves on the timescale set by the atomic unit of time, 24 attoseconds. While only a few time-dependent quantum mechanical systems can be solved theoretically, recent advances in the generation, characterization, and application of isolated attosecond pulses and few-cycle femtosecond lasers have given experimentalists the necessary tools for dynamic measurements on these systems. However, pioneering studies in attosecond science have so far been limited to the measurement of *free* electron dynamics, which can in most cases be described approximately using classical mechanics. Novel tools and techniques for studying *bound* states of matter are therefore desired to test the available theoretical models and to enrich our understanding of the quantum world on as-yet unprecedented timescales.

In this work, attosecond transient absorption spectroscopy with ultrabroadband attosecond pulses is presented as a technique for direct measurement of electron dynamics in quantum systems, demonstrating for the first time that the attosecond transient absorption technique allows for state-resolved and simultaneous measurement of bound and continuum state dynamics. The helium atom is the primary target of the presented studies, owing to its accessibility to theoretical modeling with both *ab initio* simulations and to model systems with reduced dimensionality. In these studies, ultrafast dynamics – on timescales shorter than the laser cycle – are observed in prototypical quantum mechanical processes such as the AC Stark and ponderomotive energy level shifts, Rabi oscillations and electromagnetically-induced absorption

and transparency, and two-color multi-photon absorption to “dark” states of the atom. These features are observed in both bound states and quasi-bound autoionizing states of the atom. Furthermore, dynamic interference oscillations, corresponding to quantum path interferences involving bound and free electronic states of the atom, are observed for the first time in an optical measurement. These first experiments demonstrate the applicability of attosecond transient absorption spectroscopy with ultrabroadband attosecond pulses to the study and control of electron dynamics in quantum mechanical systems with high fidelity and state selectivity. The technique is therefore ideally suited for the study of charge transfer and collective electron motion in more complex systems.

The transient absorption studies on atomic bound states require ultrabroadband attosecond pulses − attosecond pulses with large spectral bandwidth compared to their central frequency. This is due to the fact that the bound states in which we are interested lie only 15-25 eV above the ground state, so the central frequency of the pulse should lie in this range. On the other hand, the bandwidth needed to generate an isolated 100 *as* pulse exceeds 18 eV – comparable to or even larger than the central frequency. However, current methods for characterizing attosecond pulses require that the attosecond pulse spectrum bandwidth is small compared to its central frequency, known as the central momentum approximation. We therefore explore the limits of attosecond pulse characterization using the current technology and propose a novel method for characterizing ultrabroadband attosecond pules, which we term PROOF (phase retrieval by omega oscillation filtering). We demonstrate the PROOF technique with both simulated and experimental data, culminating in the characterization of a world-record-breaking 67 *as* pulse.

for Jackie

ACKNOWLEDGMENTS

The work that I present in this thesis could not have been done without the support of many people. First, I must acknowledge the never-ending patience and encouragement of my wife, Jackie. Research often requires sacrificing nights and weekends to work in the lab or office, and I can’t thank her enough for her understanding. I would also like to thank my family for believing in me and providing mental and emotional support.

I had the great opportunity to work under the guidance of several talented postdoctoral researchers during my time at K-State and UCF. In particular, I would like to thank Dr. Chengquan Li and Dr. Ximao Feng, who helped me to get involved in research as a junior student, Dr. Shouyuan Chen and Dr. Baozhen Zhao, who trained me on the laser, Dr. Hiroki Mashiko, who taught me to maximize my strengths and minimize my weaknesses in research, and Dr. Kun Zhao, who played a vital role in the development of the FAST lab at UCF. Each one of them helped me to grow as a scientist and shaped my views on how to approach my research.

The attosecond transient absorption experiments were performed with the help of a great team, mainly Dr. He Wang, Dr. Shouyuan Chen, Xiaowei Wang, and Yan Cheng. More than anyone else, He Wang taught me to always be curious and to carefully consider my next step in research in order to make the maximum impact. Xiaowei and Yan were instrumental in developing the transient absorption setup at UCF, and the three of us spent many late nights in the lab to obtain the helium data. Additional contributions came from theoretical simulations performed by Dr. Feng He, Dr. Chang-hua Zhang, Prof. Uwe Thumm, Dr. Suxing Hu, Di Zhao, Dr. Dmitry Telnov, and Prof. Shih-I Chu.

The work on FROG-CRAB and PROOF also relied on a large team in order to make the maximum impact. He Wang and Sabih Khan worked with me on the development of the PCGPA code, and Sabih helped me to develop the evolutionary algorithm for the PROOF. I learned the value of hard work from Steve Gilbertson, who took most of the experimental data used to test the FROG-CRAB and PROOF. The development of the PCGPA-based PROOF program was spurred on by the excellent work done by Dr. Zhao and Qi Zhang with their streak camera. It is a great honor to have the PROOF method demonstrated on a world-record breaking pulse.

Yi Wu has done an amazing job of developing and maintaining the FAST laser at UCF, and I couldn't possibly give him the credit he deserves. I truly believe that the quality of a laser system can be judged by the publications it enables. In a few short years at UCF, Yi's laser has generated the world-record shortest attosecond pulse and several submissions and publications to high impact journals. In addition to those mentioned above, I would like to recognize the input of Dr. Eric Moon, Chenxia Yun, Yang Wang, Yiduo Zhan, Eric Cunningham, Huaping Zang, Al Rankin, Wei Cao, Prof. Lew Cocke, Guillaume Laurent, and Mohammad Zohrabi.

Finally, I would like to acknowledge my advisor, Prof. Zenghu Chang, and my committee members at KSU and UCF, Prof. Vinod Kumarappan, Prof. Brian Washburn, Prof. Lee Chow, Prof. Hari Saha, and Prof. Axel Schülzgen. Prof. Chang has been a mentor to me and has truly taught me the value of great research and how to conduct research effectively. Additionally, he has served as an excellent model for how to mentor students and to stimulate them to take ownership of their experiments and to take pride in their work.

TABLE OF CONTENTS

LIST OF FIGURES

LIST OF TABLES

CHAPTER ONE: INTRODUCTION

When Isaac Newton first described the laws governing the dynamics of an object acted on by a force, he laid the first foundations for using physical models to *observe*, *predict*, and *control* the dynamics underlying physical processes. Now, more than three centuries later, much of scientific research is still predicated on the goals of observing, predicting, and controlling the dynamic evolution of matter. In that time span, new frontiers have been forged by pushing the limits of measurement and control on progressively smaller length and time scales. With advancing technology, researchers have been able to test their predictions and "steer" motion down to the scale of electron motion in the atom (10^{-9} m, 10^{-18} s) [1].

The electromagnetic force is indisputably the most fundamental interaction in atomic and chemical physics. It is responsible for the electronic structure unique to every atom and for the chemical bonds which define molecules and solids, and it is the origin of the light absorption and emission characteristics distinct to these and more complex systems at the heart of modern spectroscopy. Since the first observation of Fraunhofer absorption and emission lines in the spectrum of sunlight passing through a flame [2], spectroscopic methods were critical to the study of the elemental composition of the sun and other stellar bodies and of Earth's atmosphere, as well as for the discovery of new elements. With the discovery and formulation of the Balmer [3], Lyman [4], and Paschen [5] spectral lines in atomic hydrogen, and culminating in the groundbreaking development of quantum mechanics in the early 20th century, spectroscopic techniques could be used not only for observation, but also for prediction. Further technical developments have allowed for the first hints of control − measurement and manipulation of *changes* in the absorption and emission spectra of atoms placed in strong electric and magnetic fields or in different chemical environments.

It is only more recently, with the advent of laser light sources, that *light itself* has been demonstrated as a tool for the control of atomic and molecular structure [6]. Laser light is both spatially and temporally coherent – its energy can be compressed in both space and time – making it an ideal tool for measurement and control in the microcosm. Laser and laser-like sources of light have been demonstrated spanning the mid- and near-infrared ($\lambda \sim$ 1000-10,000 nm), visible and near-ultraviolet ($\lambda \sim$ 100-1000 nm), and extreme ultraviolet and soft x-ray ($\lambda \sim$ 1-100 nm) wavelength ranges, with few-optical-cycle pulse durations [7]. Since the bulk of the dipole oscillator strength in atoms and molecules lies in the extreme ultraviolet (ground state to excited state transitions) and visible/infrared (excited state to excited state transitions) [8], laser control techniques can be adapted to the study of nearly any system. To date, lasers have been used to control both external and internal degrees of freedom in atomic and molecular systems, with applications (and respective time scales of control) ranging from trapping and “tweezing” (nanoseconds to seconds) [9,10], molecular alignment and orientation (10s to 100s of picoseconds) [11], molecular dissociation and chemical reaction pathway selection (femtoseconds to picoseconds) [12,13], and strong field ionization and rescattering (attoseconds to few-femtoseconds) [14-16].

The demonstration of isolated attosecond pulses in 2001 [17] opened a new frontier for laser control. For the first time, attosecond pulses allow for measurement of electron motion on the natural atomic time scale. While attosecond pulses are currently too weak to be used to drive electron motion, they can instead be used to *probe* the dynamics initiated by a strong laser field, on time scales comparable to and even shorter than the laser cycle. However, few experiments have so far focused on the attosecond electron dynamics in bound states of the atom, due primarily to the inaccessibility of attosecond pulses with the relatively low photon energies needed to excite the atomic bound states and also to the relative ease of interpreting attosecond dynamics in continuum states, which can often be described using semi-classical models. In this thesis, I will present measurements of attosecond electron dynamics, applying moderately intense few-cycle laser fields (~10^{11}-10^{13} W/cm^2) to drive the motion of electrons in both bound and continuum states, and using isolated attosecond pulses to probe the dynamics.

Application of attosecond pulses to the study of bound states of matter requires ultrabroadband, few-cycle attosecond pulses – attosecond pulses with large spectral bandwidth compared to their central frequency. This can be understood simply by comparing the energy needed to promote ground state electrons to excited states through absorption of a photon (~15-25 eV for helium and neon atoms) with the optical bandwidth needed to generate an isolated 100 *as* pulse (18 eV). Pushing the limits of experiments to study even faster bound state dynamics requires shorter pulses, and therefore broader bandwidths, while maintaining sufficient spectrum at relatively low frequencies. Therefore, the bandwidth of the attosecond pulse must be comparable to, or even larger than, the central frequency.

However, both generation and characterization of such pulses remains difficult. The problem of generating ultrabroadband attosecond pulses has been solved previously in our laboratory with the invention of the double optical gating (DOG) [18]. DOG produces isolated attosecond pulses which can span the full spectral range from extreme ultraviolet to soft x-ray wavelengths [19], covering many atomic and molecular bound and quasi-bound state resonances.

Still, the methods available for attosecond pulse measurement have so far been limited to attosecond pulses containing several optical cycles (i.e.; pulses with bandwidth much smaller than their central frequency) [20]. Here, I will present a novel technique for attosecond pulse characterization based on the well-established technique of attosecond streaking spectroscopy, wherein the free electron wavepacket photoionized by the attosecond pulse is modified by a moderately intense, low frequency laser field. The technique, known as PROOF (phase retrieval by omega oscillation filtering), is not limited by the attosecond pulse bandwidth and is found to be quite robust in the retrieval of attosecond pulses from simulated and experimental streaking measurements. Using the PROOF, a world-record-breaking 67 *as* pulse generated using DOG is fully characterized from the streaked electron spectrogram.

In addition to the pulse duration measurements using free electrons in attosecond streaking spectroscopy, I will present the first measurements of sub-cycle electron dynamics in atomic bound and quasi-bound states using a novel all-optical technique known as attosecond transient absorption spectroscopy. This research addresses fundamental questions in ultrafast science concerning the response of excited electron wavepackets, with characteristic timescales of motion that are often much longer than the laser cycle (or even the laser pulse), to an intense laser field. In particular, sub-cycle dynamics are demonstrated for the first time in several prototypical quantum mechanics processes covered in graduate-level quantum mechanics courses [8], such as the AC Stark shift and Autler-Townes splitting of atomic energy levels, the ponderomotive shift of the ionization threshold, Rabi oscillations and electromagnetically-induced absorption and transparency, and nonresonant two-photon absorption. Furthermore, oscillatory structures corresponding to two-path quantum-optical interferences are observed in the absorption spectrum far from any resonance structures of the atom. The transient absorption experiments are primarily done in the helium atom in order to facilitate future calculations based on *ab initio* numerical solution of the time-dependent Schrödinger equation, although other targets are also compared where possible. Theoretical results based on simplified models and numerical calculations in reduced-dimensionality systems will be presented in order to aid in the interpretation of the experimental results.

The thesis will be organized as follows. In Chapter Two, I will discuss the dynamics of an electron in the laser field. I will begin by defining the laser field and discussing the parameter space in which the laser can be used to control electron dynamics. I will then discuss the laser-atom interaction in various intensity regimes separately for a continuum (ionized) electron wavepacket and for a bound (or quasi-bound) electron wavepacket. In Chapter Three, I will discuss the generation and characterization of the ultrabroadband isolated attosecond pulses which will be used in the experiments to probe the dynamics of the laser-dressed atom. In particular, I will focus on the difficulties of generating and characterizing ultrabroadband attosecond pulses (that is, attosecond pulses with large bandwidth compared to their carrier frequency), and demonstrate the PROOF technique for characterizing such pulses. In Chapter Four, I will discuss the attosecond transient absorption spectroscopy, including the fundamental principles of the technique, the experimental setup (including the laser systems), and a theoretical model of the transmission of an isolated attosecond pulse through a laser-dressed medium. In Chapter Five and Chapter Six, I will present the first measurement of bound state dynamics in helium on the attosecond timescale. Chapter Five will focus on the measurement of laser-induced Stark shifts in helium in the cases of nonresonant (1s3p, 1s4p) and resonant (1s2p) couplings. In particular, I will focus on the sub-cycle energy level shift of the 1s3p and higher-lying states of helium and the Autler-Townes doublet formation in the 1s2p state. Chapter Six will focus on two-color multi-photon excitation of “dark” states of helium by the combined attosecond and few-cycle femtosecond laser pulses. Here, emphasis will be placed on the sub-cycle dynamics in the two- and three-photon absorption and in the dynamic two-path quantum-optical interference oscillations observed both above and below the ionization threshold, far from any resonance structures. In Chapter Seven, I will describe the first time-domain measurement of the lifetime of a quasi-bound autoionizing state, using argon as the target atom. Finally, Chapter Eight will conclude with a summary of the presented experiments as well as the implications for future work. Atomic units are used throughout the thesis, except where otherwise noticed.

CHAPTER TWO: ELECTRON DYNAMICS IN THE LASER FIELD

When an atom (or molecule, or solid) is exposed to a light field, the induced electron motion instigates a time-dependent polarization that depends on both the system parameters and on the light field [8]. Therefore in order to achieve *control* over the electron motion in the light field, it is critical to define the parameters of both the system of study and of the laser light. This chapter will cover the interaction of a hydrogen-like atom with a moderately intense light field. I will begin by discussing in general terms the laser source needed for control and proceed by describing the interaction of both a continuum ("free") electron and a bound electron with the laser field. Various phenomena, including the origin of spectral absorption and emission lines, laser-induced line widths and shifts, ionization resulting from single- and multi-photon absorption, and continuum electron momentum "streaking" will be discussed in detail. While the material in this chapter is covered in many graduate-level courses in quantum mechanics and laser-matter interactions and is familiar to the specialist, these concepts will be critical for later discussions of the time-resolved experiments. This chapter will present these various phenomena in general terms; more technical aspects of the laser, such as the experimental setups for generation of few-cycle femtosecond and isolated attosecond pulses, as well as the target-specific features of the pump-probe experiments, will be covered in later chapters.

The Laser Light Field

Strictly speaking, a rigorous description of the laser field would have to be defined in the framework of quantum electrodynamics, in which the electromagnetic field is expressed in terms of the photon. However, even in relatively weak fields, the number of photons is extremely large; the milliJoule-level laser pulses used in the experiments described later contain on the order of 10^{15} photons per pulse, and even the comparatively weak attosecond pulses contain more than 10^{7} photons per pulse. Therefore, the photon number can be considered as a continuous variable and the laser-atom interaction treated *semi-classically* – that is, the laser field will be described using classical electrodynamics, while the atom is in general treated quantum mechanically. The photon will however be invoked in situations where it enhances understanding of a particular process.

In classical electrodynamics, the laser field will be described in terms of its electric field $\boldsymbol{F}$ and vector potential $\boldsymbol{A}$. In the plane wave approximation, a monochromatic laser field with angular frequency (photon energy) ω_0 and with linear polarization along the z-axis can be written as:

$$\boldsymbol{F}(\boldsymbol{r},t) = \boldsymbol{z}F_0\cos(-\boldsymbol{k}\cdot\boldsymbol{r}+\omega_0 t+\delta) \tag{2.1}$$

$$\boldsymbol{A}(\boldsymbol{r},t) = -\int_{-\infty}^{t} dt'\boldsymbol{F}(t') = \boldsymbol{z}\frac{F_0}{\omega_0}\sin(-\boldsymbol{k}\cdot\boldsymbol{r}+\omega_0 t+\delta), \tag{2.2}$$

where F_0 is the electric field strength, $\boldsymbol{k}$ is the wavevector which denotes the propagation direction of the laser field, and δ is the phase of the laser field. For our purposes, we can consider a limiting case where the electric field and vector potential do not vary much over the scale of the atom, known as the dipole approximation. This is valid for both the femtosecond near-infrared (NIR, $\lambda_0 \approx 750$ nm) and attosecond extreme ultraviolet (XUV, $\lambda_0 \approx 50$ nm) laser pulses used in the experiments presented in this thesis, for which the wavelengths are much larger than the spatial wavefunction of the atom (typically confined within a region of radius $a \approx$

1 nm). In this case, $|\boldsymbol{k}\cdot\boldsymbol{r}| = \frac{2\pi}{\lambda_0}a$ becomes negligible, and the laser field can be considered to vary only with time.

In order to control the electron dynamics in the time domain, it is first necessary to control the electric field of the laser on time scales comparable to that of the electron motion. This can be done using pulsed lasers, and by tailoring the laser pulse on the few- and sub-femtosecond timescales [7]. In attosecond transient absorption spectroscopy, in which the laser-dressed photoabsorption of an isolated attosecond pulse is measured as a function of the time delay between the attosecond pulse and a few-cycle femtosecond pulse, control over the electric fields is especially critical. This is not only due to the well-known constraints on the driving laser for generating an isolated attosecond pulse, but also due to the fact that the dressing laser waveform intimately shapes the light-induced electron polarization and the rise time determines the peak field strength to which an atom can be exposed before its polarizability drops to nearly zero due to ionization of the electronic bound state. It is therefore necessary to discuss the requirements and constraints on the few-cycle laser pulses used in the experiments.

The electric field and vector potential described above correspond to waveforms that extend infinitely in time. A short laser pulse with full-width at half-maximum (FWHM) pulse duration τ, on the other hand, can be produced by coherent addition of plane waves with different frequencies but with the same polarization direction and with a well-defined phase relationship between different frequency components. In this case, the electric field can be rewritten as:

$$\boldsymbol{F}(t) = \boldsymbol{z}F_0 f(t)\cos(\omega_0 t + \delta(t)), \tag{2.3}$$

where $f(t)$ is the envelope function which is primarily confined within a time range $-\tau/2 < t < \tau/2$. I will primarily consider Gaussian-shaped pulse envelope functions, $f(t) = e^{-2\ln(2)(t/\tau)^2}$.

Generation of very short (few-optical-cycle) light pulses requires the coherent combination of a wide bandwidth of light frequencies. This can be seen by taking the Fourier transform of the laser field in Equation 2.3 to obtain the frequency spectrum. The FWHM frequency span $\Delta\omega$ required to obtain a given pulse duration can be specified by the time-bandwidth product, which for Gaussian pulses is given by $\tau\Delta\omega \geq 0.44$. This time-bandwidth product is able to give a simple estimate of the bandwidths and photon energies needed to obtain few-cycle femtosecond and attosecond pulses. For example, a 5 *fs* laser pulse (two optical cycles of 750 nm light) requires a FWHM bandwidth of nearly 0.4 eV (165 nm at 750 nm), which is achievable in the near-infrared and visible. On the other hand, generation of a 300 *as* pulse (approximately two optical cycles at 50 nm) requires a FWHM bandwidth of more than 6 eV (more than 12 nm at 50 nm), which necessitates a central frequency in the XUV spectral range.

Large spectral bandwidth is certainly necessary for generating short, controlled optical waveforms. However, it is not sufficient; phase control is also needed. In fact, two types of phase control are needed. This can be seen by parameterizing the phase in Equation 2.3 as follows:

$$\boldsymbol{F}(t) = \boldsymbol{z}F_0 f(t)\cos[\omega_0 t + \beta(t) + \varphi_{CE}], \tag{2.4}$$

where $\beta(t) = \sum_{n>1} \beta_n t^n$ represents the phase terms that result in a frequency "chirp" of the laser pulse – changes of the oscillation frequency with time. φ_{CE} is the carrier-envelope phase (CEP) [21], which represents the offset between the peak of the pulse envelope function and the nearest positive peak of the carrier wave oscillation and must be actively controlled from pulse to pulse [22]. $\beta(t)$ can be measured and controlled relatively easily in femtosecond laser systems, and is typically set to zero in order to generate few-cycle femtosecond pulses. Control of the CEP is also achievable with a variety of femtosecond laser systems, and is a common feature in both commercial and home-built systems. For attosecond pulses on the other hand, measurement and control of the frequency chirp across the entire spectral bandwidth is a current focus of research in attosecond technology [23] which will be discussed in more detail in Chapter Three.

Attosecond Continuum Electron Dynamics in the Laser Field

The majority of experiments in attosecond science have so far relied on attosecond streaking spectroscopy, which is based on pump-probe photoelectron spectroscopy. In attosecond streaking [24], the attosecond pulse produces a continuum electron by single-photon ionization of the target gas in the ground state with ionization potential I_p smaller than the photon energies included in the attosecond pulse spectrum. In this case, the laser field strength is small compared to the Coulomb field for the electron in the atomic ground state, and the electron dynamics are dominated by the action of the moderately intense (typically in the NIR with intensity of ~10^{11}-10^{13} W/cm^2) laser on the continuum electron. The photoelectron kinetic energy spectrum is then measured as a function of the time delay between the attosecond pulse and the NIR pulse. Because the streaking laser electric field amplitude varies rapidly within the laser optical cycle, attosecond streaking is capable of measuring sub-laser-cycle events and has been used extensively to measure the attosecond pulse duration [17,25-27]. More recently, the attosecond streaking technique has been extended to the measurement of Auger [28] and autoionization [29] lifetimes in atoms, quantum path interferences in electron wavepackets [30], and intrinsic time delays in photoionization of electrons from core and conduction bands in single-crystal metal substrates [31], and from different electronic orbitals in atoms [32].

The attosecond streaking spectroscopy can be formulated quantum mechanically within the strong field approximation (SFA) [33], wherein the influence of the atomic Coulomb field is neglected for the free electrons, and interpreted using semi-classical arguments [24]. The problem requires solution of the time-dependent Schrödinger equation for the electron initially in the atomic ground state and acted upon by the combined XUV and NIR laser fields $\boldsymbol{F}_X(t)$ and $\boldsymbol{F}_L(t)$, respectively. The time-dependent Schrödinger equation (TDSE) for this system is given by:

$$i\frac{\partial}{\partial t}\Psi(\boldsymbol{r},t) = [H_0 - \boldsymbol{r}\cdot\boldsymbol{F}_{\boldsymbol{X}}(t-\tau_D) - \boldsymbol{r}\cdot\boldsymbol{F}_L(t)]\Psi(\boldsymbol{r},t), \tag{2.5}$$

where $\Psi(\boldsymbol{r},t)$ is the electron wavefunction and H_0 is the Hamiltonian of the field-free atom. The XUV and NIR laser fields are characterized in terms of their respective amplitudes $F_{X,0}$ and $F_{L,0}$, carrier frequencies ω_X and ω_L, and pulse durations τ_X and τ_L, as well as the arrival time of the peak of the XUV pulse (time delay) τ_D. The NIR pulse is assumed to arrive at time zero. The wavefunction can be expanded in terms of the ground state and continuum wavefunctions, which are treated as plane waves within the SFA:

$$|\Psi(\boldsymbol{r},t)\rangle = |0\rangle e^{iE_0 t} + \int d^3\boldsymbol{v}\, b(\boldsymbol{v},t)|\boldsymbol{v}\rangle. \tag{2.6}$$

Here, $|0\rangle$ is the atomic ground state with energy $E_0 = 0$, $|\boldsymbol{v}\rangle$ are the plane waves denoted by the electron momentum $\boldsymbol{v}$, and $b(\boldsymbol{v},t)$ gives the complex amplitude of the momentum-space wavefunction. The continuum amplitudes can then be calculated to obtain the energy and delay-dependent photoelectron spectrum:

$$S(\boldsymbol{v},\tau_D) = |b(\boldsymbol{v},\infty)|^2 \approx \left|\int_{-\infty}^{\infty} dt\boldsymbol{F}_X(t-\tau_D)\cdot \boldsymbol{d}[\boldsymbol{v}+\boldsymbol{A}_L(t)]e^{i\varphi(\boldsymbol{v},t)}e^{-i(v^2/2+I_p)t}\right|, \quad (2.7)$$

$$\varphi(\boldsymbol{v},t) = -\int_{t}^{\infty} dt'\left[\boldsymbol{v}\cdot\boldsymbol{A_L}(t') + {A_L}^2(t')/2\right]. \quad (2.8)$$

Here, $\boldsymbol{A}_L(t) = \int_{-\infty}^{t} dt'\boldsymbol{E_L}(t')$ is the NIR laser vector potential and $\boldsymbol{d}(\boldsymbol{v}) = \langle \boldsymbol{v}|\boldsymbol{r}|0\rangle$ is the dipole transition matrix element. We have assumed for simplicity that the XUV light only acts on the ground state (through single-photon ionization), and the NIR laser only acts on continuum states. This assumption is valid when the XUV photon energy is large compared to the ionization potential and the NIR laser intensity is too weak to ionize the ground state atom, which is the case in most attosecond streaking experiments.

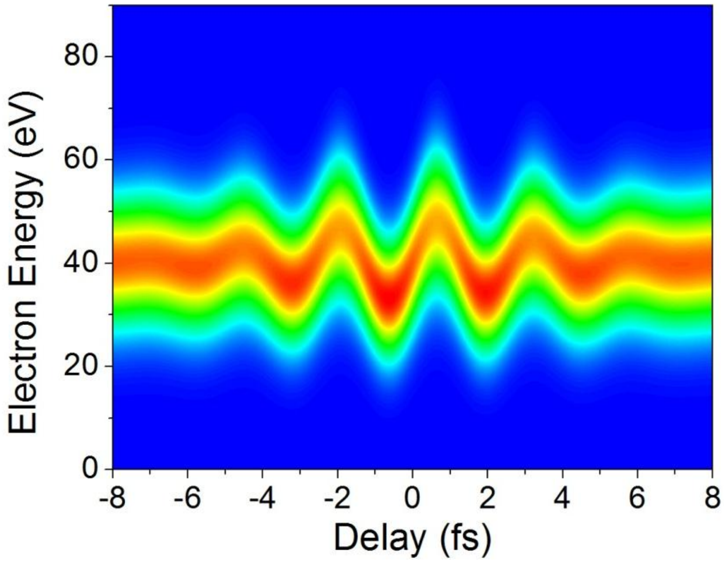

Figure 2.1: The laser-dressed photoelectron spectrum plotted as a function of the time delay results in a streaked spectrogram.

If the two laser fields are linearly polarized (say, along the z-axis) and the photoelectron kinetic energy spectrum is measured along the polarization axis, the measured electron momentum will be shifted by the laser vector potential at the instant of photoionization.

Measurement of the photoelectron spectrum as a function of the delay then results in a streaked spectrogram, shown in Figure 2.1. In this way, the instantaneous field of the streaking laser provides a time reference with which fast electron dynamics and time delays can be recorded. In particular, the photoelectron spectrogram is well-suited to the measurement of the attosecond pulse duration [20,34]. Furthermore, Equations 2.6-2.8 can be modified to consider more complex situations, such as laser-dressed photoexcitation and subsequent autoionization [35,36] of quasi-bound states, streaking of photoelectrons in the presence of nano-plasmonic fields [37], and streaking of electrons originating from different initial states [31].

Several variants of the attosecond streaking spectroscopy that rely upon Equations 2.7 and 2.8 in the limit of low dressing laser intensities have also been demonstrated [34,38]. One of these techniques, applicable to the measurement of ultrabroadband isolated attosecond pulses, will be discussed in detail in Chapter 3.

Laser-Driven Dynamics in Bound Atomic States

In bound states, attosecond dynamics result from wavepacket motion that can be induced by both the attosecond XUV pulse and femtosecond NIR laser field. In this section, I will address several of the various dynamic processes which occur in laser-dressed bound states. First, the perturbative treatment of ground-to-excited state transitions initiated by an isolated attosecond pulse will be presented, as it is critical to the understanding of the attosecond transient absorption process. Then, I will discuss the fast bound state dynamics induced by the moderately intense few-cycle NIR laser field, including AC Stark shifts and absorption line splitting, which can be treated using second-order perturbation theory with respect to the NIR field. Finally, I will discuss the strong-field ionization process, especially as it relates to relatively loosely-bound excited states.

Absorption of an Isolated Attosecond Pulse

The most fundamental interaction of light with an atom is the absorption of a weak light field leading to excitation of the ground state electron to an excited state through resonant absorption of single photons. This interaction is at the heart of attosecond studies of bound atomic states, since the attosecond pulses are relatively weak but overlap spectrally with ground-to-excited state transitions. On the other hand, population of atomic excited states (the 1s2p state of helium, for example, lies at 21.22 eV) requires the simultaneous absorption of thirteen NIR laser photons, which is improbable at moderate laser intensities ($\lesssim 10^{13}$ W/cm^2).

In the simplest case, we can consider the Schrödinger equation of Equation 2.5 with H_0 corresponding to a two-level atom, consisting of the ground state $|0\rangle$ with energy $E_0 = 0$ and a single excited state $|a\rangle$ with energy E_a. The XUV laser field $\boldsymbol{F}_X(t)$ is assumed to be linearly polarized along the z-axis. In that case, we can expand the wavefunction on the basis of the field-free states:

$$|\Psi(\boldsymbol{r},t)\rangle = c_0(t)e^{-iE_0t}|0\rangle + c_a(t)e^{-iE_at}(t)|a\rangle \tag{2.9}$$

where $c_0(t)$ and $c_a(t)$ are the complex amplitudes of the states $|0\rangle$ and $|a\rangle$. The probability of finding the electron in the state $|a\rangle$ is given by $P_a(t) = |c_a(t)|^2$. In this case, solution of the TDSE can be reduced to a set of coupled differential equations:

$$i\dot{c}_0 = d_{0,a}F_X(t)c_a(t) \tag{2.10}$$

$$i\dot{c}_a = \omega_{a,0} c_a(t) + d_{a,0} F_X(t) c_0(t), \tag{2.11}$$

where $\omega_{a,0} = E_a - E_0$ is the energy difference between states and $d_{a,0} = {d_{0,a}}^* = \langle a|z|0\rangle$ is the projection of the dipole matrix element on the polarization axis. Equations 2.11 and 2.10 can be solved using first-order perturbation theory, under the assumption that the ground state amplitude $c_0(t) \approx 1$. In that case, the excited state amplitude can be obtained:

$$c_a(t) \approx -i \int_{-\infty}^{t} dt' d_{a,0} F_X(t') e^{i\omega_{a,0} t'}. \tag{2.12}$$

Using the definition of the XUV pulse in Equation 2.4, and using $\cos\theta = \left(e^{i\theta} + e^{-i\theta}\right)/2$,

$$c_a(t) \approx -\frac{i}{2} \int_{-\infty}^{t} dt' d_{a,0} F_{X,0} f_X(t') \left(e^{i\omega_X t'} + e^{-i\omega_X t'}\right) e^{i\omega_{a,0} t'}. \tag{2.13}$$

When the photon energy is near resonance with the ground-to-excited state transition $\omega_X \approx \omega_{a,0}$, the first exponential term will contain high-frequency oscillations, and the integral will be negligible. In that case,

$$c_a(t) \approx -\frac{i}{2} \int_{-\infty}^{t} dt' d_{a,0} F_{X,0} f_X(t) e^{i(\omega_{a,0} - \omega_X)t\prime}, \tag{2.14}$$

which is approximately proportional to the integrated laser pulse envelope. As the light oscillation frequency becomes farther from the ground-to-excited state transition frequency, the oscillation frequency $\omega_{a,0} - \omega_X$ increases, and the integral becomes negligible for $t \to \infty$ indicating a lack of excitation for off-resonant frequencies. Near resonance, however, $c_a(t \to \infty)$ is approximately constant. Therefore, although the attosecond pulse provides a nearly-instantaneous excitation impulse, the absorption takes place only within a narrow linewidth and the excited electron wavefunction does not maintain the attosecond duration of the excitation pulse. This is in stark contrast to the case of continuum states, where the attosecond pulse spectrum is absorbed relatively uniformly and the free electron wavepacket maintains the attosecond time duration of the pulse.

The emission of light can similarly be observed in Equation 2.13, when the photon energy $\omega_X \approx -\omega_{a,0}$ and the second term becomes negligible. The implications of the state amplitude on the emission linewidth and temporal behavior are the same as for absorption.

Laser-Induced Couplings: Stark Shifts and Line Splittings

For electrons in excited states, the influence of the NIR laser becomes dominant. This is due to both the proximity of excited energy levels to the ionization threshold (which will be discussed in the following section) and to the close spacing of energy levels. For hydrogen-like atoms, the energy level of a state with principle quantum number n is given by:

$$E_n = I_p\left(1 - \frac{1}{n^2}\right) \tag{2.15}$$

relative to the ground state (n=1). Therefore, the energy spacing between adjacent states is given by:

$$\omega_{m,n} = E_m - E_n = I_p\left(\frac{1}{n^2} - \frac{1}{m^2}\right), \tag{2.16}$$

which can be approximately equal to the laser photon energy (or its negative) for $n, m \geq 2$, $n \neq m$, facilitating absorption and emission of NIR photons. Although single-photon transitions similar to those in the previous section can also be observed at NIR frequencies, we will focus on higher-order couplings due to the higher intensity of the NIR laser. These couplings will be treated in second-order perturbation theory.

As in the case of the two-level atom, we will expand $\Psi(\boldsymbol{r}, t)$ in the basis of the field free states:

$$\Psi(\boldsymbol{r}, t) = \sum_k c_k(t)\, e^{-iE_k t}|k\rangle. \tag{2.17}$$

Again, insertion of Equation 2.17 into the TDSE (Equation 2.5) results in a set of coupled differential equations for the amplitudes $c_k(t)$. While numerical solutions to the coupled equations in the presence of the XUV and NIR laser pulses will be discussed in Chapters Four, Five, Six, and Seven, analytical solutions are invaluable to a deeper understanding of the physical processes underlying the complex phenomena observed in experiments. Assuming that the atom is instantaneously excited (by the attosecond pulse) into the state $|a\rangle$ at time $t = \tau_D$ with respect to the NIR laser pulse centered at time $t = 0$, such that $c_k(\tau_D) = \delta_{ka}$, the coupled equations can be analytically solved for the time-dependent amplitudes in the cases of resonant and nonresonant couplings.

When the dressing laser frequency is far from resonance ($\omega_L \neq \omega_{ka}$), transitions to states with $k \neq a$ are highly improbable. In that case (just as for Equation 2.14 in the case of a nonresonant field), the probability $P_k(t) = |c_k(t)|^2 \ll 1$, and the first-order correction to the amplitude ${c_a}^{(1)}(t)$ vanishes. Therefore, the coupled equations must be solved using second-order perturbation theory:

$$c_a(t) \approx 1 - \sum_{k\neq a} \int_{\tau_D}^{t} dt' H'_{ak}(t') e^{i\omega_{ak}t'} \int_{\tau_D}^{t'} dt'' H'_{ka}(t'') e^{i\omega_{ka}t''}, \tag{2.18}$$

where $H'_{ka}(t) = -d_{ka}F_{L,0}f_L(t)\cos(\omega_L t)$ is known as the interaction Hamiltonian between the states $|k\rangle$ and $|a\rangle$.

Since $P_a(t) \approx 1$, the perturbation to the amplitude primarily affects the *phase* of $c_a(t)$. The significance of the time-dependent phase can be understood by writing the complex amplitude $c_a(t)$ as:

$$c_a(t) = |c_a(t)| e^{-i\eta(t)}. \tag{2.19}$$

Then, the component in the expansion of Equation 2.17 with $k = a$ can be written in the form:

$$c_a(t) e^{-iE_a t} = |c_a(t)| e^{-i\int_{\tau_D}^{t}[E_a + \Delta E_a(t\prime)]dt\prime}, \tag{2.20}$$

with $\Delta E_a(t) = \dot{\eta}(t)$. This suggests that the perturbation to $c_a(t)$ can be interpreted as a time-dependent energy shift of the state $|a\rangle$. Recalling that the unperturbed amplitude ${c_a}^{(0)} = 1$ and that the perturbation to the state is relatively small, we find:

$$\dot{c_a}(t) = \left(\frac{d}{dt}|c_a(t)|\right) e^{-i\eta(t)} - i c_a(t)\dot{\eta}(t) \approx -i\dot{\eta}(t). \tag{2.21}$$

Then,

$$\Delta E_a(t) = -i \sum_{k \neq a} H'_{ak}(t) e^{i\omega_{ak}t} \int_{\tau_D}^{t} dt' H'_{ka}(t') e^{i\omega_{ka}t\prime}. \tag{2.22}$$

The energy shift can be evaluated analytically for a double-exponential pulse shape $f_L(t) = e^{-\ln(2)|t|/\tau_L}$ containing multiple cycles of the laser field [39]:

$$\begin{aligned} \Delta E_a(t) &= -\frac{1}{2}\left(F_{0,L} f_L(t)\right)^2 \sum_{k \neq a} \left[\frac{\omega_{ka}|d_{ka}|^2}{\omega_{ka}^2 - \omega_L^2} \cos^2(\omega_L t) - i \frac{\omega_L |d_{ka}|^2}{\omega_{ka}^2 - \omega_L^2} \sin(2\omega_L t)\right] \\ &= -\tfrac{1}{2}\left(F_{0,L} f_L(t)\right)^2 [\alpha_a \cos^2(\omega_L t) - i\gamma_a \sin(2\omega_L t)], \end{aligned} \tag{2.23}$$

where $\alpha_a = \sum_{k \neq a} \frac{\omega_{ka}|d_{ka}|^2}{\omega_{ka}^2 - \omega_L^2}$ is the polarizability of the state $|a\rangle$ and $\gamma_a = \sum_{k \neq a} \frac{\omega_L |d_{ka}|^2}{\omega_{ka}^2 - \omega_L^2}$ specifies the changes in the magnitude of $c_a(t)$ due to the laser coupling, resulting in broadening of the energy level. The real and imaginary parts of $\Delta E_a(t)$, calculated for both the 1s3p and 1s4p states of helium, are plotted in Figure 2.2 as a function of the laser intensity.

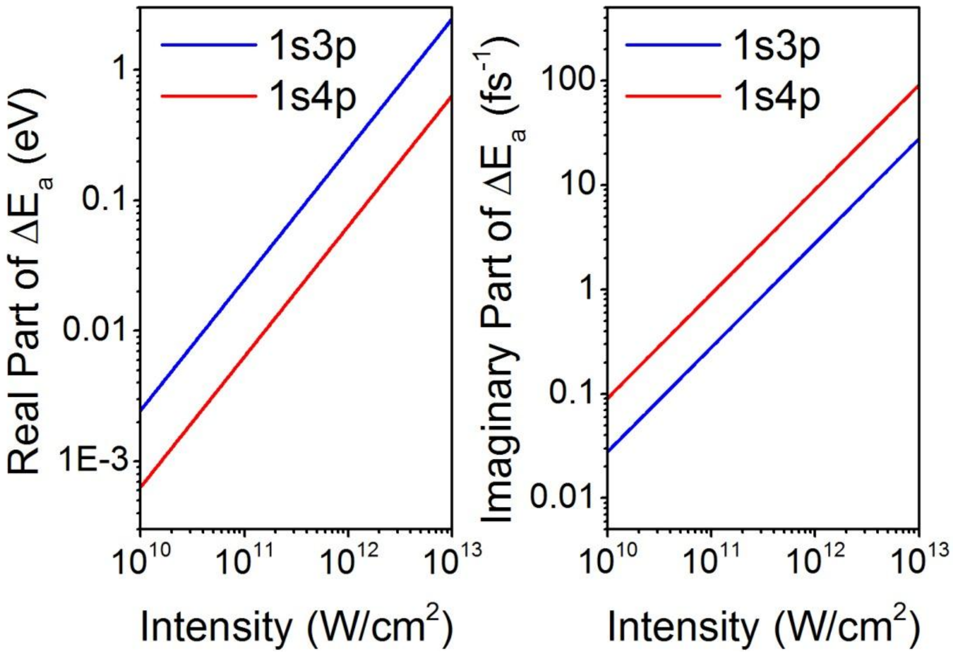

Figure 2.2: Real and imaginary parts of $\Delta E_a(t)$ calculated for the 1s3p and 1s4p excited states of helium.

Before the advent of attosecond pulses, it was not possible to access dynamics on timescales shorter than the laser cycle period due to the lack of laser pulses with sufficient time resolution. Therefore, the physical quantity measured in all previous time-resolved experiments (see for example [40-42]) is obtained by averaging $\Delta E_a(t)$ over time and is called the AC Stark shift [43]:

$$\overline{\Delta E_a}(t) = -\frac{1}{4}\alpha_a\left(F_{L,0}f_L(t)\right)^2. \tag{2.24}$$

We will refer to $\Delta E_a(t)$ as the *sub-cycle* AC Stark shift.

On the other hand, when the dressing laser field is near resonance with a given transition frequency $\omega_L = \omega_{ba} + \delta$ (here, $\delta \ll \omega_{ba}$), transitions between states $|a\rangle$ and $|b\rangle$ become probable and we can neglect all other states. In this case, a solution to Equation (2.17) in the limit of a long laser pulse can be obtained using the Floquet theorem [8]:

$$c_a(t) = \sum_{n=-\infty}^{\infty} \psi_n^{(a)} e^{-in\omega_L t} \tag{2.25}$$

$$c_b(t) = \sum_{n=-\infty}^{\infty} \psi_n^{(b)} e^{-in\omega_L t}, \tag{2.26}$$

where $\psi_n^{(a)}$ is the n^{th} harmonic component of the amplitude $c_a(t)$ with energy $E_a + n\omega_L$ [44]. Note that the component of $c_a(t)$ with $n = m$ and the component of $c_b(t)$ with $n = m - 1$ are degenerate for $\delta \to 0$. In the limit of weak fields, only the lowest-order (n = 0) component is populated, but higher-order splittings of the states are also possible. In general, a solution of the form $\psi_n^{(a)} = e^{-i\lambda_n t}$ can be found, which (along with Equations 2.17, 2.25, and 2.26) can be used to solve Equation 2.5 for λ, yielding (for n = 0):

$$\lambda_\pm = \frac{1}{2}\left(\delta \pm \sqrt{\delta^2 + \left(\frac{1}{2}|d_{ba}|F_{L,0}f_L(t)\right)^2}\right). \tag{2.27}$$

The general solution in the weak field limit is then:

$$c_a(t) = c_a^{(+)} e^{-i\lambda_+ t} + c_a^{(-)} e^{-i\lambda_- t}. \tag{2.28}$$

$$c_b(t) = c_b^{(+)} e^{-i\lambda_+ t} + c_b^{(-)} e^{-i\lambda_- t}, \tag{2.29}$$

and the wavefunction can be written as:

$$|\Psi(\boldsymbol{r},t)\rangle = e^{-iE_0 t}|0\rangle + e^{-i(E_a+\delta/2)t}\left(c_a^{(+)} e^{-i(\Omega_R/2)t} + c_a^{(-)} e^{i(\Omega_R/2)t}\right)|a\rangle$$

$$+e^{-i(E_b+\delta/2)t}\left(c_b^{(+)} e^{-i(\Omega_R/2)t} + c_b^{(-)} e^{i(\Omega_R/2)t}\right)|b\rangle, \tag{2.30}$$

where $\Omega_R = \sqrt{\delta^2 + \left(|d_{ba}|F_{L,0}f_L(t)\right)^2}$ is known as the Rabi frequency. Clearly, the energy levels of both $|a\rangle$ and $|b\rangle$ will be split into two symmetric lines with energies $E_a + \delta/2 \pm \Omega_R/2$, separated by the Rabi frequency, as illustrated in Figure 2.3. Since the Rabi frequency is approximately proportional to the laser electric field strength, the time-dependent line splitting will follow the laser pulse envelope.

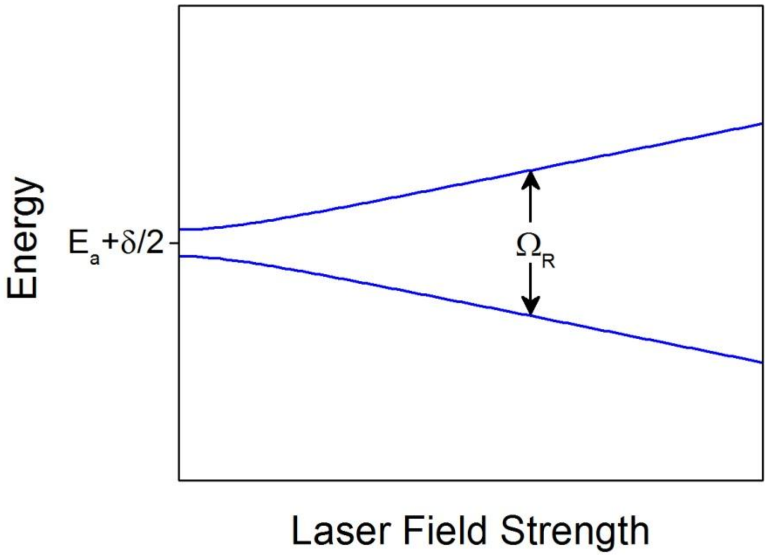

Figure 2.3: Autler-Townes splitting, specified by the Rabi frequency $\boldsymbol{\Omega_R}$.

This splitting was first observed in the formation of the so-called Autler-Townes doublet in the absorption spectrum of the OCS molecule [45]. In general, since couplings are primarily mediated by the resonance condition, that is, couplings between components of $c_a(t)$ with $n = m$ and components of $c_b(t)$ with $n = m - 1$ are dominant, the above derivation is also valid for stronger fields where multiple harmonic components are populated. In that case, each harmonic component will form an Autler-Townes doublet, and time-dependent interferences between adjacent components can occur when $\Omega_R \approx n\omega_L$. However, such time-resolved measurements have so far remained out of reach for experimentalists, due to the lack of short (attosecond) probe pulses.

Multi-Photon and Strong Field Ionization

When the laser field is sufficiently intense, processes in which multiple photons are absorbed or emitted can play a significant role, or even dominate. For example, a bound electron in an atom can be excited to a higher energy bound state by the absorption of multiple photons, a process known as multi-photon excitation (the inverse process of multi-photon emission is also possible). Generally, however, such processes can be understood by extending the treatments in the previous sections to higher orders of perturbation theory and the effects of multi-photon couplings are much weaker for moderate laser intensities than their single-photon counterparts. Of more significance, especially for excited states of the atom, are the processes of multi-photon and strong-field tunneling ionization, which will be discussed in this section. Note that the term "strong field" here refers to the strong field approximation, which neglects the influence of bound states other than the initial state.

For a low-frequency field ($\omega_L \ll I_p/n^2$) to ionize an atom in a given state $|n\rangle$ in the absence of additional resonances, the laser field strength must become comparable to the Coulomb field which binds the electron to the nucleus. For the ground state of hydrogen, this corresponds to the atomic unit of intensity, $I_{a.u.}$ = 3.5×10^{16} W/cm^2. However, for hydrogen-like atoms the Coulomb binding field drops as $V_C \sim 1/n^2$, and the critical intensity for which the laser field and Coulomb field are equal drops as $I_{crit} \sim 1/n^4$. Therefore, the laser peak field strengths needed to substantially ionize the excited states can be on the order of 10-100 times smaller than those for the ground state. Furthermore, for a fixed laser frequency, the low-frequency condition cannot be met for highly excited states, for which only a few photons are needed for ionization. Since the polarizability of the atom drops off rapidly when the ionization is substantial, understanding of strong-field and multi-photon ionization in these excited states is critical to the interpretation of attosecond time-resolved studies of laser-dressed bound state dynamics.

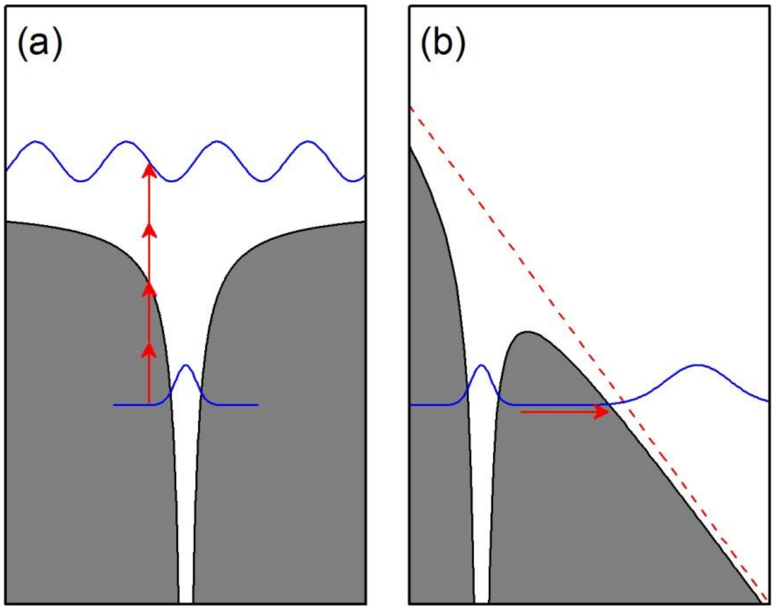

Figure 2.4: Ionization mechanisms in the Keldysh formalism. (a) Multi-photon ionization for $\gamma \gg 1$. (b) Tunneling ionization for $\gamma \ll 1$.

In the 1960's, Keldysh introduced a dimensionless parameter with which to categorize different "regimes" of strong field ionization [46]. The Keldysh parameter is given by:

$$\gamma = \frac{t_{tu}}{T_L} = \sqrt{\frac{E_I}{2U_p}}, \tag{2.31}$$

where $E_I = I_p/n^2$ is the energy needed to ionize a given state $|n\rangle$ with energy $E_n = I_p(1 - 1/n^2)$ and

$$U_p = F_L^2/4\omega_L^2 \tag{2.32}$$

is the cycle-averaged "quiver" energy of a free electron in the laser field, known as the ponderomotive energy. Physically, the Keldysh parameter represents the ratio between the tunneling time t_{tu} (the time needed for an electron to traverse the Coulomb barrier) and the laser cycle period $T_L = 2\pi/\omega_L$. When $\gamma \gg 1$, the tunneling time is much larger than the cycle period, and the ionization mechanism is classified as multi-photon ionization. The multi-photon ionization mechanism is characterized by the sequential absorption of multiple photons over many cycles of the laser. On the other hand, when $\gamma \ll 1$ the tunneling time is small, indicating that the ionization is dominated by tunneling through the suppressed Coulomb barrier within a fraction of the laser cycle. The two ionization mechanisms are illustrated in Figure 2.4.

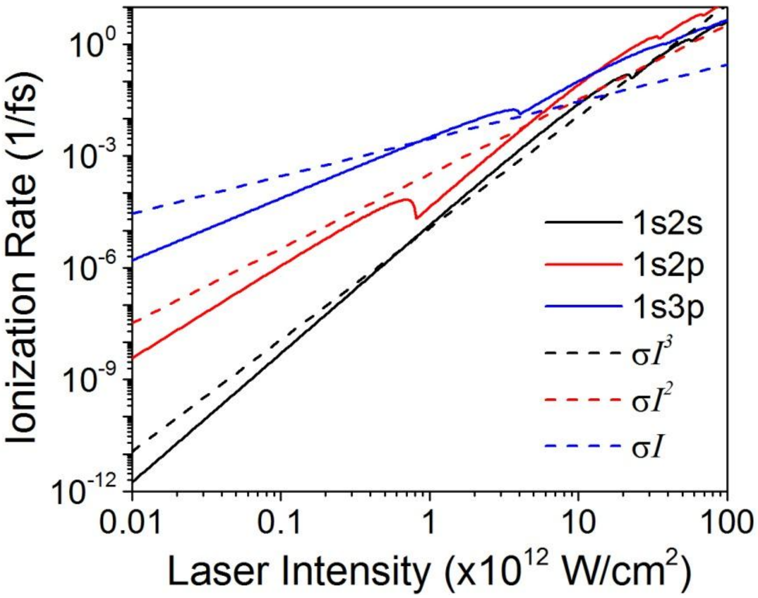

Figure 2.5: PPT ionization rates for the 1s2s, 1s2p, and 1s3p excited states of helium, compared with the simplified formula.

In 1966, Perelomov, Popov, and Terent'ev (PPT) developed a formula for the photoionization rate for a hydrogen-like atom with arbitrary initial state in a short-range Coulomb potential, which can be applied in both the multi-photon and tunneling ionization regimes [47]. The PPT model gives the total rate of single ionization from an initial state characterized by the quantum numbers (principle, orbital, and magnetic, respectively) n, l, and m as:

$$w_{PPT} = \sum_{q \geq q_{thr}} w_q(F_L, \omega_L), \tag{2.33}$$

where $q_{thr} \geq \left(E_I + U_p\right)/\omega_L$ is an integer representing the minimum number of photons needed to exceed the laser-shifted ionization threshold and w_q represents the rate of ionization through absorption of q photons. The q-photon ionization rate is given by:

$$w_q = A_q(\gamma, \omega_L)|C_{n^*l^*}|^2 G_{lm} E_I \left(\frac{2F_0}{F_L}\right)^{2n^*} \left(\frac{2F_0}{F_L\sqrt{1+\gamma^2}}\right)^{-|m|-1} \frac{4}{\sqrt{3\pi}} \frac{1}{|m|!} \frac{1}{1+\gamma^2} e^{-\frac{2F_0}{3F_L}g(\gamma)}. \tag{2.34}$$

Here,

$$A_q(\gamma, \omega_L) = e^{-(q-v)\alpha(\gamma)} w_m\left(\sqrt{(q-v)\beta(\gamma)}\right), \tag{2.35}$$

$$v = \frac{E_I + U_p}{\omega_L}, \tag{2.36}$$

$$\alpha(\gamma) = 2\left(\sinh^{-1}\gamma - \frac{\gamma}{\sqrt{1+\gamma^2}}\right), \tag{2.37}$$

$$\beta(\gamma) = \frac{2\gamma}{\sqrt{1+\gamma^2}}, \tag{2.38}$$

and

$$w_m(x) = \frac{x^{2|m|+1}}{2} \int_0^1 dt \frac{e^{-x^2 t} t^{|m|}}{\sqrt{1-t}}. \tag{2.39}$$

$(2F_0/F_L)^{2n^*}$ represents a first-order correction to the short-range Coulomb potential $F_0 = (2E_I)^{3/2}$. The effective principle quantum number is given by $n^* = Z/\sqrt{2E_I}$ and the effective orbital quantum number is $l^* = n^* - 1$. The coefficients are given by:

$$|C_{n^*l^*}|^2 = \frac{2^{2n^*}}{n^*\Gamma(n^*+l^*+1)\Gamma(n^*-l^*)}, \tag{2.40}$$

$$G_{lm} = \frac{(2l+1)(l+|m|)!}{2^{|m|}|m|!(l-|m|)!}, \tag{2.41}$$

$$g(\gamma) = \frac{3}{2\gamma}\left[\left(1+\frac{1}{2\gamma^2}\right)\sinh^{-1}\gamma - \frac{\sqrt{1+\gamma^2}}{2\gamma}\right]. \tag{2.42}$$

For moderate laser intensities (≤10^{13} W/cm^2), the PPT rate can be approximated by $w_{PPT} \approx \sigma I^{q_{thr}}$, where σ is the cross section and $q_{thr} \approx E_I/\omega_L$ [48]. This simplified formula clearly demonstrates the disparate ionization rates for different individual excited states, which are typically separated from the ionization threshold by only a few (~3 or fewer) photons. The PPT rates for the 1s2s ($q_{thr} \approx 3$ for λ_L = 750 nm), 1s2p ($q_{thr} \approx 2$), and 1s3p ($q_{thr} \approx 1$) excited states of helium are shown in Figure 2.5, and compared with the simplified formula. Clearly the simplified formula works best for the more deeply-bound excited states at relatively low intensities.

CHAPTER THREE:ISOLATED ATTOSECOND PULSES

The most critical tool in the studies of few- and sub-femtosecond dynamics is the isolated attosecond pulse. In particular, attosecond transient absorption studies on bound states in atoms and molecules require a stable source of isolated attosecond pulses with continuous spectra extending below the ionization potential of the target atom and covering the ground-to-excited state transition frequencies. In this chapter, I will discuss the current technology in isolated attosecond pulse generation, focusing in particular on the generalized double optical gating (GDOG) scheme used in the experiments presented in Chapters Five, Six, and Seven.

Attosecond Pulse Generation

When a femtosecond laser pulse is focused onto an atomic or molecular gas target, the laser peak field strength can become comparable to the Coulomb field, and electrons can be tunnel ionized within a fraction of the laser cycle. However, in addition to the signature of strong-field above-threshold ionization in the photoelectron signal, high-order harmonics of the driving laser frequency can also be generated. The generation of odd high-order harmonics was independently observed by researchers in France and the USA in the late 1980s [49,50]. Unlike the perturbative generation of optical harmonics [51], which were observed to decrease in intensity exponentially with the harmonic order, high-order harmonic generation (HHG) was characterized by a *plateau* in the harmonic spectrum within which the intensity is relatively constant and an abrupt *cutoff* above which no harmonics are produced. An illustration of the HHG spectrum, with the plateau and cutoff indicated, is shown in Figure 3.1.

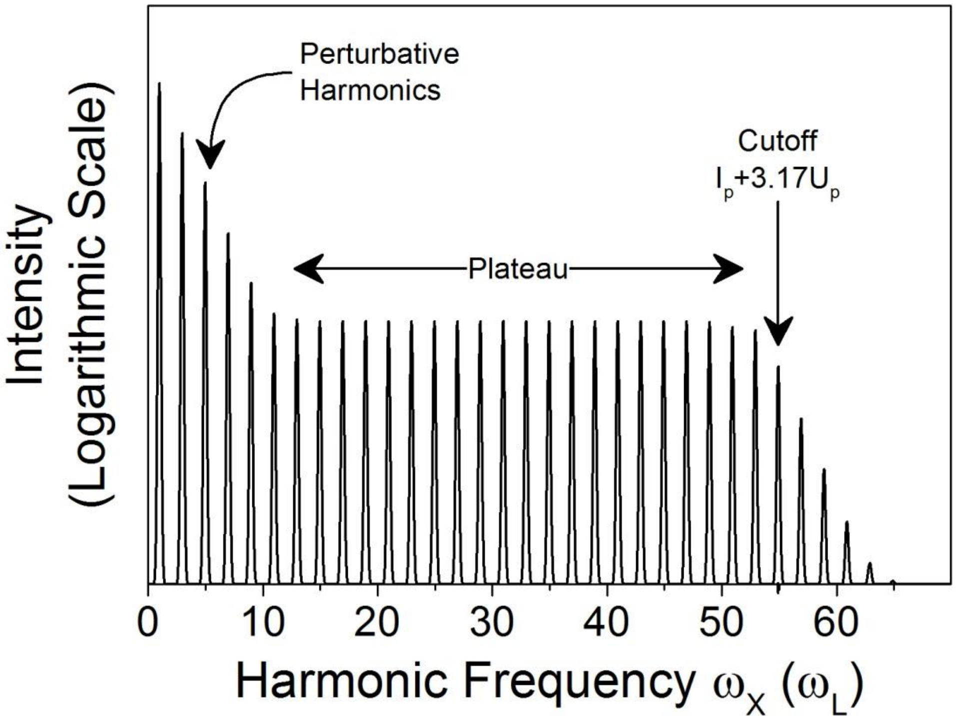

Figure 3.1: Illustration of the HHG spectrum driven by a linearly-polarized laser with frequency ω_L.

Recollision Model of High-Order Harmonic Generation

In 1993, a semiclassical model based on the strong field approximation was proposed to explain the generation of high-order harmonics [16,52], and was subsequently extended to a quantum mechanical description [53]. In its simplest form, the so-called recollision model consists of three steps: tunnel ionization of the valence electron, classical electron trajectories governed by the laser electric field, and recombination of the electron with the parent ion resulting in emission of a high energy photon. Despite its simplicity, the recollision model is capable of reproducing many of the defining characteristics of HHG. For example, by solving

Newton's equations, one can obtain two distinct electron trajectories leading to emission of a given photon energy, as illustrated in Figure 3.2. These two trajectories converge at the cutoff energy of $\omega_{cutoff} = I_p + 3.17U_p$, in good agreement with quantum mechanical simulations [53] and experimental observations [54-56]. Most importantly, the semiclassical recollision model suggests that the observation of the high-order harmonic spectrum results from the recurrent generation of an *attosecond pulse* once every half-cycle of the driving laser period: the attosecond pulse train with a repetition frequency of twice the laser frequency in the time domain results in a frequency spectrum consisting of discrete peaks at odd harmonic orders. The emergence of an attosecond pulse train from HHG was confirmed experimentally in 2001[57].

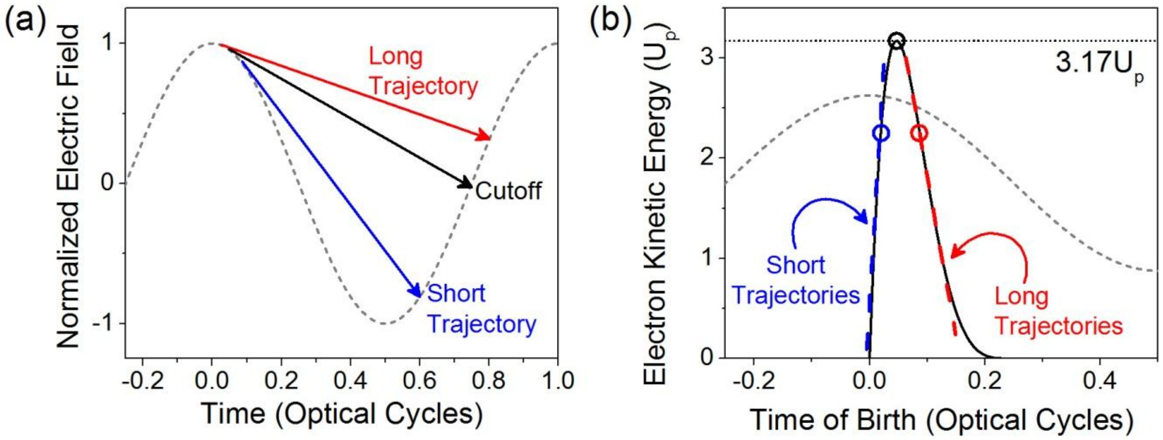

Figure 3.2: Recollision model of attosecond pulse generation. (a) Illustration of long and short trajectories. (b) Electron kinetic energy as a function of the time of birth. The trajectories shown in panel (a) are indicated by open circles in panel (b).

The predictions of the recollision model have guided the development of laser sources for HHG. For example, the cutoff harmonic order is predicted to scale quadratically with the driving laser wavelength. This dramatic extension of the HHG cutoff was observed experimentally in

2001 [58], and has since spurred significant research effort in the generation of shorter attosecond pulses [59-61] and the generation of hard x-ray high-order harmonics [62,63] with long-wavelength driving lasers. On the other hand, the recollision model predicts enhanced efficiency of high harmonic generation with short-wavelength driving lasers, which has recently been realized with 400 nm lasers [64,65]. Further extensions of the recollision model in elliptically-polarized fields have also been valuable in guiding the generation of isolated attosecond pulses [66,67].

Isolated Attosecond Pulses

Around the same time that attosecond pulse trains were first measured in the time domain, intense few-cycle laser pulses capable of generating only a few attosecond pulses in each train were available in a few laboratories [7,68,69]. When the driving laser pulse approaches a single optical cycle, the probability of ionization in the leading and trailing edges of the pulse can be orders of magnitude smaller than at the peak of the laser pulse, and an isolated attosecond pulse can be generated. This is the principle behind amplitude gating of attosecond pulses [17,70,71]. In practice, more than one attosecond pulse will always be generated due to the lack of temporally “clean” half-cycle pulses. However, an isolated attosecond pulse can be selected by applying a spectral filter to select only the cutoff orders, which are generated during the most intense half-cycle of the driving laser. Pulses as short as 80 attoseconds have been generated from the cutoff region (~80 eV photon energy) of the HHG spectrum using 3.3 *fs* driving laser pulses (less than 1.5 cycles at 720 nm) using this technique [71].

The amplitude gating technique can be extended to somewhat longer driving laser pulses by fully ionizing the target atom within the first few laser cycles. In this case, although the laser pulse contains several cycles, the atomic polarizability will drop to nearly zero upon the full ionization of the atom by the leading edge of the pulse, and attosecond pulses can be efficiently generated only within a single half-cycle of the laser pulse. This technique is known as ionization gating [72,73].

Isolated attosecond pulses can also be generated by multi-cycle (~5 *fs*) laser pulses with a time-dependent ellipticity [26,66,74]. This polarization gating takes advantage of the fact that attosecond pulses are generated efficiently only by linearly polarized driving lasers, as will be discussed in more detail in the next section. Whereas the amplitude gating and ionization gating can produce isolated attosecond pulses only from the cutoff regions of the harmonic spectrum, the polarization gating technique can produce attosecond pulses spanning both the plateau and cutoff regions [75].

Double Optical Gating

The double optical gating technique developed by our group is an extension of the polarization gating technique, which allows the generation of isolated attosecond pulses from relatively long (5 to 30 *fs*) driving laser pulses [27,76], which are available commercially and accessible to many laboratories. The DOG technique is covered extensively in several references (see, for example, [18,27,76-80]). However, since the attosecond pulses used in the experiments presented later in this thesis were generated primarily with the DOG technique, the principle of DOG and several key features will be covered here.

Principle of Double Optical Gating

The double optical gating combines the polarization gating with the two color gating [81,82] in order to relax the constraints on the driving laser pulse duration. In the polarization gating, the linearly polarized laser pulse is converted into two counter-rotating elliptically polarized pulses, which are combined with a fixed delay between them as illustrated schematically in Figure 3.3. Since the efficiency of high-order harmonic generation drops off rapidly with increasing ellipticity [83], generation of an isolated attosecond pulse can be confined to a single half-cycle of the driving laser field, in which the two elliptically polarized pulses overlap to produce a temporal “gate” within which the polarization is approximately linear. The temporal width of the polarization gate is given by [75]:

$$\delta t_G = \varepsilon \frac{1}{\ln 2} \xi_{thr} \frac{\tau_L^2}{T_D}, \tag{3.1}$$

where ε is the ellipticity of the counter-rotating pulses, ξ_{thr} is the threshold ellipticity (typically ~0.2) above which HHG becomes negligible [83], τ_L is the laser pulse duration, and T_D is the delay between the two counter-rotating pulses. Some constraints on the driving laser for the polarization gating can be set rather intuitively. Practically speaking, the delay between the two pulses should not exceed the pulse duration due to the need for high laser intensity to drive HHG within the gate. Therefore, τ_L/T_D cannot be made much smaller than one, and the gate width is limited to $\delta t_G \gtrsim \tau_L/4$ for circularly polarized pulses (ε = 1). Since a half-cycle gate width is desired to suppress the generation of satellite pulses and extract an isolated attosecond pulse, this implies that the pulse duration should contain fewer than two optical cycles (in practice, somewhat longer gate widths can be used in combination with carrier-envelope phase stabilization while still suppressing the satellite pulse emission). Polarization gating was demonstrated in 2006 to produce isolated attosecond pulses from 5 *fs* laser pulses [26], which are still difficult to maintain on a daily basis.

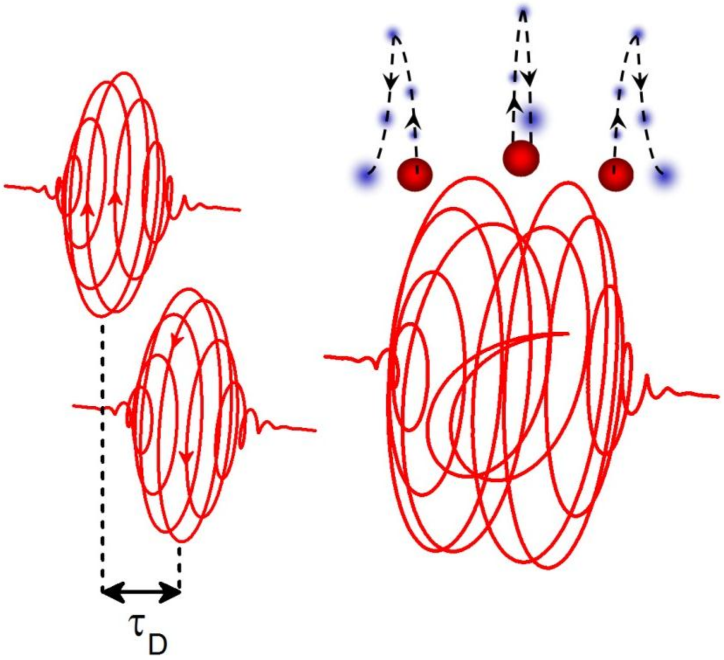

Figure 3.3: Illustration of polarization gating. Right and left elliptically-polarized laser pulses are combined with a fixed time delay to produce a pulse with a time-varying ellipticity. Only electrons produced within the linearly polarized "gate" will return to the parent ion.

To reduce this constraint, a weak second harmonic field is added to the driving laser, breaking the symmetry of the laser field. Due to the strong nonlinear dependence of the tunneling ionization rate on the laser intensity, attosecond pulses will be generated once every full-cycle of the driving laser field, instead of every half-cycle [81]. In this case, satellite pulses can be fully suppressed even when the gate width is increased to a full optical cycle, and isolated attosecond pulses can be generated from ~10 *fs* driving laser pulses [18]. Compared to 5 *fs* lasers, the generation and maintenance of 10 *fs* pulses is a relatively mature and robust technology.

The DOG technique was extended to even longer pulse durations in 2009 using the generalized double optical gating. As can be seen from Equation 3.1, when the ellipticity of the counter-rotating pulses is less than one, a half- or full-cycle gate width can be obtained with longer driving lasers. This was demonstrated for polarization gating in 2007 [84], although the gate width used could not fully suppress the generation of satellite pulses. Later, the GDOG was demonstrated with an ellipticity of 0.5 to generate isolated attosecond pulses from driving lasers as long as 28 *fs* [27], which can easily be generated directly from a Ti:Sapphire amplifier. The GDOG technique has additional advantages when used with relatively short driving laser pulses to reduce the polarization gate width, as will be discussed below.

Application of DOG to Absorption Measurements

The broadband supercontinuum spectra [19] generated by DOG and GDOG are particularly suited to time-resolved absorption studies in atoms and molecules. Most atoms and molecules have the bulk of their oscillator strength in the XUV wavelength region, corresponding to transitions from the atomic ground state to excited bound and quasi-bound states near the ionization threshold. For example, the bound states of helium lie between 20 and 25 eV above the ground state, while xenon, krypton, and argon all contain autoionizing state manifolds between 14 and 30 eV. Therefore, attosecond pulses with photon energies below 30 eV are needed. Whereas attosecond pulses generated with amplitude gating [71] and ionization gating [72] are typically centered at relatively high photon energies (~80-90 eV in both of these cases), polarization gating techniques allow isolated attosecond pulses to be produced from the high-order harmonic plateau.

Gating of the lowest harmonic orders remains a challenge, however. The threshold ellipticity ξ_{thr} is dependent on the harmonic order, growing larger for the lower orders [83] where the reduced excursion of the classical electron trajectories results in a relatively higher recombination probability in the elliptical field [67]. For harmonics around the 15th order (harmonic photon energy near 25 eV), the threshold ellipticity can exceed 0.4, resulting in an increase of the polarization gate width by a factor of two as compared to the previous discussion. By applying the GDOG technique with sub-10 *fs* driving laser pulses, the reduced ellipticity of the counter-rotating pulses in Equation 3.1 can counteract the increase of the threshold ellipticity for lower harmonic orders, allowing the gating of low-order harmonics. Using ε = 0.5, and ξ_{thr} = 0.4 (for generation of the 9th harmonic, ~15 eV, from xenon gas [83]) a full-cycle gate width can be achieved for a three-cycle pulse (7-8 *fs*), while a half-cycle gate width requires driving laser pulse durations below 4 *fs*. Since 5 *fs* pulses can be reliably achieved in our laboratory, half-cycle gate widths and attosecond pulses with spectra extending to nearly 15 eV can be applied to attosecond time-resolved absorption studies.

A further advantage of the GDOG technique is the ability to produce an isolated attosecond pulse which is phase-locked to the driving laser pulse even in the absence of carrier-envelope phase stabilization [80]. While other methods have been proposed to generate an isolated attosecond pulse in the absence of CEP locking [85], those pulses could not be stabilized to the driving laser pulse for pump-probe experiments. Instead, when an attosecond pulse is generated from GDOG with a half-cycle gate width, a maximum of one attosecond pulse can be generated within the gate width, which is intrinsically phase locked to the positive peak of the carrier-wave electric field due to the asymmetry in the two-color field. As the CEP changes on a shot-to-shot basis, the polarization gate moves with respect to the carrier-wave, and the efficiency of the attosecond pulse generation is modulated, but only one attosecond pulse is ever generated. In absorption measurements, which are typically averaged over many laser shots, the CEP instability amounts to an overall reduction in the measured signal level by a factor of ~2. Due to the difficulty of reliably locking the CEP over a period of several hours, the reduced count rate is an acceptable tradeoff for the ability to perform experiments in optically dense samples on a daily basis. The ability to generate isolated attosecond pulses without locking the carrier-envelope phase further allows for the extension of attosecond science and pump-probe measurements with attosecond pulses to petawatt-class lasers, for which CEP control has not been achieved.

Characterization of Isolated Attosecond Pulses

The characterization of isolated attosecond pulses relies upon the attosecond streaking spectroscopy discussed in Chapter Two. When an atom is photoionized by an isolated attosecond pulse, a photoelectron replica of the attosecond pulse is created. The interaction of the attosecond photoelectron wavepacket with a moderately intense (~10^{11}-10^{13} W/cm^2) dressing laser field can be used to extract the temporal profile of the attosecond pulse. In this chapter, two methods, FROG-CRAB (frequency-resolved optical gating for complete reconstruction of attosecond bursts) [20] and PROOF (phase retrieval by omega oscillation filtering) [34], for extracting the attosecond pulse duration from the laser-dressed photoionization spectrogram will be discussed. In particular, the performance of the principal component generalized projections algorithm (PCGPA) [86] for FROG-CRAB will be investigated for noisy traces with reduced energy resolution. Furthermore, the breakdown of the FROG-CRAB for ultrabroadband attosecond pulses will be discussed, and the PROOF technique will be introduced and demonstrated through simulations of extremely broadband attosecond pulses and also through the experimental characterization of a world-record-breaking 67 *as* pulse. Finally, a new implementation of the PROOF which takes advantage of the robustness of the PCGPA will be proposed and demonstrated.

Complete Reconstruction of Attosecond Bursts

When an atom in its ground state with ionization potential I_p absorbs an attosecond pulse with field $\boldsymbol{F}_X(t)$ in the presence of a delayed femtosecond laser pulse with vector potential $\boldsymbol{A}_L(t)$, the measured delay-dependent photoelectron spectrum can be obtained from Equations (2.7) and (2.8). When the two pulses share a common polarization axis, and the electrons with kinetic energy $W = v^2/2$ are detected at an angle θ with respect to the laser polarization direction, the photoelectron spectrum can be simplified as:

$$S(W,\tau_D) = |b(v,\infty)|^2 \approx \left|\int_{-\infty}^{\infty} dt F_X(t-\tau_D)\, d_z[v + A_L(t)] e^{i\varphi(v,t)} e^{-i(W+I_p)t}\right|, \qquad (3.2)$$

$$\varphi(v,t) = -\int_t^{\infty} dt' \left[v A_L(t') \cos\theta + {A_L}^2(t')/2\right]. \qquad (3.3)$$

The form of Equations 3.2 and 3.3 resembles that of the FROG trace [87]:

$$S_{FROG}(\omega,\tau) = \left|\int_{-\infty}^{\infty} dt P(t-\tau) G(t)\, e^{-i\omega t}\right|^2, \qquad (3.4)$$

which has been used for decades to characterize femtosecond laser pulses [87,88]. In the FROG language, $P(t)$ represents the pulse to be measured and $G(t)$ represents a gate function, which is usually a function of the pulse itself, but can also be unknown [89].

In applying the FROG to the retrieval of the attosecond pulse, it is natural to replace $P(t)$ with the attosecond pulse $F_X(t)$. However, whereas the FROG gate function can depend only on time, both the dipole matrix element $d_z[v + A_L(t)]$ and the phase $\varphi(v,t)$ depend on both momentum and time. When the bandwidth of the attosecond pulse spectrum is small compared to its central momentum v_0 (that is, the attosecond pulse contains several optical cycles), however, these terms do not vary much. Therefore, the FROG-CRAB removes the momentum dependence of these terms by substituting the central momentum $v_0 = \sqrt{2W_0}$, where W_0 is the central energy, into the gate function. In that case $d_z[v + A_L(t)]$ can be treated as a constant, and

$$\varphi(t) \approx -\int_t^\infty dt' U_p(t') + \frac{\sqrt{8W_0 U_p(t)}}{\omega_L} \cos\theta \cos(\omega_L t) - \frac{U_p(t)}{2\omega_L} \sin(\omega_L t) \qquad (3.5)$$

depends only on time. This substitution is known as the *central momentum approximation*, and suggests that the FROG-CRAB is only valid for multi-cycle attosecond pulses. Under this approximation, the streaking spectrogram will be referred to as a FROG-CRAB trace. In all further discussion of FROG and FROG-CRAB traces, the trace will be assumed to be normalized to the maximum signal level in the trace.

Reconstruction of FROG-CRAB Traces with Limited Signal Levels

Experimentally-obtained FROG-CRAB traces, unlike their femtosecond FROG counterparts, suffer from low count rates in the spectrogram [90]. A typical attosecond streak camera set-up, such as that shown in Figure 3.4 [91], consists of a laser focused to a gas jet or cell for generation of an isolated attosecond pulse. The attosecond pulse generated in a noble gas contains on the order of 10^6-10^7 photons per laser shot [78], very small compared to the photon number of femtosecond NIR lasers (~10^{15} photons per shot in a mJ-level laser with λ_L = 750 nm). After transmission of the XUV pulse through a metal foil filter (for example aluminum foil with a thin oxide layer), the photon number can be reduced to as little as 10%.

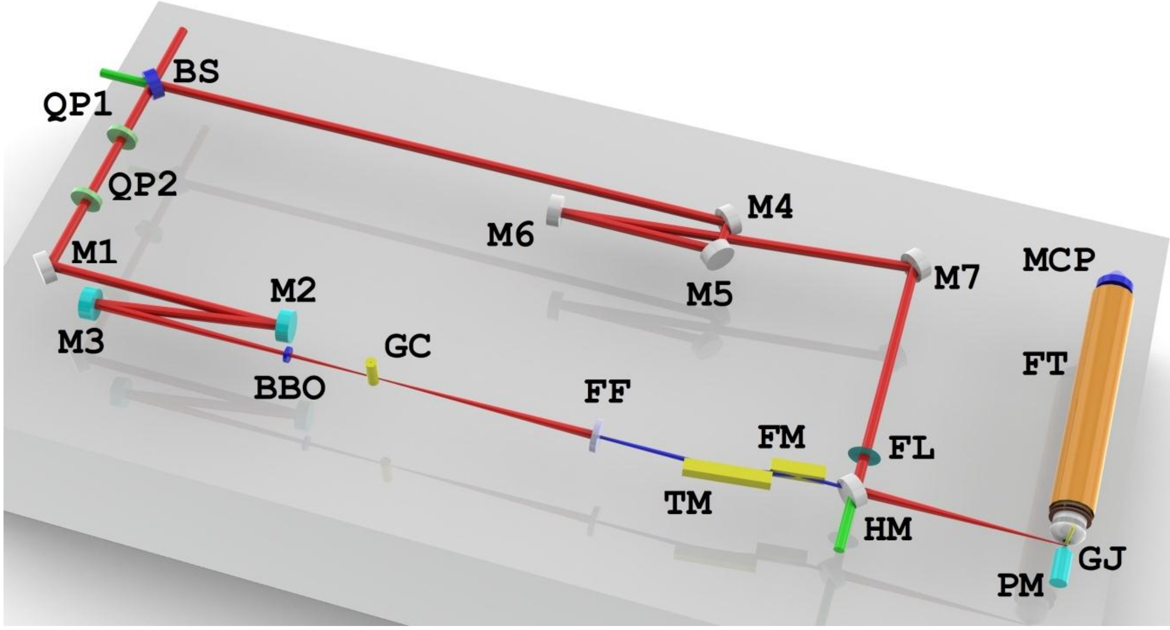

Figure 3.4: Attosecond streak camera setup with a Mach-Zehnder interferometer configuration. BS: beam splitter; QP1, QP2, and BBO: DOG optics; M1-7: mirrors; GC: gas cell; FF: foil filter; TM: Toroidal focusing mirror; FM: flat mirror; FL: focusing lens; HM: hole-drilled mirror; GJ: gas jet; PM, FT, and MCP: permanent magnet, flight tube and microchannel plate in the magnetic bottle photoelectron time-of-flight spectrometer.

While further reductions to the photon number occur due to the low reflectivity of the XUV optics, the most limiting factor for the count rate occurs in the conversion of the attosecond photons to photoelectrons at the second gas target. The atomic gases used to generate photoelectrons have XUV photoabsorption cross sections on the order of 10^{-17} cm^2 [92]. The absorption probability is also a function of the pressure-length product, but the gas pressure is limited by the microchannel plate (MCP) detector, which requires a vacuum of ~10^{-6} Torr to avoid damage. Even if the local gas density is maximized by using a small gas jet and high backing pressure, the gas density is limited by electron scattering and the probability of photoelectron production is less than 1%. Altogether, taking into account the XUV mirror reflectivity, as well as the small acceptance angle and quantum efficiency of the MCP, the overall efficiency of the photoelectron measurement can be as low as 10^{-6}-10^{-7}. Combined with the low XUV photon flux from the source, the poor detection efficiency limits the number of detected photoelectrons to approximately 1 per laser shot.

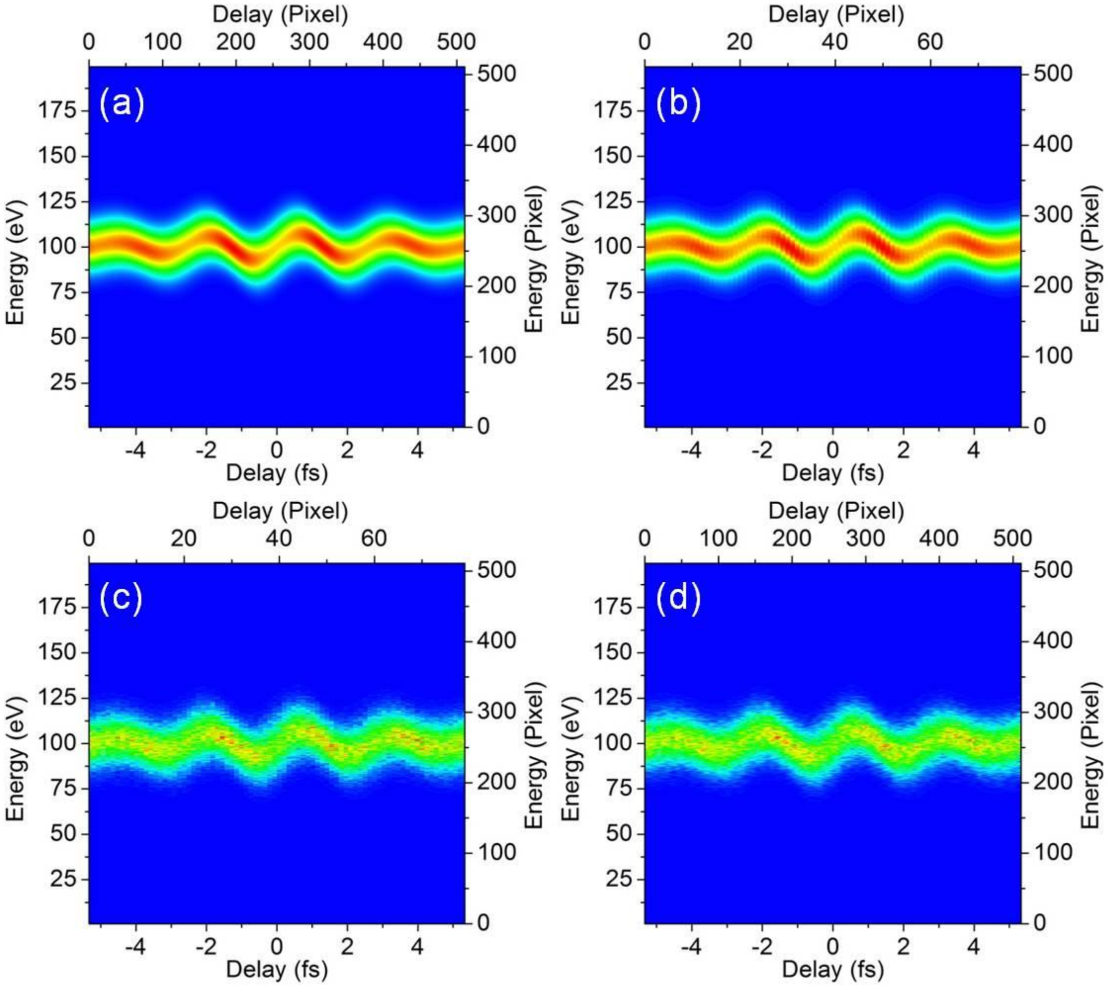

Figure 3.5: Preparation of simulated traces with added shot noise (adapted from [90]).

For such a small number of photoelectrons, statistical counting error or shot noise can significantly degrade the integrity of the FROG-CRAB trace unless the spectra are accumulated over many laser shots. In general, the attosecond streaking experiment requires milliJoule-level, CEP-stabilized laser pulses, which are available at repetition rates of only a few kHz. Maintaining pulse-to-pulse stability in energy, pulse duration, and CEP over even a few hours requires significant effort, making it a challenge to obtain a large statistical sample of photoelectron counts such that shot noise is negligible. Therefore, it is critical to investigate the retrieval of attosecond pulses from FROG-CRAB traces with low signal levels and to determine the signal-to-noise ratio needed for an accurate reconstruction of the attosecond pulse.

To investigate the effects of low signal levels in the FROG-CRAB trace, shot noise was added to simulated spectrograms. To achieve this, streaking spectrograms with XUV pulses for which the central momentum approximation is valid were simulated. The photoelectron spectrum, centered at 100 eV and with bandwidth to support a 90 *as* transform-limited pulse, was streaked by a 5 *fs* NIR laser pulse centered at 800 nm with a peak intensity of 1×10^{12} W/cm^2. The attosecond pulse was assumed to have an intrinsic linear chirp of 5000 as^2, broadening the pulse duration by approximately a factor of two to ~180 attoseconds. The detection angle θ was set to zero. To simulate shot noise in the traces, the simulated spectrogram described above and shown in Figure 3.5(a) was resampled to 80 delay steps separated by 130 *as* and 512 energy grids separated by 0.4 eV. The spectrogram was then normalized to a given peak count number (200, 100, 50, 25, and 10 counts in the peak pixel of the spectrogram, corresponding to roughly 10000, 5000, 2500, 1250, and 500 total photoelectron counts per delay step) and quantized to integer values, as shown in Figure 3.5(b). Shot noise following a Poisson distribution was then simulated using a Monte Carlo method and added to the trace, as shown in Figure 3.5(c) for a peak count number of 50. Finally, since the FROG-CRAB based on PCGPA requires the delay and energy step sizes $\delta\tau$ and δE, respectively, to satisfy the constraint $\delta\tau\delta E = 2\pi/N_E$, where N_E is the total number of energy samples [86], the trace was interpolated along a bicubic spline to a square grid of 512 × 512 pixels suitable for reconstruction with the PCGPA, shown in Figure 3.5(d). The process was also repeated for an attosecond pulse spectrum supporting 180 *as* pulses, again with a linear chirp of 5000 as^2.

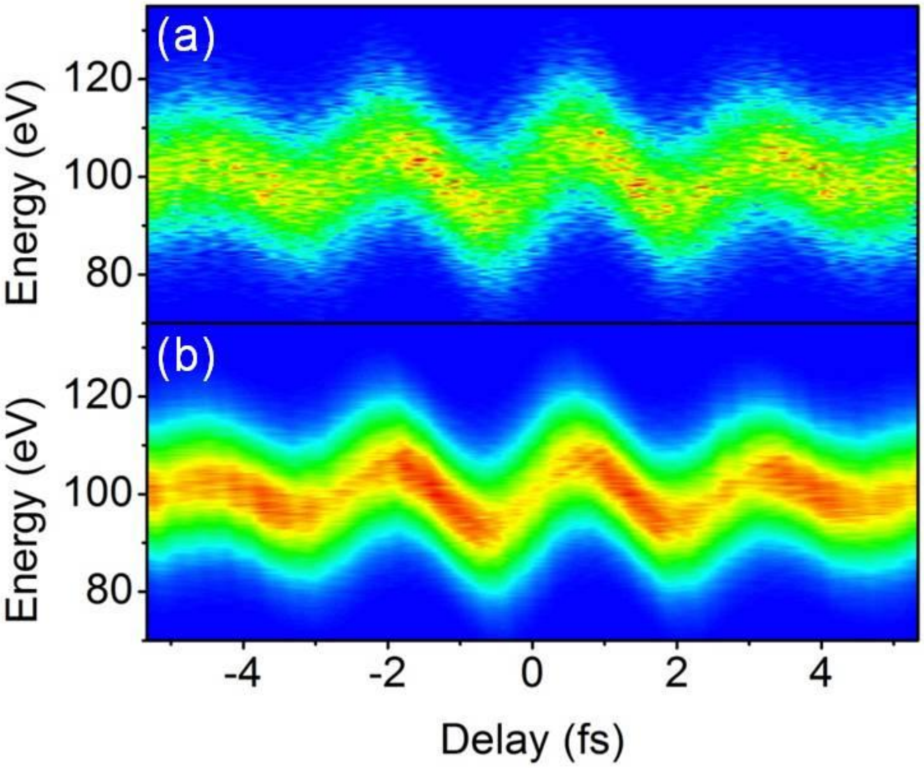

Figure 3.6: Comparison of (a) the simulated trace with added shot noise with (b) the trace retrieved from the PCGPA using the trace in (a) as input (adapted from [90]).

Figure 3.6 compares the input trace with that retrieved from the PCGPA. Qualitatively, the reconstructed trace in Figure 3.6(b) matches the noise-free trace in Figure 3.5(a) more closely than the noisy trace in Figure 3.6(a), reproduced from Figure 3.5(d). However, a quantitative comparison is necessary to assess the applicability of the FROG-CRAB to noisy traces.

Convergence of the PCGPA in FROG and FROG-CRAB is typically assessed using the FROG error, defined as the root-mean-square (RMS) difference between the guessed trace $\tilde{S}_{FROG}$ and input trace S'_{FROG}, both normalized to their maximum values:

$$\epsilon\left(\tilde{S}_{FROG}, S'_{FROG}\right) = \left\{\frac{1}{N^2}\sum_{i=1}^{N}\sum_{j=1}^{N}\left[\tilde{S}_{FROG}(W_i,\tau_j) - S'_{FROG}(W_i,\tau_j)\right]^2\right\}^{1/2}. \tag{3.6}$$

However, for a noisy trace, the FROG error will increase dramatically with the noise, even when the pulse is correctly retrieved. It is therefore useful to define a convergence criterion for simulations which simultaneously assesses the convergence to both the noisy and noise-free simulated traces.

We choose to adopt the convergence criterion proposed by Fittinghoff *et al.* [93], and consider convergence to have occurred for a trace with noise for:

$$R = \frac{\epsilon(\tilde{S}_{FROG}, S_{FROG})}{\epsilon(S'_{FROG}, S_{FROG})} < 2, \tag{3.7}$$

where S_{FROG} is the noise-free trace and the FROG error between the retrieved and noise-free traces is compared to that between the noisy and noise-free traces. The convergence criterion is chosen for an R below 2 (rather than 1) because the algorithm is given only the noisy trace as input, and we therefore cannot be expect the algorithm to converge to reproduce the noise-free trace. As is shown in Figure 3.7, the convergence criterion is found to be much less than 2 for all values of the maximum pixel count regardless of the attosecond pulse parameters and NIR laser intensities between 5×10^{11} and 2×10^{12} W/cm^2, indicating that the PCGPA converges to a solution much closer to the noise-free FROG-CRAB trace than to the noisy input trace.

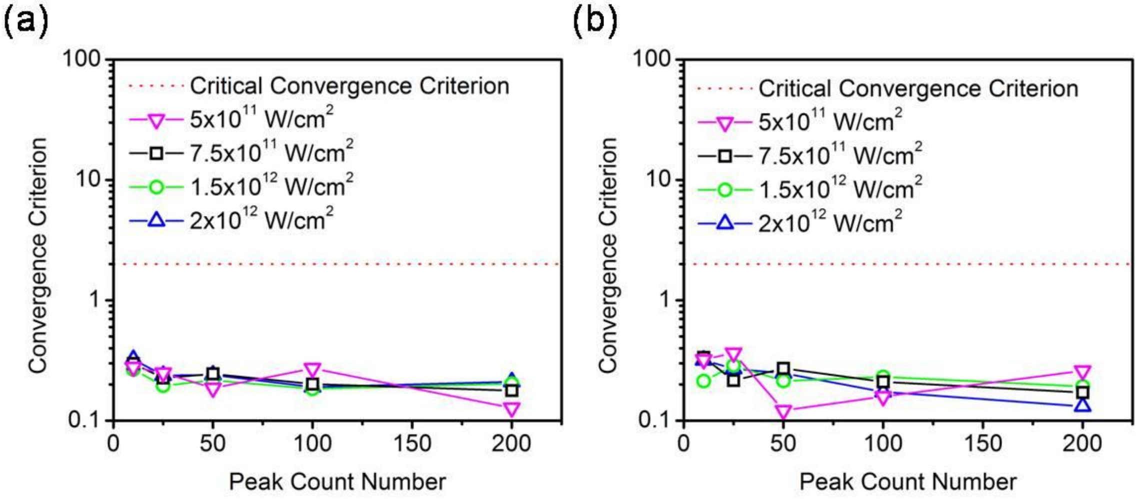

Figure 3.7: Convergence criterion for retrieved FROG-CRAB traces with various streaking laser intensities. The XUV spectrum in panel (a) supported 90 *as* transform-limited pulses, with 5000 *as*^{2} linear chirp, while the XUV spectrum in panel (b) supported 180 *as* transform-limited pulses. In both cases, 5000 *as*^{2} linear chirp was added to the pulse. In all cases, the convergence criterion is much less than one (adapted from [90]).

The retrieved attosecond pulse intensity and phase are shown for the cases of 200 and 10 counts in Figure 3.8(a) and (b) on linear and logarithmic scales, respectively. The retrieved FWHM pulse duration and linear chirp are plotted in Figure 3.9. For FROG-CRAB traces with at least 50 counts for the maximum pixel, we find that we are able to retrieve the pulse duration and linear chirp within 5% of their actual values when the streaking intensity is greater than 5×10^{11} W/cm^2 for XUV pulses with spectrum supporting 90 *as* transform limited pulse durations. These values are similar to the experimental error in previous measurement of sub-100 *as* pulses [71]. Similarly, when the XUV spectrum supports 180 *as* transform-limited pulses, we are able to retrieve the pulse duration within 3% and the linear chirp within 5% for traces with 50 counts or more. However, as the number of counts is further decreased, the PCGPA begins to severely miscalculate the pulse duration, indicating that it has failed to converge to an accurate result.

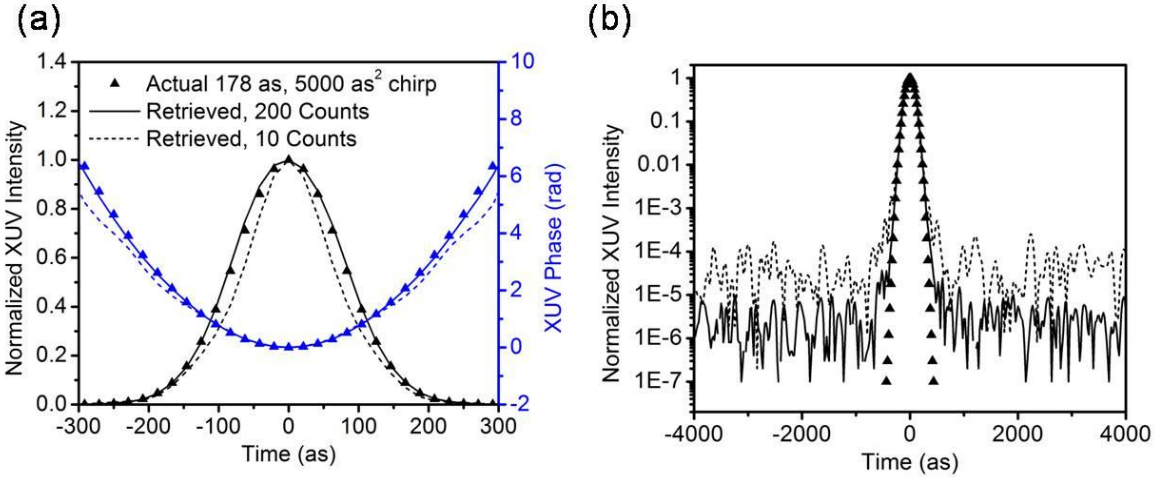

Figure 3.8: Comparison of the retrieved XUV pulse intensity and phase with a streaking laser intensity of 10^{12} W/cm^2 on (a) a linear scale and (b) a logarithmic scale for traces with added shot noise (adapted from [90]).

In order to further test the pulse retrieval with FROG-CRAB, experimental attosecond streaking data was used [27]. The isolated attosecond pulses were generated with the double optical gating. Because the data acquisition system records the photoelectron energy spectrum for each laser shot, we are easily able to select only a sample of data taken within a given time frame. In the experiment, the photoelectron energy was measured at 32 delay steps with a step size of 333 *as* for 60 s each. The spectral bandwidth supported attosecond pulses with transform-limited pulse durations of 137 *as*. The detector had 100 energy channels spanning 50 eV and a resolution of 0.7 eV determined by the precision of the timing electronics and the length of the TOF tube. By analyzing only the data from selected laser shots, we can observe what the resulting CRAB trace would be for accumulation times of less than 60 s.

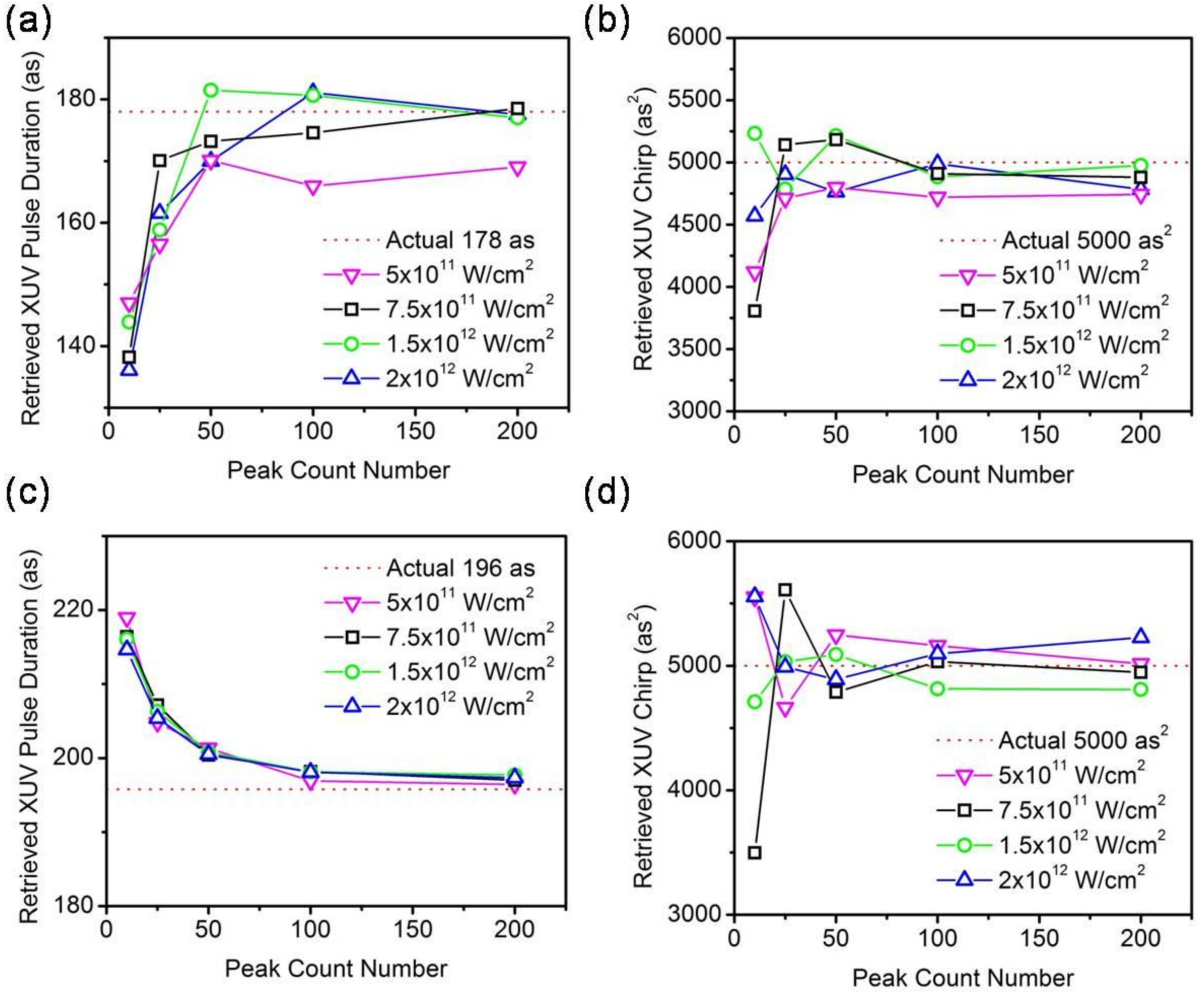

Figure 3.9: (a) Retrieved attosecond pulse duration and (b) linear chirp for pulses with spectrum supporting 90 *as* transform-limited pulses. For peak count numbers above 50, the pulse duration and linear chirp are retrieved within 5% of their actual values when the streaking laser intensity is greater than 5×10^{11} W/cm^{2}. (c) Retrieved attosecond pulse duration and (d) linear chirp for pulses with spectrum supporting 180 as transform-limited pulses. For peak count numbers above 50, the pulse duration and linear chirp are retrieved within 5% of their actual values for all tested streaking laser intensities (adapted from [90]).

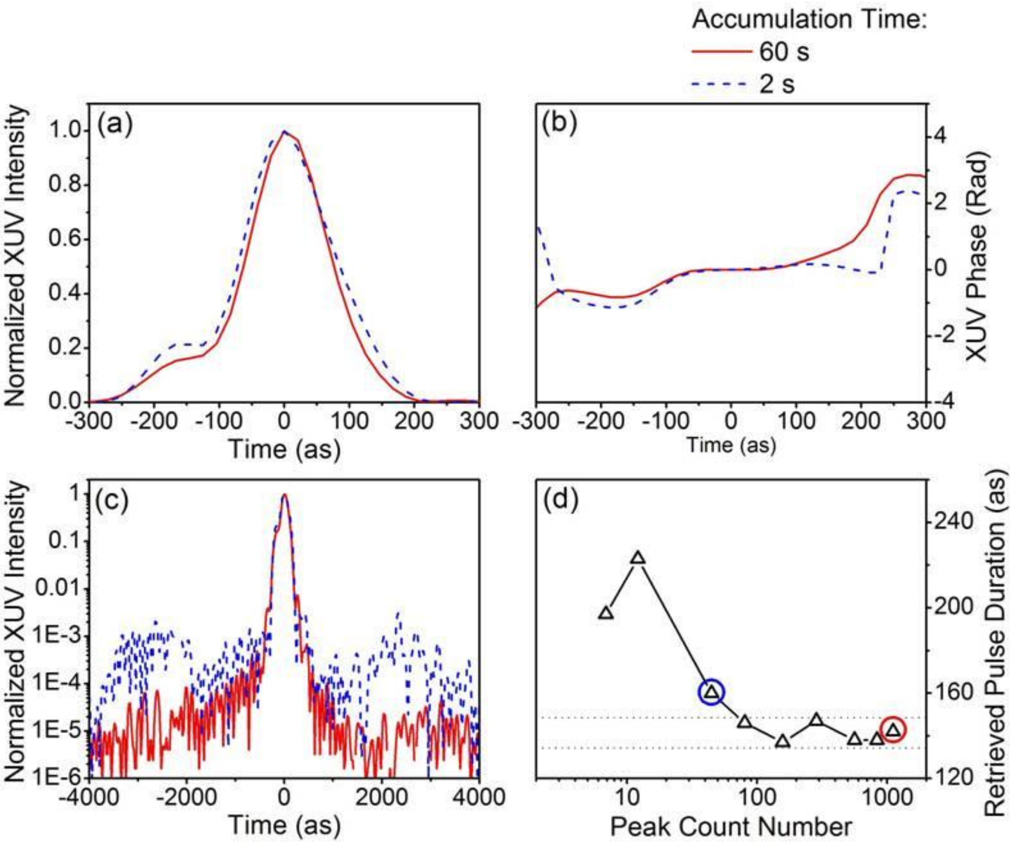

Figure 3.10: (a) Retrieved intensity and (b) temporal phase of the of the attosecond pulse generated with DOG in argon gas. The solid red line indicates a data accumulation time of 60 *s*, whereas the dashed blue line indicates an accumulation time of 2 *s*. The intensity profile in panel (a) is plotted on a logarithmic scale in panel (c). (d) Retrieved attosecond pulse duration for various accumulation times. The red and blue circles indicate retrievals with 60 *s* and 2 *s* accumulation times, respectively (adapted from [90]).

Figure 3.10 shows the reconstructed attosecond temporal profile and phase for effective accumulation times of 60 and 2 s (corresponding to total photoelectron counts of roughly 24500 and 800 for each delay step). It is important to note that the measured FROG-CRAB traces are corrected for background noise, such as above-threshold ionization electron counts, and the dipole transition matrix element corresponding to measured photoelectron momentum before reconstruction. However, such a correction is easily made and is independent of the shot noise. As can be seen in Figures 3.10(a) and (b), a decrease in the accumulation time by more than an order of magnitude yields only small differences in the temporal profile and phase of the reconstructed XUV pulse. Figure 3.10(c) shows the same temporal profiles as in (a) on a logarithmic intensity scale. A substantial increase in the noise in the wings of the pulse is present, just as in the simulated pulses. Such an error in the wings of the pulse is to be expected, due to the small number of photoelectron counts corresponding to the low-intensity portions of the pulse. Figure 3.10(d) shows the FWHM pulse duration for the different retrievals, as a function of the peak count number. The peak count number here must include the shot noise, as it is taken from experimental data. These simulations clearly demonstrate the robustness of the PCGPA to characterize isolated attosecond pulses even when the count rate in the experiments is low.

Reconstruction of Satellite Pulses of Isolated Attosecond Pulses

As discussed above, isolated attosecond pulses have been generated using a variety of gating techniques and characterized by attosecond streaking [26,27,71,72]. However, pre- and post-pulses always accompany the main pulse, separated by a half- or full-cycle of the driving laser field depending on the gating scheme [94]. Amplitude gating and polarization gating use single-color driving laser fields. In these cases, attosecond bursts are produced from photoelectrons ionized at both positive and negative extremes of the driving laser field, leading to a half-cycle separation between the main pulse and adjacent satellite pulses. In DOG and GDOG, however, a second harmonic field is added to the polarization gating field in order to break the symmetry of the driving laser field. This two-color technique leads to the production of attosecond bursts with full-cycle periodicity. Accurate characterization of the relative intensity of satellite pulses is crucial for proving the presence of a single isolated attosecond pulse as well as for improving the pulse contrast for experimental applications.

Ideally, the presence of satellite pulses can be determined from features in the FROG-CRAB trace. The interference between the main and satellite pulses will lead to modulations in the electron energy spectrum, with a period of one or two photon energy units for full- or half-cycle separations, respectively. However, the streaking field may influence the interference and introduce fringes along both the energy and delay axes, and fringes in the delay axis can be lost when the delay step is large [95]. Furthermore, experimental FROG-CRAB traces are susceptible to distortion due to the resolution of the electron spectrometer [96] and spatial variation of the streaking laser intensity, which can mask the presence of interference fringes in the spectrogram and lead to error in the reconstruction. These issues were certainly prevalent in the recent measurements of 80 *as* pulses [71], for which an alternative method was needed to estimate the relative intensity of the satellite pulses. Other groups have also reported the need for new methods to characterize the satellite pulse contrast [97]. Here, we determine the severity of these issues for retrieval of satellite pulses with full- and half-cycle separations from the FROG-CRAB.

In the simulations discussed below, the NIR streaking laser pulse was assumed to be 9 *fs* in duration with a spectrum centered at 800 nm and with peak intensity of 1×10^{12} W/cm^2. The XUV spectrum was assumed to support a 90 *as* transform-limited pulse duration, with satellite pulses separated by a half- or full-cycle of the NIR field. The satellite pulse contrast I_s/I_m was set to be 0.01 or 0.1, as indicated below, where I_m and I_s are the peak intensities of the main and satellite pulses, respectively. To account for the intrinsic chirp of the attosecond pulse, a linear chirp of 5000 as^2 was added in the spectral domain except where otherwise noted, such that the main and satellite pulses had identical temporal phase. The electron collection angle was set to zero. Using these parameters FROG-CRAB traces were generated and used as input to the PCGPA.

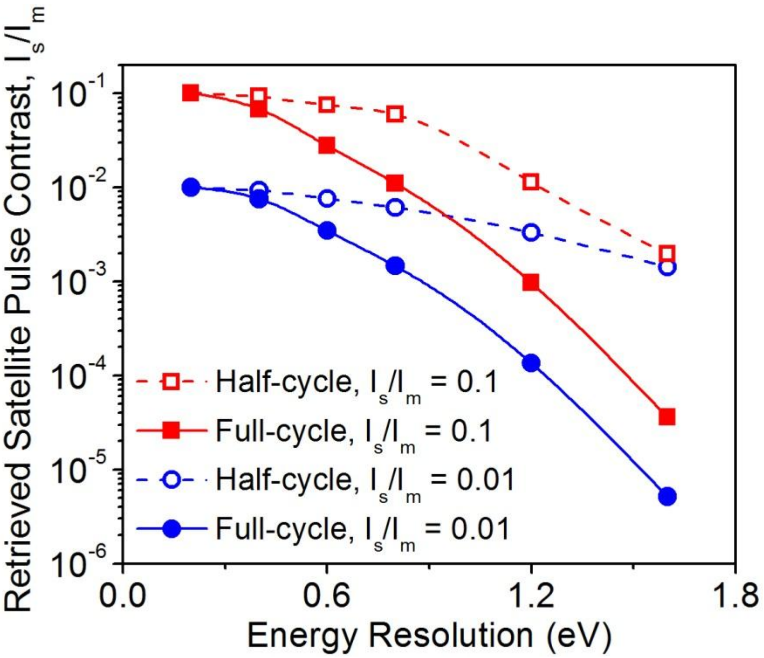

Figure 3.11: Retrieved satellite pulse contrast for half-cycle and full-cycle separations (adapted from [96]).

The most critical limiting factor on the retrieval of satellite pulses is the energy resolution of the electron spectrometer. Satellite pulses in DOG and GDOG are especially susceptible to the spectrometer energy resolution, since the full-cycle separation of satellite pulses results in interference modulations in energy with a period of only ~1.6 eV (compared to 3.2 eV for half-cycle separations). Figure 3.11 shows the satellite pulse contrast retrieved for both half-cycle and full-cycle periodicities from the FROG-CRAB method with simulated noise-free data, as a function of the spectrometer energy resolution [96]. The results show that the required resolution in the whole energy range should be better than 0.6 eV if the retrieved satellite pulse contrast is to be retrieved within 50% of the real value for satellite pulses with full-cycle separation.

Volume Effects on Retrieving Satellite Pulses

Clearly the phase $\varphi(t)$ in Equation 3.5 and thus the FROG-CRAB trace depend on the streaking laser intensity. However, in experiments, the electrons are produced within a volume of the target gas determined by the XUV spot size and the length of the interaction region. Within this volume, the streaking laser intensity varies both transversely and longitudinally. Specifically, the intensity varies by a factor of two within the Rayleigh range and has a Bessel-Gaussian profile along the transverse direction [98]. Typical mirrors used to focus the XUV and NIR pulses to the target gas have surface figure errors much larger than the XUV wavelength, which can lead to a distorted XUV focal spot similar in size to the NIR focal spot [99]. Photoelectrons born at different locations are thus streaked by different laser intensities, which causes smearing along the energy axis of the FROG-CRAB trace.

In order to study this effect, FROG-CRAB traces simulated using different NIR streaking intensities were averaged together and sent to the PCGPA for retrieval. We assumed the XUV and NIR focal spots to be Gaussian in shape and weighted the average by the relative XUV flux corresponding to each intensity. Figures 3.12(a) and (b) show the retrieval results for XUV pulses with satellite pulses of 1% contrast separated by a full- and half-cycle of the streaking field, respectively. The spot size ratio was set to w_{XUV}/w_{NIR} = 0.5, where w_{XUV} and w_{NIR} are the

$1/e^2$ radii of the XUV and NIR focal spots, respectively. We find that for full-cycle separation, the relative intensity and temporal phase of the satellite pulses can be retrieved when the XUV-to-NIR spot size ratio is 0.5. For half-cycle separation, the relative intensity of the satellite pulses is underestimated by nearly 30% for the same spot size ratio.

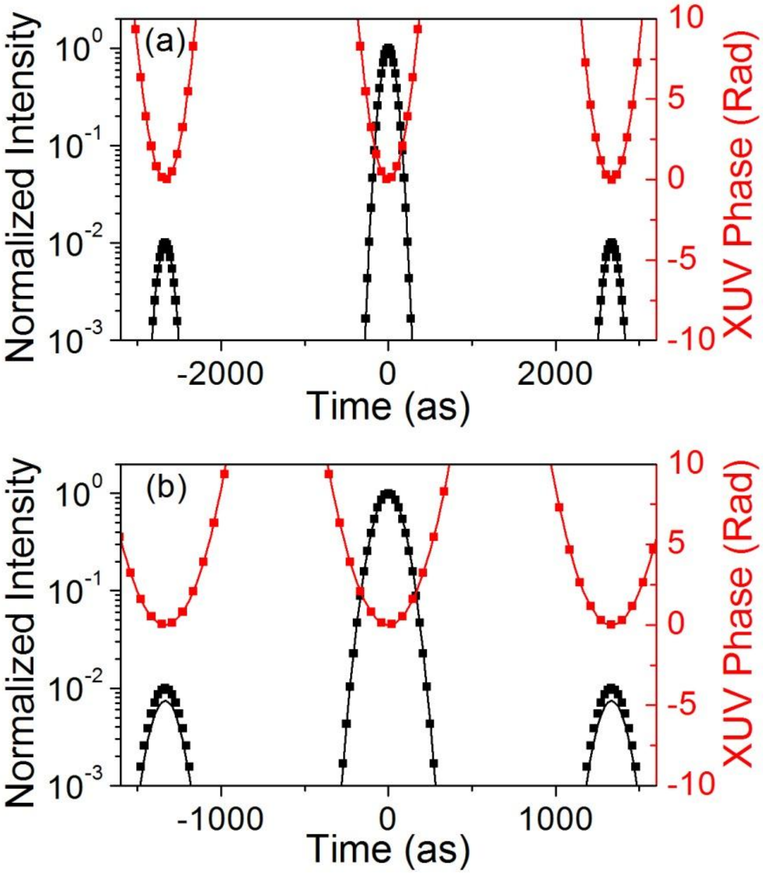

Figure 3.12: Comparison of actual (symbols) and retrieved (solid lines) intensity and phase of attosecond pulses with satellite pulses separated from the main pulse by (a) a full cycle and (b) a half cycle of the driving laser field (adapted from [94]).

As the spot size ratio is further increased, thus increasing the intensity variation, the satellite pulses with full-cycle separation can still be retrieved accurately, whereas those with half-cycle separation are underestimated even more. This is shown for chirped attosecond pulses in Figures 3.13(a) and for transform-limited pulses in Figure 3.13(b). As the intensity variation increases, the satellite pulses with full-cycle separation are always retrieved within 2%, whereas those with half-cycle separation are underestimated by nearly an order of magnitude. For half-cycle separation with a contrast of 0.1, the PCGPA failed to converge properly for spot size ratios greater than 0.9 for chirped pulses and greater than 0.7 for transform-limited pulses.

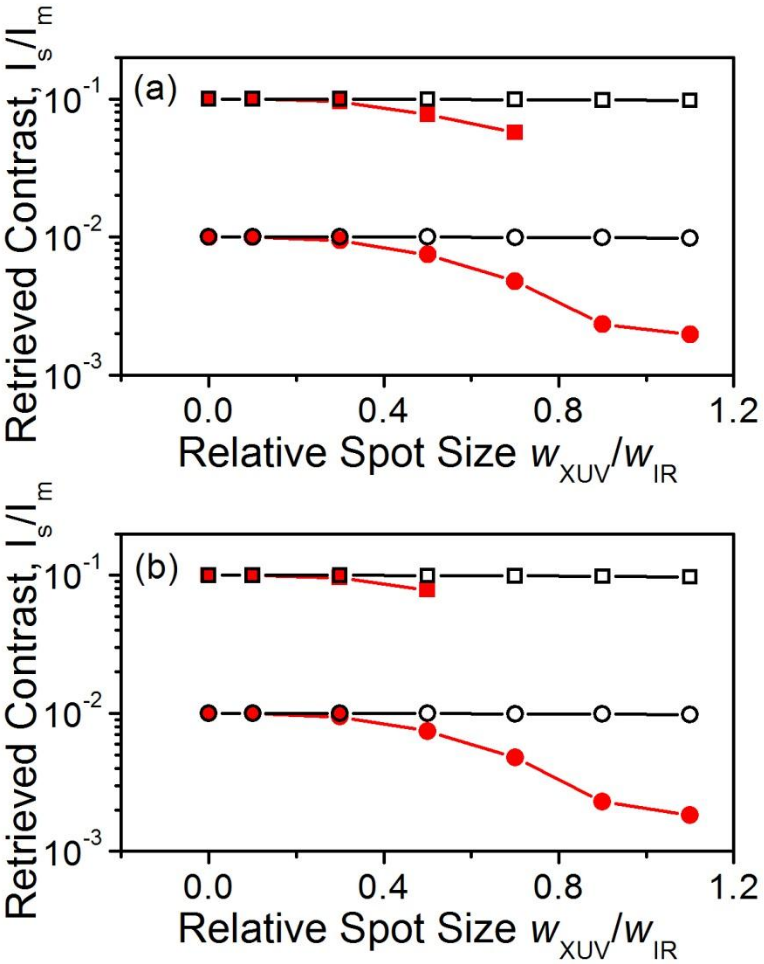

Figure 3.13: Retrieved satellite pulse contrast for attosecond pulses with full-cycle (black open symbols) and half-cycle (red filled symbols) separation, and with (a) 5000 *as*^{2} linear chirp and (b) flat phase. The satellite pulses with full-cycle separation are always retrieved within an accuracy of 2%, whereas those with half-cycle separation are severely underestimated when the laser intensity variation is large (adapted from [94]).

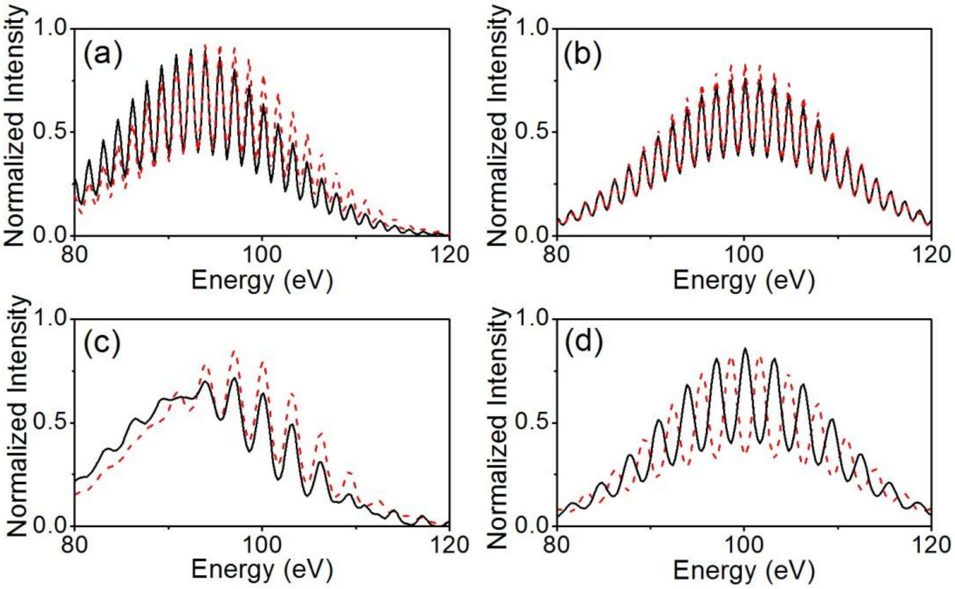

Figure 3.14: Interference of satellite pulses in the photoelectron energy spectrum with intensities of 1×1012 W/cm2 (black solid line) and 5×1011 W/cm2 (red dashed line). (a) Full-cycle separation, delay τ_D = 2 *fs*. (b) Full-cycle separation, delay τ_D = 0 *fs*. (c) Half-cycle separation, delay τ_D = 2 *fs*. (d) Half-cycle separation, delay τ_D = 0 *fs* (adapted from [94]).

This effect can in fact be easily understood when the streaking laser field contains several optical cycles. For satellite pulses with full-cycle separation, the main and satellite pulses are streaked in the same direction. Therefore, when the temporal phase of the satellite pulse is similar to that of the main pulse, only the full-cycle separation determines the spectral interference. Therefore, the interference from photoelectron spectra produced by different streaking intensities will remain in phase, as is shown in Figures 3.14(a) and (b). However, for satellite pulses with half-cycle separation, the main and satellite pulses are streaked in opposite directions. The features of this interference pattern differ for different streaking intensities, and the interference patterns will move in and out of phase with one another, as is shown in Figures

3.14(c) and (d). This effect will smear out the spectral fringes when the intensity fluctuates, leading to an underestimation of the satellite pulse intensity.

Effects of the Delay Step Size

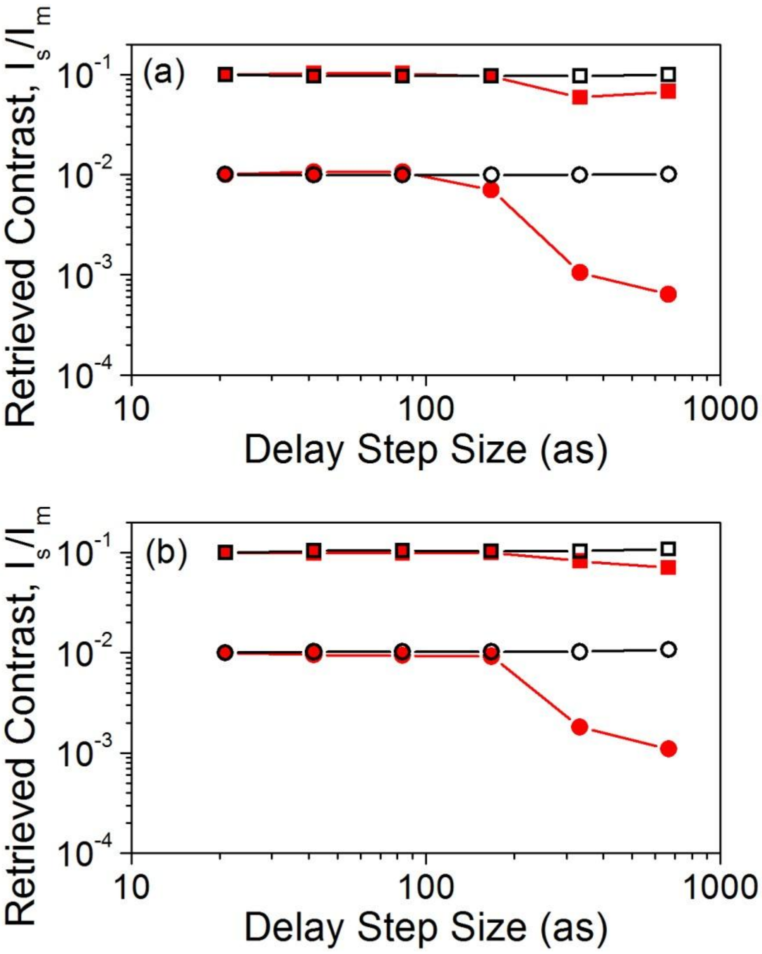

Figure 3.15: Retrieved Satellite pulses for attosecond pulses with full-cycle (black open symbols) and half-cycle (red filled symbols) separation and with (a) 5000 *as*^{2} linear chirp and (b) flat phase. The satellite pulse contrast is always retrieved within 4% for full-cycle separation. For half-cycle separation, the contrast can be underestimated by more than an order of magnitude (adapted from [94]).

Error in the reconstruction of satellite pulses can also stem from poor resolution along the delay axis in experimental FROG-CRAB traces [100]. Because streaking experiments must be performed with finite delay step sizes, fast modulation of the interference along the delay axis may be lost if the delay step is too large [95,101]. To study this effect on the reconstruction of satellite pulses, simulated traces with no streaking intensity variation were resampled to a smaller number of delay steps, and then interpolated to a square grid of 512×512 pixels suitable for the PCGPA. The results are shown in Figures 3.15(a) and (b) for chirped and transform-limited attosecond pulses, respectively. We find that the satellite pulse contrast is accurately retrieved for delay steps below ~100 as when the pulses are separated by a half cycle of the streaking field, whereas the contrast is always retrieved accurately for full-cycle separation.

Breakdown for Ultrabroadband Pulses

Recent progress in gating of isolated attosecond pulses from HHG promises to push the limits on optical pulse durations below the atomic unit of time, 24 *as*, which corresponds to a bandwidth broader than 75 eV. Already, generation of shorter attosecond pulse durations has not been limited by the available bandwidth of the XUV light, as continuum spectra supporting 45 *as* from polarization gating [102] and 16 *as* from DOG [19] have recently been demonstrated. However, such pulses could not be temporally characterized with current pulse measurement techniques.

The FROG-CRAB technique has a major limitation: the central momentum approximation, which assumes that the bandwidth of the attosecond pulse is much smaller than the central energy of the photoelectrons. This approximation is needed to apply the FROG phase retrieval techniques developed for measurement of femtosecond lasers, as discussed above, and it poses a limitation on the shortest attosecond pulses that can be characterized at a given center photon energy. Even in the current state-of-the-art experiments [26,27,71], the central momentum approximation is only barely met, and measurement of even shorter pulses would almost certainly violate the approximation. Furthermore, in the attosecond streaking model, the time resolution is determined by the streaking laser intensity [28,90]. High NIR laser intensity is needed so that the broadening of the electron spectrum width is comparable to the bandwidth of the attosecond pulse to be measured [24], which requires intensity greater than 10^{14} W/cm^2 to characterize a 70 *as* pulse centered at 100 eV. Note that such a large spectral broadening can lead to a breakdown of the central momentum approximation even for relatively narrow bandwidth pulses. Recent work done in our group indicates that the streaking model overestimates the required streaking intensity for FROG-CRAB [90], but that high intensities are still needed to measure even shorter pulses. For characterizing 25 *as* pulses centered at 100 eV, the required laser intensity would almost certainly produce high-energy photoelectrons through multi-photon and tunnel ionization of the target atoms, which would overlap with the attosecond photoelectron spectrum and destroy much of the information encoded in the streaked spectrogram.

Phase Retrieval by Omega Oscillation Filtering

For this reason, new methods are needed to characterize ultrabroadband attosecond pulses. Here, we propose and demonstrate the PROOF technique (phase retrieval by omega oscillation filtering), which requires only modest dressing laser intensities and is not limited by the attosecond spectrum bandwidth [34]. It should be noted here that the spectral phase (and therefore the average pulse duration) of attosecond pulse trains can also be obtained using the PROOF, although we will focus exclusively on isolated attosecond pulses.

An isolated attosecond pulse can be described by the Fourier transform:

$$F_X(t) = \int_{-\infty}^{\infty} d\omega U(\omega) e^{i\phi(\omega)} e^{i\omega t}. \tag{3.8}$$

Because it is relatively easy to measure the power spectrum $I(\omega) = |U(\omega)|^2$, only an accurate measurement of the spectral phase $\phi(\omega)$ is needed to fully describe the pulse. Here we show that the phase of isolated attosecond pulses can be accurately measured using spectral interference in the low-intensity limit of the laser-dressed photoionization process described in Chapter Two.

For the characterization of attosecond XUV pulses with PROOF, the experimental setup for obtaining the photoelectron spectrogram is very similar to that used for FROG-CRAB, except that the laser intensity can be much lower. Just as in FROG-CRAB, the spectrum of photoelectrons produced by the XUV pulse in the presence of a NIR field is measured as a function of the time delay τ_D between the two pulses. The difference between the PROOF and the FROG-CRAB is in the mechanism of phase encoding in the electron spectrogram and the method of pulse retrieval.

The spectral phase encoding in PROOF can be described by quantum interference of continuum states caused by the dressing laser. The interference of those states coupled by the laser causes the electron signal at a given kinetic energy W to oscillate with the delay as illustrated in Figure 3.16(a). This sinusoidal oscillation is governed by the amplitude and phase of each of the interfering spectral components. When the component of the oscillation with the dressing laser frequency ω_L is extracted, as shown in Figures 3.16(b) and (c), the interference is related to the spectral phases $\phi(\omega_v)$, $\phi(\omega_v + \omega_L)$, and $\phi(\omega_v - \omega_L)$ of the three frequency components separated by the laser photon energy, where $\omega_v = W + I_p$ is the photon energy which produces a photoelectron with momentum v in the absence of the NIR laser field. The spectral phase can therefore be decoded from the ω_L oscillation of the signal at each energy, measured as a function of the delay between the XUV pulse and the NIR field.

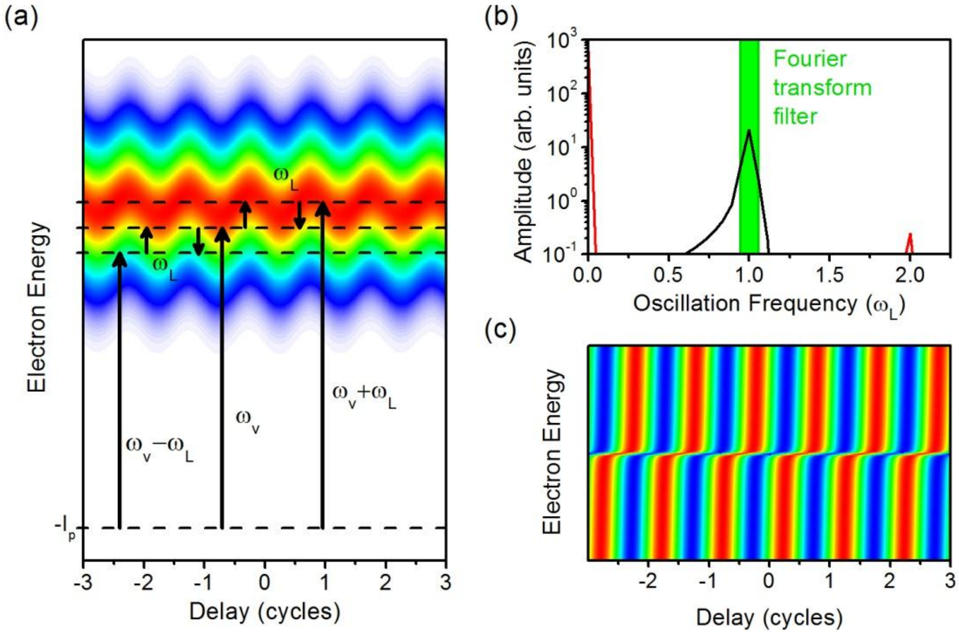

Figure 3.16: Phase encoding in PROOF. (a) Principle of quantum interference in PROOF. Continuum states with energy separated by ω_L are coupled by the dressing laser, leading to the characteristic oscillation of the photoelectron signal with delay. (b) Fourier transform amplitude of the signal at one electron energy in panel (a). (c) Spectrogram obtained by inverse Fourier transform of the filtered component (adapted from [34]).

In the PROOF, which like FROG-CRAB relies on XUV and NIR pulses polarized along the detector axis, the photoelectron spectrum is given by Equations 3.2 and 3.3, with the phase $\varphi(v,t)$ given by:

$$\varphi(v,t) \approx -\int_t^\infty dt' U_p(t') + \frac{vF_{L,0}f_L(t)}{\omega_L^2}\cos\theta\cos(\omega_L t) - \frac{U_p(t)}{2\omega_L}\sin(\omega_L t). \quad (3.9)$$

Equation 3.9 differs from Equation 3.5 in that the central momentum is not substituted for the photoelectron momentum v. For relatively long, low intensity fields and $\theta \approx 0$, the second term dominates, and

$$\varphi(v,t) \approx \frac{vF_{L,0}}{\omega_L^2}\cos(\omega_L t) = \frac{vF_{L,0}}{2\omega_L^2}\left(e^{i\omega_L t} + e^{-i\omega_L t}\right). \tag{3.10}$$

When the energy shift of the streaking is much less than the energy of a single NIR photon (i.e.; $vF_{L,0}/\omega_L \ll \omega_L$) then:

$$e^{i\varphi(v,t)} \approx 1 + i\varphi(v,t), \tag{3.11}$$

and the amplitude of the electron wavepacket is given by:

$$b(v,\tau_D) \propto \int_{-\infty}^{\infty} dt F_X(t-\tau)\left[1 + i\frac{vF_{L,0}}{2\omega_L^2}\left(e^{i\omega_L t} + e^{-i\omega_L t}\right)\right] e^{-i\left(v^2/2+I_p\right)t}. \tag{3.12}$$

Then, integration of Equation 3.12, substituting Equation 3.8 for the XUV pulse yields:

$$b(v,\tau_D) \approx e^{-i\omega_v\tau_D}\left\{U(\omega_v)e^{i\phi(\omega_v)} + i\frac{vF_{L,0}}{2\omega_L^2}\left[U(\omega_v+\omega_L)e^{i\phi(\omega_v+\omega_L)}e^{-i\omega_L\tau_D} + U(\omega_v-\omega_L)e^{i\phi(\omega_v-\omega_L)}e^{i\omega_L\tau_D}\right]\right\}. \tag{3.13}$$

The measured signal then has three components, $S(W,\tau_D) = |b(v,\tau_D)|^2 \approx S_0 + S_{\omega_L} + S_{2\omega_L}$, where

$$S_0 = |U(\omega_v)|^2 + \left(vF_{0,L}/2\omega_L^2\right)^2\left(|U(\omega_v+\omega_L)|^2 + |U(\omega_v-\omega_L)|^2\right) \tag{3.14}$$

does not change with the delay,

$$S_{\omega_L}(W,\tau_D) = \frac{vF_{0,L}}{\omega_L^2}U(\omega_v)\left[U(\omega_v+\omega_L)\sin\left(\omega_L\tau_D + \phi(\omega_v) - \phi(\omega_v + \omega_L)\right) - U(\omega_v-\omega_L)\sin\left(\omega_L\tau_D - \phi(\omega_v) + \phi(\omega_v-\omega_L)\right)\right] \tag{3.15}$$

oscillates with the dressing laser frequency, and

$$S_{2\omega_L} = \left(\frac{vF_{0,L}}{{\omega_L}^2}\right)^2 [U(\omega_v + \omega_L)^2 + U(\omega_v - \omega_L)^2 +$$

$$2U(\omega_v + \omega_L)U(\omega_v - \omega_L)\cos(2\omega_L\tau_D)] \tag{3.16}$$

oscillates with twice the laser frequency. While the $2\omega_L$ component can be used to obtain the relative phase of harmonics produced from attosecond pulse trains [38,57], we are primarily interested in the laser-frequency oscillation (LFO) component $S_{\omega_L}(W, \tau_D)$, which results from transitions to final states with energy ω_v, $\omega_v + \omega_L$, and $\omega_v - \omega_L$ [34]. Clearly the spectral phase differences between those frequency components coupled by one NIR photon are encoded in the LFO component.

Equation 3.15 can be rewritten as:

$$S_{\omega_L} = |U(\omega_v)|^2 \frac{vF_{0,L}}{\omega_L} \gamma \sin(\omega_L\tau_D + \alpha), \tag{3.17}$$

where

$$\gamma^2 = \frac{1}{|U(\omega_v)|^2}\Big\{I(\omega_v + \omega_L) + I(\omega_v - \omega_L) - 2\sqrt{I(\omega_v + \omega_L)I(\omega_v - \omega_L)}\cos[2\phi(\omega_v) -$$

$$\phi(\omega_v + \omega_L) - \phi(\omega_v - \omega_L)]\Big\}, \tag{3.18}$$

is proportional to the modulation depth of the oscillation, and

$$\tan\alpha = \frac{\sqrt{I(\omega_v+\omega_L)}\sin[\phi(\omega_v)-\phi(\omega_v+\omega_L)]-\sqrt{I(\omega_v-\omega_L)}\sin[\phi(\omega_v-\omega_L)-\phi(\omega_v)]}{\sqrt{I(\omega_v+\omega_L)}\cos[\phi(\omega_v)-\phi(\omega_v+\omega_L)]-\sqrt{I(\omega_v-\omega_L)}\cos[\phi(\omega_v-\omega_L)-\phi(\omega_v)]} \tag{3.19}$$

is the tangent of the phase angle of the LFO. The spectral phase is encoded in both the modulation depth and phase angle.

As an example, the modulation amplitude and phase angle from two different filtered spectrograms are shown in Figure 3.17. The power spectra of the pulses are identical, but the spectral phases are different. In both cases, the Gaussian attosecond pulse spectrum supported 90 *as* pulses, and the dressing laser was chosen to be 20 *fs* in duration centered at 800 nm and with a peak intensity of 10^{11} W/cm^2. Clearly, the spectral phase is encoded in both γ and α.

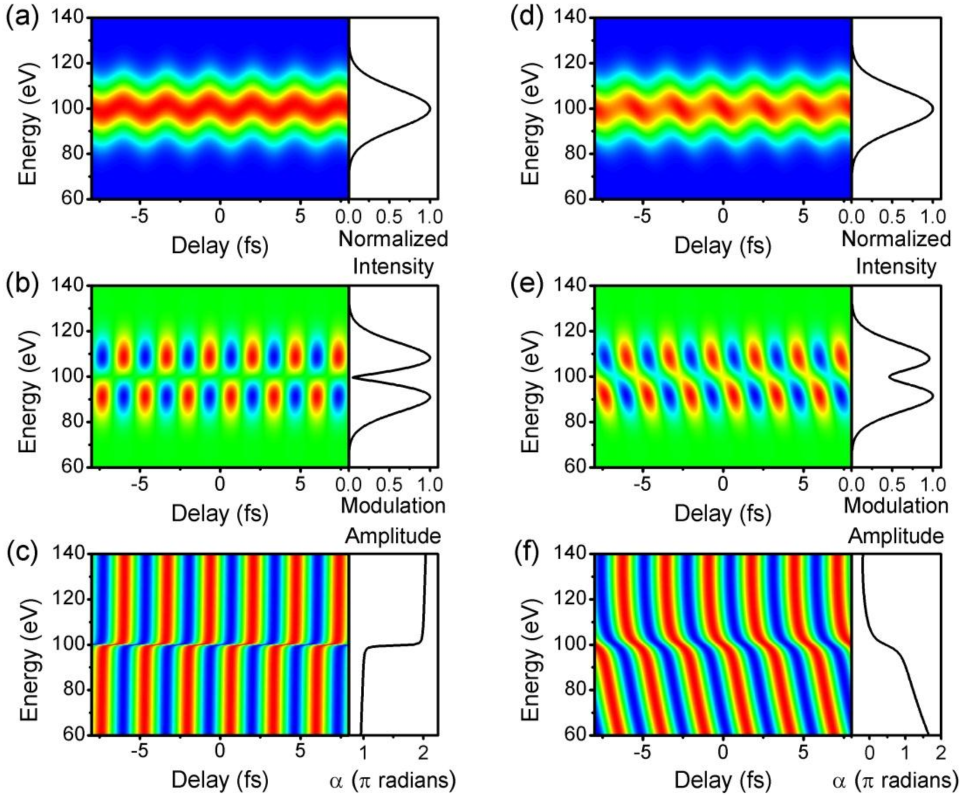

Figure 3.17: Extraction of the modulation amplitude and phase angle from the spectrogram for (a-c) a nearly transform-limited 95 *as* pulse and (d-f) a strongly-chirped 300 *as* pulse. (a, d) (left) Laser-dressed photoionization spectrogram and (right) attosecond pulse power spectrum. The two spectra are identical. (b, e) (left) Filtered LFO component and (right) extracted modulation amplitude. (c, f) Filtered LFO, normalized to the peak signal at each electron energy and (right) extracted phase angle (adapted from [34]).

The spectral phase can be directly obtained from the modulation amplitude γ and the phase angle α by solving coupled Equations 3.18 and 3.19, taking advantage of the recurrence nature of the equations. However, this is impractical for experimental traces, for which noise in the trace will be accumulated as phase error, due to the dependence of the guessed phase on the previous one.

PROOF Retrieval with an Evolutionary Algorithm

When the signal-to-noise ratio is low, as is often the case in attosecond streaking experiments, Equations 3.18 and 3.19 may not have an analytical solution and the two equations, if solved independently, may yield somewhat different spectral phases. Therefore, the most straightforward way to extract the phase $\phi(\omega_v)$ is by defining an error function based on the phase angle α and modulation depth γ which can be minimized. In the simplest implementation of PROOF, we minimize the least square error function between the measured and guessed phase angles:

$$R[\phi(\omega_v)] = \left(\sum_{\omega_v} I(\omega_v)(\alpha - \tilde{\alpha})^2\right)^{1/2}, \tag{3.20}$$

where α is the phase angle extracted from the measured trace and $\tilde{\alpha}$ is calculated from the measured spectrum and the guessed values of the spectral phase using Equation 3.19.

We choose to minimize the error function in Equation 3.20 using an evolutionary algorithm [103], as shown schematically in Figure 3.18. For this, the spectral phase is represented as an array (chromosome) of real numbers (genes) between 0 and 2π corresponding to the phase at each energy W. The algorithm is initialized with a population of randomly generated phase patterns, with no assumptions made about the behavior of the phase. Reproduction is carried out using roulette wheel selection; in addition, cloning, mutation, and crossover operations are used in order to improve the speed of convergence. Furthermore, randomly generated phase patterns are added to the population periodically to increase genetic diversity and to prevent stagnation. The fitness of a given chromosome is determined by how well it minimizes the error function in Equation 3.20. The algorithm has been found to be quite robust, converging to the global minimum in all cases for simulated traces with known spectral phase.

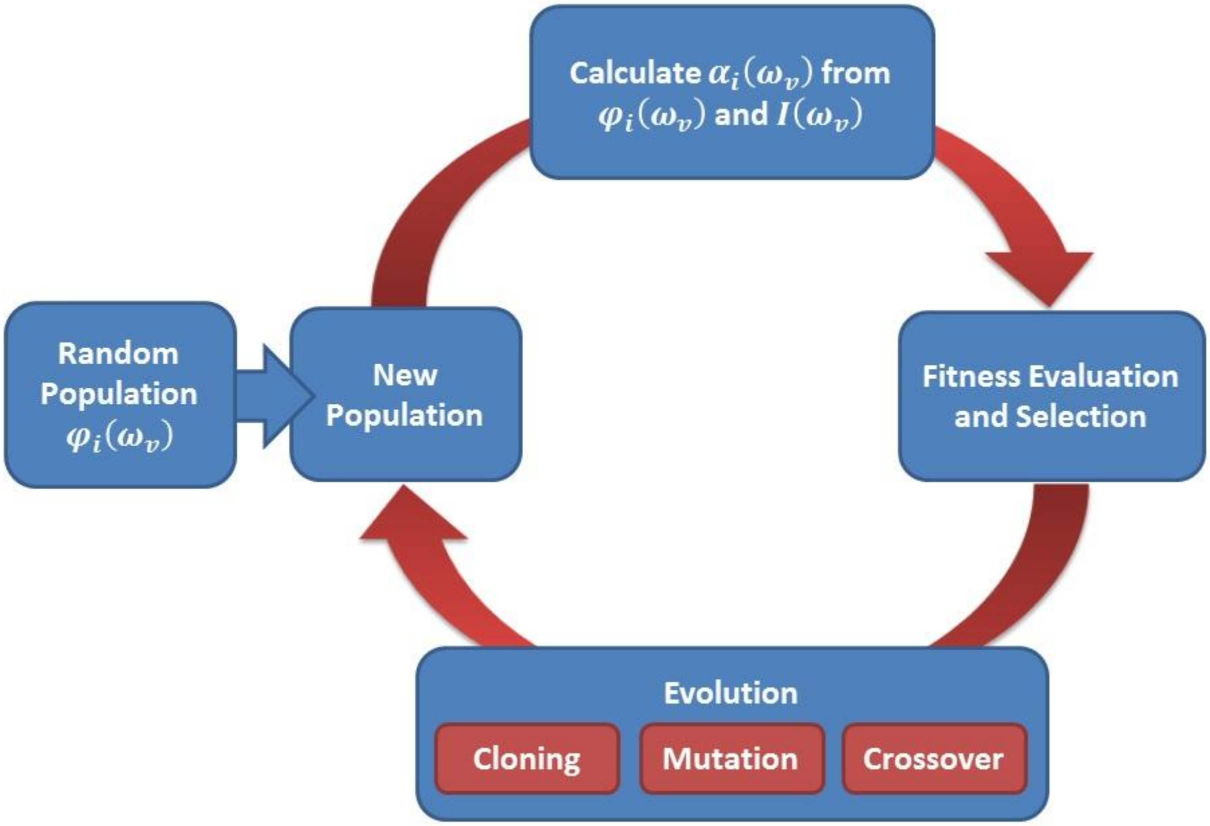

Figure 3.18: Schematic of the evolutionary algorithm used for PROOF.

We first demonstrated the PROOF technique on a relatively narrow bandwidth attosecond pulse generated with the GDOG, as shown in Figure 3.19. For such a spectrum, the FROG-CRAB also works well and can serve as a benchmark. The details of the experiment are published elsewhere [79]. The dressing laser pulse was 25 *fs* in duration centered at 790 nm and was focused to an intensity of ~10^{12} W/cm^2 at the detection gas jet, which is sufficient for an accurate FROG-CRAB retrieval for this spectrum [90]. The PCGPA was run for 1000 iterations, at which point convergence had been established. Figure 3.19(a) shows the experimentally-obtained electron spectrogram. After spectral filtering, the LFO component is shown in Figure 3.19(b), which is normalized to the peak signal at the electron energy to see the phase angle α clearly. The spectral phase is then extracted from the one-dimensional array of phase angles α_W in PROOF, whereas the FROG-CRAB retrieves the attosecond pulse by fitting the full two-dimensional spectrogram. Finally, the retrieved XUV spectral phase and pulse are compared with those retrieved from FROG-CRAB in Figures 3.19(c) and (d). Clearly, the PROOF retrieval agrees very well with the FROG-CRAB result in this case.

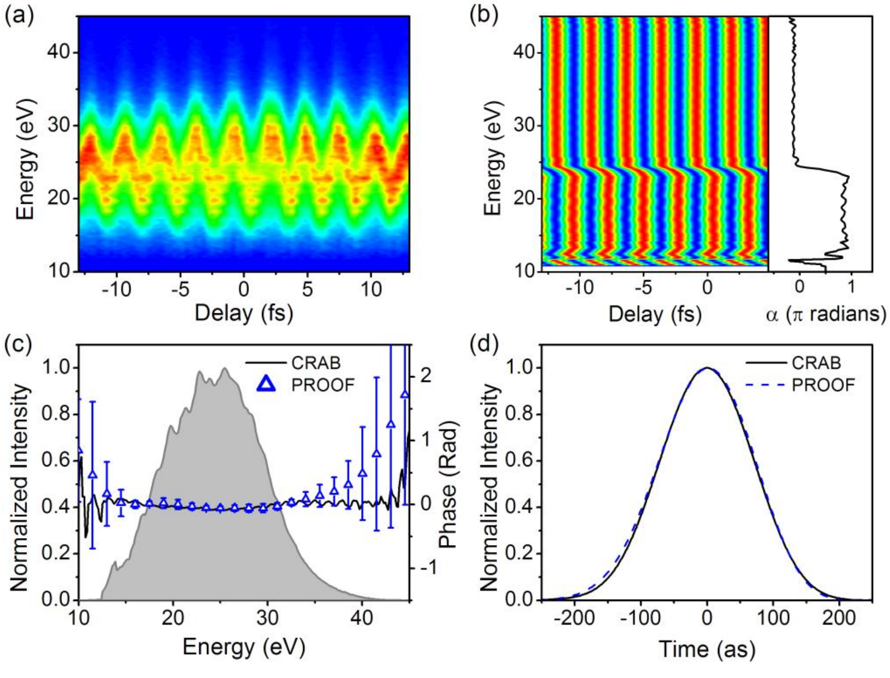

Figure 3.19: Retrieval of a narrow-bandwidth attosecond pulse with PROOF. (a) Experimentally-obtained spectrogram. (b) Filtered and normalized LFO component and extracted phase angle. (c) Photoelectron spectrum (shaded) and retrieved phase from PROOF and FROG-CRAB. (d) Retrieved 170 *as* pulses from PROOF and FROG-CRAB (adapted from [34]).

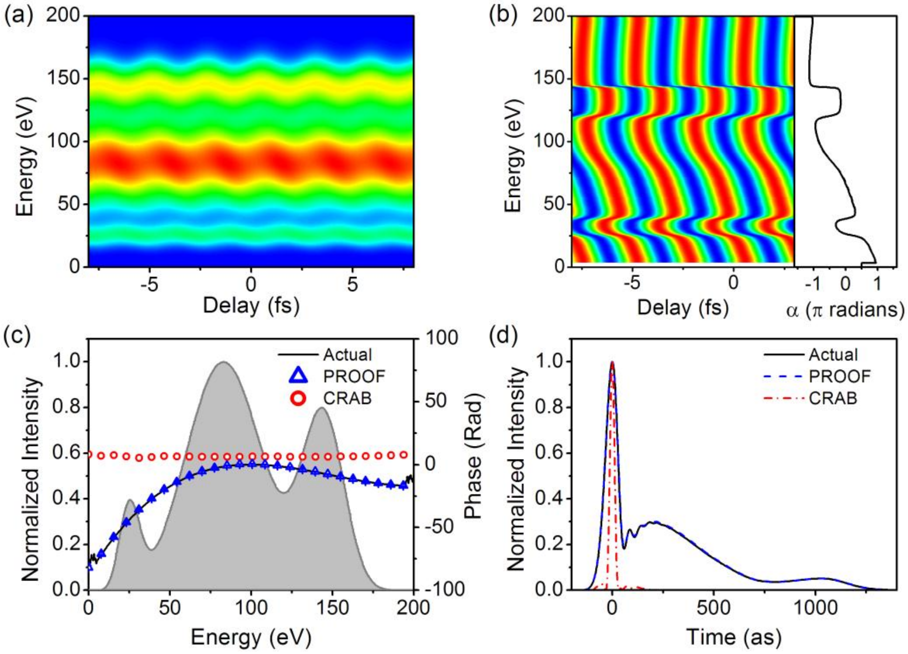

Figure 3.20: PROOF retrieval of an ultrabroadband attosecond pulse. (a) Simulated spectrogram. (b) Filtered and normalized LFO component and extracted phase angle. (c) Photoelectron spectrum (shaded) and retrieved phase from PROOF and FROG-CRAB. (d) Retrieved pulses from PROOF (73 *as* pulse duration) and FROG-CRAB (26 *as* pulse duration), compared with the actual 73 *as* pulse (adapted from [34]).

The ability of the PROOF technique to retrieve broadband, very short attosecond pulses is first demonstrated with simulated data. Figure 3.20(a) shows the electron spectrogram from a relatively complicated spectrum extending from 0 to 200 eV, which supports transform-limited pulses 25 *as* in duration, with a dressing laser pulse 20 *fs* in duration and with peak intensity of 10^{11} W/cm^2. Spectral phase was added to give an asymmetric pulse with a pulse duration of 73 *as*. Figures 3.20(c) and (d) compare the actual spectral phase and temporal profile of the pulse with those retrieved from PROOF and FROG-CRAB. Clearly, PROOF is able to fully reproduce the spectral phase and pulse profile, whereas the FROG-CRAB technique retrieves a nearly flat phase. Here, the bandwidth of the spectrum is larger than the central electron energy; thus the central momentum approximation for FROG-CRAB is not valid.

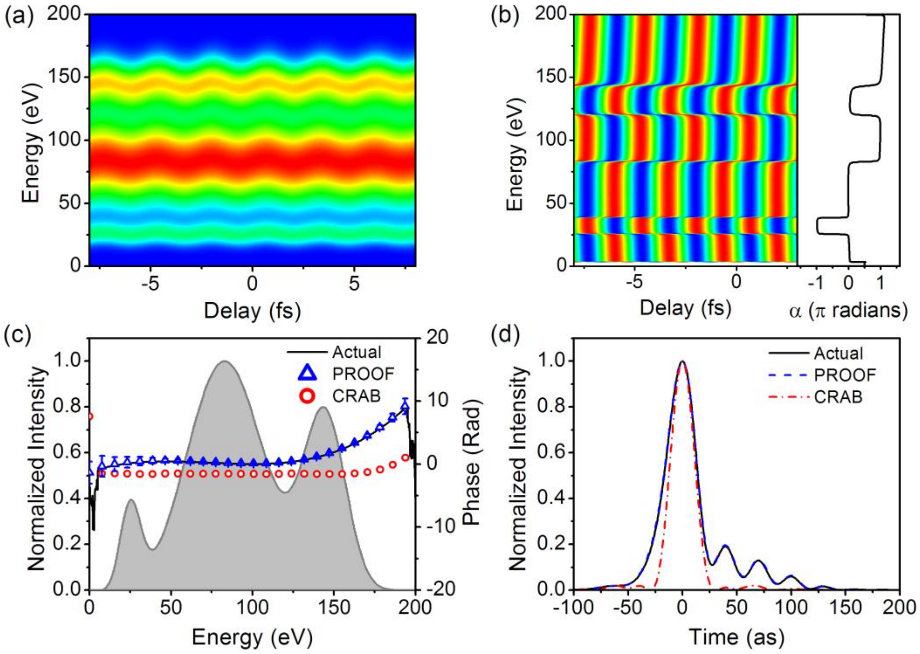

Figure 3.21: PROOF retrieval of a nearly transform-limited ultrabroadband attosecond pulse. (a) Simulated spectrogram. (b) Filtered and normalized LFO component and extracted phase angle. (c) Photoelectron spectrum (shaded) and retrieved phase from PROOF and FROG-CRAB. (d) Retrieved pulses from PROOF (31 *as* pulse duration) and FROG-CRAB (25 *as* pulse duration), compared with the actual 31 *as* pulse (adapted from [34]).

PROOF is compared with FROG-CRAB for a nearly transform-limited pulse with the same broad spectrum in Figure 3.21. In this case, the spectral phase was chosen to vary only slightly over the spectrum, to create an asymmetric pulse with a duration of 31 *as*. As is shown in Figure 3.21(c), the phase was retrieved quite well with PROOF, whereas the FROG-CRAB again underestimated the chirp. Although the two methods retrieved similar pulse durations due to the nearly transform-limited nature of the pulse, differences are apparent in the pulse shape, shown in Figure 3.21(d). Whereas PROOF retrieved the asymmetric pulse profile quite accurately, FROG-CRAB could not.

A PROOF Trace for FROG Algorithms

While the evolutionary algorithm-based PROOF technique is demonstrated to accurately and reliably retrieve the spectral phase from simulated spectrograms and from experimental traces with high signal-to-noise ratio, new algorithms are desired to improve the robustness of the PROOF by taking advantage of the inherently redundant data in the full two-dimensional spectrogram. Since the method of generalized projections has proven to be relatively insensitive to shot noise and other experimental artifacts [90,94,95], it would be ideal to take advantage of the PCGPA used in FROG-CRAB.

As discussed above, the PCGPA requires that the phase $\varphi(v,t)$ depends only on time, which is not satisfied for ultrabroadband attosecond pulses. Since the target gas can be chosen such that the continuum dipole matrix element does not vary much over the spectrum range, this requirement specifies that the *up-streaking* and *down-streaking* of the spectrum must be symmetric. In fact, because the streaking amplitude is proportional to $v = \sqrt{2W}$, the up-streaking at the highest energies will always exceed the down-streaking at the low energies, with the streaking effect approaching zero as the photoelectron energy decreases. This is illustrated in Figure 3.22, where the spectrogram generated from Equations 3.2 and 3.3 is compared with that generated using the central momentum phase in Equation 3.5. However, the retrieved FROG-CRAB trace must always have symmetric up- and down-streaking due to its reliance on the central momentum approximation, which leads to errors in the retrieved pulse.

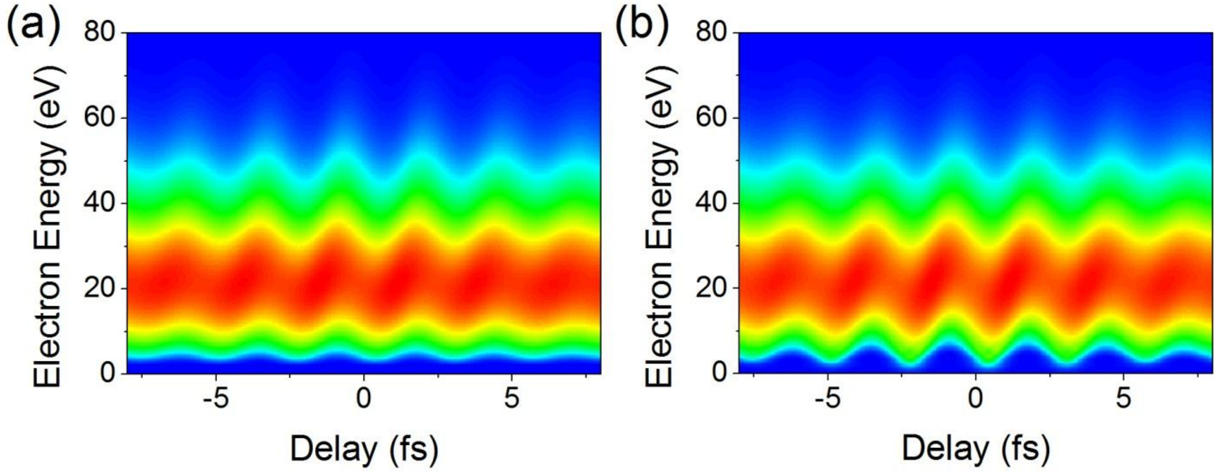

Figure 3.22: Comparison of (a) the streaked photoelectron spectrogram generated from Equations 3.2 and 3.3 without making the central momentum approximation and (b) the FROG-CRAB trace generated from Equation 3.5 using the same attosecond pulse and streaking laser field. While the streaked spectrogram exhibits a larger streaking effect for higher photoelectron energies, the streaking amplitude is uniform for the FROG-CRAB trace.

In the FROG-CRAB, the momentum dependence is tied up in the exponential term of the integral in Equation 3.3, and the equation cannot be separated analytically to satisfy the central momentum approximation. However, this is not the case in PROOF. When the streaking intensity is low and the phase term can be approximated by the first-order Taylor series expansion, the dependence of the three components in Equations 3.14-3.16 on the electron momentum is more transparent. From these components, it is clear that we can construct a new trace, which we term the PROOF trace, for which the phase does not depend on the momentum:

$$S_{PROOF}(W, \tau_D) = S_0 + \frac{\sqrt{2W_0}}{v} S_{\omega_L} + \frac{2W_0}{v^2} S_{2\omega_L}. \qquad (3.21)$$

The PROOF trace corresponds to the delay-dependent electron spectrum described in Equation 3.12, but with the photoelectron momentum substituted by the central momentum:

$$b_{PROOF}(v, \tau_D) = \int_{-\infty}^{\infty} dt F_X(t-\tau)\left[1 + i\frac{v_0 F_{L,0}}{2\omega_L^2}\left(e^{i\omega_L t} + e^{-i\omega_L t}\right)\right] e^{-i\left(v^2/2+I_p\right)t}. \tag{3.22}$$

The PCGPA can then be applied to the PROOF trace without violation of the central momentum approximation as described below. This is possible in PROOF since the electron momentum can be removed from the second term in the integral analytically, whereas the electron momentum cannot be removed from the phase gate $\varphi(v, t)$ in FROG-CRAB. The PROOF trace generated from the spectrogram in Figure 3.22(a) is shown in Figure 3.23, and it bears a strong resemblance to the central momentum trace in Figure 3.22(b).

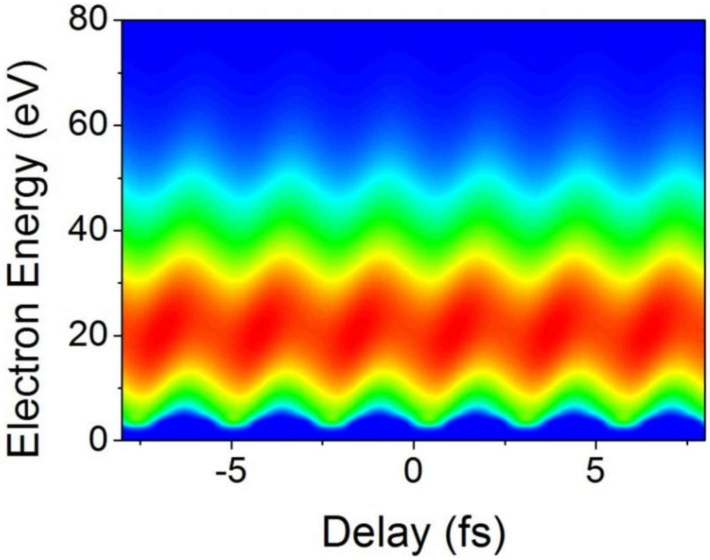

Figure 3.23: PROOF trace generated from the streaked photoelectron spectrogram in Figure 3.22(a).

The PCGPA retrieval of the pulse from the PROOF trace essentially amounts to a phase retrieval problem. $S_{PROOF}(W, \tau_D)$ is a real, positive quantity and therefore does not explicitly contain the phase information. The goal of the PCPGA, whether in FROG, FROG-CRAB, or PROOF, is to determine the phase by solving the equation:

$$\sqrt{S_{PROOF}(W, \tau_D)}\exp[i\Phi(W, \tau_D)] = b_{PROOF}(v, \tau_D), \tag{3.23}$$

for $\Phi(W,\tau_D)$ which represents the phase of the PROOF trace. The PCGPA algorithms used for FROG-CRAB and PROOF are illustrated in flow chart diagrams in Figure 3.24 and Figure 3.25, respectively. The retrieval proceeds iteratively as follows:

1. An initial guess for the attosecond pulse $F_X(t)$ and the dressing laser pulse $F_L(t)$ is used to generate a signal matrix $E_{sig}(t,\tau_D) = F_X(t-\tau)e^{i\varphi(v_0,\tau_D)}$. This is accomplished using the outer product of $F_X(t)$ and $\varphi(W_0,t)$ and manipulation of the resulting matrix. In the case of PROOF, $e^{i\varphi(v_0,\tau_D)} \approx 1 + i\frac{v_0 F_{L,0}}{2\omega_L^2}\left(e^{i\omega_L t} + e^{-i\omega_L t}\right)$, since low dressing laser intensities are used.

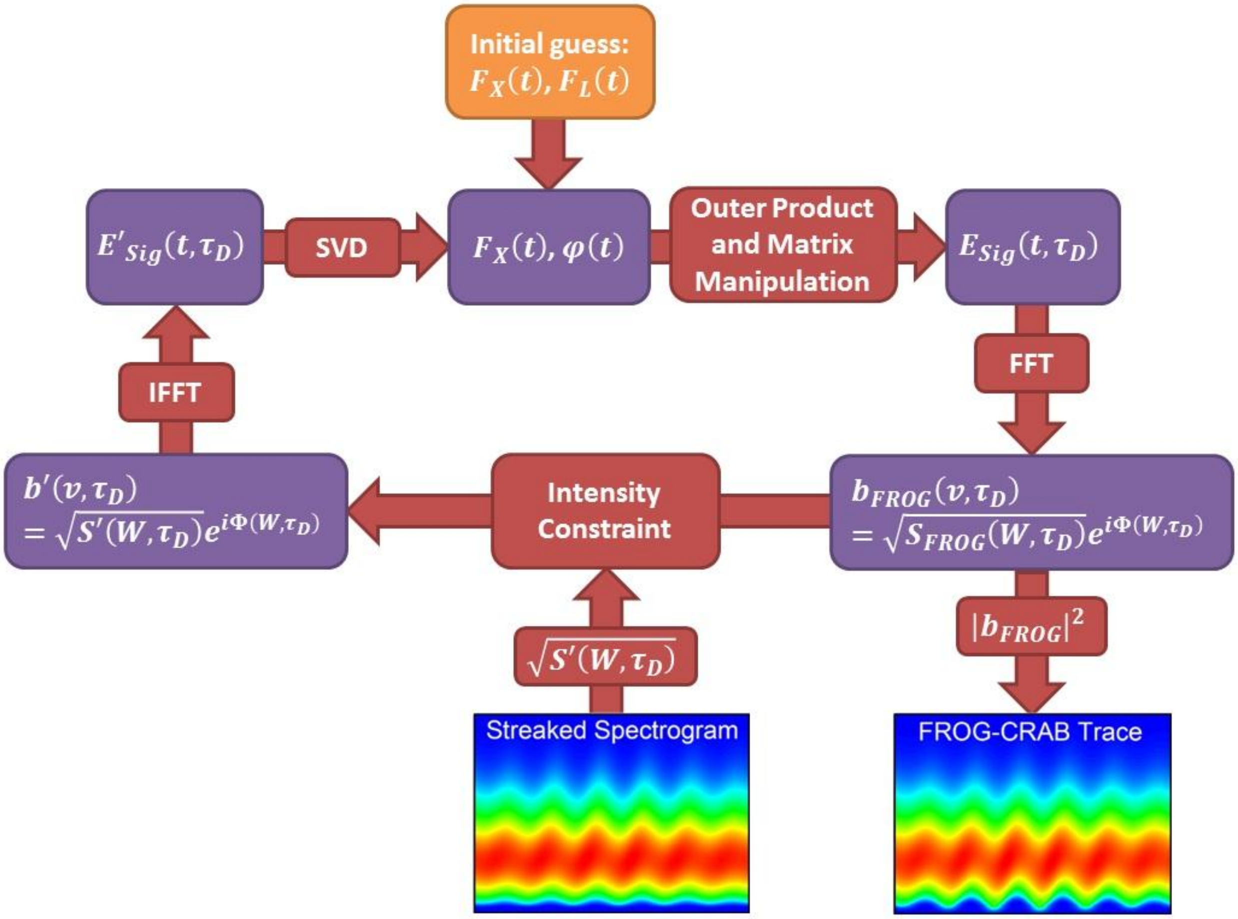

Figure 3.24: Flow chart diagram for the PCGPA as used in FROG-CRAB.

2. The electron spectrum $b(v, \tau_D)$ is calculated by taking the Fourier transform of $E_{sig}(t, \tau_D)$ along the time axis. This is accomplished numerically using the fast Fourier transform (FFT).

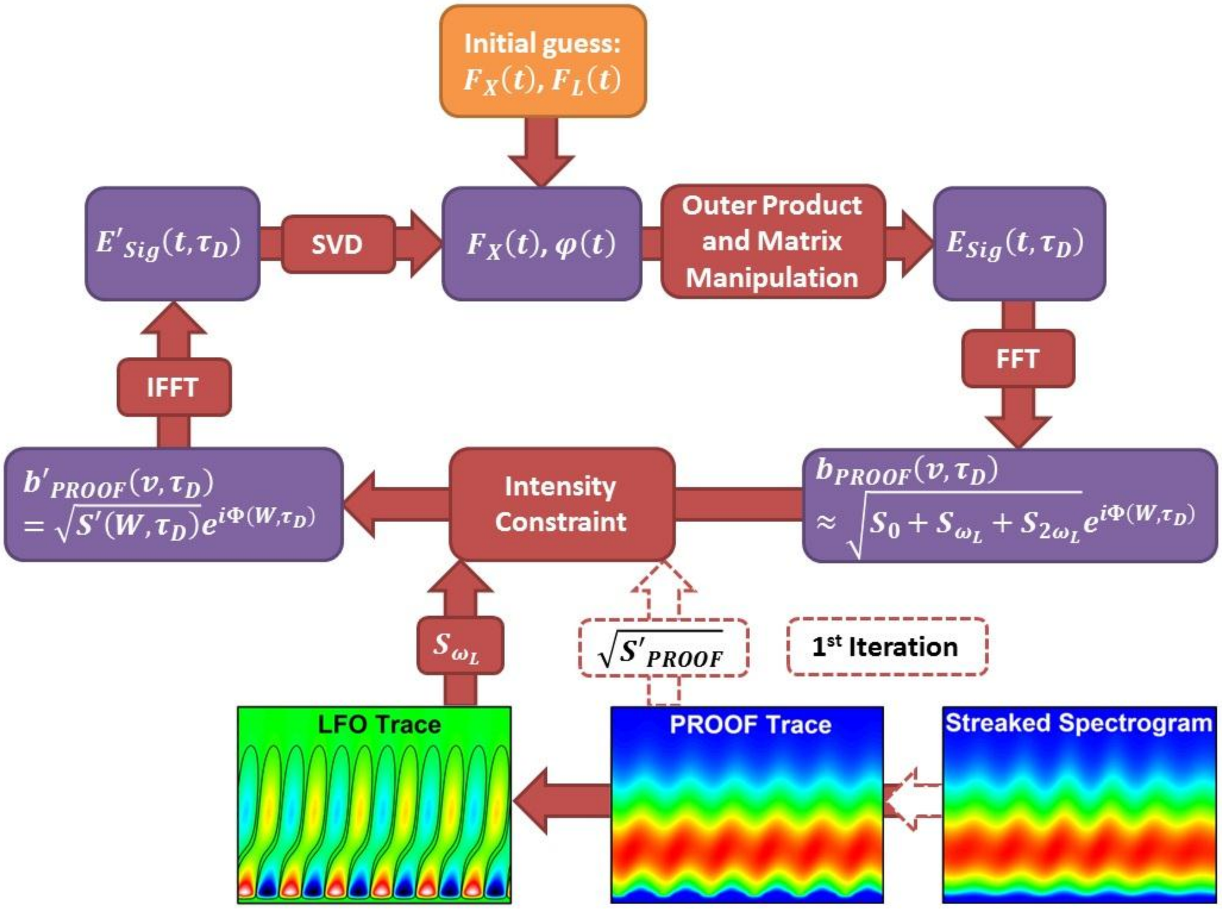

Figure 3.25: Flow chart diagram of the PCGPA as used in PROOF.

3. An intensity constraint is applied to the trace. In the case of FROG-CRAB, the magnitude of the electron spectrum $|b(v, \tau_D)| = \sqrt{S(W, \tau_D)}$ is substituted with the square-root of the measured trace $\sqrt{S'(W, \tau_D)}$. The phase term $\Phi(W, \tau_D)$ is left alone. In the case of PROOF, the intensity constraint is a dynamic one. In the first iteration, the constraint is

identical to that of FROG-CRAB, with $|b_{PROOF}(v,\tau_D)|$ substituted with $\sqrt{S'_{PROOF}(W,\tau_D)}$. In later iterations, however, both are broken up into their respective components, $|b_{PROOF}(v,\tau_D)| \approx \sqrt{S_0 + \frac{\sqrt{2W_0}}{v} S_{\omega_L} + \frac{2W_0}{v^2} S_{2\omega_L}}$ and $\sqrt{S'_{PROOF}(W,\tau_D)} = \sqrt{S'_0 + \frac{\sqrt{2W_0}}{v} S'_{\omega_L} + \frac{2W_0}{v^2} S'_{2\omega_L}}$, and the magnitude of the guessed electron spectrum $|b(v,\tau_D)|$ is substituted with $\sqrt{S_0 + \frac{\sqrt{2W_0}}{v} S'_{\omega_L} + \frac{2W_0}{v^2} S_{2\omega_L}}$. Therefore, the electron spectrum after substitution is given by:

$$b'_{PROOF}(v,\tau_D) = \sqrt{S_0 + \frac{\sqrt{2W_0}}{v} S'_{\omega_L} + S_{2\omega_L}} \exp[i\Phi(W,\tau_D)]. \tag{3.24}$$

In practice, the transition from the full substitution of FROG-CRAB to the LFO substitution of PROOF is gradually introduced over the first several iterations to avoid sudden changes in the algorithm. It is this substitution of only the LFO component which separates the PCGPA used in FROG-CRAB from that used in PROOF. The algorithms are otherwise identical, and the robustness of the PCGPA against noise and other experimental artifacts is therefore maintained for PROOF.

4. The new signal matrix $E'_{sig}(t,\tau_D)$ is obtained by taking the inverse Fourier transform of $b'(v,\tau_D)$, which can be seen as resulting from a combination of a revised XUV pulse $F'_X(t)$ and laser field $F'_L(t)$.
5. The revised pulse $F'_X(t)$ and phase gate $\varphi'(v,t)$ are obtained from $E'_{sig}(t,\tau_D)$ by inverting the matrix manipulations in Step 1 using the method of singular value decomposition. The revised pulses are then used as input for the next iteration.

After a suitable number of iterations (typically on the order of 10^4), when it is determined that the algorithm is converged and the error is suitably low, the final guess of the pulse and phase gate are exported by the program, and the PROOF trace $\tilde{S}_{PROOF}(W, \tau_D)$ generated using the guessed result can be compared to that obtained from the experimentally measured spectrogram $S'_{PROOF}(W, \tau_D)$.

The construction of the PROOF trace also reveals a fundamental flaw in the application of FROG techniques to attosecond streaking spectrograms. Typically, the convergence of both FROG and FROG-CRAB algorithms is evaluated using the FROG error, defined in Equation 3.6. However, the FROG-CRAB trace, unlike femtosecond FROG traces, is dominated by a zero-frequency component which does not change with the delay and which does not encode the spectral phase. Therefore, minimization of the FROG error in experimental FROG-CRAB traces will generally occur when the guessed *spectrum* matches the photoelectron spectrum $I(\omega_v)$. For this reason, we propose the use of a different error function, which we term the PROOF error, which is found by computing the RMS difference between the LFO components of the guessed and measured PROOF traces:

$$\epsilon_{PROOF}\left(\tilde{S}_{PROOF}, S'_{PROOF}\right) = \left\{\frac{1}{N^2}\sum_{i=1}^{N}\sum_{j=1}^{N}\left[\tilde{S}_{\omega_L}(W_i, \tau_j) - S'_{\omega_L}(W_i, \tau_j)\right]^2\right\}^{1/2}. \qquad (3.24)$$

Here, we use only the LFO component, and not the component $S_{2\omega_L}$ which oscillates with twice the laser frequency, since the error in the approximations of Equations 3.10 and 3.11 is to second order in the laser frequency.

Still, the PCGPA as used in FROG-CRAB relies heavily on the DC component S_0 of the electron spectrogram. This is a result of substituting the measured trace for the magnitude of the guessed trace, which occurs in every iteration of the PCGPA for FROG-CRAB, as illustrated in

Figure 3.24. For simulated noise-free traces, this does not adversely affect the reconstruction, since the measured electron spectrogram is self-consistent and described approximately by Equations 3.14-3.16. However, experimental traces often contain spurious electron signal which can result from multi-photon or tunneling ionization of the atom ground state by the streaking laser or electron scattering by the target gas and which is difficult to remove. These signals will not oscillate with the delay, and will contribute to the DC component of the PROOF trace and can cause the algorithm to converge to a result which superficially matches the input trace, but which does not describe the pulse. Therefore, in the PCGPA for PROOF, the influence of the DC component on the retrieval is removed from the intensity constraint, as illustrated in the flow chart in Figure 3.25.

Figure 3.26 shows the reconstruction of a simulated trace with both additive and shot noise to simulate the effects of spurious electron signal and low count rate. The parameters of the attosecond pulse and NIR dressing laser are the same as in Figure 3.22, and the spectrogram is assumed to have 50 electron counts in the maximum pixel. Random additive noise with an average count of 2 electrons per pixel is added to the trace to simulate the spurious electron signals which remain after background subtraction in experimental traces. The PROOF retrievals on the noisy trace in Figure 3.26(a) are performed separately with the evolutionary algorithm and with the PCGPA. While both the evolutionary algorithm and PCGPA roughly retrieve the correct phase, the error in the spectral phase retrieval and pulse duration is clearly smaller for the PCGPA retrieval. Although the improvement in the phase measurement is only modest, generalized projections algorithms such as the PCGPA are well studied and known to be more robust than evolutionary algorithms. Furthermore, the PROOF algorithm based on the PCGPA does not require that the photoelectron spectrum be used as an input, and both the spectrum and spectral phase are guessed by the algorithm. Therefore, the guessed spectrum can be compared to the measured spectrum, in addition to the comparison of the LFO components, in order to confirm the accuracy of the retrieval.

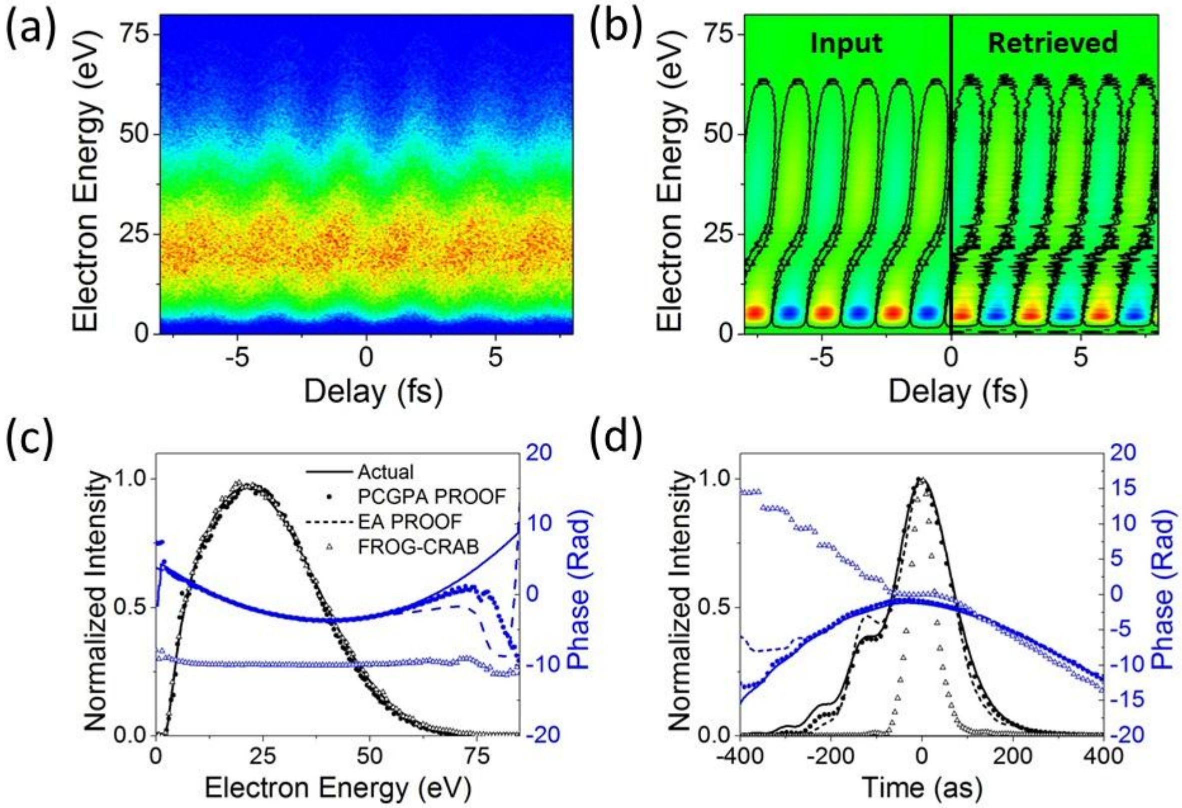

Figure 3.26: PROOF retrieval for simulated noisy data using both the PCGPA-based PROOF (PCGPA PROOF) and the evolutionary algorithm-based PROOF (EA PROOF). The PCGPA retrieval yields excellent agreement of both spectrum and phase, in spite of the noisy input trace.

Experimental characterization of short attosecond pulses requires near-complete compensation of the attosecond pulse chirp, such that the spectral phase is flat over the full bandwidth. The full compensation of a pulse with a bandwidth of more than 40 eV, supporting 63 attosecond transform-limited pulses, has been demonstrated in our laboratory using a zirconium foil filter to compress the pulse generated from a high intensity laser (1×10^{15} W/cm^2 in the center of the double optical gate) focused to a high-density gas target. The experimental details are published elsewhere [91]. Figure 3.27 shows the PROOF characterization of the pulse with the PCGPA, revealing a 67 *as* pulse. The excellent agreement between the LFO traces extracted from the measured and retrieved traces indicates that the retrieval is correct. The experimental confirmation of the PROOF with such a short pulse sets the stage for the future application of PROOF to characterize even shorter attosecond pulses for which the FROG-CRAB fails.

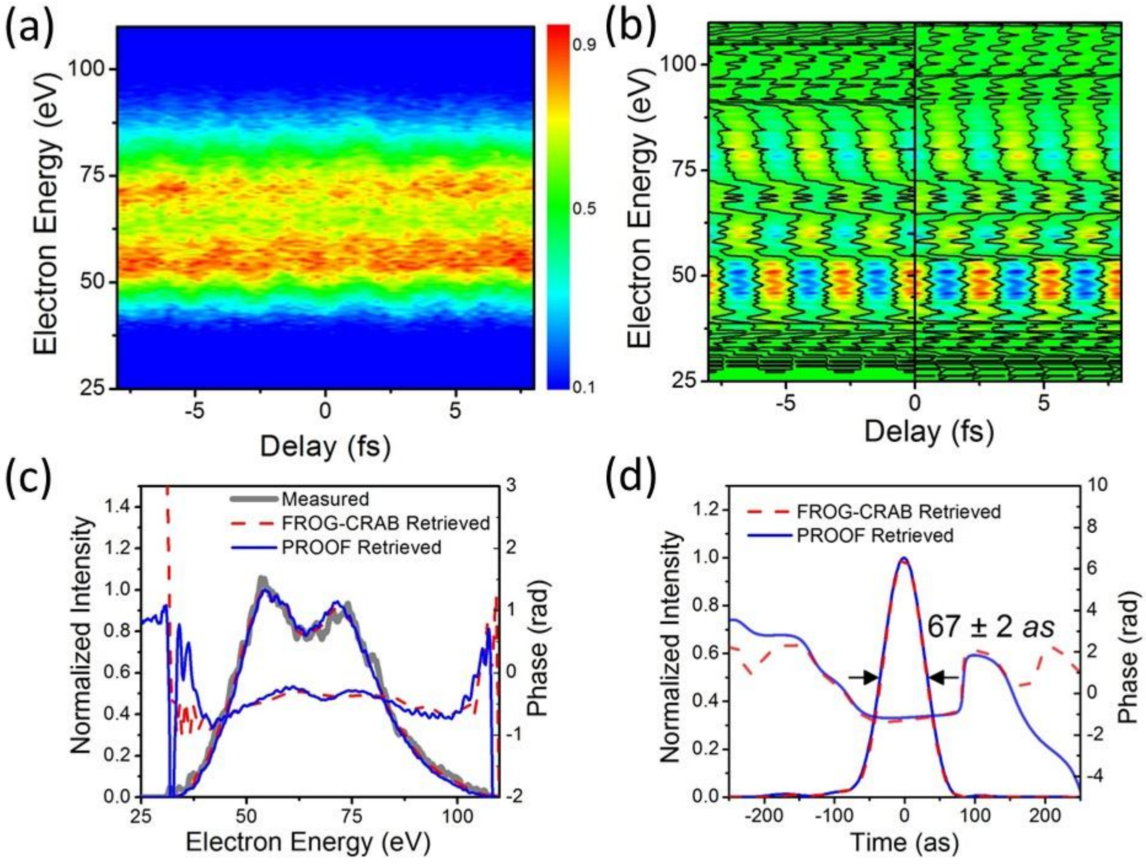

Figure 3.27: Retrieval of a 67 attosecond pulse with PROOF and confirmed with FROG-CRAB (adapted from [91]).

Notes

Portions of this chapter were used or adapted with permission from the following:

> He Wang, Michael Chini, Sabih D. Khan, Shouyuan Chen, Steve Gilbertson, Ximao Feng, Hiroki Mashiko, and Zenghu Chang. Practical issues of retrieving isolated attosecond pulses. *Journal of Physics B:Atomic, Molecular, and Optical Physics* **42**, 134007 (2009).
>
> Ximao Feng, Steve Gilbertson, Sabih D. Khan, Michael Chini, Yi Wu, Kevin Carnes, and Zenghu Chang. Calibration of electron spectrometer resolution in attosecond streak camera. *Optics Express* **18**, 1316 (2010).
>
> Michael Chini, He Wang, Sabih D. Khan, Shouyuan Chen, and Zenghu Chang. Retrieval of satellite pulses of isolated attosecond pulses. *Applied Physics Letters* **94**, 161112 (2009).
>
> Michael Chini, Steve Gilbertson, Sabih D. Khan, and Zenghu Chang. Characterizing ultrabroadband attosecond lasers. *Optics Express* **18**, 13006 (2010).
>
> Kun Zhao, Qi Zhang, Michael Chini, Yi Wu, Xiaowei Wang, and Zenghu Chang. Tailoring a 67 attosecond pulse through advantageous phase-mismatch. *Optics Letters* **37**, 3891 (2012).

CHAPTER FOUR: ATTOSECOND TRANSIENT ABSORPTION SPECTROSCOPY

In order to apply ultrabroadband attosecond pulses to the study of fast dynamics in atomic systems, we use the attosecond transient absorption technique [104,105], which is based on the measurement of transient *changes* in the absorption of an isolated attosecond pulse by a target atom (or molecule, or solid) in the presence of a perturbing laser pulse. Transient absorption has several technical advantages over attosecond streaking spectroscopy, which relies on the measurement of photoelectrons, due primarily to the comparatively large number of photons available for detection (~10^6 photons per laser shot compared to less than ~10 photoelectrons per shot) and the high energy resolution attainable with XUV spectrometers. The transient absorption technique has been demonstrated extensively using femtosecond lasers in the infrared, visible, and near-ultraviolet spectral regions (see, for example, the work of Mathies and Shank [6,106,107], as well as [108] and references therein), and has recently been extended to time-resolved absorption measurements with XUV [109-112] and x-ray [113] light. In this chapter, we will discuss the attosecond transient absorption experiments used to apply the attosecond pulses generated with DOG and characterized with PROOF to the study of electron dynamics in helium, neon, and argon atoms.

The Laser Systems

Attosecond transient absorption experiments were carried out using two different laser systems: the MARS (Manhattan Attosecond Radiation Source) laser at the James R. Macdonald Laboratory (Kansas State University, Manhattan, KS) and the FAST (Florida Attosecond

Science and Technology) laser in the FAST Laboratory (University of Central Florida, Orlando, FL). Both lasers were capable of producing high-energy few-cycle pulses in the visible and near-infrared spectral regions. Here, we will discuss the two laser systems, including the relevant laser pulse parameters and exceptional characteristics of each system.

Manhattan Attosecond Radiation Source (MARS) Laser

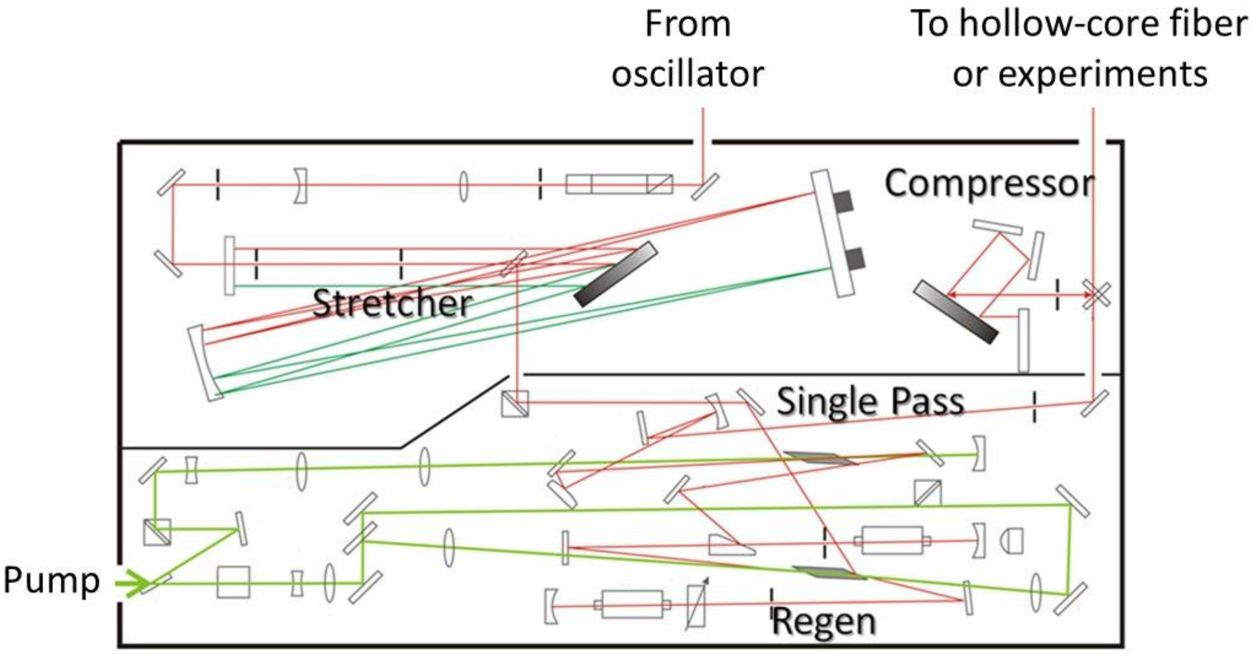

Figure 4.1: Layout of the MARS laser system.

The layout of the MARS laser system is shown in Figure 4.1. The laser consists of a Ti:Sapphire-based regenerative chirped pulse amplifier (CPA) laser system (Coherent Legend™ Elite Duo) operating at 1 kHz repetition rate, seeded by a carrier-envelope phase stabilized oscillator (Femtolasers Rainbow™) with 78 MHz repetition rate and pulse energy of approximately 2 nJ. The pulse-to-pulse carrier-envelope offset phase slip φ_{CEO} in the oscillator

CEP was stabilized using the monolithic CEP stabilization scheme [114,115]. With the assistance of a slow feedback loop to monitor and control the oscillator crystal temperature, φ_{CEO} of the oscillator could be locked for approximately 12 hours on a daily basis [116].

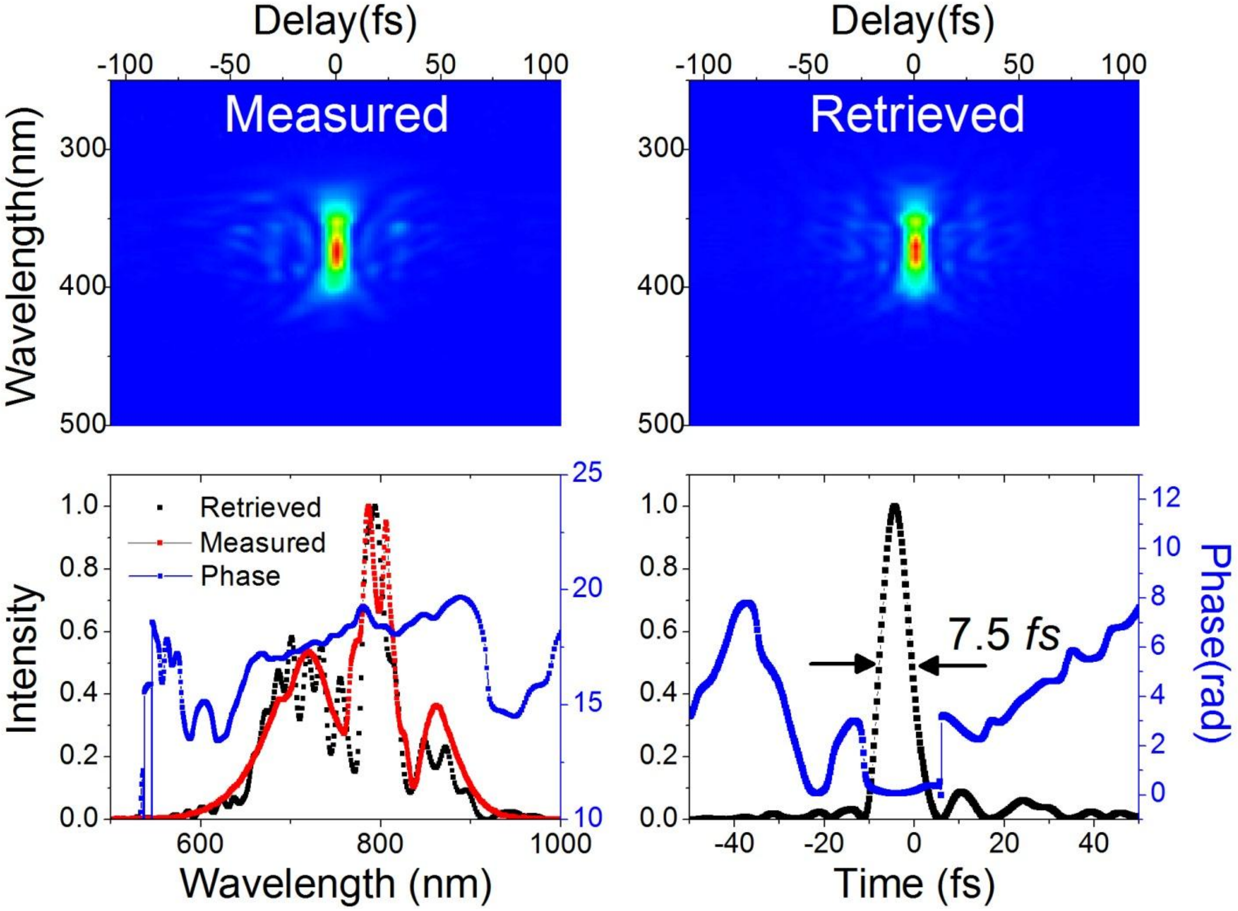

Figure 4.2: FROG retrieval of a sub-8 *fs* pulse from the MARS laser system. (a) Measured FROG trace. (b) Retrieved FROG trace). (c) Comparison of the spectrum retrieved from FROG with an independently measured spectrum. (d) Temporal profile of the laser pulse (adapted from [117]).

The amplifier consists of a grating-based stretcher, two amplification stages, and a grating-based compressor, with the amplification of the laser broken up into a 14 round-trip regenerative amplifier stage to amplify the laser pulse to 4 mJ and a single-pass amplifier to boost the laser pulse energy to 8 mJ. Each stage was pumped by 50% of a 45 mJ Coherent Evolution™ HE pump laser, and the Ti:Sapphire crystals in both amplification stages were thermo-electrically cooled to -12° C. After compression, the final output pulse energy is 6 mJ with a central wavelength of 800 nm and a near-transform limited pulse duration of 30 *fs*. The laser pulse was split into two beamlines, one of which was further compressed to 6-8 *fs* on a daily basis with an energy of 1.2 mJ using a hollow-core fiber and chirped mirror compressor [117], with the other beamline available for other experiments. The FROG measurement of a 7.5 *fs* pulse from the MARS laser is shown in Figure 4.2.

Regenerative amplification is an attractive choice for the generation of ultrafast high-power lasers [118-120], and regenerative amplifiers have commonly been used as the preamplifier for high-energy femtosecond lasers systems. In comparison with multipass amplifiers, the laser pulses generated from regenerative amplification have a better beam profile, pointing stability, power stability, and energy extraction efficiency. On the other hand regenerative amplifiers suffer from relatively large amplified spontaneous emission, and stabilization of the amplified laser CEP, which is a fairly mature technology in multipass amplifiers [21,121], is difficult in regenerative amplifiers due to the large material dispersion [119]. Taking extreme care to isolate the regenerative amplifier cavity from any external acoustical or vibrational disturbances, we demonstrated for the first time CEP control in a regenerative amplifier and CEP-dependent XUV supercontinuum generation [117] from the double optical gating, as shown in Figure 4.3. The continuum spectrum resulted from the generation of an isolated attosecond pulse, as later confirmed by attosecond streaking measurements.

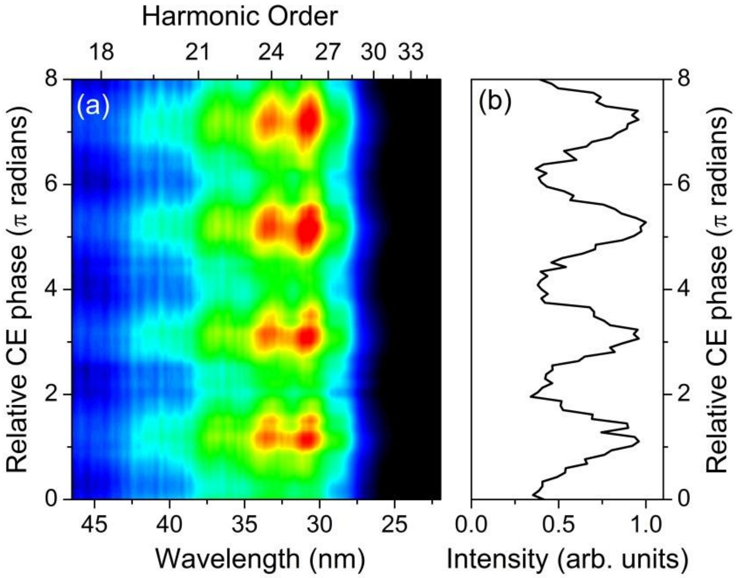

Figure 4.3: XUV supercontinuum generation with the MARS laser. (a) Carrier-envelope phase dependence of the HHG spectrum. (b) Integrated HHG signal as a function of the CE phase (adapted from [117]).

Florida Attosecond Science and Technology (FAST) Laser

The layout of the FAST laser system is shown in Figure 4.4. Like the MARS laser, the FAST laser is a CPA system using two amplification stages in order to achieve multi-mJ pulses. Here, however, the first stage uses a multi-pass configuration consisting of 14 passes through a cryogenically-cooled Ti:Sapphire crystal in order to achieve 3 mJ pulse energy, while the second stage uses one pass through a second Ti:Sapphire crystal with thermo-electric cooling to increase the energy to 5 mJ. After compression, the pulse energy is more than 3 mJ, with a central wavelength of 800 nm and a pulse duration of 22 *fs*. Using a hollow-core fiber and chirped mirror compressor, pulses of 4-6 *fs* with a central wavelength of 750 nm and up to 1.4 mJ of energy can be achieved on a daily basis. The FROG characterization of a typical 5 *fs* pulse from the FAST laser is shown in Figure 4.5.

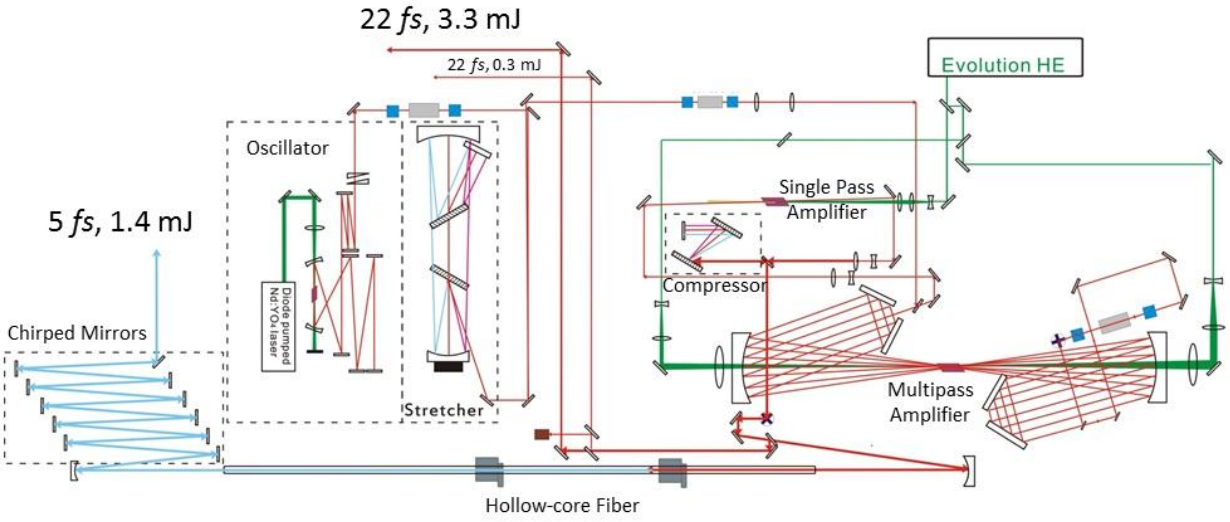

Figure 4.4: Layout of the FAST laser system.

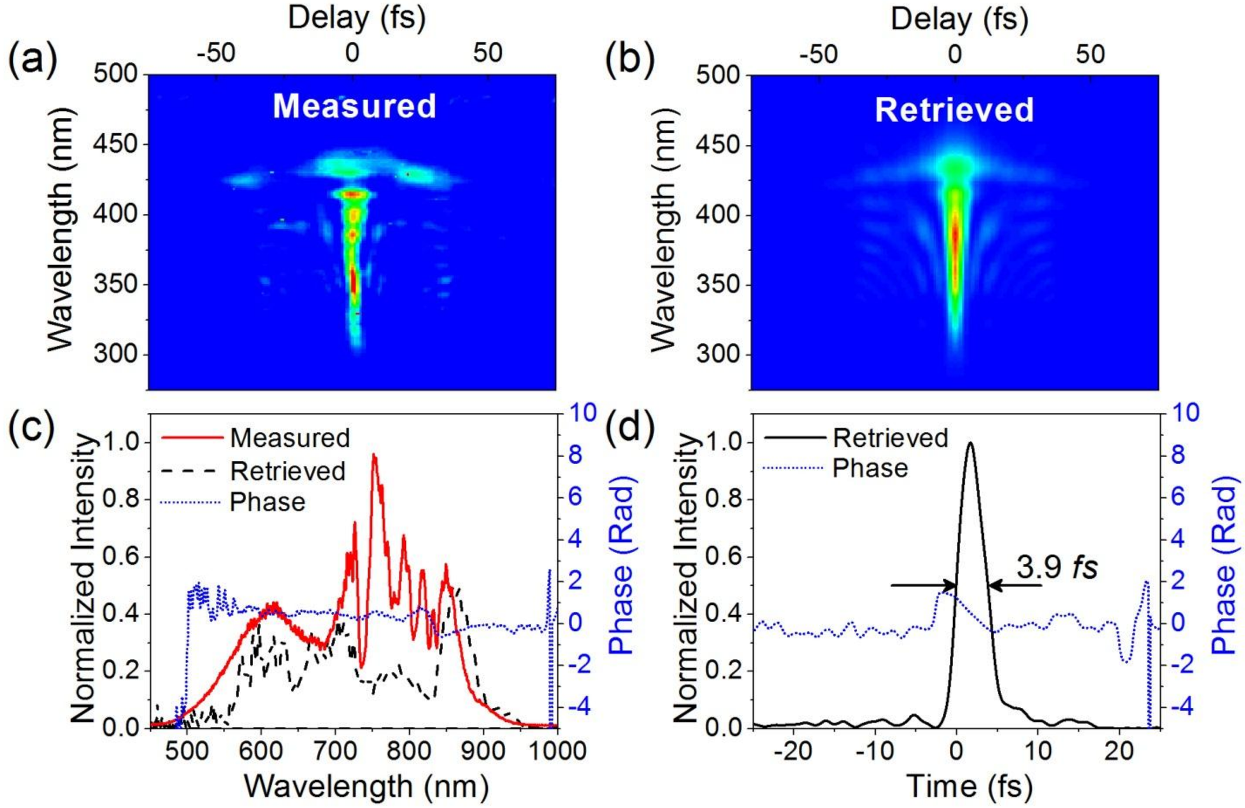

Figure 4.5: FROG retrieval of a sub-4 *fs* pulse from the FAST laser system.

Attosecond Transient Absorption Experimental Setup

While transient absorption spectroscopy is a mature technology which has been demonstrated with a broad range of frequencies, the application of isolated attosecond pulses to transient absorption measurements has only been achieved in the last several years [39,104,105]. In this section, we will discuss the experimental setup for measuring the transient absorption of a gas target in the presence of a moderately intense few-cycle laser.

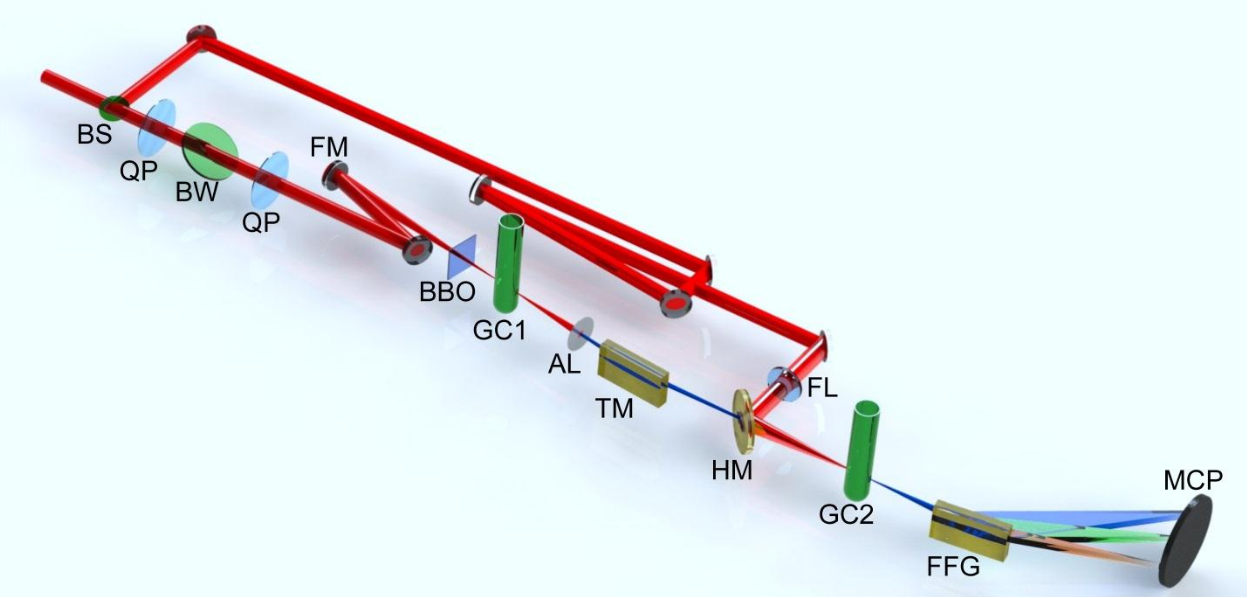

Figure 4.6: Schematic of the attosecond transient absorption setup. BS: beam splitter; QP, BW, and BBO: GDOG optics; FM: focusing mirror; GC1: first gas cell; AL: aluminum foil filter; TM: toroidal focusing mirror: FL: focusing lens; HM: hole-drilled mirror; GC2: absorption gas cell; FFG and MCP: flat field grating spectrometer (adapted from [122]).

The experimental setup used for the transient absorption measurements presented in the next chapters is shown schematically in Figure 4.6. Two separate setups were constructed for use with each of the laser systems described above. The setups both consist of a Mach-Zehnder type interferometer with a variable delay introduced between the two interferometer arms.

The few-cycle NIR laser pulses from the hollow-core fiber and chirped mirror compressor were split into the two interferometer arms by a broadband dielectric beam-splitter. In one arm of the interferometer, a portion of the laser energy was used to drive the generation of the isolated attosecond pulses, which then passed through an aluminum foil filter to block the residual NIR laser and compensate the intrinsic chirp of the attosecond pulses. The attosecond pulses were then focused by a toroidal mirror through the hole in a hole-drilled mirror. In the other arm, the other half of the pulse was sent through an equal optical path length before being focused by a lens and recombined collinearly with the attosecond pulse upon reflection by the hole-drilled mirror. The variable time delay between the attosecond pulse and the few-cycle NIR laser field was controlled by a piezoelectric transducer (PZT) stage. The exact parameters of the optical elements in the two interferometric setups were not identical, and are listed in Table 4.1.

Table 4.1: Optical parameters for the two transient absorption setups.

Laser system	**MARS**	**FAST**
Beam splitter (BS)	50% reflectivity for s-polarization	80% reflectivity for p-polarization
Focusing mirror (FM)	$f =$ 375 mm	f = 500 mm
First gas cell (GC1)	1.0 mm inner diameter	1.0 mm inner diameter
Aluminum filter (AL)	300 nm thickness	150 nm thickness
Toroidal mirror (TM)	f_{eff} = 250 mm, AOI = 9.6°	f_{eff} =250 mm, AOI = 5°
Focusing lens (FL)	$f =$ 420 mm	$f =$ 420 mm
Absorption gas cell (GC2)	1.5 mm inner diameter	1.0 mm inner diameter
Spectrometer	Transmission grating (2000 lines/mm) and spherical mirror (R = 29.2 m, AOI = 2°)	Grazing-incidence spherical reflection grating (Hitachi 001-0640)

The two pulses were focused together into the target gas cell, which was a glass capillary with a laser-drilled hole through which the two pulses passed, in which the absorption occurred. The transmitted spectrum of the attosecond pulse was then dispersed using an XUV spectrometer onto an MCP/phosphor detector which was imaged using a CCD camera. Two spectrometers were used, which will be described below. The transmitted XUV spectrum was recorded as a function of the time delay between the attosecond pulse and the NIR laser. The attosecond pulse spectrum passing through the evacuated target gas cell was also recorded, in order to obtain the spectrally-resolved absorbance $A(\omega)$ of the target, given by:

$$A(\omega) = \ln(|U_{in}(\omega)|^2/|U_{out}(\omega)|^2), \tag{4.1}$$

where $|U_{in}(\omega)|^2$ and $|U_{out}(\omega)|^2$ are the attosecond pulse spectra before and after the absorption cell, respectively. When the target gas cell is evacuated, the measured spectrum is equivalent to $|U_{in}(\omega)|^2$.

Delay Control in Attosecond Pump-Probe Experiments

While many attosecond experiments use co-propagating XUV and NIR beams and normal-incidence multi-layer mirrors for reflecting the XUV light which are limited in both reflectivity and bandwidth [27,71], the Mach-Zehnder interferometer configuration allows us to use grazing incidence metal-coated XUV mirrors, which offer reflectivity of more than 80% over very broad bandwidths [26,91,123]. Furthermore, this configuration offers the flexibility to control the driving and dressing laser fields (through amplitude or phase control, or by nonlinear frequency conversion) independently of one another [124]. However, stabilization of the time delay between the attosecond pulse and few-cycle dressing laser is necessary in the Mach-

Zehnder configuration, for which fluctuations in the environmental conditions as well as mechanical vibrations are likely to affect the optical path length difference between the two interferometer arms.

Interferometric stability can easily be obtained in conventional Mach-Zehnder optical interferometers by propagating a continuous wave (CW) laser through both arms of the interferometer and stabilizing the spatial interference pattern [18,125]. However, sending a CW laser beam through the XUV attosecond generation arm is non-trivial, as there are no beam-splitting optics available to combine the XUV and NIR pulses while allowing a reference beam to pass through for stabilizing the interferometer. Furthermore, the attosecond beam is generated in a gas target and any residual NIR must be removed with a metal foil, which also blocks the CW pilot beam. To date, all pump-probe experiments with attosecond pulses have relied on passively "stable" interferometers to measure dynamics on time scales of ~1 *fs* (0.3 µm optical path length difference). However, active delay stabilization and control is necessary to measure true attosecond dynamics, which require delay steps of only a few nanometers.

Measurement of attosecond dynamics requires much finer delay control than is afforded by conventional translation stages. However, piezoelectric stages suffer from hysteresis and the motion is not repeatable. Therefore, the field oscillations of a reference laser must be used as a "ruler" to stabilize the interferometer and control the delay. To accomplish this, a weak single-mode 532 nm CW laser was co-propagated through both arms of the interferometer. In the attosecond generation arm, the Al foil filter had a diameter of 3 mm and was mounted on a hole-drilled fused silica window. The filter size and CW laser beam size were chosen to allow a portion of the CW laser to pass around the edge of the metal foil while blocking the NIR. The two arms were recombined at a drilled mirror, which was silver-coated on both sides, to allow reflection of the annular 532 nm laser on the backside of the mirror. In the dressing laser arm, the 532 nm laser co-propagated with the NIR laser and a portion of the CW laser (along with the NIR) passed through the hole in the drilled mirror. The strong NIR light which also passed through the hole-drilled mirror was filtered out using a narrow-bandwidth filter to transmit only the 532 nm light. The interference pattern of the CW laser was detected by a CCD camera, with high-contrast interference fringes arising in the spatial overlap of the two beams.

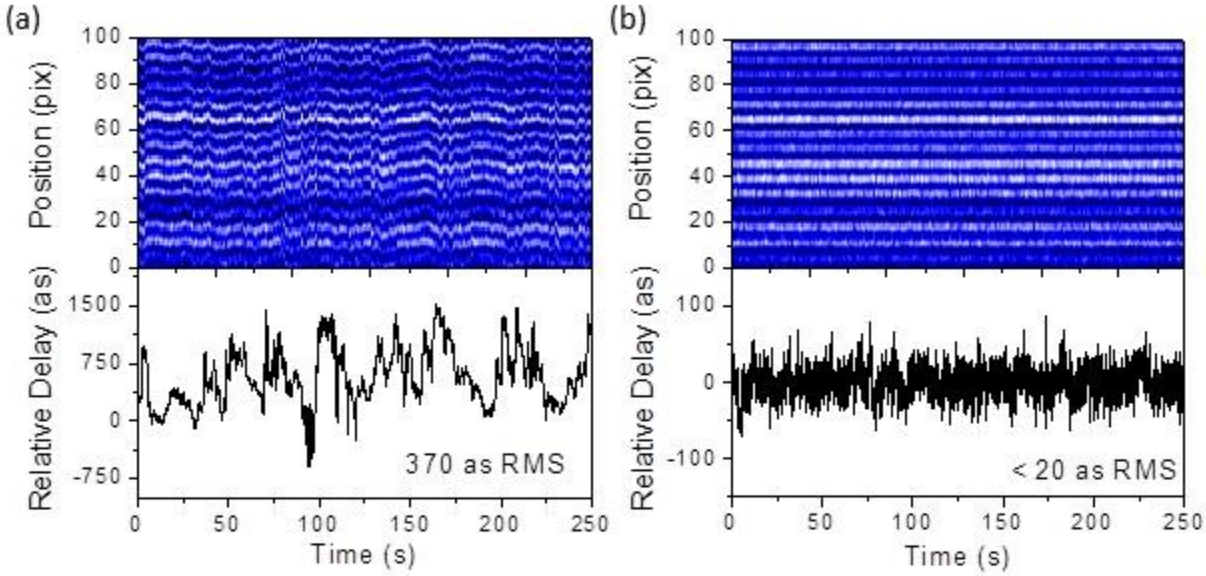

Figure 4.7: Interference measurement and time delay fluctuation with (a) the free-running and (b) the stabilized interferometer (adapted from [100]).

The relative phase and time delay were extracted from the shifts of the interference fringes using Fourier-transform interferometry [126]. Home-built computer software was used to extract the relative delay shifts from the interference fringes and generate an error signal used to control a mirror mounted to the piezoelectric translation stage in the dressing laser arm of the interferometer. The software locking was able to overcome the slow delay drifts below ~20 Hz, limited by the CCD frame rate. Figure 4.7(a) shows the interference fringe measurement and relative time delay drift of the free-running interferometer, and Figure 4.7(b) shows the interference and relative time delay when the interferometer was locked. The relative delay between the two arms was locked to within 20 *as* RMS for the entirety of the measurement.

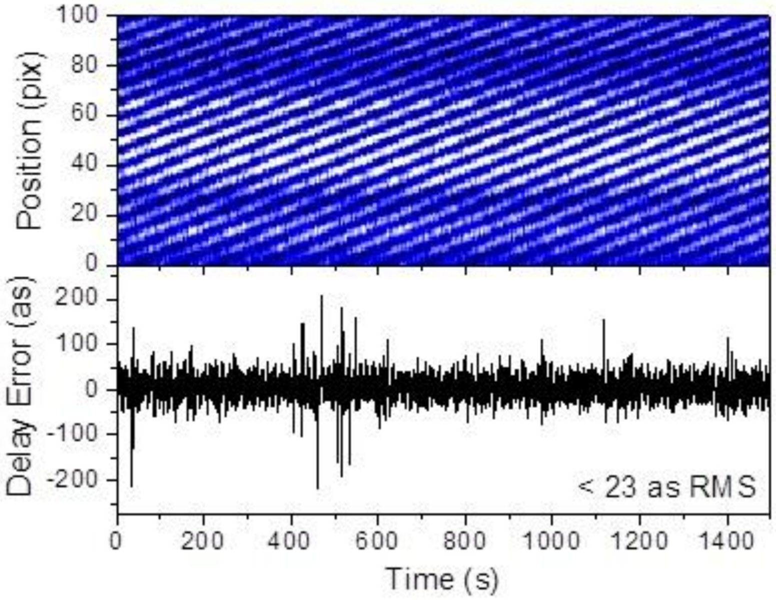

Figure 4.8: Interference fringes and residual delay error for feedback-controlled delay scan (adapted from [100]).

To control the relative delay between the two arms, only a modification of the feedback loop was required. When the delay was set to a new value, the feedback loop was used to scan the PZT to the new locking point, as determined from the interference fringes, and then stabilize the interferometer at that position. The interferometer thus maintains stability even as the delay is changed, as shown in Figure 4.8. The piezoelectric stage had a full extension range of 15 μm, giving delay control with a full range of 200 *fs*. This technique thus allows for fine control of the delay between the two arms over a large range, such that fast electron dynamics of a laser-dressed system which persist for long time delays can be measured with high precision and repeatability.

The applicability of the feedback control over the delay was demonstrated in the measurement of a streaking spectrogram. Figure 4.9 shows the spectrograms measured with and without the feedback control. Clearly, when the interferometer was unlocked, even features on the timescale of the laser cycle are smeared out and become difficult to resolve.

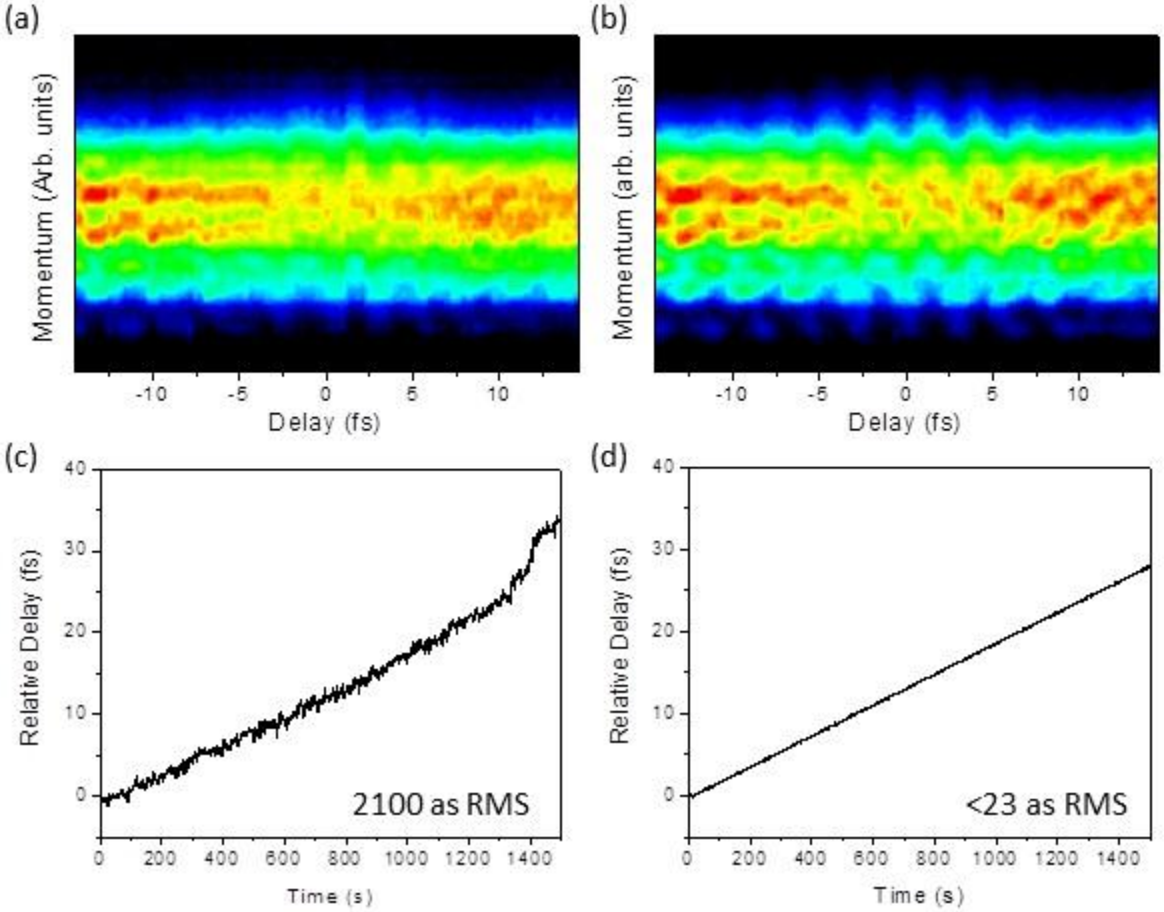

Figure 4.9: Attosecond streaking spectrograms measured (a) without and (b) with feedback control over the delay. The residual RMS delay error for (c) the unlocked case was comparable to the laser cycle period, whereas with the locking it was reduced to below 23 *as* (adapted from [100]).

Transmission Grating Spectrometer

The most critical factor in the transient absorption experiment is the XUV spectrometer, which must have a high energy resolution in the energy range of interest. Insufficient energy resolution will not only broaden the absorption lines in the transmitted spectrum but also reduce the contrast between the absorption lines and the background signal [122]. The transient absorption setup used with the MARS laser was based around a transmission grating spectrometer [127], which is depicted schematically in Figure 4.10. The XUV focal spot at the target gas cell was imaged to the MCP/phosphor detector by a grazing incidence spherical mirror (2° grazing incidence angle), and the different frequency components were dispersed by a transmission grating with 2000 lines/mm.

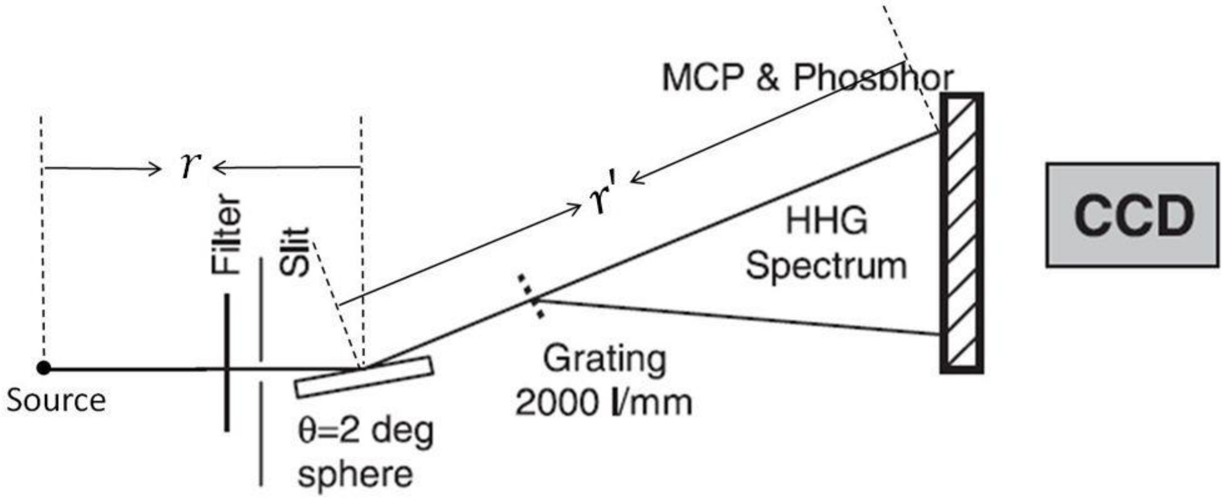

Figure 4.10: Schematic of the transmission grating XUV spectrometer.

In order to optimize the energy resolution, several factors must be considered. First, since the spectrometer resolution is based on the imaging of the XUV focal spot at the gas target, it is important to optimize the focusing of the toroidal mirror. After careful alignment, the XUV focal spot was found to have a Gaussian profile with beam waist w_0 = 20 μm. Second, the image distance should be made as large as possible, since the spatial separation of different frequency components on the detector is proportional to the grating-MCP distance. In the imaging condition, the object and image distances r and r' are related by:

$$\frac{1}{r}+\frac{1}{r'}=\frac{1}{f}, \tag{4.2}$$

where $f=(R/2)\cos\alpha$ is the effective focal length of the spherical mirror, determined by the radius of curvature R = 29.1 m and the incidence angle α = 88° to be f = 50.8 cm. The shortest object distance was limited by the spectrometer configuration to 94 cm, giving an image distance of 106 cm. Applying the grating diffraction equation $\sin\beta=\lambda/D$, the spatial dispersion of the different XUV photon energies on the MCP is given by:

$$\frac{d\omega}{dl}=\frac{\omega\cos\beta}{\lambda r\prime}, \tag{4.3}$$

where D is the groove separation (0.5 μm for 2000 lines/mm grating) and β is the diffraction angle.

For the experiments presented in the next chapters, we are primarily interested in absorption features between 20 and 30 eV (XUV wavelengths from 40-62 nm). We find that for 25 eV, the diffraction angle is approximately 5.7°, and $d\omega/dl$ is found to be 0.24 eV/mm. In the experiment, the grazing incidence angle of the spherical mirror was fine tuned in order to optimize the energy resolution, since the accuracy in our measurement of the image and object distances was on the order of 1 cm. Coupled with the 20 μm object size, and the magnification close to one, one might expect to obtain an energy resolution of 5 meV. However, the energy resolution is limited further by the spatial resolution of the MCP/phosphor and CCD imaging system. Typically, the spatial resolution of an MCP detector is limited to 100 µm or more [128].

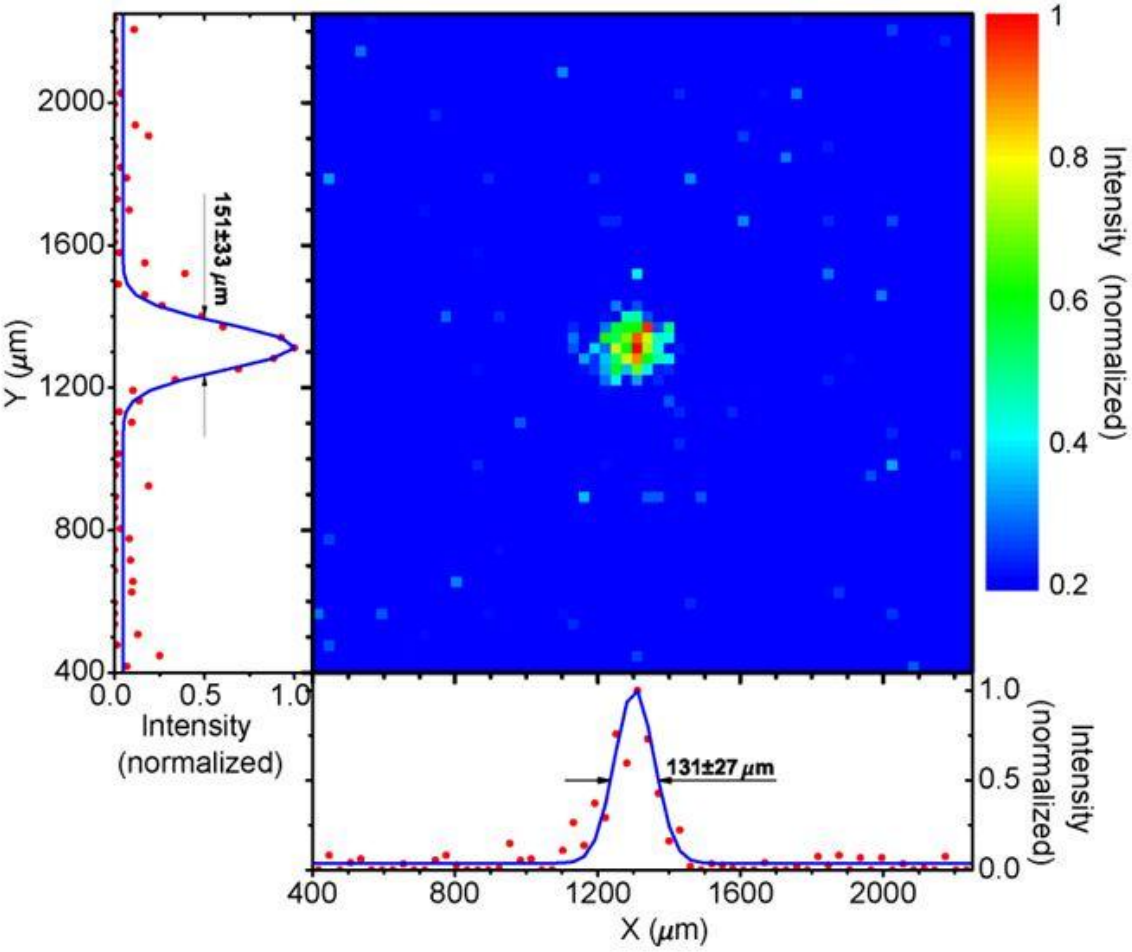

Figure 4.11: CCD image of the quantum noise, demonstrating a spatial resolution of approximately 140 µm (adapted from [122]).

To determine the resolution of our imaging system, we measured the phosphor emission corresponding to “quantum noise” arising from stray ions or photons in the vacuum chamber hitting the MCP detector and producing an electron avalanche. The observed phosphor emission can then be considered to result from an electron produced in a single microchannel pore, giving the ultimate spatial resolution of the system. The CCD image of the quantum noise is shown in Figure 4.11, showing a near-Gaussian spatial profile with a spot size of approximately 130 × 150 μm. This corresponds to an achievable energy resolution of 35 meV. Experimentally, we obtain an energy resolution of 50 meV near 28 eV, determined by measuring the transmitted XUV spectrum in the vicinity of the absorption lines corresponding to excitation of the 3s3p^6*n*p autoionizing state manifold in argon with a pressure-length product of 40 torr×mm, as shown in Figure 4.12. The 3s3p^{6}5p absorption line has a natural linewidth of 12 meV, making it an ideal candidate for the measurement of our spectrometer energy resolution.

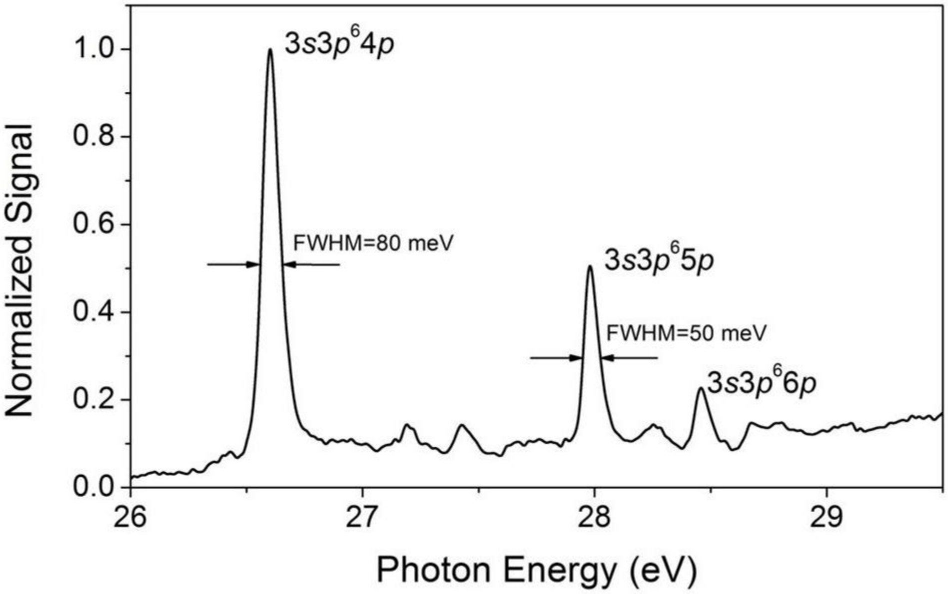

Figure 4.12: Transmitted XUV spectrum of argon gas in the vicinity of the 3s3p^6*n*p autoionizing state manifold. The resolution of the spectrometer was found to be 50 meV by measurement of the 3s3p^{6}5p absorption line with natural linewidth of 12 meV (adapted from [104]).

Flat-Field Grazing Incidence Reflection Grating Spectrometer

Due to the configuration of the transmission grating spectrometer, the observable energy range was limited to photon energies above 22 eV without severe reduction of the signal level (due to the small clear aperture) and worsening of the energy resolution when the grazing incidence angle is decreased below 1° on the spherical mirror. Furthermore, the spherical mirror in the transmission grating spectrometer images the different frequency components on a *spherical* surface, whereas the MCP detector lies in a plane. For these reasons, when constructing the spectrometer for the transient absorption spectrometer for use with the FAST laser, we chose to use a flat-field grazing incidence reflection grating spectrometer, using a Hitachi 001-0640 XUV grating with a flat-field spectrum range of 11-62 nm (20-112 eV). However, due to the size of the MCP detector (75 mm), only 70% of the wavelength range could be detected by the MCP at one time. The spectrometer is shown schematically in Figure 4.13.

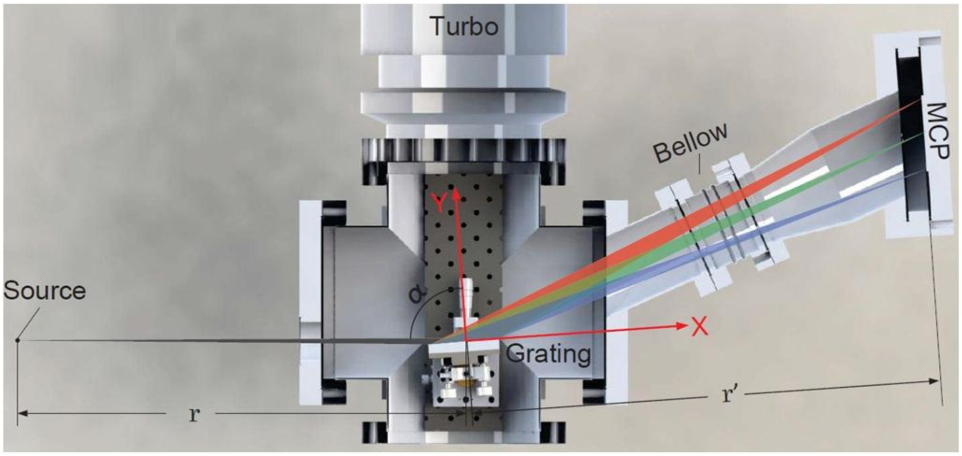

Figure 4.13: Schematic of the flat-field grazing incidence reflection grating spectrometer (adapted from [122]).

In order to obtain the optimum energy resolution within the range of 20 to 112 eV, the grating manufacturer specifies the incidence angle, object distance, and image distance to be α = 85.3°, r = 350 mm, and r' = 469 mm, respectively. However, even though the grating is specified as a flat-field grating, not all the spectrum components in the designed energy range can be perfectly focused to a flat plane. In Figure 4.14, focal "planes" corresponding to six different incidence angles are plotted for spectral components from 11 nm (triangles) to 62 nm (squares). The 40 nm components (circles), corresponding to the upper limit of the energy range of interest in our experiments near 30 eV, are also marked in each focal plane. The Z-axis is parallel to the grating surface, as indicated in Figure 4.13, and the X-axis is parallel to the MCP surface.

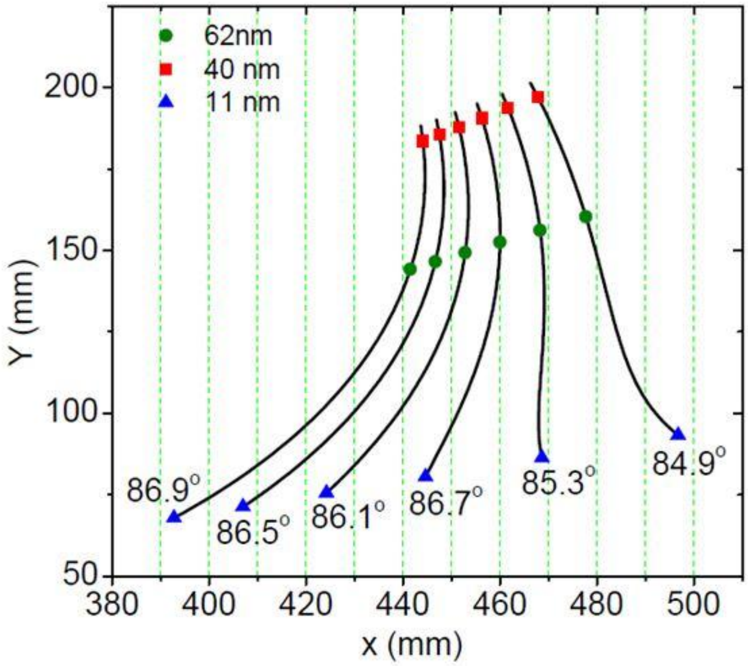

Figure 4.14: Focal "planes" of the flat-field spherical grating for different incidence angles (adapted from [122]).

When the incidence angle is set to the specified value of 85.3°, only the 11-40 nm spectral components are focused to a plane parallel to the MCP, while the focus of the 40-62 nm spectral components, in which we are most interested, lies on a curved surface. Instead, the incidence angle of 86.5° allows the flat-field imaging of the 40-62 nm components, with a corresponding image distance of 448 mm. The optimized resolution with the preferred configuration (α = 86.5°, r = 350 mm, and r' = 448 mm) was confirmed by ray tracing simulations in Zemax. Thus we can focus the 40-62 nm spectral components quite well by tuning the incidence angle and the grating-to-MCP distance. Furthermore, we can optimize the spectral resolution *in situ* by manipulating the grating angle, which can be controlled manually using rotary feedthroughs on the side flange of the vacuum chamber, and the grating-to-MCP distance, which can be adjusted by stretching or compressing the vacuum bellow shown in Figure 4.13 [122].

In order to calibrate the energy range and resolution, the transmitted XUV spectra after absorption by both helium and argon gas were measured. In argon, we again observe the 3s3p^6*n*p autoionizing state absorption line manifold, whereas in helium we can observe the step-like absorption threshold at the ionization potential (24.58 eV), as well as absorption lines corresponding to excitation of 1s*n*p bound states. These excited states will be discussed in more detail in Chapter Five and Chapter Six. Without external disturbance to the atom, the 1s*n*p excited state lifetimes can be as long as several nanoseconds [129], corresponding to nano-eV absorption linewidths. However, since the limited energy resolution of the spectrometer results in not only a broadening of the absorption line, but also in a reduction of the measured absorption strength, such narrow features could not be observed experimentally. In order to observe these absorption lines, the delayed few-cycle NIR laser field in the dressing laser arm of the interferometer was also focused to the target gas cell. Due to the few-photon ionization of the helium excited states in the delayed NIR pulse, the excited state lifetimes can be reduced to the femtosecond timescale, leading to broadened energy resonances and increased absorption. Note that this enhancement of the absorption lines should be observed when the XUV pulse arrives on the target *before* the NIR laser pulse in order to achieve shorter effective lifetimes of the excited states. In our case, the time delay was set to τ_D = -40 *fs* and the dressing laser intensity was on the order of 10^{12} W/cm^2.

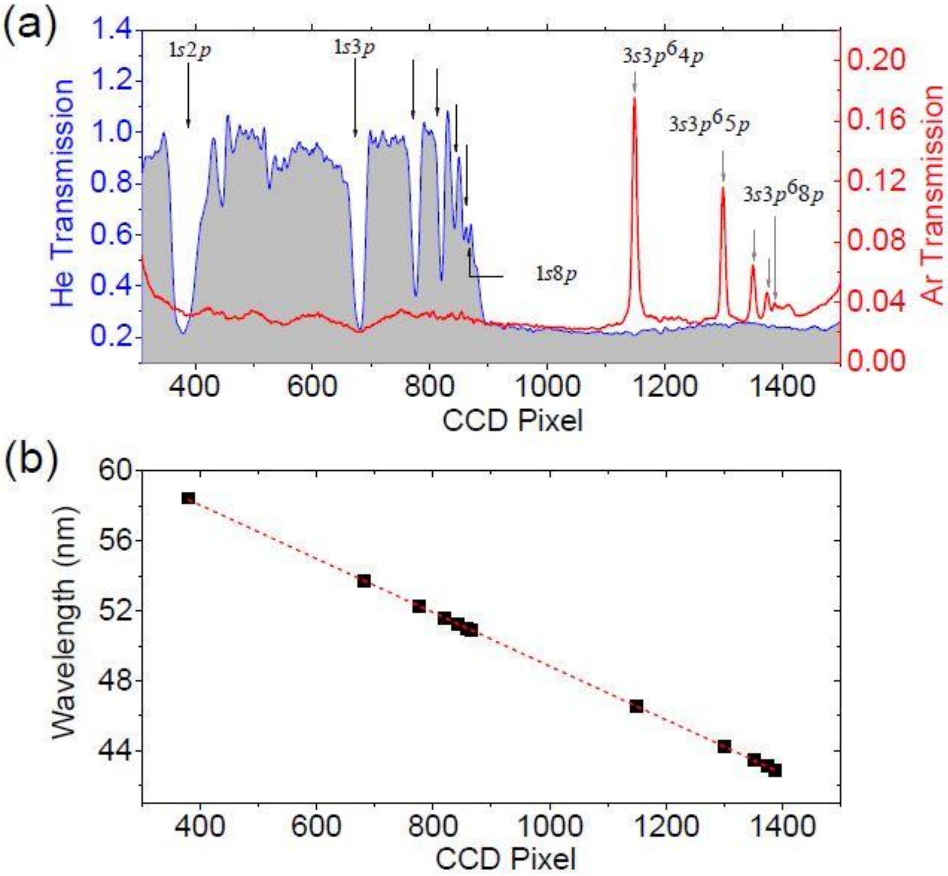

Figure 4.15: *In situ* calibration of the spectrometer. (a) Transmission of helium in the vicinity of the 1s*n*p excited state manifold and of argon in the vicinity of the 3s3p^6*n*p autoionizing state manifold. (b) Location of the known absorption features on the CCD detector, fit to a line (adapted from [122]).

The transmission of the XUV pulses after passing through the argon and helium gases is shown in Figure 4.15. The backing pressure of the target gas cell was 35 Torr for argon gas and 50 Torr for helium gas. In the argon transmission curve, we observe five peaks corresponding to the 3s3p^6*n*p autoionizing states with n = 4-8 as indicated in Figure 4.15(a). In helium, we observe strong absorption above the ionization threshold (around the 900th pixel), and absorption lines corresponding to 1s*n*p states for n = 2-8. The energies of these features are well known from previous experimental and theoretical studies [130-133] and can be used to calibrate the spectrometer.

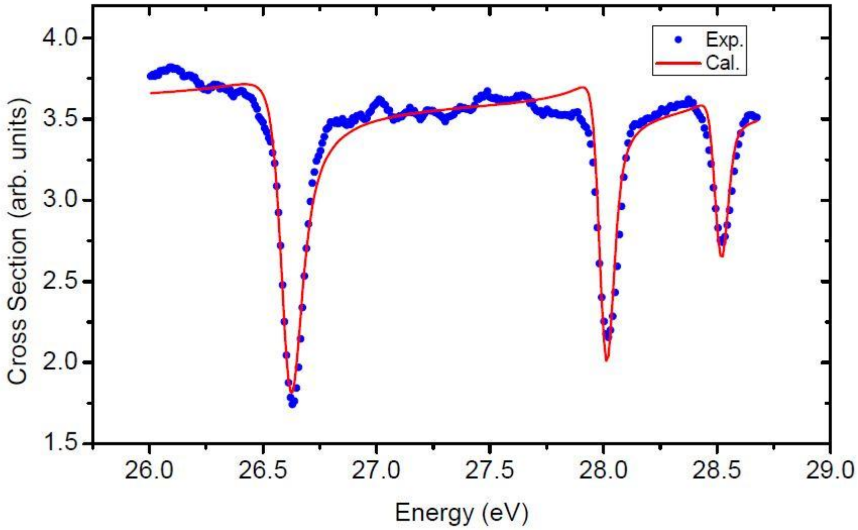

Figure 4.16: Fit of the measured absorption cross section of argon to the Fano profile with a resolution of 60 meV (adapted from [122]).

The wavelengths of the different spectral lines are plotted against their observed pixel locations on the CCD in Figure 4.15(b), which is fit to a linear function. Using this fitting function, we find that energies between 19.3 eV and 31.3 eV can be resolved within the 1600 pixels of the CCD camera. After calibration of the spectrometer energy range, the resolution was again obtained by comparing the measured argon absorption peaks to the known Fano absorption line profiles for the argon autoionizing states, as shown in Figure 4.16. The calculated Fano profiles were convoluted with a Gaussian function representing the spectrometer resolution, and a resolution of 60 meV was obtained by minimizing the error between the calculated convolution result and the measured resonance profiles. The optimum resolution calculated by considering the dispersion of the grating and the resolution of the MCP/phosphor was approximately 48 meV, which is quite close to the measured value.

Theory of Attosecond Transient Absorption Spectroscopy

While the all-optical measurement of transient absorption spectroscopy has technical advantages over the attosecond streaking spectroscopy, interpretation of time-resolved absorption measurements presents a major challenge to the application of transient absorption spectroscopy to dynamic studies. In streaking spectroscopy, the free electron propagation in the laser field can be treated semi-classically, as described in Chapter Two, and the influence of the atomic system is therefore limited to the first few tens of attoseconds in which attosecond time delays in the photoionization process influence the measurement [31,32]. However, this process is nearly instantaneous, and any time structure in photoionization is neglected in nearly all attosecond streaking experiments. On the other hand, calculation of the absorption spectrum of an atom requires knowledge of the full electron wavefunction (including contributions of bound and continuum states) in the combined XUV and NIR fields at all times, since the bound state absorption within a narrow linewidth necessarily results from the long-time structure of the electron wavefunction as described in Chapter Two. Currently, there is no comprehensive theory of attosecond transient absorption spectroscopy which is applicable in all cases, though many recent advances in the theoretical treatment have allowed for modeling of several systems [134-141]. In this section, we will extend the derivations in Chapter Two to describe the transient absorption of an attosecond pulse by a laser-dressed atom, following the formalisms described in references [134-141] where convenient.

The spectrum of a light pulse transmitted through a thin target is given by the Beer-Lambert law, assuming that no temporal reshaping of the incident light pulse or nonlinear frequency generation occurs, as:

$$|\tilde{\varepsilon}_{out}(\omega)|^2 = |\tilde{\varepsilon}_{in}(\omega)|^2 \exp\left\{-\frac{2\pi\omega}{c}\Im\left[\frac{\tilde{P}(\omega)}{\tilde{\varepsilon}_{in}(\omega)}\right]NL\right\}, \tag{4.4}$$

where $\tilde{P}(\omega)$ is the Fourier transform of the time-dependent polarization

$$P(t) = \langle\Psi(\boldsymbol{r},t)|z|\Psi(\boldsymbol{r},t)\rangle \tag{4.5}$$

of the atom described by the wavefunction $|\Psi(\boldsymbol{r},t)\rangle$, $\tilde{\varepsilon}_{in}(\omega) = \int_{-\infty}^{\infty} dt[F_L(t) + F_X(t-\tau_D)]\, e^{i\omega t}$ is the complex spectrum amplitude of the combined laser field, and NL is the density-length product. Provided that the NIR pulse is not strong enough to generate HHG in the absence of the XUV pulse, the output spectrum in the XUV region will be modified only by absorption of light by the laser-dressed atom, and the absorbance is given approximately by:

$$A(\omega) \approx \frac{2\pi\omega}{c}\Im\left[\frac{\tilde{P}(\omega)}{\tilde{\varepsilon}_{in}(\omega)}\right]NL. \tag{4.6}$$

Here, we note that even when both pulses are transform-limited, the inter-pulse time delay will introduce a linear phase in the XUV region of the spectrum, and therefore the imaginary component of $\tilde{\varepsilon}_{in}(\omega)$ is nonzero and must be accounted for.

From Equation 4.6, we find that modeling the transient absorption requires knowledge of the two laser pulses and the laser-dressed atom wavefunction. Clearly the most difficult aspect of this lies in accurate calculation of the wavefunction. While *ab initio* techniques are available for accurate calculation of laser-dressed atom wavefunctions in the single active electron approximation, and the helium atom can be solved numerically without approximation [142], these calculations are by and large inaccessible to experimentalists. We instead choose to write the time-dependent wavefunction analytically as a time-dependent superposition of stationary states of the field free atom, similar to the wavefunction expansions used in Chapter Two. We then numerically solve the coupled differential equations for the time-dependent state amplitudes to obtain the wavefunction.

The TDSE of the laser-dressed atom is given in the dipole approximation by Equation 2.5. When the two laser pulses are linearly polarized along the z-axis, we can rewrite the time-dependent Hamiltonian in terms of the field-free atom Hamiltonian H_0 and the interaction Hamiltonian $H'(t)$:

$$H(t) = H_0 + H'(t), \tag{4.7}$$

where $H'(t) = -zF_L(t) - zF_X(t-\tau_D)$ describes the interaction of the atom with both laser fields. A natural choice of basis set for expansion is the set of stationary states of the field-free atom $|j\rangle$, for which $H_0|j\rangle = E_j|j\rangle$. Then, the wavefunction can be written as $|\Psi(\boldsymbol{r},t)\rangle = \sum_j c_j(t)|j\rangle$, and Equation 2.5 can be rewritten:

$$i\frac{\partial}{\partial t}\sum_j c_j(t)|j\rangle = \left[E_j - zF_L(t) - zF_X(t-\tau_D)\right]\sum_j c_j(t)|j\rangle. \tag{4.8}$$

Multiplying both sides by the unity operator $\sum_k |k\rangle\langle k|$, and using $\langle k|j\rangle = \delta_{kj}$ and $\langle k|z|j\rangle = d_{kj}$ for $j \neq k$, we obtain:

$$i\frac{\partial}{\partial t}\sum_j c_j(t)|j\rangle = \sum_j E_j c_j|j\rangle - \sum_j \sum_{k\neq j}\left[d_{kj}F_L(t) + d_{kj}F_X(t-\tau_D)\right]c_k(t)|k\rangle. \tag{4.9}$$

Collecting terms with $j = a$, we get a set of coupled differential equations:

$$i\dot{c}_a = E_a c_a(t) - \sum_{k\neq a} d_{ka}[F_L(t) + F_X(t)]c_k(t), \tag{4.10}$$

which can be solved numerically using tabulated values of energies and dipole matrix elements to obtain the time-dependent amplitudes and the full wavefunction. In our case, we solve the set of coupled Equations 4.10 using the fourth-order Runge-Kutta differential equation solver in LabVIEW. This formulation of the transient absorption calculation allows simulation of bound state systems, and can be extended, as we will see later, to more complicated scenarios involving electron correlation. These calculations, unlike current *ab initio* simulations, are easily accessible to experimentalists, and can be applied to a wide range of targets due to the breadth of spectroscopic data acquired previously with synchrotron radiation sources.

Notes

Portions of this chapter were used or adapted with permission from the following:

> Shouyuan Chen, Michael Chini, He Wang, Chenxia Yun, Hiroki Mashiko, Yi Wu, and Zenghu Chang. Carrier-envelope phase stabilization and control of 1 kHz, 6 mJ, 30 fs laser pulses from a Ti:Sapphire regenerative amplifier. *Applied Optics* **48**, 5692 (2009).
>
> Xiaowei Wang, Michael Chini, Yan Cheng, Yi Wu, and Zenghu Chang. *In situ* calibration of an Extreme Ultraviolet Spectrometer for Attosecond Transient Absorption Experiments. *Submitted* (2012).
>
> Michael Chini, Hiroki Mashiko, He Wang, Shouyuan Chen, Chenxia Yun, Shane Scott, Steve Gilbertson, and Zenghu Chang. Delay control in attosecond pump-probe experiments. *Optics Express* **17**, 21459 (2009).
>
> He Wang, Michael Chini, Shouyuan Chen, Chang-Hua Zhang, Feng He, Yan Cheng, Yi Wu, Uwe Thumm, and Zenghu Chang. Attosecond Time-Resolved Autoionization of Argon. *Physical Review Letters* **105**, 143002 (2010).

CHAPTER FIVE: SUB-CYCLE AC STARK SHIFTS IN HELIUM

The primary target of the attosecond transient absorption studies is the helium atom. This is due to both its accessibility with the ultrabroadband isolated attosecond pulses from DOG and to its convenience for *ab initio* calculations and reduced-dimensionality models. Different aspects of the helium excited state dynamics observed in the transient absorption measurements will be presented in the next two chapters. In Chapter Five, we will discuss those dynamic features which can be described by the coupling of a single 1s*n*p excited state to the nearby excited state manifolds by absorption or emission of a NIR photon. Then, in Chapter Six, we will discuss new absorption features which result from the dynamic evolution of the excited state wavepacket excited by the isolated attosecond pulse in the presence of the few-cycle laser.

Excited States of Helium

The helium ground state and excited state energy levels of interest are shown in Figure 5.1, including the 1s*n*p excited states (red) which can be populated from the ground state through absorption of an XUV photon as well as the 1s*n*s (blue) and 1s*n*d states (green) which cannot absorb or emit XUV light but can be coupled to the 1s*n*p states by absorption or emission of a NIR photon. Whereas the 1s*n*p states extend between 21.22 eV ($n = 2$) up to the ionization threshold at 24.58 eV, the 1s2s state lies at a lower energy of 20.6 eV. The 1s*n*d ($n \geq 3$) energy levels, on the other hand, are nearly coincident with the 1s*n*p levels. The hatched areas indicate continuum states lying above the ionization threshold.

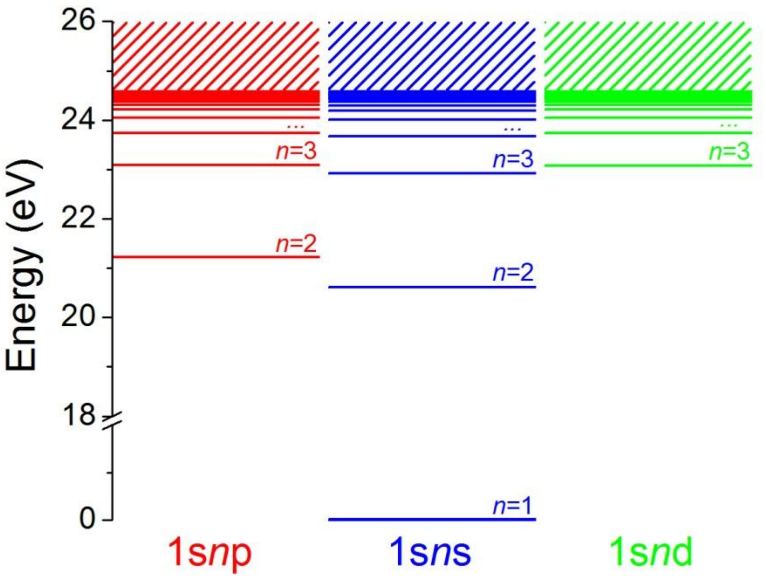

Figure 5.1: Helium energy levels of interest.

Bound State Energies and Dipole Matrix Elements

The bound state energies are given in Table 5.1. The energies are taken from tabulated values based on very high-precision variational calculations [8] up to $n = 10$ and $l = 7$, which are essentially exact for our purposes [133] and in good agreement with compiled data from measurements [132]. The energies do not take into account the finite mass corrections, and therefore the tabulated energies assume a nucleus of infinite mass.

The magnitudes of the dipole matrix elements $|d_{ka}|$ are listed in atomic units in Table 5.2 [133]. Here, the dipole matrix elements are determined from oscillator strengths f_{ka} calculated in the limit of infinite nuclear mass from the variational eigenstates, using the definition:

$$f_{ka} = \frac{2\omega_{ka}}{3}|d_{ka}|^2. \tag{5.1}$$

Since the phases of the dipole transition matrix elements are unknown, in the numerical simulations based on the theoretical treatment of Chapter Four, we assume the dipole matrix elements to be positive real numbers.

Table 5.1: Helium excited state energy levels (from [133], [132])

Excited State Designation	**Energy relative to $1s^2$ (eV)**
1s2s	20.61
1s2p	21.22
1s3s	22.92
1s3p	23.09
1s3d	23.08
1s4s	23.67
1s4p	23.74
1s4d	23.74
1s5s	24.01
1s5p	24.05
1s5d	24.05
1s6s	24.19
1s6p	24.21
1s6d	24.21
1s7s	24.30
1s7p	24.31
1s7d	24.31
1s8*l*	24.37
1s9*l*	24.42

Table 5.2: Magnitudes of the dipole matrix elements $|d_{ka}|$ from tabulated values [133].

	1s2p	1s3p	1s4p	1s5p	1s6p	1s7p
$1s^2$	0.73	0.36	0.23	0.16	0.12	0.095
1s2s	4.97	1.57	0.79	0.51	0.36	0.28
1s3s	1.87	12.26	2.68	1.34	0.87	0.64
1s4s	0.66	4.61	24.16	4.01	2.02	1.3
1s3d	3.95	9.26	0.97	0.36	--	--
1s4d	1.39	6.38	16.92	2.27	--	--
1s5d	0.79	2.45	9.24	27.85	--	--
1s6d	0.54	1.43	3.65	13.07	--	--
1s7d	0.4	0.98	2.14	5.06	--	--
1s8d	0.3	0.74	1.48	2.97	--	--

Experimental Absorption Spectra

The MCP images of the isolated attosecond pulse spectrum transmitted through the evacuated gas cell and the spectrum transmitted through the helium-filled cell with a pressure-length product of ~40 Torr×mm are shown in Figures 5.2(a) and (b), respectively. Absorption features corresponding to excitation of the 1snp excited states up to n = 4 are labeled in Figure 5.2(b). The long-wavelength edge at 60 nm represents the edge of the MCP detector in the flat-field grazing incidence reflection grating spectrometer, which could be shifted by changing the grating angle and the image distance. The absorption features are difficult to observe in the absence of a dressing laser pulse, due to the long lifetimes of the excited states which result in narrow (~10^{-9} eV) linewidths, so the absorption was measured in the presence of a delayed ($\tau_D \approx$ -40 *fs*) few-cycle NIR laser with intensity on the order of 10^{12} W/cm^2. The presence of the laser reduces the excited state lifetime to be approximately equal to the pump-probe delay τ_D, since the laser can transfer population to other excited states, and thereby results in broader absorption lines which can be more easily observed with the limited resolution of the spectrometer. Additional features near the 1s2p absorption line are caused by the NIR laser and will be discussed in Chapter Six.

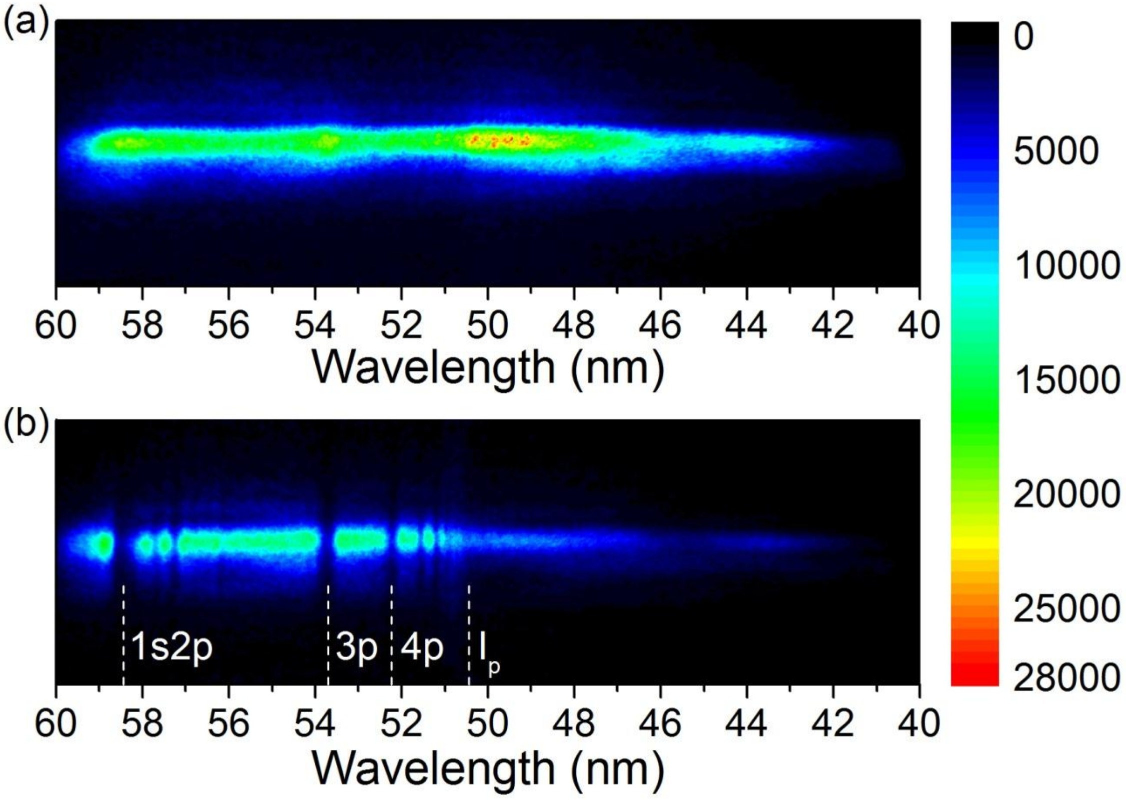

Figure 5.2: Continuum spectrum of an isolated attosecond pulse (a) before and (b) after absorption in a helium-filled gas cell.

Theoretical Laser-Dressed Absorption Spectra

Several recent theoretical studies have addressed the absorption of a short XUV pulse or pulse train by the helium atom in the presence of a dressing laser field [134,136,137]. Each of these studies suggests the possibility of controlling the atom's absorption through control of the dressing laser parameters, and together serve as a starting point for understanding the laser-dressed absorption process. However, the computationally-intensive calculation prohibits prediction of the time delay-dependent absorption spectrum for a variety of laser pulse parameters, and these studies therefore cannot yield a complete understanding of the absorption process. Moreover, no one has so far reported a theoretical study of the laser-dressed absorption of an *isolated attosecond* pulse in helium, making interpretation of the theoretical results extremely difficult. On the other hand, the current experimental tools allow for absorption measurements in helium (as well as more complicated systems) using isolated attosecond pulses and synchronized few-cycle NIR laser pulses. The results of these experiments can guide theoretical simulations and aid in the development of new models for the calculation of the time-resolved absorption process.

Sub-Cycle Nonresonant AC Stark Shifts of the 1s3p and 1s4p Energy Levels

The first studies in helium were performed on the 1s3p, 1s4p and higher-lying excited states, for which the laser frequency ω_L is much larger than the energy differences ω_{ka} between the state of interest and the nearest excited states with the largest dipole matrix elements. According to existing theory, when the frequency of the monochromatic laser field is far from any atomic resonance transition frequencies, the optical AC Stark shift is equivalent to the quadratic DC Stark shift [43]. The measured energy level shift of a given state $|a\rangle$ is then given in Equation 2.24.

While the AC Stark shift in Equation 2.24 is *by definition* cycle-averaged, it originates from the bound electron dynamics induced by the instantaneous laser field on the sub-optical-cycle time scale, given in Equation 2.23. However, the instantaneous energy level shifts have not been directly measured experimentally. Early experiments using monochromatic or long-pulse (~ns) laser sources [42] could verify the cycle-averaged perturbation theory predictions but lacked time resolution. More recently, pump-probe measurements using probe laser pulses substantially longer than the oscillation period of the Stark field revealed Stark shifts on the time scale of the laser intensity envelope with a time resolution of ~10 *fs* [40,41]. However, even in these measurements only the cycle-averaged energy shifts could be measured, as the available probes lacked the temporal resolution to reveal the possibility of a faster response of the bound states to the laser field. Furthermore, dynamics in field-free atomic excited states evolve on characteristic time scales similar to the classical orbital periods, which are typically longer than the Stark laser cycle, and it is therefore unclear whether the sub-cycle AC Stark shifts exist.

Time-Resolved Absorption Spectra

To resolve the sub-cycle AC Stark shifts, we probed the singly-excited states of helium using isolated attosecond pulses with a pulse duration nearly 20 times smaller than the NIR Stark laser period using the attosecond transient absorption setups described in Chapter Four [39]. Isolated 140 *as* pulses and 6 *fs* laser pulses with intensity of ~3×10^{12} W/cm^2 were focused together to a helium-filled gas cell with a pressure-length product of ~40 Torr×mm. The spectrum of the XUV light passing through the laser-perturbed target was measured as a function of the time delay between the attosecond pulse and femtosecond Stark field oscillation, unveiling the dynamic response of each energy level.

Figure 5.3(a) shows the absorbance of the helium target as a function of the time delay between the attosecond pulse and the near infrared laser field. Negative delays indicate that the attosecond pulse arrives on the target before the NIR laser pulse. The isolated attosecond pulses with spectra covering photon energies from the lower limit of the spectrometer energy range (~20 eV) to more than 30 eV were generated with DOG in argon gas using the MARS laser system, and the spectra were obtained using the transmission grating spectrometer. The spectral features are caused by absorption to 1s*n*p states as described above and in Chapter Two, with roughly half of the signal above the ionization potential being absorbed. Prominent absorption lines corresponding to the excitation of the laser-dressed 1s3p (23.1 eV) and 1s4p (23.74 eV) states, as well as the ionization potential, are indicated in the figure. The photon energies below 22 eV, including absorption to the laser-perturbed 1s2p state (21.2 eV), could not be observed with the transmission grating spectrometer and will be discussed later in this chapter. We find that the cycle-averaged positions of the absorption lines follow the intensity profile of the NIR laser, as indicated in the figure. The observed energy shifts at the peak of the laser pulse agree well with recent calculations [134,136] and measurement of the cycle-averaged 1s3p Stark shift [143].

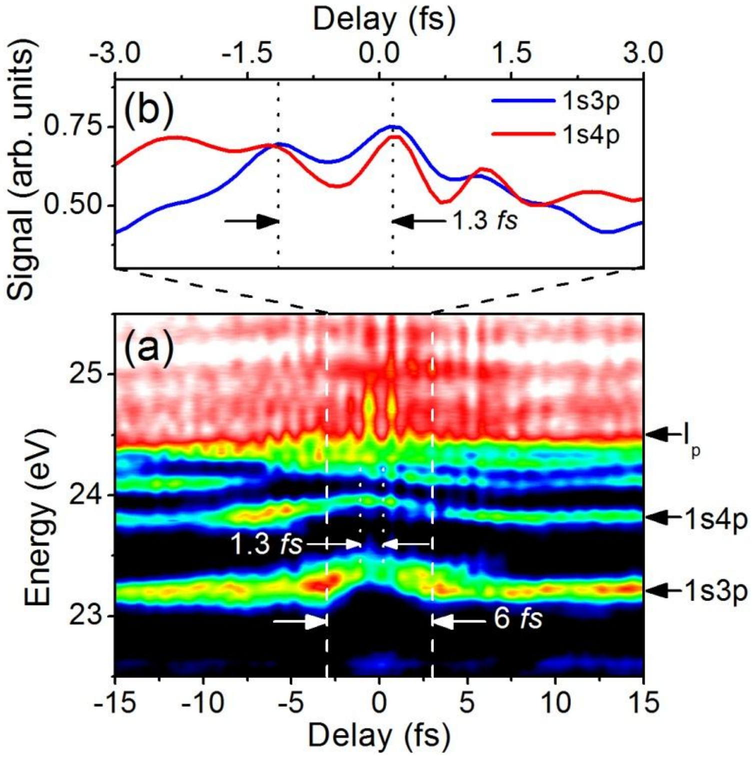

Figure 5.3: Absorbance of the laser-dressed helium target as a function of the pump-probe delay. (a) The absorbance spectra show dynamics on the 6 *fs* and 1.3 *fs* timescales. (b) The absorbance near the field-free 1s3p (23.09 eV) and 1s4p (23.74 eV) absorption lines oscillates near zero delay with a frequency of $\omega_L/2$ = 1.3 *fs* (adapted from [39]).

One surprising feature in the measured spectrogram is the fast modulation of the absorption with a period of ~1.3 *fs*, half the laser oscillation period, indicated in Figure 5.3(a) and shown for absorption near the unperturbed 1s3p and 1s4p absorption lines in Figure 5.3(b). Interestingly, this modulation is present not only near the absorption peaks of the 1s*n*p states, but persists in regions of low absorption between the absorption lines. Such modulations in the transient absorption signal were previously observed by using an attosecond pulse train [144], and the authors also noted that the transmitted signal far from any absorption peaks was modulated. These modulations of the absorption probability can be explained by the laser-induced changes to the amplitudes $c_k(t)$, leading to interferences in the electron wavepacket [145-148], which will be discussed in more detail in Chapter Six. However, previous studies have not considered the effects of the sub-cycle AC Stark shifts.

Line Shifts and Broadening

Because of the broad continuum spectrum of the isolated attosecond pulse, we were able to extract the sub-cycle energy shifts and linewidths of the excited state energy levels. In Figure 5.4, we plot the shifts of the central energies and the absorption linewidths of the laser-dressed 1s3p and 1s4p absorption lines, obtained by fitting each absorption line to a Gaussian function for every delay step. We find that the half-cycle dynamics are apparent in each absorption line, but there are differences in the features of the different excited states. From the plots, we find that the 1s3p absorption line exhibits a periodic shift and broadening with approximately twice the laser frequency, superimposed on the overall shift on the time scale of the pulse envelope. The sub-cycle shift and broadening of the 1s4p energy level, however, is substantially reduced in comparison to that of the 1s3p state.

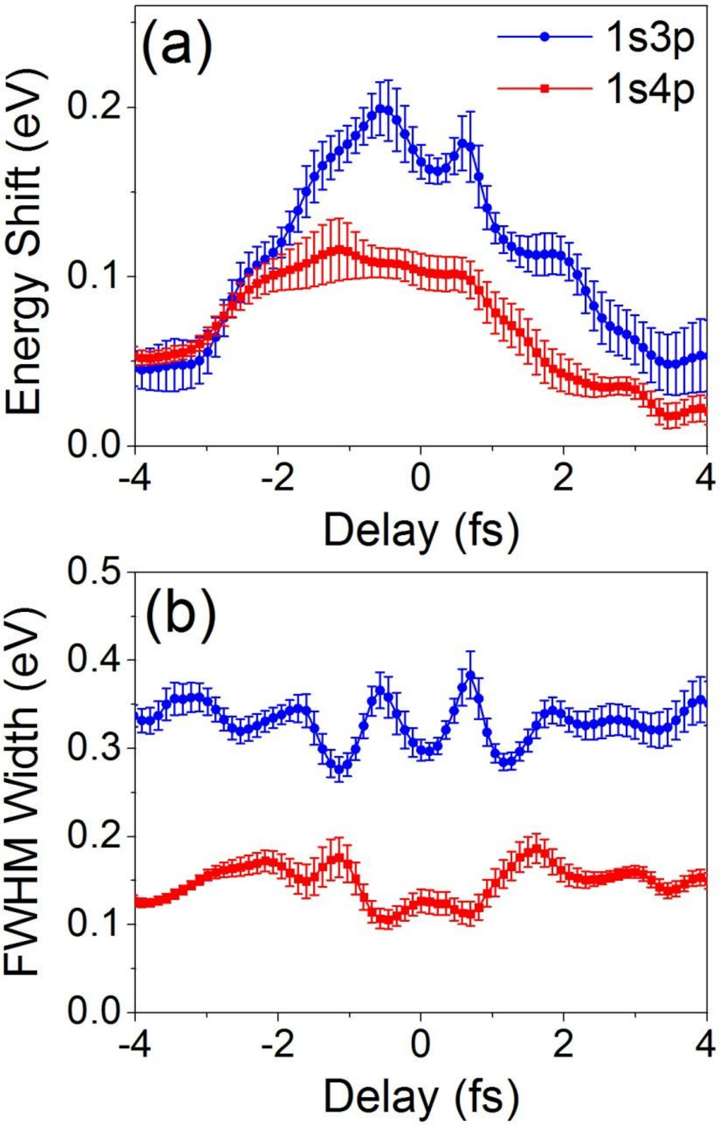

Figure 5.4: Measured (a) energy shift and (b) linewidth of the 1s3p and 1s4p absorption lines. Both parameters change rapidly on timescales shorter than the laser cycle period (adapted from [39]).

Theoretical Model and Simulations

As discussed in Chapter Four, the interaction of the atom with XUV and NIR pulses in the transient absorption experiment induces a time-dependent polarization $P(t)$, which emits an electromagnetic field. It is this polarization-induced radiation which is then measured by the XUV spectrometer, with the measured spectrum at each time delay related to the Fourier transform of the polarization in Equation 4.5. Therefore, the absorption measurement samples the dynamics induced by the two fields over a long time period after the XUV pulse excitation [135,138]. We therefore follow the theoretical treatment described in Chapter Four, and calculate the absorption from the time-dependent polarization.

Calculation of the polarization requires that we know the time-dependent electron wavefunction $|\Psi(\boldsymbol{r},t)\rangle$ in the presence of both the XUV and NIR fields, as discussed in Chapter Four. However, solution of the coupled equations for the amplitudes $c_k(t)$ is impractical, due to the large number of bound and continuum states involved (both 1s3p and 1s4p states can be ionized by only one NIR photon) and the limited number of dipole matrix elements available. We therefore calculate $|\Psi(\boldsymbol{r},t)\rangle$ under several assumptions: (i) the NIR pulse has no effect on the ground state because of its large binding energy and the low NIR intensity (~10^{12} W/cm^2) and its effects on excited states were treated with second-order perturbation theory, with the form of the NIR-perturbed wavefunction given by Equations 2.20 and 2.23, (ii) the XUV pulse was treated as a δ-function arriving at time τ_D, which is justified since the XUV duration is much shorter than the NIR laser cycle, (iii) the XUV-atom interaction was treated perturbatively due to the low intensity of the XUV field, as in Chapter Two, and (iv) each excited state was treated independently. Under these assumptions, we can calculate the time-dependent electron wave function as:

$$|\Psi(\boldsymbol{r},t)\rangle \approx \begin{cases} |0\rangle e^{-iE_0 t}, & t < \tau_D \\ |0\rangle e^{-iE_0 t} + d_{a0} F_{X,0} \left| c_a^{ion}(t) \right| e^{-i\int_{\tau_D}^{t} dt' [E_a + \delta E_a(t')]} |a\rangle, & t > \tau_D \end{cases}, \tag{5.2}$$

where δE_a is defined as in Equation 2.23 and

$$\left|c_a^{ion}\right| = e^{-\int_{-\infty}^{\infty} dt w_{PPT}(t)} \tag{5.3}$$

describes the reduction in the excited state population due to ionization, determined from the PPT ionization rate [47].

For the excited states of interest, we calculated α_{1s3p} and γ_{1s3p} (as well as α_{1s3p} and γ_{1s3p}) from tabulated values of transition frequencies and oscillator strengths [133] with a laser wavelength of 750 nm. The excited state energies and magnitudes of the dipole matrix elements are listed in Tables 5.1 and 5.2. From these, we then calculated the sub-cycle AC Stark shift for each state. Based on these assumptions, we calculated $P(t)$ and its Fourier transform $\tilde{P}(\omega)$ for the wavefunction defined in Equation 5.2. The XUV absorbance, defined in Equation 4.6, was calculated for each delay using the same parameters as in the experiment and is shown in Figure 5.5. In Figures 5.6(a) and (b), we plot the calculated energy shifts and widths of the laser-dressed 1s3p and 1s4p states and find that the sub-cycle features in the measured line shifts and widths are reproduced quite well by the sub-cycle AC Stark shifts. Figures 5.6(a) and (b) also show the calculated energy level shift and width for the 1s3p state when only the ionization is included. In this case, there is no observed energy level shift or sub-cycle modulations in the linewidth, confirming that these features are caused by the sub-cycle AC Stark shift. Although several features, for example, the exact magnitude of the energy level shift and the FWHM width of the shift profile along the delay axis, cannot be reproduced exactly, these discrepancies likely arise from the approximations made in the calculation. For example, the available tabulated dipole matrix elements are limited, and couplings to continuum states may not be accurately treated by the PPT model.

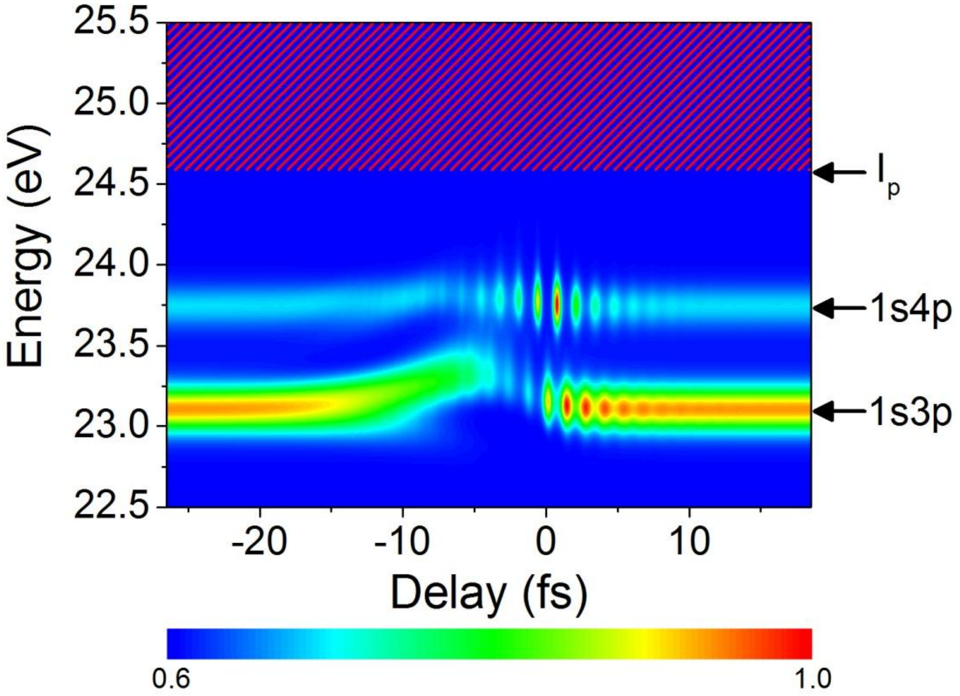

Figure 5.5: Calculated absorbance of helium using the model wavefunction in Equation 5.2, demonstrating the effects of the sub-cycle AC Stark shifts (adapted from [39]).

This model, however, explains the capability of attosecond transient absorption to measure sub-cycle changes in absorption lines, in spite of the fact that the absorption is by definition a time-integrated process. As illustrated by using the electron wavefunction in Equation 5.2 to calculate the polarization given in Equation 4.5, we see that the time-dependent polarization can be effectively cut off by a strong NIR laser field, dropping to nearly zero as the atom is fully ionized. Therefore, when the two pulses overlap, the observed absorption lines are shaped by both the sub-cycle AC Stark shifts and the strong ionization, allowing the measurement of attosecond dynamics in bound atomic states.

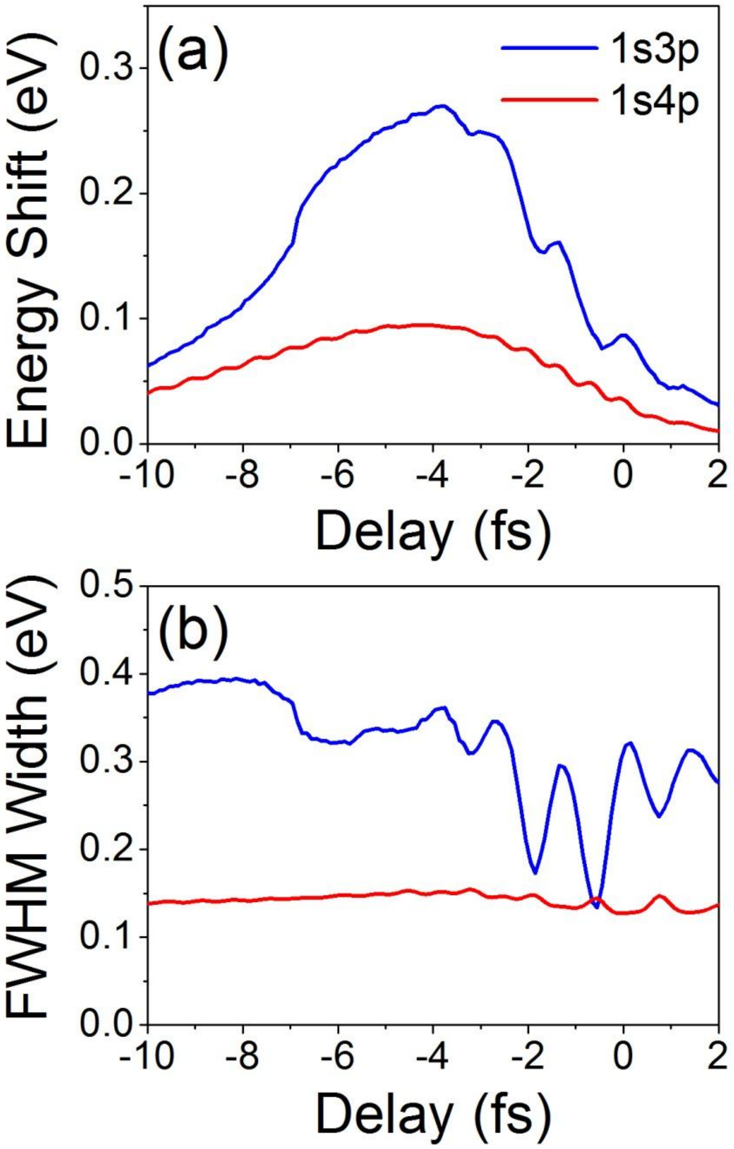

Figure 5.6: Calculated (a) energy shift and (b) linewidth for the 1s3p and 1s4p absorption lines (adapted from [39]).

Evidence of a Sub-Cycle Ponderomotive Energy Shift

The ponderomotive energy, defined in Equation 2.32, is the quiver energy of an electron in a laser field, averaged over the laser cycle. For our purposes, the ponderomotive energy represents an effective shift of the ionization potential for an electron ionized into a laser-dressed continuum state. In this chapter, we have so far demonstrated that the energy levels of bound states exhibit a sub-cycle energy shift, which is caused by the sub-cycle AC Stark shift. However, this effect can be observed in transient absorption experiments only when the laser intensity is high enough to substantially ionize the excited state population, giving the state an effectively short lifetime.

The ponderomotive shift extends the AC Stark shift of the bound energy levels into the continuum states, where energy levels are infinitesimally spaced and the nonresonant Stark laser frequency is much larger than the spacing between energy levels. However, in the continuum states, the time resolution of attosecond transient absorption spectroscopy is not in any way limited by the long excited state lifetimes, as the electrons are already ionized. Therefore, the energy shift of the ionization potential can in principle be measured with high fidelity.

The measurement of the ponderomotive energy shift does require high laser intensity, since the magnitude of the shift is typically smaller than the AC Stark shift. This can be understood by examination of the polarizability α_a in Equation 2.23. For bound states, $|\omega_{ka}^2 - \omega_L^2|$ is typically smaller than ω_L^2, and α_a can be quite large. However, ω_{ka}^2 drops to zero for continuum states, and the AC Stark shift reduces to the ponderomotive shift of Equation 2.32.

The delay-resolved absorbance near the ionization threshold, measured with the FAST laser and grazing incidence reflection spectrometer, is shown in Figure 5.7 for a higher intensity of 1.5×10^{13} W/cm^2. Two features are evident near the ionization threshold. At negative delays, we observe interference structures which will be discussed in detail in the next chapter. Near zero delay, however, we observe a shift in the absorption threshold that exhibits a strong half-cycle periodicity. This half-cycle oscillation is a strong evidence of a sub-cycle ponderomotive shift which follows the square of the instantaneous laser field strength (indicated by the dashed line in the figure), analogous to the sub-cycle AC Stark shift. Figure 5.8(a) shows the measured absorbance at the maximum energy shifts for dressing laser intensities of 7×10^{11}, 5×10^{12}, and 1.5×10^{13} W/cm^2, along with the corresponding ponderomotive-shifted ionization potential. In Figure 5.8(b), we show the measured absorbance for the intensity of 1×10^{13} W/cm^2 for three different values of the time delay. For a delay of -0.42 *fs*, we observe a maximum energy shift, whereas the shift is minimal at a delay of -1.27 *fs*. These delays are separated by an odd number of laser quarter-cycles. We compare the absorbance at these delays with that at -25 *fs* delay, where no energy shift is observed. While the absorption threshold can be found at the ionization potential for the delays of -25 *fs* and -1.27 *fs*, it is shifted by nearly 1 eV at 0.42 *fs* delay.

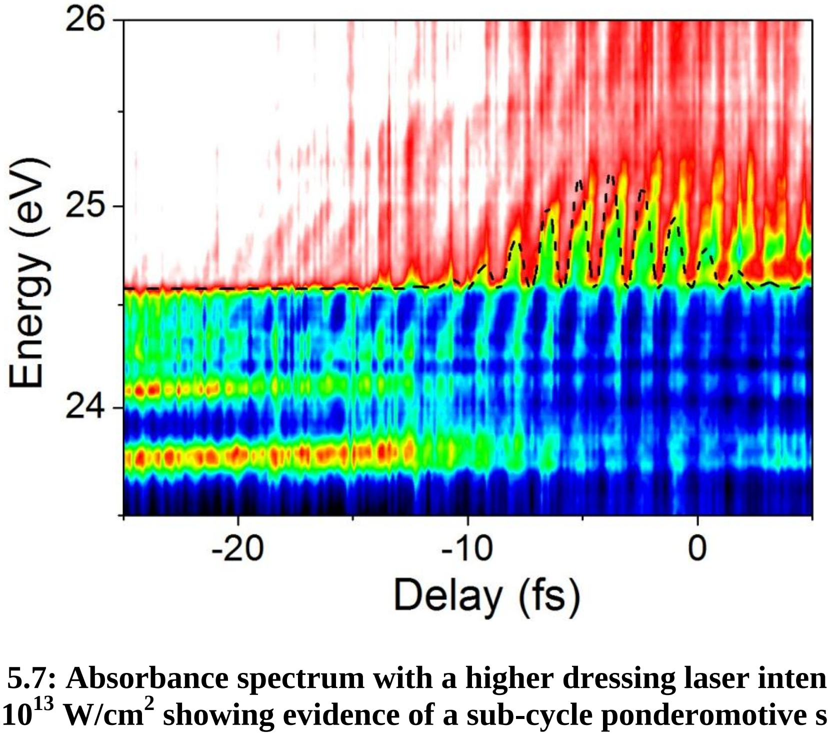

Figure 5.7: Absorbance spectrum with a higher dressing laser intensity of 1.5×10^{13} W/cm^2 showing evidence of a sub-cycle ponderomotive shift (adapted from [149]).

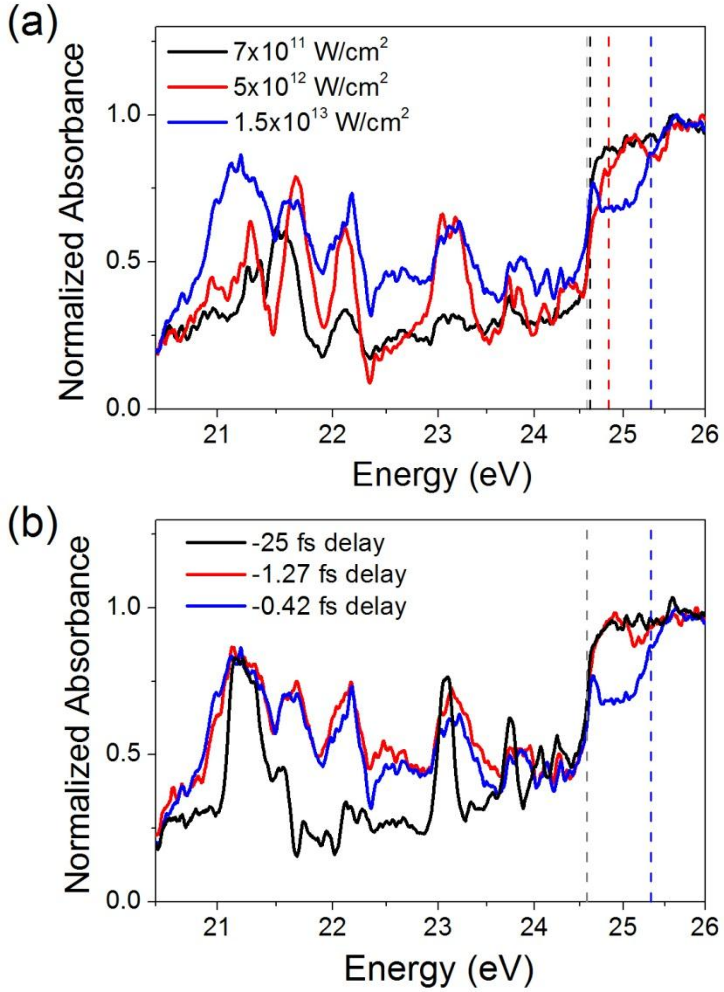

Figure 5.8: Absorbance of helium measured (a) at a fixed delay with different laser intensities and (b) for different delays with an intensity of 1×10^{13} W/cm^{2} (adapted from [149]).

Resonant Coupling: Autler-Townes Splitting of the 1s2p Energy Level

Subsequent experiments focused primarily on the 1s2p excited state of helium. Unlike the 1s3p and higher lying states, for which the dynamics are predominantly driven by the *nonresonant* interaction of the laser with the atom which primarily results in the nonresonant AC Stark shift, the 1s2p state (21.2 eV) can be strongly coupled to 1s3s (22.9 eV) and 1s3d (23.1 eV) states through absorption of a NIR photon. This is schematically illustrated in Figure 5.9, which shows the coupling of the 1s2p state to the 1s3s and 1s3d states by the few-cycle NIR laser. The central frequency of the FAST laser is approximately ω_L = 1.7 eV, equal to the energy difference between the 1s2p and 1s3s states, and the broad spectrum also includes 1.85 eV photons, resonant with the 1s2p-to-1s3d transition frequency. In Figure 5.10 the polarizabilities α_{1s2p} and α_{1s3p} are plotted for different laser frequencies along with the spectrum of the 5 *fs* laser pulse measured from the FAST laser, further illustrating the effects of the resonance on the interaction. Whereas α_{1s3p} is approximately constant between 500 and 900 nm and Equation 2.23 can be applied to obtain the energy shift, α_{1s2p} varies by orders of magnitude in the vicinity of resonance conditions for which $\omega_L = \omega_{1snl,1s2p}$, where $l = s, d$.

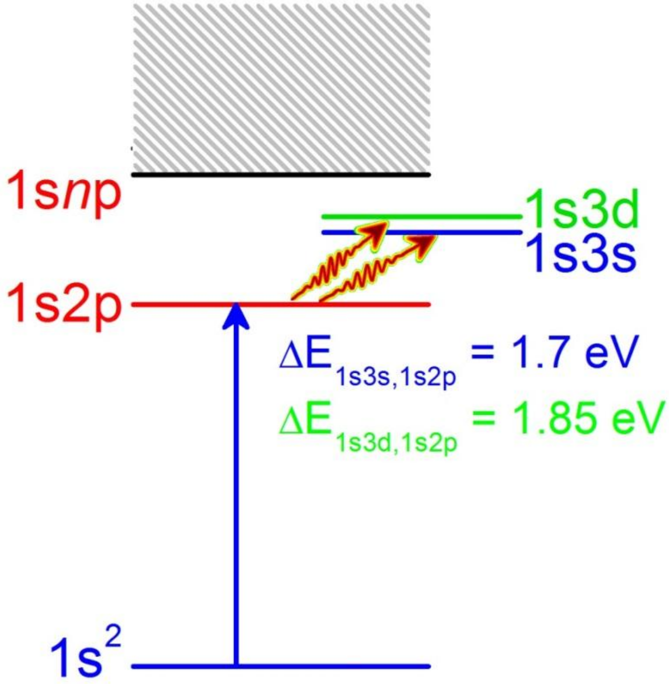

Figure 5.9: Resonant coupling of the 1s2p to 1s3s and 1s3d states.

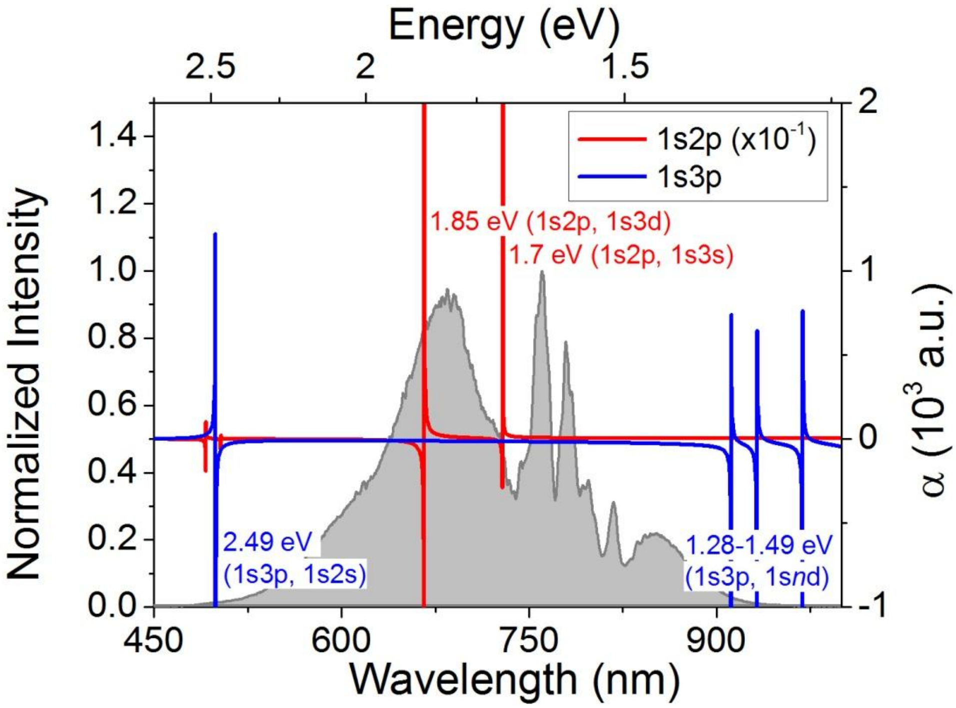

Figure 5.10: Polarizabilities of the 1s2p and 1s3p states for photon energies within the few-cycle NIR laser bandwidth, along with the laser spectrum. Resonances within the laser bandwidth are indicated.

Time-Resolved Absorption Spectra

The delay-dependent absorption spectrum in the vicinity of the 1s2p state is therefore radically different from that of the 1s3p and higher-lying states. This is demonstrated in Figure 5.11, which shows the absorption spectrum in the immediate vicinity of the 1s2p state. Acquisition of the spectra including the 1s2p absorption line required the use of the flat-field grazing incidence reflective grating spectrometer. The experiments were also performed using the FAST laser, which produced 5 *fs* pulses with more than 1 mJ pulse energy on a daily basis. Due to the short pulse duration and relatively high energy, isolated attosecond pulses could be generated using either the DOG in argon gas or the ionization gating in xenon gas. In both cases, the XUV continuum covered the spectral range between the aluminum filter transmission edge at ~15 eV to more than 30 eV. Experiments were performed in both conditions to confirm the reliability of the data, with no significant differences. However, due to the high conversion efficiency of HHG in xenon, the data taken with the ionization gating could be obtained by integrating over only 5,000 laser shots, compared with 30,000 laser shots for the double optical gating in argon gas.

While several features are apparent in the dynamics of the 1s2p absorption line near zero delay, here we focus on the splitting of the 1s2p line near $-10\ fs < \tau_D < 0\ fs$, indicated in Figure 5.11. The other features will be discussed in more detail in Chapter Six. Qualitatively, this splitting resembles the Autler-Townes splitting discussed in Chapter Two, in which the absorption line is split symmetrically into two absorption lines separated by the Rabi frequency Ω_R (defined in Figure 2.3) due to the resonant coupling between two states.

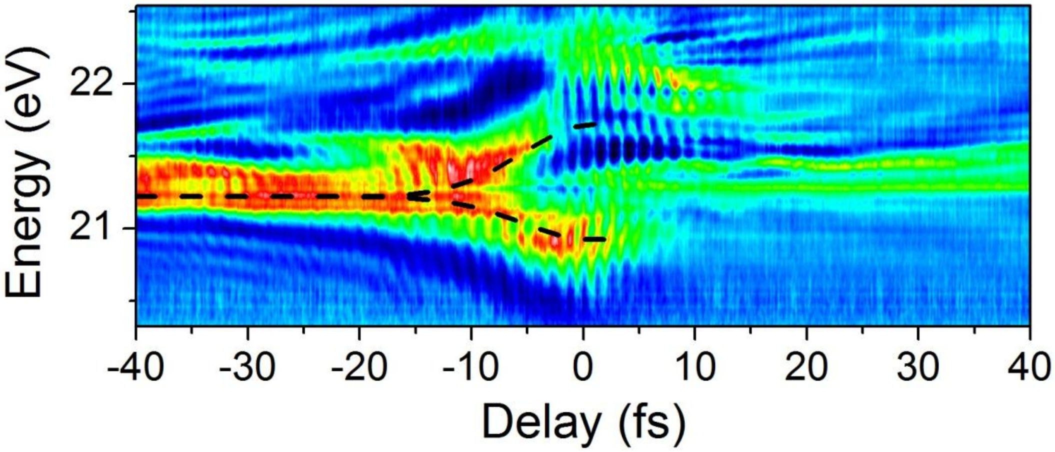

Figure 5.11: Delay-dependent absorbance spectrum of helium in the vicinity of the 1s2p state showing evidence of the Autler-Townes splitting (adapted from [149]).

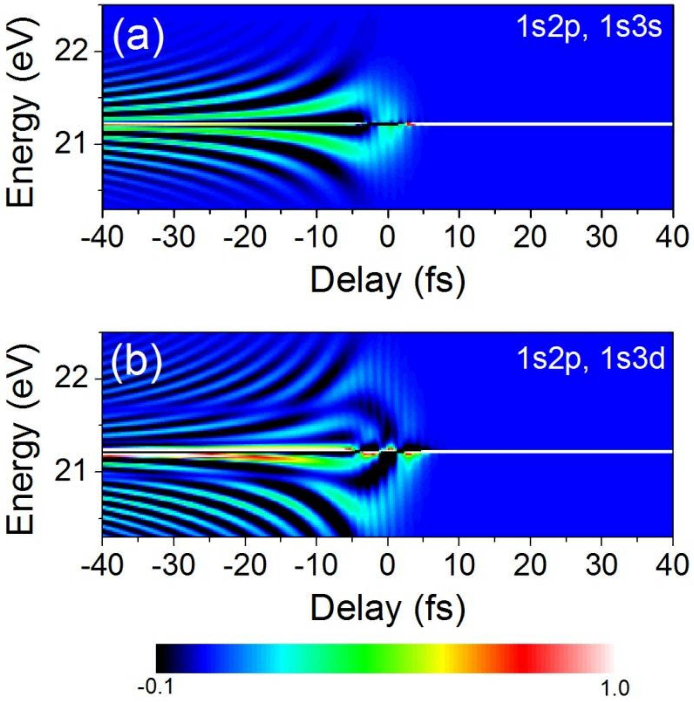

Figure 5.12: Calculated absorbance of the 1s2p state when coupled to the (a) 1s3s and (b) 1s3d states demonstrating the Autler-Townes splitting (adapted from [149]).

To determine the source of the splitting of the 1s2p line in Figure 5.11, we write the time-dependent wavefunction as:

$$|\Psi(\boldsymbol{r},t)\rangle = c_{1s^2}(t)e^{-iE_{1s^2}t}|1s^2\rangle + c_{1s2p}(t)e^{-iE_{1s2p}t}|1s2p\rangle + c_{1s3l}(t)e^{-iE_{1s3l}t}|1s3l\rangle, \tag{5.4}$$

where $l = s, d$. The energies of the excited states are listed in Table 5.1 for excited states $|1snl\rangle$. The coupled differential equations for the amplitudes c_{1snl} are then calculated numerically using the fourth order Runge-Kutta method with a variable step size. The simulated transient absorption spectrogram for the three level system described by Equation 5.4 are shown in Figures 5.12(a) and (b) for $l = s$ and $l = d$, respectively. The splitting is apparent in both states, but is more symmetric for $l = s$ as expected since the detuning $\delta = 0$ for the laser central frequency ω_L = 1.7 eV. Higher-order splittings are also observed for 1s3d, which can be understood by including higher orders in the derivation of Equation 2.27 using the Floquet theory.

Contribution of Resonant Coupling of 1s2p and 1s3*l* States

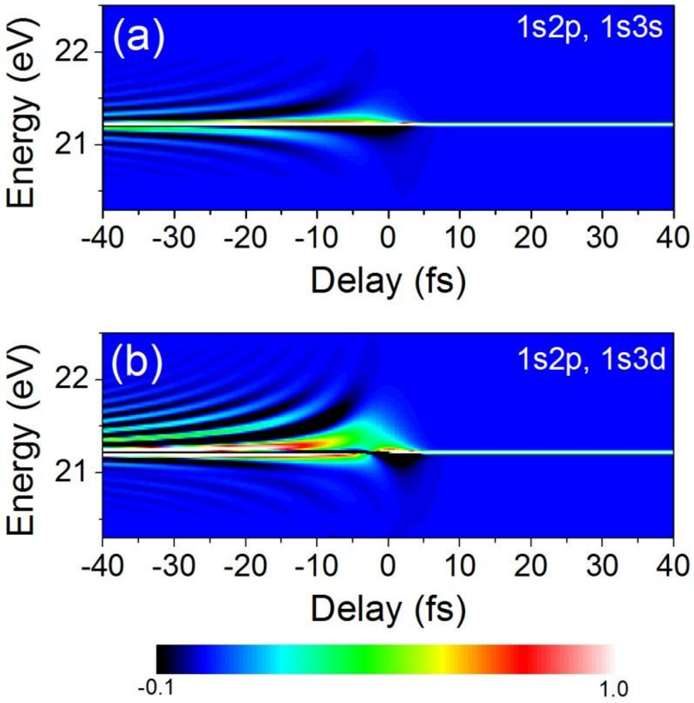

Figure 5.13: Calculated absorbance of the 1s2p state when coupled to the (a) 1s3s and (b) 1s3d states with a laser central frequency of ω_L = 3.2 eV. The Autler-Townes splitting disappears when the resonance condition is not met (adapted from [149]).

The effects of the resonant coupling of the 1s2p and 1s3s (or 1s3d) states can be seen by changing the laser central frequency in the simulation, so that the resonance condition is no longer met. Figure 5.13(a) and (b) show the simulated transient absorption for the three-level systems consisting of the $1s^2$, 1s2p, and 1s3s or 1s3d states for a dressing laser with the same intensity and pulse duration as in Figure 5.12(a) and (b), but with a laser central frequency of ω_L = 3.2 eV (similar to the second harmonic of the laser used in the experiments). In this case, the strong splitting of the 1s2p line consistent with the Autler-Townes splitting disappears, replaced by an energy level shift and broadening of the excited state consistent with the sub-cycle AC Stark shift. The sub-cycle energy level shifts are present in Figure 5.13, but are difficult to see due to the fast oscillation period of the laser and the large range of delays shown.

Notes

Portions of this chapter were used or adapted with permission from the following:

> Michael Chini, Baozhen Zhao, He Wang, Yan Cheng, S. X. Hu, and Zenghu Chang. Subycle ac Stark Shift of Helium Excited States Probed with Isolated Attosecond Pulses. *Physical Review Letters* **109**, 073601 (2012).
>
> Michael Chini, Xiaowei Wang, Yan Cheng, Yi Wu, Di Zhao, Dmitry A. Telnov, Shih-I Chu, and Zenghu Chang. Sub-cycle Oscillating Dark States Brought to Light. *Submitted* (2012).

CHAPTER SIX: SUB-CYCLE CONTROL OF BOUND-CONTINUUM WAVEPACKETS

Many of the observed dynamics in the transient absorption experiments in helium can be described by considering the coupling of a single 1s*n*p state with one or more 1s*n*s and/or 1s*n*d states as described in Chapter Five, yielding good qualitative agreement with the experimental measurements as well as intuitive physical models which can be used to explain the origins of the absorption features. In actuality, however, the attosecond pulse populates a dynamically-evolving *wavepacket* of 1s*n*p states, which can then be coupled to the entire manifold of 1s*nl* excited states and continuum of 1sεl free states with electron momentum $v = \sqrt{2\varepsilon}$. The transient absorption therefore reveals the dynamic motion of this wavepacket, which manifests itself not only through the changes of the absorption line energies and linewidths, but also through the formation of new absorption features which depend intimately on the laser parameters and pump-probe delay as well as the energy level spacing of the atomic system.

Two- and Three-Photon Absorption to Helium Dark States

The laser interaction with the 1s*n*p wavepacket produced by absorption of the isolated attosecond pulse primarily causes population transfer to 1s*n*s and 1s*n*d states through the dipole coupling described in Chapter Two and Chapter Five. These states are known as “dark states” of the atom, that is, states which cannot be observed through absorption or emission of a photon, since the dipole interaction with the initial (ground) state of the atom is forbidden by selection rules [8]. In the case of the helium atom, the ground state 1s^2 has orbital angular momentum $l = 0$

and can therefore only be coupled by absorption of a photon to states with $l = 1$. Only the 1s*n*p states satisfy this condition in the energy range of interest. Additional couplings can be made to doubly-excited autoionizing states [29,111], but these lie far from the 1s*n*p absorption line manifold and will not be discussed.

However, when excited in the presence of the NIR laser, two-color multi-photon couplings to the dark states become possible, and can leave their mark on the transient absorption of the isolated attosecond pulse in a process similar to the electromagnetically-induced transparency (EIT) and absorption previously observed in experiments using femtosecond XUV [111] and x-ray [150] light in combination with a moderately intense NIR laser. In Figure 6.1 we show the measured absorbance of the helium atom between 20.5 eV and 26 eV as a function of the intensity of the overlapping ($\tau_D \approx 0$) 6 *fs* NIR laser. The broad continuum spectrum of the isolated attosecond pulse again allows us to observe the absorption lines corresponding to each 1s*n*p state as well as the absorption above the ionization potential simultaneously. As the intensity of the dressing laser is increased, the absorption in the vicinity of the 1s*n*p excited state manifold changes significantly [134,136,137]. For the 1s3p and higher-lying states, these changes amount to energy shifts of the absorption lines, which increase linearly with the intensity and correspond to the AC Stark and ponderomotive shifts discussed in Chapter Five. However, the laser-dressed 1s2p absorption line exhibits more complicated structure which cannot solely be described by the AC Stark shift and Autler-Townes splitting of the absorption line. In addition to the features already discussed, we also observe the formation of new absorption structures between 21.5 and 22.5 eV, which become prominent at intensities above approximately 2×10^{12} W/cm^2. These complex features have previously been attributed to couplings between the 1s2p state and dark 1s*n*s and 1s*n*d states [136,137], but the individual substructures could not be identified.

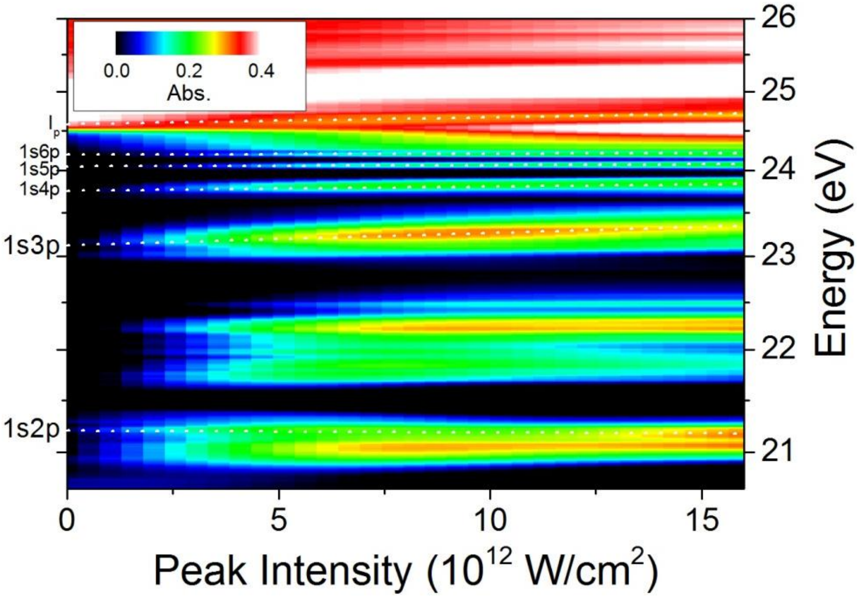

Figure 6.1: Laser-dressed absorbance of helium as a function of the intensity of an overlapping ($\tau_D \approx 0$) NIR laser (adapted from [149]).

By scanning the time delay between the attosecond XUV and few-cycle NIR pulses, we can trace the dynamics of the individual sub-structures and elucidate their origins. Figure 6.2 shows the absorbance spectrum measured as a function of the time delay for relatively low dressing laser intensities of 7×10^{11} W/cm^2 in Figure 6.2(a) and 5×10^{12} W/cm^2 in Figure 6.2(b). The experiments were performed using the FAST laser and the flat-field grazing incidence reflection grating, and negative delays indicate that the attosecond pulse arrives on target before the NIR pulse. While the new absorption sub-structures are most prominent near zero delay where the two pulses overlap, they can still be observed for fairly large (τ_D < -10 *fs*) delays). Furthermore, the absorption line energies and amplitudes change dynamically near zero delay, whereas they are relatively constant for larger negative delays. These dynamic features allow us to identify the origins of each sub-structure.

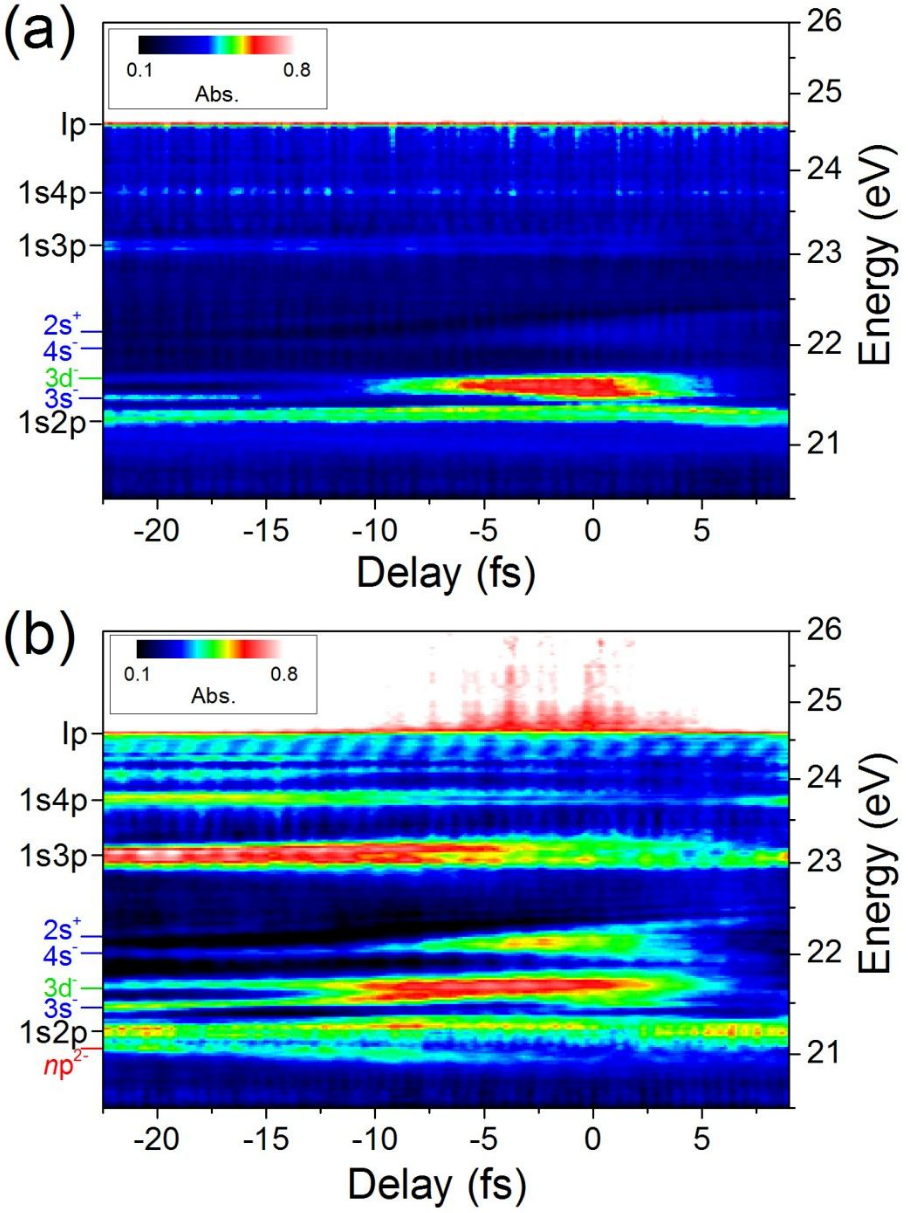

Figure 6.2: Delay-dependent absorbance spectrum for dressing laser intensities of (a) 7×10^{11} W/cm^2 and (b) 5×10^{12} W/cm^2 showing the absorption features corresponding to dark state sidebands (adapted from [149]).

Classification of Dressed Dark State Sidebands

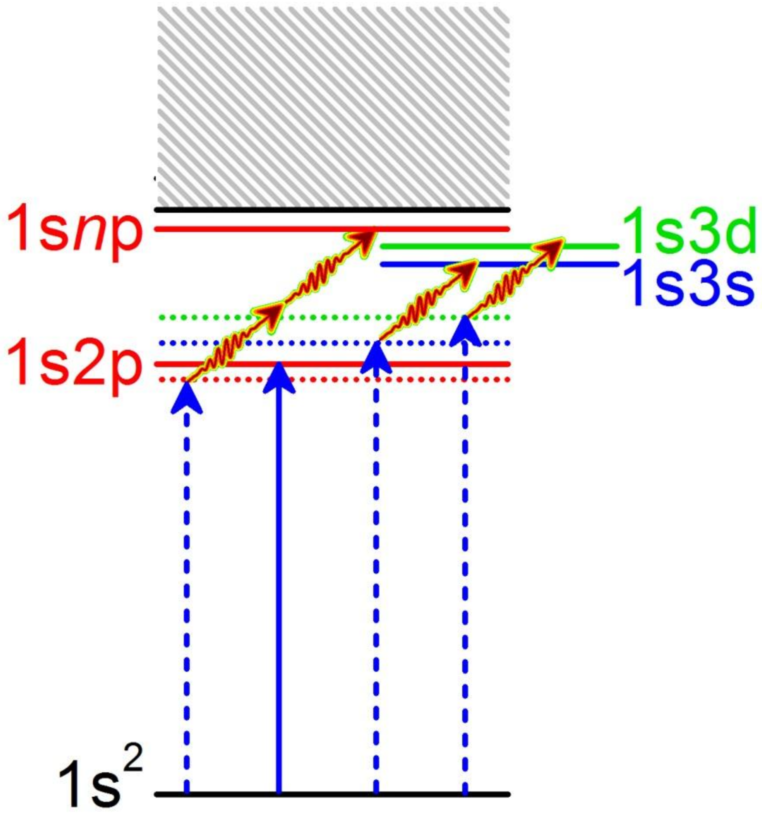

Figure 6.3: Schematic illustration of dark state sidebands formed by two-color two-photon transitions to 1s3s and 1s3d states and by three-photon transitions to 1s*n*p states (adapted from [149]).

The observed absorption sub-structures can each be assigned to an excitation pathway to a 1s*nl* excited state by the simultaneous absorption of an XUV photon and one or more NIR photons, as shown schematically in Figure 6.3. In other words, the sub-structures can be thought of as Floquet-like *sidebands* of the dark states. The dark state sidebands are labeled in Figures 6.2(a) and (b), designated by the field-free dark state designation with a “+” or ‘-’ to indicate a sideband formed by absorption or emission of a NIR photon, respectively. For example, the designation “nl^+” indicates that the absorption features results from the +1st order Floquet sideband of the 1snl dark state with an energy of $E_{1snl} + \omega_L$. The two predominant absorption structures which appear near zero delay each result from two overlapping dark state sidebands. Near 21.6 eV, the absorption feature results from the $3s^-$ and $3d^-$ sidebands, while the feature near 22.3 eV results from the $2s^+$ and $4s^-$ sidebands.

The assignment of these dark state sidebands was confirmed by numerical solution of the time-dependent Schrödinger equation in the two-color field, as shown in Figure 6.4(a) and by numerical solution of the coupled differential equations for the amplitudes $c_k(t)$ as discussed in Chapter Four (Equations 4.10) and shown in Figure 6.4(b). The solution of the time-dependent Schrödinger equation is based on the non-perturbative treatment of the NIR field by means of the non-Hermitian Floquet theory [151] and first-order perturbation theory with respect to the attosecond pulse (these calculations are courtesy of Di Zhao and Dr. Dmitry A. Telnov in the group of Prof. Shih-I Chu at the University of Kansas). In both calculations, the absorption can be found for both high-dimensionality systems containing many excited states and for reduced-dimensionality systems in which key resonances are removed. By comparing the calculated absorption with and without selected 1s*n*s and 1s*n*d states, we can confirm the importance of these dark states on the absorption spectrum and therefore on the excited state wavepacket dynamics. Both calculations used a dressing laser with intensity of 7×10^{11} W/cm^2 and central energy of ω_L = 1.7 eV. However, the Floquet theory assumes an infinitely long dressing laser pulse, whereas the solution to Equations 4.10 used a dressing laser pulse with 6 *fs* duration and a time delay τ_D = 0. For this reason, the sidebands of the 1s3s and 1s3d states, which are narrow in the Floquet calculation of Figure 6.4(a), cannot be separated in Figure 6.4(b) or in the experimental spectra near zero delay. The energy shift and broadening of the main 1s2p absorption peak in both figures is due to the nonresonant AC Stark shift and additional couplings to higher-lying states.

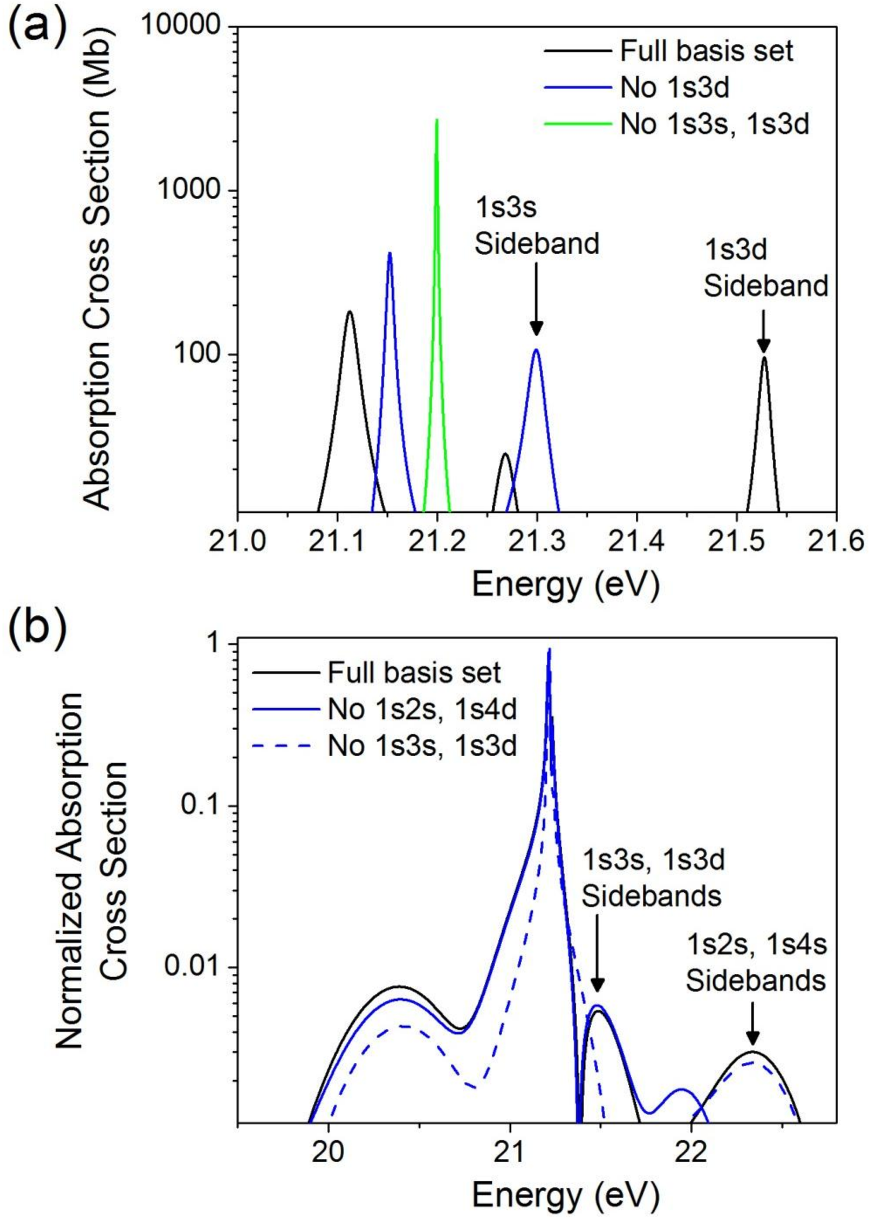

Figure 6.4: Calculated absorption cross sections using (a) non-Hermitian Floquet theory (courtesy D. Zhao, D. A. Telnov, and S. I. Chu) and (b) numerical solution of Equations 4.10 (adapted from [149]).

Sub-Cycle Oscillations in Dark State Absorption

Unlike the single-XUV photon absorption rate for excitation to the 1s*n*p states in the absence of the laser field, which is proportional to the cycle-averaged intensity, the probability of two-color multi-photon absorption depends on the timing of the XUV pulse with respect to the maximum and minimum of the instantaneous laser field. Therefore, we expect to see a strong half-cycle periodicity in the absorption lines corresponding to two-photon (XUV+NIR) excitation to 1s*n*s and 1s*n*d states as well as a quarter-cycle periodicity in the absorption lines corresponding to three-photon (XUV+NIR+NIR) excitation to 1s*n*p states. These periodicities are apparent by observing the absorbance within a narrow energy band near each dark state sideband, as shown in Figure 6.5.

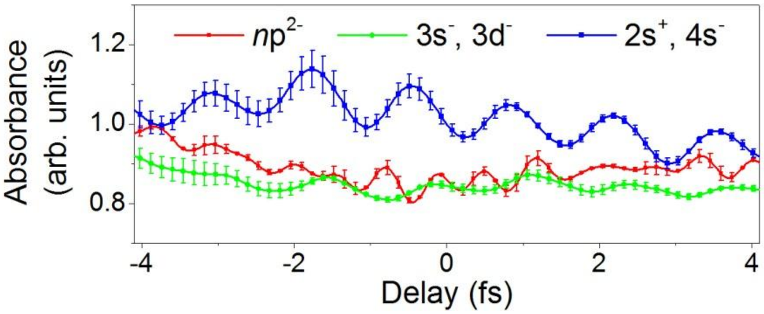

Figure 6.5: Delay-dependent absorbance within a narrow energy band near each dark state sideband (adapted from [149]).

The relative strengths of the half-cycle and quarter-cycle periodicities can be evaluated by taking the Fourier transform along the delay axis for every photon energy and comparing the strengths of the different oscillatory components. The normalized oscillation amplitudes of the half-cycle and quarter-cycle oscillations for the data in Figure 6.2(b) are plotted in Figures 6.6(a) and (b), respectively, with the two- and three-photon excitation pathways responsible for the oscillations labeled. The quarter-cycle oscillations, which are clearly apparent for three-photon excitation to the 1s*n*p ($n \geq 6$) excited states at an XUV photon energy near 21 eV, are the fastest dynamic feature observed to date in pump-probe spectroscopy.

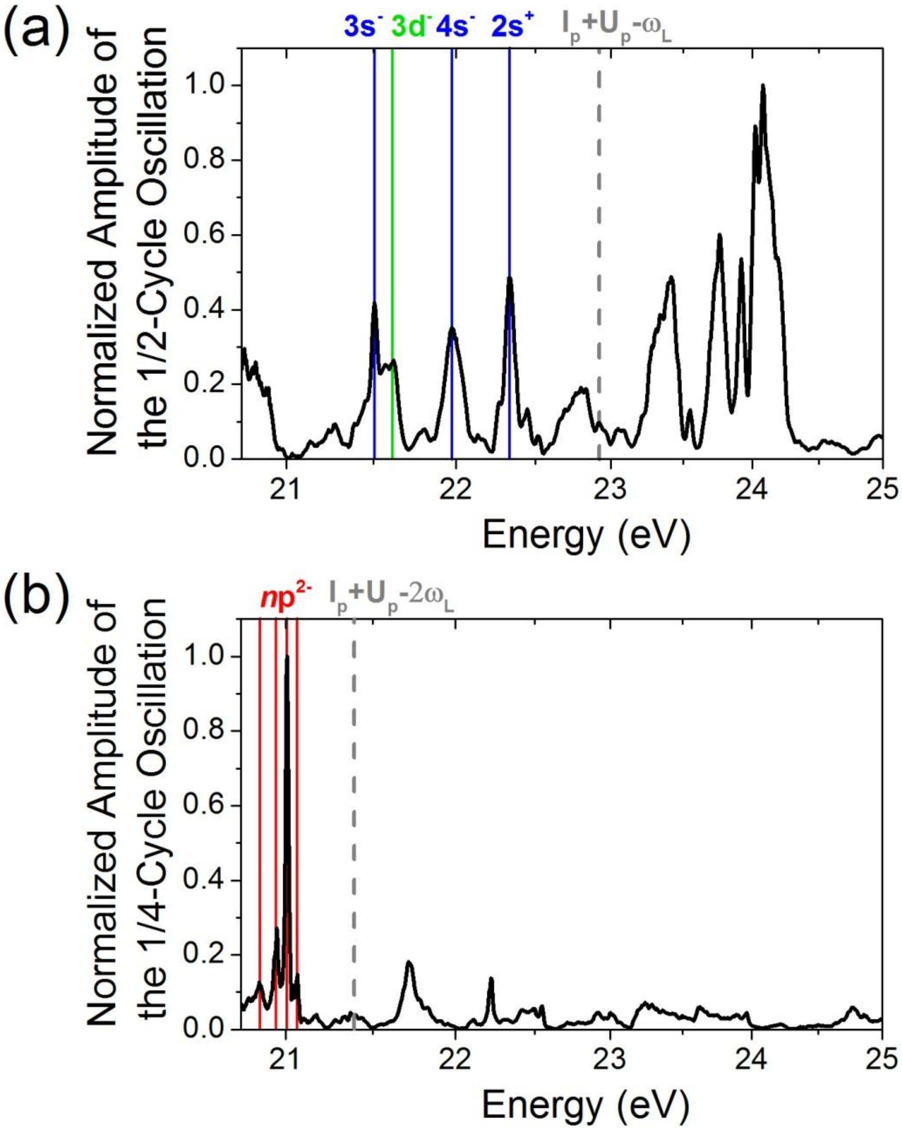

Figure 6.6: Normalized amplitudes of the (a) half-cycle and (b) quarter-cycle oscillations for the data in Figure 6.2(b) (adapted from [149]).

Optical Measurement of Two-Path Quantum Interferences

At higher intensities, the excited state dynamics become more complicated owing to the interactions of bound and continuum states with the strong laser field. Figures 6.7(a) and (b) show two time delay-dependent absorbance spectrograms with a dressing laser intensity of 1×10^{13} W/cm^2. The two data sets were obtained with different grazing incidence angles of the grating in the spectrometer in order to observe a larger spectral range while preserving the high energy resolution, and were taken consecutively under identical conditions. At this intensity, the 1s*n*p excited states lie above the laser-suppressed Coulomb barrier and the excited state lifetime is therefore very short. However, absorption features corresponding to 1s*n*p bound states and dark state sidebands are still observable even near zero delay, similar to those observed in Figure 6.2(b). Furthermore, the fast laser-induced wavepacket dynamics lead to dynamic absorption structures which extend far from the 1s*n*p resonances, covering the energy range between 18 and 28 eV. In addition to the persisting discrete absorption lines, we observe dynamic features at negative delays both above the ionization threshold (I_p = 24.58 eV) near 25 eV and 27 eV and below the 1s*nl* excited state manifolds near 19 eV. These features oscillate with the delay, with the oscillations following hyperbolic lines, and are consistent with the observation of two-path quantum interferences in photoelectron spectroscopy [30]. However, while the modulations above the ionization threshold could in principle be explained by “direct-indirect” interference of electrons ionized by the XUV alone (direct) and by the combined XUV and NIR (indirect), the modulations near 19 eV cannot be explained in this way and should instead be described as *optical* interferences.

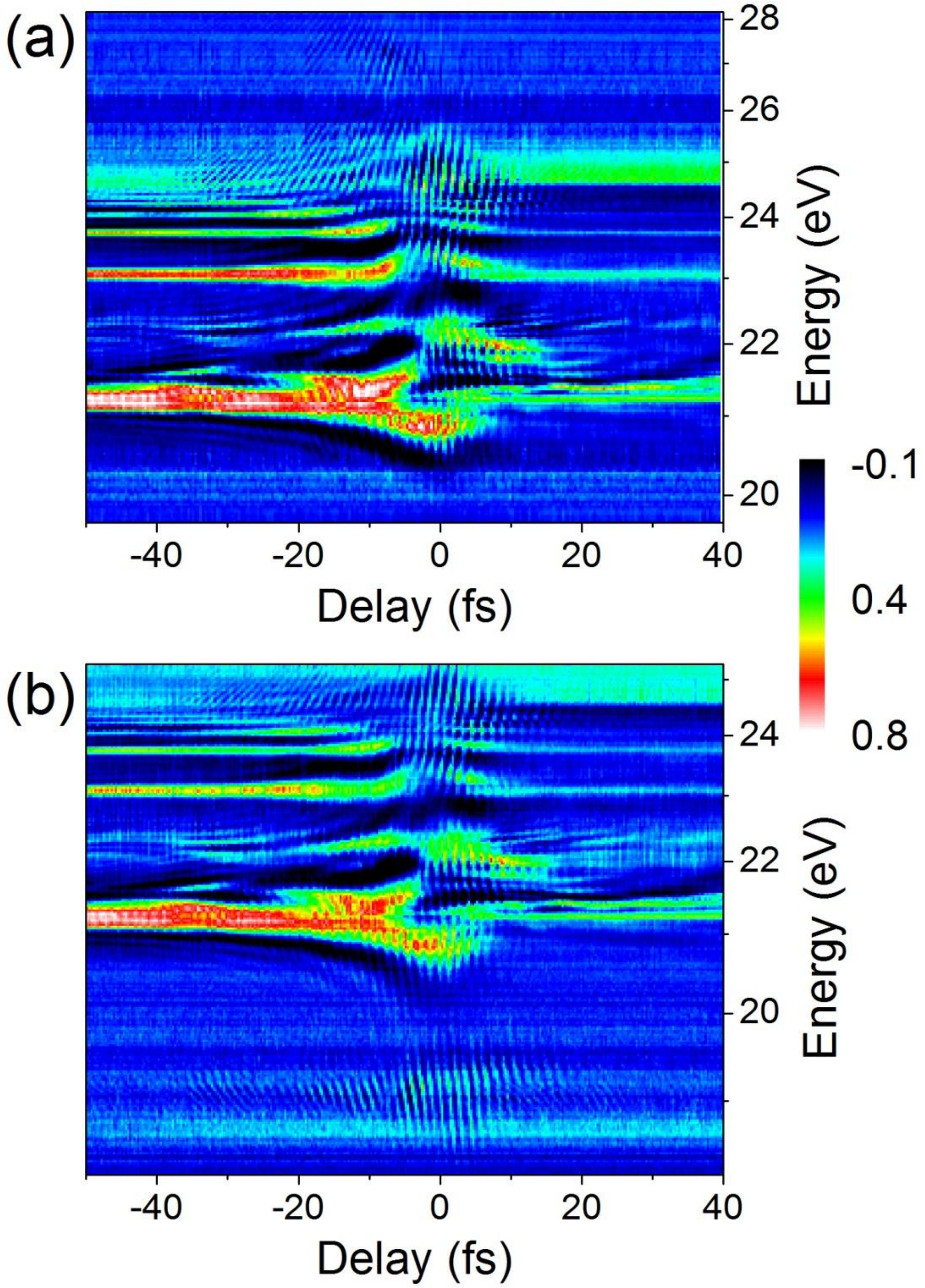

Figure 6.7: Delay-dependent absorbance spectra taken consecutively with different angles of the flat-field grazing incidence reflection grating. Interferences are observable above the ionization threshold near 25 eV and 27 eV in (a) and below the 1s2p state near 19 eV in (b) (adapted from [149]).

Above- and Below-Threshold Interferences

The observed optical interferences, analogous to the two-path quantum interference of electrons, are due to polarizations with the same frequency arising from two distinct quantum pathways. As is apparent from Equation 4.4, the output spectrum far from any atomic resonances is equal to the input spectrum in the absence of the dressing laser, which results from a frequency-dependent polarization with no imaginary component, $\Im[\tilde{P}(\omega)] = 0$. This implies that the phase of the polarization is $\tan^{-1}\{\Im[\tilde{P}(\omega)]/\Re[\tilde{P}(\omega)]\} = 0$. However, the dressing laser can also excite a polarization with frequencies far from the resonance frequencies. For example, the polarization of the 1s2p (or other 1s*n*p states) state includes contributions from Floquet sidebands separated by $2\omega_L$ as discussed in Chapter Two (here, of course, the laser pulse is short and the Floquet sidebands will be rather broad [148,151]). Therefore, the polarization response at frequencies of $E_{1s2p} \pm 2\omega_L$ will include contributions from both the nonresonant interaction and from the first-order Floquet sidebands. Since the population of the sidebands (and therefore the instigation of the frequency-shifted polarization) is initiated by the arrival of the NIR dressing laser pulse, a phase difference of $(\omega - E_{1s2p})\tau_D$ arises between the two components of the frequency-dependent polarization $\tilde{P}(\omega)$. The interference fringes will therefore follow the lines of constant phase, becoming more closely spaced in energy as the delay increases. The absorption features also oscillate with the delay on sub-cycle timescales as will be discussed below.

The optical interferences in the Floquet sidebands near $E_{1s2p} + 2\omega_L = 24.5$ eV, $E_{1s3p} + 2\omega_L = 26.5$ eV and $E_{1s2p} - 2\omega_L = 19$ eV can be reproduced quite well by numerical simulation following the theoretical treatment in Chapter Four. The calculated transient absorption spectrogram is shown in Figure 6.8. With the inclusion of all helium states listed in Table 5.2 as well as the multi-photon ionization, most features of the experimental data, including the above- and below-threshold interferences, can be reproduced quite well.

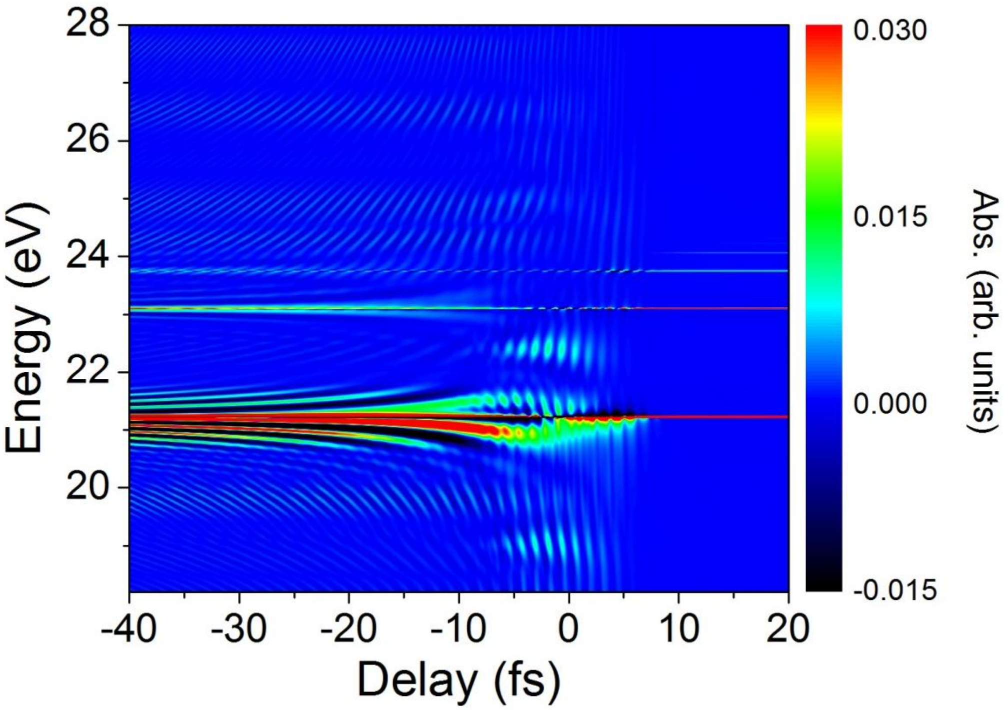

Figure 6.8: Delay-dependent absorbance calculated by numerical solution of Equations 4.10 demonstrating above- and below-threshold two-path optical interferences (adapted from [149]).

Classification of Indirect Absorption Pathways

The two-path interference model implies that the absorption pathways can be classified from the sub-cycle oscillations using the two-dimensional Fourier transform (2DFT) spectroscopy [30,152]. This is done by taking the Fourier transform of the delay-dependent absorption at every photon energy, as plotted for the negative delay (-50 *fs* < τ_D < -17 *fs*) region of Figure 6.7 in Figure 6.9(a) and for the simulated data of Figure 6.8 in the same delay range in Figure 6.9(b). Since the interference maxima (and minima) follow lines of constant phase, the photon energy-dependent oscillation frequency peaks follow 45° lines $\omega_{FT} = E_k - \omega$ in the 2DFT spectrogram, where ω_{FT} is the peak frequency at a given photon energy ω. These lines converge to the field-free energy levels E_k for Fourier transform frequencies $\omega_{FT} = 0$. In both the experimental and simulated data in Figure 6.9, we can observe 45° lines converging from the features at 19 eV and 24.5 eV to the field-free 1s2p absorption line energy, as well as weaker features converging to the 1s3p and 1s4p absorption lines. The 2DFT spectrograms therefore confirm the interference origin of these absorption structures.

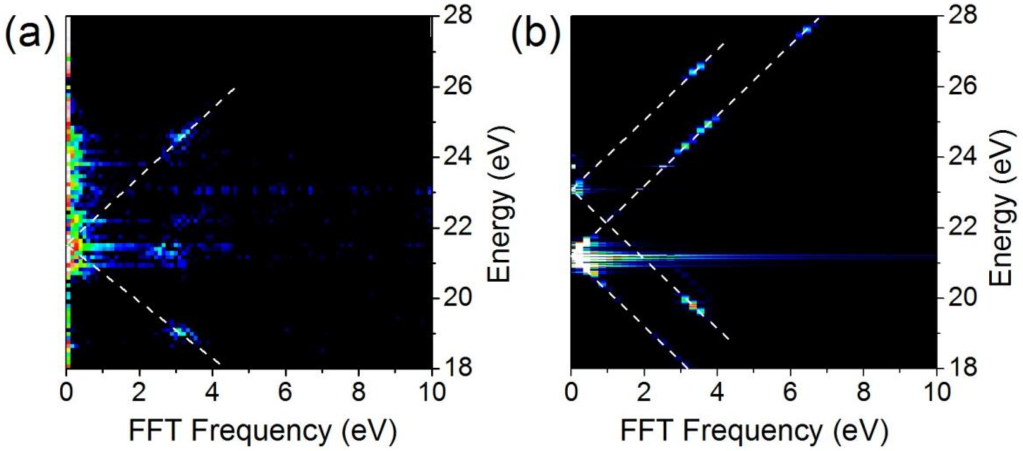

Figure 6.9: 2DFT spectrograms of (a) the experimental data in Figure 6.7 and (b) the simulated data in Figure 6.8 showing the two-path interferences (adapted from [149]).

Dark State Absorption and Quantum Interference in Neon

Having explored the wavepacket dynamics of the helium atom through attosecond transient absorption spectroscopy, we can now investigate the effectiveness of the transient absorption spectroscopy in somewhat more complicated systems and also evaluate the effectiveness of the theoretical models used to explain the helium results. Here, we present the transient absorption measurement in bound states of the neon atom.

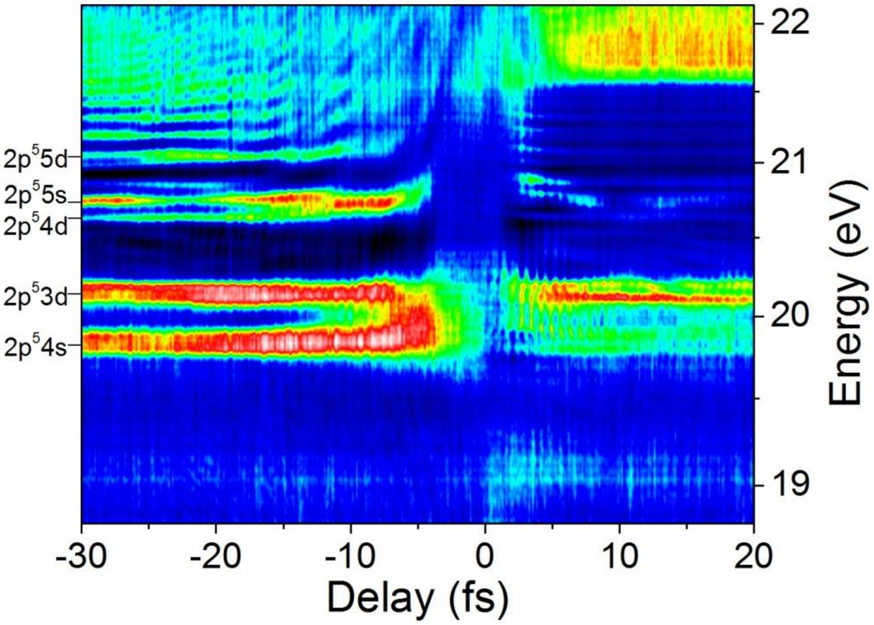

Figure 6.10: Delay-dependent absorbance of neon with relevant energy levels.

Unlike the $1s^2$ state in helium, the ground state of neon ($1s^2 2s^2 2p^6$) has orbital angular momentum of $l = 1$. Therefore, the attosecond pulse alone can excite a wavepacket consisting of both $l = 0$ ($1s^2 2s^2 2p^5 ns$, $n \geq 2$) and $l = 2$ ($1s^2 2s^2 2p^5 nd$) states, which can then be coupled to each other and to other $1s^2 2s^2 2p^5 nl$ states through absorption of one or more NIR photons. The measured absorbance spectrogram of the laser-dressed neon atom is shown in Figure 6.10. Although the large number of observed states (in addition to the couplings to dark states) precludes numerical simulation based on solution to the coupling equations in Equations 4.10, sub-cycle AC Stark shifts, absorption line splitting, dark state sidebands, and two-path interferences can be observed amidst the more complicated dynamic absorption structures of neon.

Notes

Portions of this chapter were used or adapted with permission from the following:

> Michael Chini, Xiaowei Wang, Yan Cheng, Yi Wu, Di Zhao, Dmitry A. Telnov, Shih-I Chu, and Zenghu Chang. Sub-cycle Oscillating Dark States Brought to Light. *Submitted* (2012).

CHAPTER SEVEN: ATTOSECOND TIME-RESOLVED AUTOIONIZATION

Beyond the goals of understanding the physics of hydrogen-like atoms in a strong laser field, one of the primary motivations of attosecond science is to understand the fast dynamics due to electron correlation. These dynamics arise in all multi-electron systems due to the electron-electron interaction, and can typically be observed in core-excited or doubly-excited states of the atom. These states are often “quasi-bound” states, known for their short lifetimes mediated by autoionization. For decades, spectral-domain measurements with synchrotron radiation have served as a window into the rich dynamics of autoionization [130]. However, the synchrotron pulse duration (100 *fs* to 100 *ps*) is too long to time-resolve the quasi-bound state dynamics, since the autoionization process can be as short as a few femtoseconds. In this chapter, we discuss experiments performed in short-lived quasi-bound states of argon, and demonstrate the applicability of attosecond science to the time-domain measurement of autoionization dynamics on the few- and even sub-femtosecond timescale.

Fano Theory of Autoionization

For multi-electron atoms, electron-electron interactions make it extremely difficult to solve the Schrödinger equation exactly. Instead, electrons are treated according to the independent particle approximation and assigned to a particular *configuration* (for example, as in the assignment of electron orbitals 1s, 2p, etc.). The actual stationary states can then be described by the superposition of states from different configurations, with the combination of these states mediated by the configuration interaction – terms in the Hamiltonian which are neglected in the independent particle approximation.

In the case of bound states (for example, the 1s*n*p states of helium described in previous chapters made up of the 1s and *n*p configurations), the energies of the various configurations differ greatly, and the configuration interaction becomes small. In this case, the wavefunctions can be obtained using perturbation theory or variational methods. On the other hand, when different configurations are coincident in energy, the perturbative approximations fail and the configuration interaction plays a large role. When a state arises from the mixing of two energy-coincident configurations (a bound state configuration mixing with a continuum configuration), the configuration interaction results in the autoionization process.

The problem of autoionization was solved by Fano in 1961 [153] by describing the configuration interaction between a discrete state $|\varphi\rangle$ with energy E_φ and a continuum of states $|\psi_{E'}\rangle$ with energies E'. While the states are nondegenerate, we note that E_φ lies within the range of energies E'. The Hamiltonian of the system is given by:

$$H = H_0 + V, \tag{7.1}$$

where H_0 represents the Hamiltonian in the independent particle approximation and V represents the configuration interaction. For this reduced system involving only the two configurations, the Hamiltonian can be easily expressed in matrix form, with components:

$$\langle\varphi|H|\varphi\rangle = E_\varphi, \tag{7.2}$$

$$\langle\psi_{E'}|H|\varphi\rangle = V_{E'}, \tag{7.3}$$

$$\langle\psi_{E''}|H|\psi_{E'}\rangle = E'\delta(E'' - E'). \tag{7.4}$$

Then, the new wavefunction $|\Psi_E\rangle$ can be written as a sum of the wavefunctions from different configurations,

$$|\Psi_E\rangle = a|\varphi\rangle + \int dE' b_{E'}|\psi_{E'}\rangle. \tag{7.5}$$

The coefficients a and $b_{E'}$ can be obtained by solving Equations 7.1-7.5 and normalizing the wavefunction, and are given by [153]:

$$a = \frac{1}{\pi V_E} \sin\Delta, \tag{7.6}$$

$$b_{E'} = \frac{V_{E'}}{\pi V_E}\frac{\sin\Delta}{E-E'} - \cos\Delta\,\delta(E-E'), \tag{7.7}$$

where Δ is the phase shift due to the configuration interaction and is expressed as:

$$\Delta = -\arctan\frac{\pi|V_E|^2}{E-E_\varphi-F(E)}. \tag{7.8}$$

Here, $F(E)$ represents a shift of the resonance position away from the discrete state energy E_φ in the independent particle approximation and is defined as:

$$F(E) = P\int dE' \frac{|V_{E'}|^2}{E-E'}. \tag{7.9}$$

Here P denotes the principle part of the integral.

When the autoionizing state $|\Psi_E\rangle$ is excited from the ground state $|0\rangle$, in our case by the isolated attosecond pulse through the dipole interaction, the amplitude of the transition matrix element is given by:

$$\langle\Psi_E|z|0\rangle = \frac{1}{\pi V_E^*}\langle\varphi|z|0\rangle\sin\Delta + \frac{1}{\pi V_E^*}P\int dE' \frac{V_{E'}^*\left\langle\psi_{E'}\middle|z\middle|0\right\rangle}{E-E'}\sin\Delta - \langle\psi_E|z|0\rangle\cos\Delta. \tag{7.10}$$

Since the transition matrix element between the ground state and unperturbed continuum states varies slowly with energy, the features of the autoionizing state can be intuitively understood by comparing the transition probability between the ground state and the autoionizing state to that between the ground state and continuum state. The ratio of transition probabilities is given by the so-called Fano resonance profile:

$$\frac{|\langle\Psi_E|z|0\rangle|^2}{|\langle\psi_E|z|0\rangle|^2} = \frac{(q+\varepsilon)^2}{1+\varepsilon^2}, \tag{7.11}$$

where $\varepsilon = \left(E - E_\varphi - F\right)/(\Gamma/2)$ is the reduced energy, giving the ratio between the energy detuning from resonance and the width of the autoionizing state resonance $\Gamma = 2\pi|V_E|^2$ which is related to the autoionization lifetime $\tau = 1/\Gamma$. The q parameter is determined by the ratio between transition amplitudes:

$$q = \frac{\langle\varphi|z|0\rangle + P\int dE' \frac{V_{E'}\langle\psi_{E'}|z|0\rangle}{E-E'}}{\pi V_E^*\langle\psi_{E'}|z|0\rangle}. \tag{7.12}$$

Whereas the resonance width Γ is determined by the lifetime of the autoionizing state, the q parameter determines the shape. This is shown in Figure 7.1, where the Fano profile is plotted for different values of the q parameter.

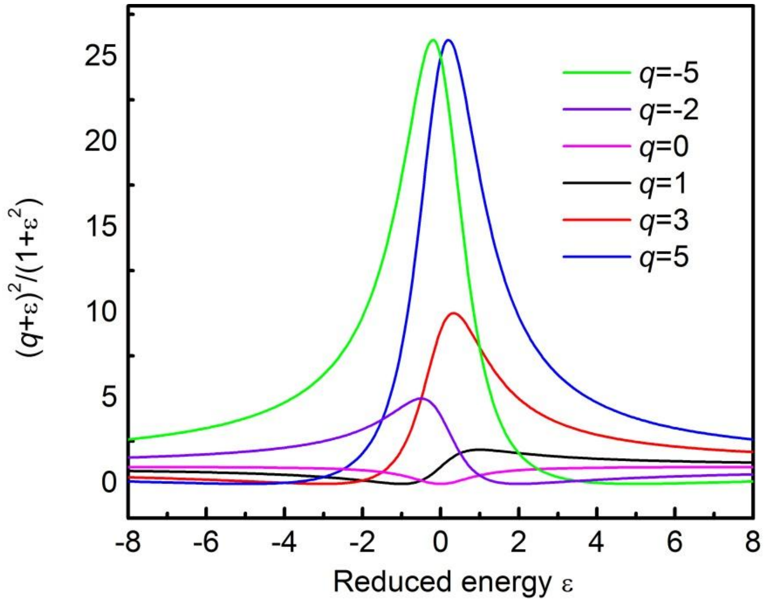

Figure 7.1: Fano profiles for different values of the *q* parameter.

Autoionizing States of Argon

In general, the absorption cross section in the vicinity of a manifold of n non-interacting autoionizing states can be determined from Equation 7.11, as:

$$\sigma = \sum_{k=1}^{n} \sigma_k \frac{(q_k+\varepsilon_k^2)}{1+\varepsilon_k^2} + \sigma_b, \tag{7.13}$$

where σ_k represent the cross sections of the continuum states which interact with the autoionizing states $|\phi_k\rangle$ and σ_b represents the cross section of continuum states that do not. Therefore, the absorption in the vicinity of a manifold of autoionizing states can easily be determined, even for relatively complex multi-electron atoms, provided that the resonance parameters are known. Here, we discuss the autoionizing resonances of argon lying between 26 and 30 eV. Although *ab initio* solutions to the time-dependent Schrödinger equation for many-electron atoms are still formidable, the Fano profiles between 26 and 30 eV are easily accessible using the attosecond pulses generated in argon and xenon gases and the same spectrometer gratings used in the helium experiments.

Energy Levels, Linewidths, and Shapes

The absorption cross section near the $3s3p^6np\ {}^1P$ manifold of core-excited autoionizing states in argon was originally measured and parameterized by Madden, and Codling in 1963 [130] and subsequently refined with high-resolution measurements [131,154]. The states of interest are illustrated schematically in Figure 7.2 and the resonance energies, widths, and q parameters [154], along with the lifetimes of the autoionizing states, are detailed in Table 7.1. Of particular interest is the short lifetime of the $3s3p^6 4p$ and $3s3p^6 5p$ states, which autoionize with lifetimes of only 8.2 *fs* and 23.5 *fs*, respectively. Isolated attosecond pulses are clearly needed to time-resolve the fast dynamics of autoionization in such states.

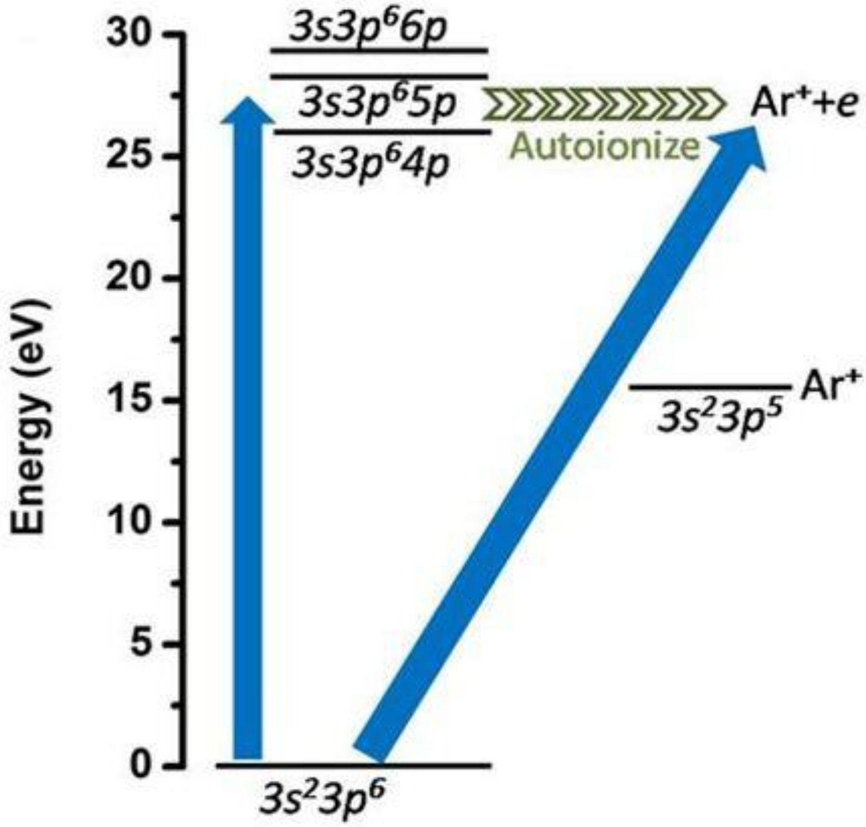

Figure 7.2: Argon autoionizing states of interest (adapted from [104]).

Table 7.1: Resonance energy, linewidth, lifetime, and q parameter of the first three autoionizing resonances in argon [154].

State	E_R (eV)	Γ (meV)	τ (*fs*)	q
3s3p^{6}4p	26.614	80	8.23	-0.22
3s3p^{6}5p	27.996	28.2	23.34	-0.21
3s3p^{6}6p	29.509	12.6	52.24	-0.17

Absorption Spectra of Argon Autoionizing States

The transmission of argon in the vicinity of the autoionizing state resonances is shown in Figures 4.12 and 4.15, and the comparison of the absorption cross section extracted from the measured transmission using the Beer-Lambert law with the known absorption cross-section is shown in Figure 4.16. Due to the specific parameters (in particular the Fano *q* parameter) of the $3s3p^6np$ Fano resonances, these particular states manifest themselves through absorption *minima* rather than maxima. Here, the isolated attosecond pulses were generated from argon gas using DOG with 7 *fs* pulses from the MARS laser system, and the spectrum was measured using the transmission grating spectrometer. Unlike the absorption lines corresponding to bound states in helium, the Fano resonances corresponding to the $3s3p^6np$ autoionizing states of argon could be measured in the absence of the dressing laser field due to the relatively large linewidths of the states, which can be comparable to or even larger than the energy resolution of the spectrometer.

Time-Resolved Autoionization by Attosecond Transient Absorption

The fast dynamics of the autoionizing states were measured using the attosecond transient absorption technique discussed in previous chapters. As before, the measured transient absorption spectrum is determined by the time-dependent polarization response of the laser-perturbed atom. However, whereas the helium polarization could be “cut off” only by ionization of the atom in the moderately intense laser pule, the autoionizing states have a natural timescale on which the polarization drops to zero, which is determined by the autoionization lifetime. Therefore, the transient absorption technique allows for direct measurement of the autoionization process in the time domain, as well as the laser-induced couplings and wavepacket dynamics of the short-lived autoionizing states. While the dynamics in the multi-electron atom are inherently more complicated than those discussed in Chapters Five and Six for the helium bound states, we can intuitively describe the observed dynamics by building on the previous studies and with the inclusion of the autoionization process.

Time-Resolved Absorption Spectra

The delay-dependent transmission spectrogram in the vicinity of the argon $3s3p^6np$ autoionizing state manifold is shown in Figure 7.3(a) for a dressing laser intensity of 5×10^{11} W/cm^2 and in Figure 7.4(a) for a dressing laser intensity of 1×10^{12} W/cm^2, both using the MARS laser system. As before, the negative delays indicate that the isolated attosecond pulse arrives on the target before the NIR pulse. The $3s3p^64p$, $3s3p^65p$, and $3s3p^66p$ states can be identified in the plot and are indicated by arrows. For negative delays, we find that the resonances are shifted to higher energies and broadened by the laser field, with the maximum shift and broadening occurring near zero delay. Most interestingly, we found that the $3s3p^64p$ absorption line exhibits a dramatic splitting at the higher laser intensity. The upper branch of the split absorption line extends nearly to the neighboring $3s3p^65p$ resonance, whereas the lower branch remains near the unperturbed energy. We further found that the effects of the laser were most apparent on the lower-lying autoionizing states.

The absorption line dynamics were found to be strongly asymmetric with respect to zero delay. This can be seen in Figures 7.3(b) and 7.4(b), for which the transmitted signal within a narrow band near the energy of the unperturbed $3s3p^64p$ and $3s3p^65p$ state energies (26.6 eV and

28.0 eV, respectively) is plotted as a function of the time delay. When the XUV and NIR overlap ($\tau_D \approx 0$), the transmission within the Fano resonance is minimized, and the recovery of the signal is substantially faster when the delay is positive. The asymmetric weakening of the signal with respect to delay can be fit very well using the convolution of an exponential decay with the autoionizing state lifetime and the Gaussian laser pulse.

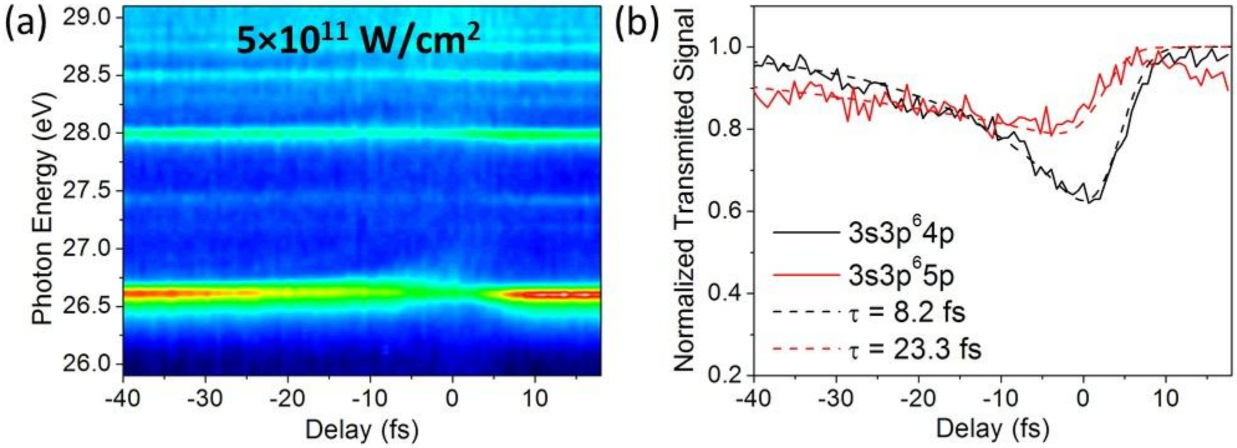

Figure 7.3: Delay-dependent transmission of argon with a dressing laser intensity of 5×10^{11} W/cm^{2} (adapted from [104]).

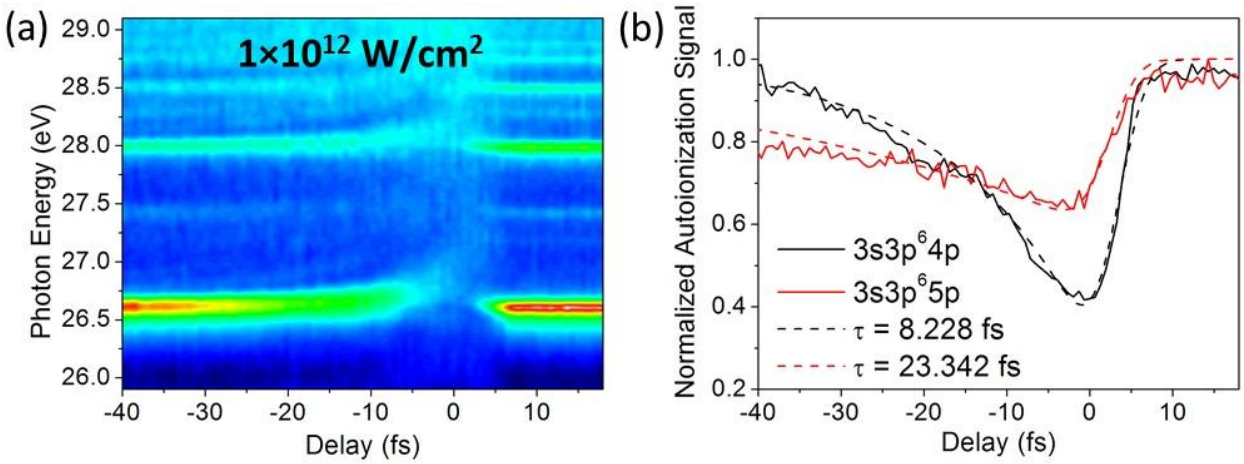

Figure 7.4: Delay-dependent transmission of argon with a dressing laser intensity of 1×10^{12} W/cm^{2} (adapted from [104]).

Qualitative Model of Laser-Perturbed Autoionization

The observed phenomena suggest a dynamic control over the autoionizing states by the NIR laser, which can be understood by considering both nonresonant coupling of the autoionizing states to continuum states through single- and multi-photon ionization and resonant coupling to other autoionizing states induced by the NIR laser [43,155]. In our experiment, the $3s3p^6np$ autoionizing states are first populated by the isolated attosecond pulse. If no NIR field is present, those states will decay exponentially to the Ar^+ ($3s^23p^5\varepsilon l$) continuum due to the configuration interaction. When those states are further dressed by an intense laser, additional couplings between the autoionizing states and Ar^{*+} ($3s3p^6\varepsilon l$) continuum states tend to speed up the decay process and therefore broaden the resonance as shown schematically in Figures 7.5(a) and (b). Similarly to the AC Stark shifts discussed in Chapters Two and Five, laser-induced couplings to bound and continuum states can also shift the central energies of the Fano resonances.

When resonant coupling to other autoionizing states is also possible, such strong coupling may take over as the dominant mechanism for controlling the autoionization process. Since the $3s3p^64p$ state (26.6 eV) is more deeply bound than the $3s3p^65p$ and $3s3p^66p$ states with respect to the Ar^{*+} ($3s3p^6\varepsilon l$) continuum, coupling only to the Ar^{*+} continuum indicates that the $3s3p^64p$ state should be least sensitive to the NIR laser. This suggests that the resonant coupling of two or more autoionizing states may play a role [155]. Specifically, the dark $3s3p^6nd$ autoionizing states of argon, which lie in the same energy range as the $3s3p^6np$ states, cannot be accessed from the ground state by absorption of an XUV photon. Instead, these states can be accessed by two-photon (XUV+NIR) absorption. In particular, the $3s3p^64d$ (28.3 eV) state lies 1.7 eV above the

3s3p^{6}4p state [154], which is within the spectral range of the few-cycle NIR laser pulse and is approximately equal to the laser central energy. When the two states are strongly coupled by the NIR laser, as is shown schematically in Figures 7.6(a) and (c), Rabi oscillations between the two states can cause the formation of an Autler-Townes-like doublet in the Fano resonance profile [111]. However, the 3s3p^{6}4p and 3s3p^{6}4d states will autoionize by themselves without the participation of the NIR laser. These dynamics, along with the slight detuning of the laser central frequency from resonance, complicate the interference and lead to the asymmetric splitting [155].

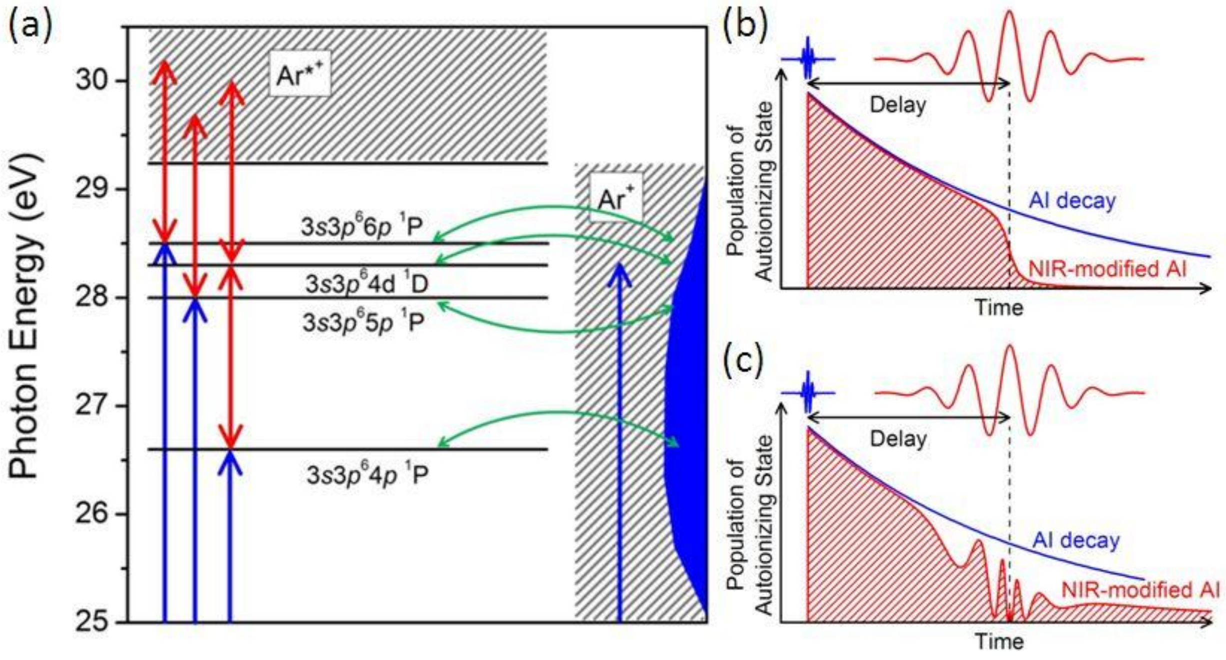

Figure 7.5: Schematic of laser control over autoionization. (a) Couplings induced by configuration interaction (green arrows) and by the laser (red arrows). Nonresonant coupling of the 3sp3p^6*n*p states to the Ar*$^+$ continuum truncates the autoionization, as shown in panel (b), leading to AC Stark shifts and absorption line broadening. Resonant coupling of the 3s3p^{6}4p and 3s3p^{6}4d states ($\Delta\omega$ = 1.7 eV) drives Rabi oscillations in the population of the autoionizing state, as shown in panel (c), leading to splitting of the absorption line (adapted from [104]).

Theoretical Simulation of Time-Resolved Autoionization

Simulations of the laser-induced coupling of the 3s3p^6np and 3s3p^6nd autoionizing states were performed following the treatment in Chapter Four, with the added inclusion of the autoionizing state lifetimes and Fano lineshapes [155]. In this case, the coupled equations of Equation 4.10 are modified by including the autoionization-induced population changes, and the problem to be solved becomes:

$$i\frac{\partial}{\partial t}\sum_j c_j(t)|j\rangle = \sum_j \left(E_j - i\,\Gamma/2\right)c_j|j\rangle - \sum_j \sum_{k\neq j}\left[d_{kj}F_L(t) + d_{kj}F_X(t-\tau_D)\right]c_k(t)|k\rangle. \quad (7.14)$$

Here all involved states have a finite autoionization lifetime, and the continuum states are not treated explicitly. The time-dependent polarization can then be found from Equation 4.5 as:

$$P(t) = \sum_j \sum_{k\neq j} c_k^*(t)c_j(t)e^{-i(E_j-E_k)t}\langle k|z|j\rangle \left(1+\frac{i}{q_k}\right)\left(1-\frac{i}{q_j}\right), \quad (7.15)$$

where the continuum states are included in the wavefunctions through the final two terms using the q parameter for each state. Note that $q \to \infty$ for pure bound states.

In the simulations, only the 3s3p^{6}4p, 3s3p^{6}5p, and 3s3p^{6}4d states were considered, due to a lack of dipole transition matrix elements between the autoionizing states. The pulse durations, central frequencies, and peak intensities of the XUV and NIR laser pulses were chosen to be the same as in the experiment, and the energies, widths, and q parameters were taken from the literature (q_a = -0.2, q_b = 2.43) [154]. The dipole matrix elements d_{a0} and d_{ba} were calculated by Dr. Chang-Hua Zhang and Dr. Feng He in the group of Prof. Uwe Thumm at Kansas State University to be 0.027 and 1.54 a.u., respectively, using single particle wave functions calculated with an effective Coulomb potential [156]. The simulated delay-dependent transmission spectra is shown in Figures 7.6 for the NIR laser intensities of 1×10^{12} W/cm^2. The features observed in the experiment, including the asymmetric splitting, broadening, and weakening of the Fano line shape, are reproduced very well by the model. Furthermore, the simulations unveil sub-cycle dynamics, analogous to the sub-cycle AC Stark shift and wavepacket interferences, which were barely observable and not initially reported in the experiments [104]. Here, we note that unlike previous simulations [104], we do not make the rotating wave approximation, which allows the observation of the sub-cycle dynamics.

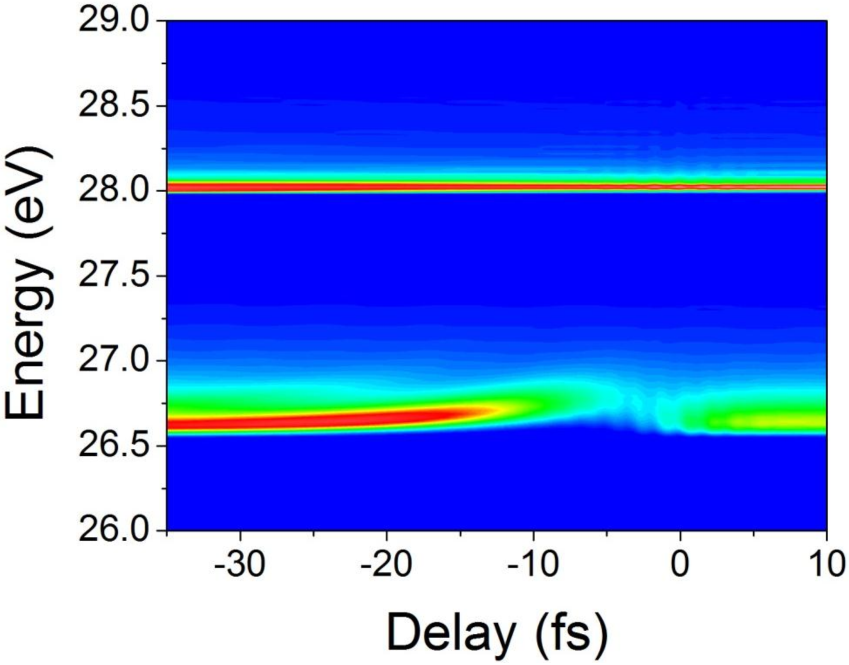

Figure 7.6: Calculated delay-dependent transmission of argon.

The Effects of Laser Polarization on the Coupling of Autoionizing States

Since the coupling of autoionizing states is governed by laser-driven dipole couplings, another parameter which we can use to control the dynamics is the polarization of the dressing NIR laser. This is due to the vector nature of the dipole matrix element $\boldsymbol{d}_{ba} = \langle b|\boldsymbol{r}|a\rangle$. When the dressing laser is polarized along the same axis as the attosecond pulse, only the projection of the dipole matrix element on the laser polarization axis matters, and we can use $d_{ba} = \langle b|z|a\rangle$. However, when the polarizations are not parallel, the polarization direction of the attosecond pulse sets the *z*-axis, and the angle of the laser polarization with respect to the z-axis can play a role. In Figures 7.7(a) and (b), we show the delay-dependent transmission spectrogram for the same dressing laser intensities as in Figures 7.3(a) and 7.4(a), but with dressing laser polarizations perpendicular to the attosecond pulse polarization axis. Clearly, the laser-induced modifications to the Fano resonances, including the line shifts, broadening, and splitting, are strongly enhanced, indicating that the perpendicular component of the dipole matrix element coupling the $3s3p^6 4p$ and $3s3p^6 4d$ autoionizing states is larger than the component along the *z*-axis. This measurement suggests that the measured resonance energy shifts and absorption line broadening and splitting can be used to determine the angle-dependent dipole matrix elements of short-lived states which are inaccessible to other methods. As theoretical methods for treating the electron-electron interaction in many-electron atoms are advanced, such a measurement could be critical in validating theoretical calculations.

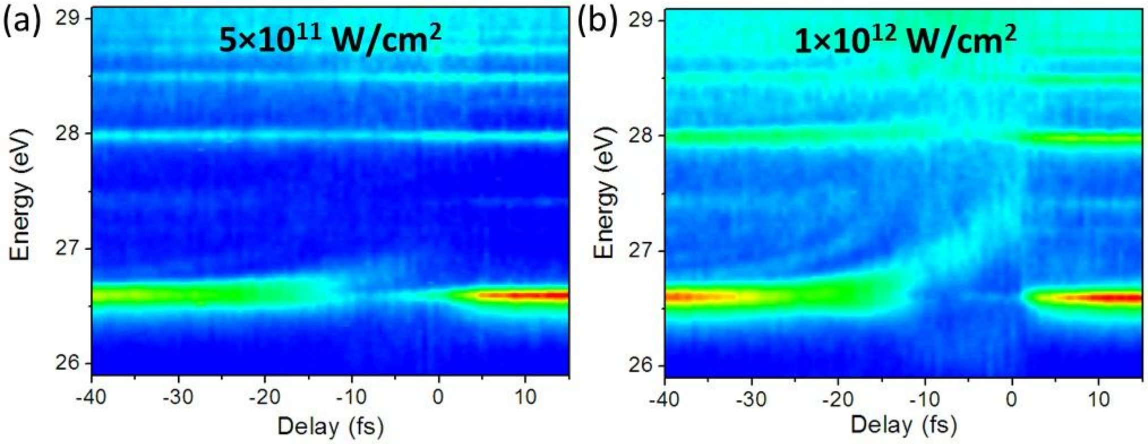

Figure 7.7: Delay-dependent transition of argon with the NIR laser polarization rotated by 90° with respect to the XUV polarization.

Notes

Portions of this chapter were used or adapted with permission from the following:

> He Wang, Michael Chini, Shouyuan Chen, Chang-Hua Zhang, Feng He, Yan Cheng, Yi Wu, Uwe Thumm, and Zenghu Chang. Attosecond Time-Resolved Autoionization of Argon. *Physical Review Letters* **105**, 143002 (2010).

CHAPTER EIGHT: CONCLUSIONS AND OUTLOOK

In this thesis, I have presented the characterization and application of isolated attosecond pulses to the time-resolved measurement of electron dynamics in atomic systems. Ultrabroadband isolated attosecond pulses, with continuum spectra covering absorption lines corresponding to bound and quasi-bound states of the atom, were generated using the double optical gating technique and characterized using a novel technique known as PROOF. The PROOF technique, unlike other available methods, is applicable to the characterization of arbitrarily short pulses, approaching and even eclipsing the atomic unit of time, 24 attoseconds. The crowning achievement of the PROOF technique to this point is in the characterization of a world record-breaking isolated 67 attosecond pulse generated with DOG, limited only by the ability to manipulate the phase of the isolated attosecond pulse. Broader spectra have already been demonstrated with DOG, supporting 16 *as* pulse durations, and it is likely that the pulse duration can be further shortened below 50 *as* without substantial changes to the experimental conditions.

In the second half of the thesis, the isolated attosecond pulses were applied to the measurement of fast dynamics in the laser-dressed atom using the attosecond transient absorption technique. These measurements shed new light on prototypical quantum mechanical processes such as the AC Stark shift and Autler-Townes splitting of the atomic energy levels, nonresonant two-photon absorption, and autoionization. In all cases, the absorption lines are modified on timescales shorter than the laser period, revealing the attosecond electron dynamics which underscore the observed phenomena. These initial experiments in relatively simple systems, and the accompanying interpretation of the results using relatively simple models and numerical calculations accessible to experimentalists and typical notebook computers, pave the way to the study and control of more complicated dynamics in many-electron atoms, as well as molecules and solid systems.

These experiments only scratch the surface of measuring and controlling bound electron dynamics on the attosecond timescale, and the potential of our current experimental tools has not yet been exhausted. Still, the next generation of ultrafast laser technology holds new frontiers for attosecond science and the measurement of fast electron dynamics on unprecedented timescales. Already, significant headway has been made in the generation of high-flux attosecond pulses [157], with microJoule-level pulse energy and focused intensities of 10^{14} W/cm^2 or more, enough to initiate nonlinear dynamics in atomic and molecular targets. Although the current technology has so far allowed only the generation of high-flux attosecond pulse trains [158], substantial effort is currently being invested into the generation of intense isolated attosecond pulses from driving laser systems with peak power exceeding 1 terawatt [159-161]. While the experiments presented in this thesis rely on the intense NIR laser field to modify and control the electron dynamics and are therefore limited in time resolution to timescales comparable to the laser half-cycle, intense attosecond pulses will allow for dynamics to be both initiated and controlled on the few-attosecond timescale.

APPENDIX A: COPYRIGHT PERMISSIONS

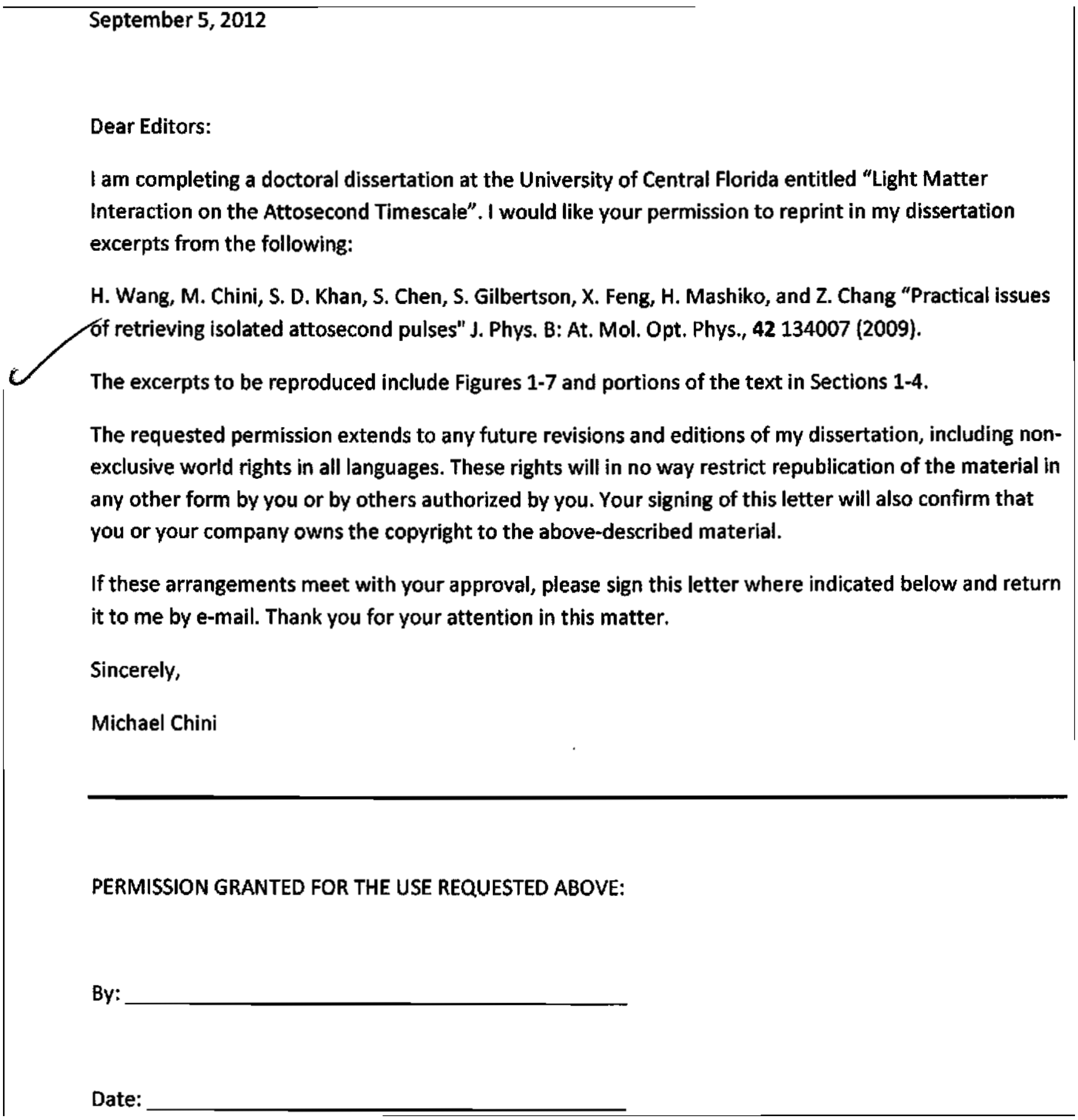

September 5, 2012

Dear Editors:

I am completing a doctoral dissertation at the University of Central Florida entitled "Light Matter Interaction on the Attosecond Timescale". I would like your permission to reprint in my dissertation excerpts from the following:

H. Wang, M. Chini, S. D. Khan, S. Chen, S. Gilbertson, X. Feng, H. Mashiko, and Z. Chang "Practical issues of retrieving isolated attosecond pulses" J. Phys. B: At. Mol. Opt. Phys., **42** 134007 (2009).

The excerpts to be reproduced include Figures 1-7 and portions of the text in Sections 1-4.

The requested permission extends to any future revisions and editions of my dissertation, including non-exclusive world rights in all languages. These rights will in no way restrict republication of the material in any other form by you or by others authorized by you. Your signing of this letter will also confirm that you or your company owns the copyright to the above-described material.

If these arrangements meet with your approval, please sign this letter where indicated below and return it to me by e-mail. Thank you for your attention in this matter.

Sincerely,

Michael Chini

PERMISSION GRANTED FOR THE USE REQUESTED ABOVE:

By: ______________________________

Date: ______________________________

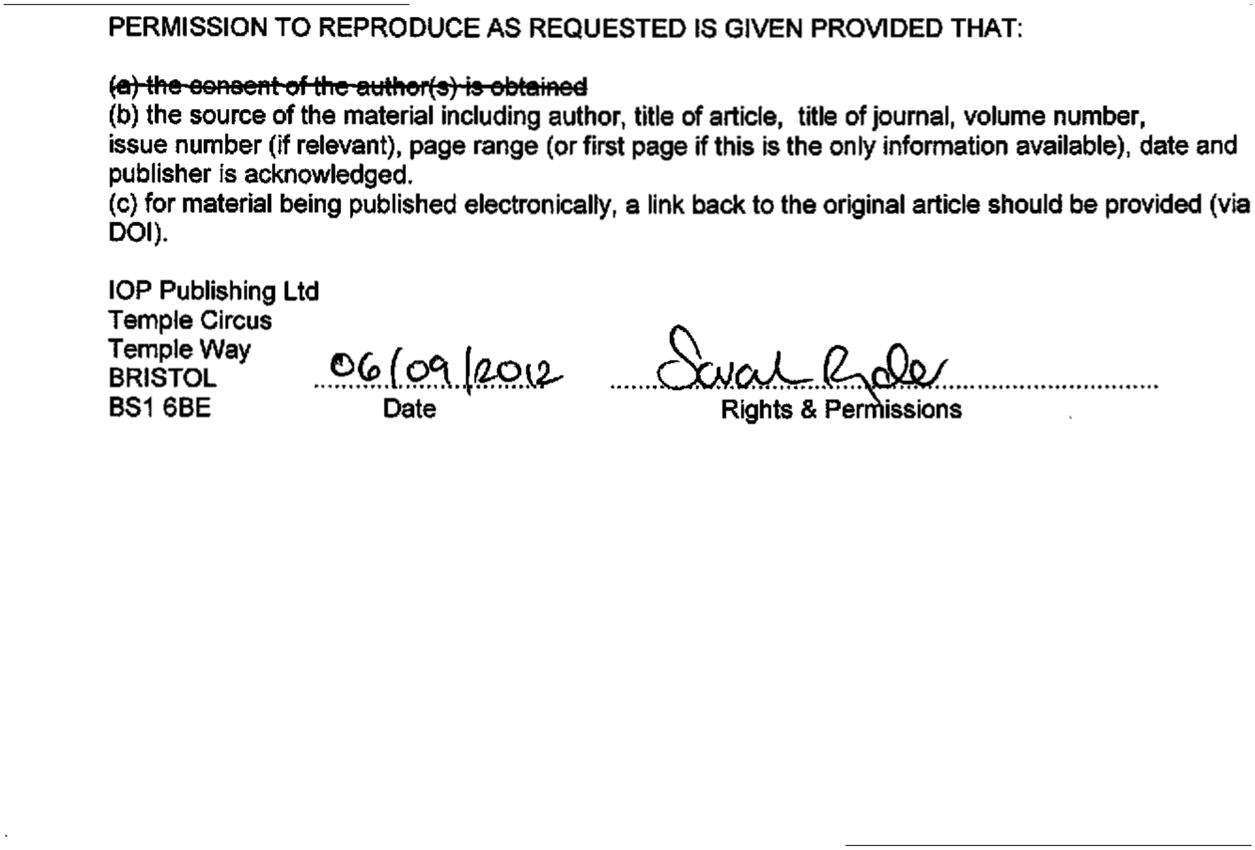

PERMISSION TO REPRODUCE AS REQUESTED IS GIVEN PROVIDED THAT:

~~(a) the consent of the author(s) is obtained~~
(b) the source of the material including author, title of article, title of journal, volume number, issue number (if relevant), page range (or first page if this is the only information available), date and publisher is acknowledged.
(c) for material being published electronically, a link back to the original article should be provided (via DOI).

IOP Publishing Ltd
Temple Circus
Temple Way
BRISTOL
BS1 6BE

06/09/2012
Date

Sarah Ryder
Rights & Permissions

September 5, 2012

Dear Editors:

I am completing a doctoral dissertation at the University of Central Florida entitled “Light Matter Interaction on the Attosecond Timescale”. I would like your permission to reprint in my dissertation excerpts from the following:

M. Chini, S. Gilbertson, S. D. Khan, and Z. Chang “Characterizing ultrabroadband attosecond lasers” Opt. Exp. **18**, 13006 (2010)

M. Chini, H. Mashiko, H. Wang, S. Chen, C. Yun, S. Scott, S. Gilbertson, and Z. Chang “Delay control in attosecond pump-probe experiments” Opt. Exp. **17**, 21459 (2009)

X. Feng, S. Gilbertson, S. D. Khan, M. Chini, Y. Wu, K. Carnes, and Z. Chang “Calibration of electron spectrometer resolution in attosecond streak camera” Opt. Exp. **18**, 1316 (2010)

S. Chen, M. Chini, H. Wang, C. Yun, H. Mashiko, Y. Wu, and Z. Chang “Carrier-envelope phase stabilization and control of 1 kHz, 6 mJ, 30 fs laser pulses from a Ti:sapphire regenerative amplifier” Appl. Opt. **48**, 5692 (2009)

C. Yun, S. Chen, H. Wang, M. Chini, and Z. Chang “Temperature feedback control for long-term carrier-envelope phase locking” Appl. Opt. **48**, 5127 (2009)

The excerpts to be reproduced include figures and portions of the text.

The requested permission extends to any future revisions and editions of my dissertation, including non-exclusive world rights in all languages. These rights will in no way restrict republication of the material in any other form by you or by others authorized by you. Your signing of this letter will also confirm that you or your company owns the copyright to the above-described material.

If these arrangements meet with your approval, please sign this letter where indicated below and return it to me by e-mail. Thank you for your attention in this matter.

Sincerely,

Michael Chini

PERMISSION GRANTED FOR THE USE REQUESTED ABOVE:

By: ____

Date: ____

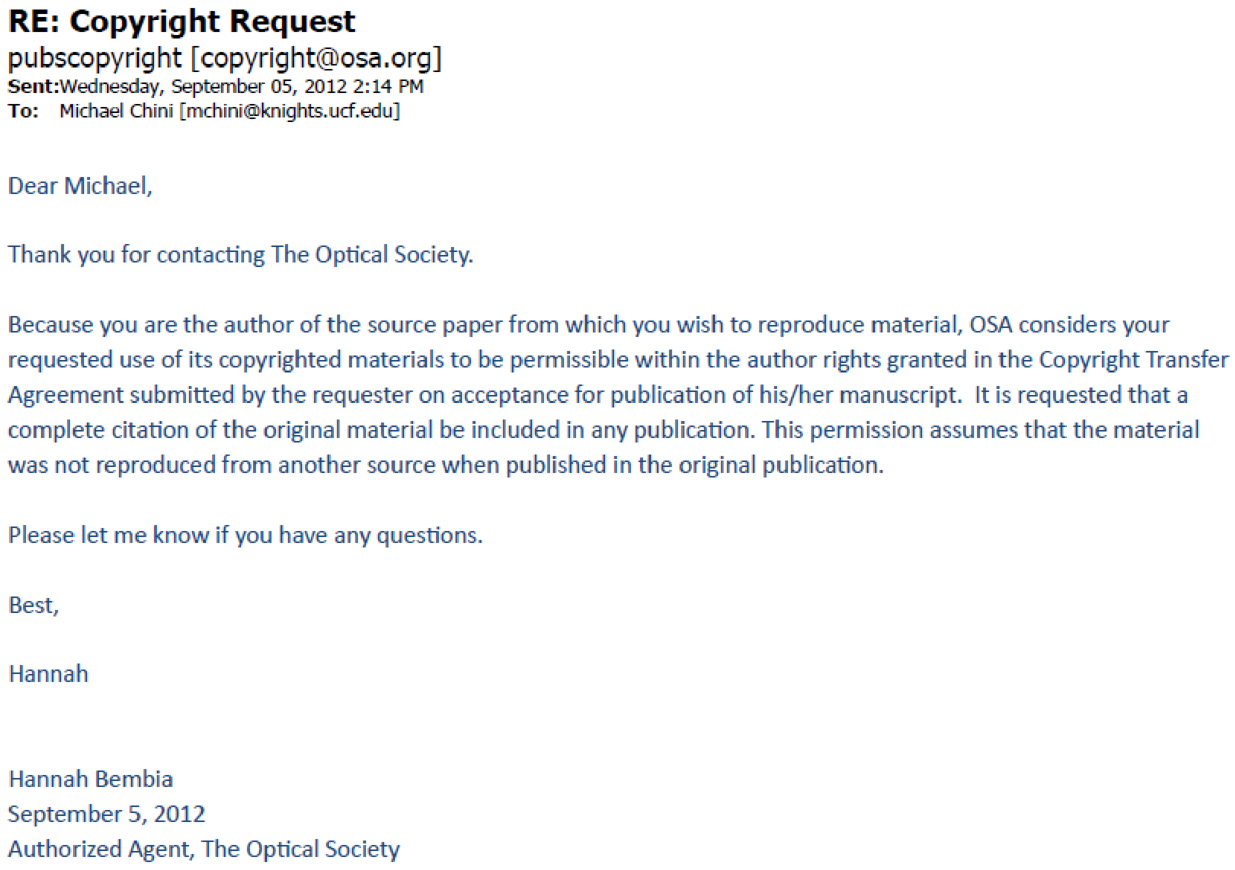

RE: Copyright Request

pubscopyright [copyright@osa.org]

Sent: Wednesday, September 05, 2012 2:14 PM

To: Michael Chini [mchini@knights.ucf.edu]

Dear Michael,

Thank you for contacting The Optical Society.

Because you are the author of the source paper from which you wish to reproduce material, OSA considers your requested use of its copyrighted materials to be permissible within the author rights granted in the Copyright Transfer Agreement submitted by the requester on acceptance for publication of his/her manuscript. It is requested that a complete citation of the original material be included in any publication. This permission assumes that the material was not reproduced from another source when published in the original publication.

Please let me know if you have any questions.

Best,

Hannah

Hannah Bembia
September 5, 2012
Authorized Agent, The Optical Society

September 5, 2012

Dear Editors:

I am completing a doctoral dissertation at the University of Central Florida entitled “Light Matter Interaction on the Attosecond Timescale”. I would like your permission to reprint in my dissertation excerpts from the following:

M. Chini, H. Wang, S. D. Khan, S. Chen, and Z. Chang “Retrieval of satellite pulses of single isolated attosecond pulses” Appl. Phys. Lett. **94**, 161112 (2009)

The excerpts to be reproduced include Figures 2-4 and portions of the text.

The requested permission extends to any future revisions and editions of my dissertation, including non-exclusive world rights in all languages. These rights will in no way restrict republication of the material in any other form by you or by others authorized by you. Your signing of this letter will also confirm that you or your company owns the copyright to the above-described material.

If these arrangements meet with your approval, please sign this letter where indicated below and return it to me by e-mail. Thank you for your attention in this matter.

Sincerely,

Michael Chini

From: AIPRights Permissions
To: Michael Chini
Subject: RE: Copyright Request
Date: Thursday, September 13, 2012 3:01:46 PM

Dear Dr. Chini:

Thank you for requesting permission to reproduce material from American Institute of Physics publications.

Permission is granted – subject to the conditions outlined below – for the following:

Figures 2-4 and portions of the text
M. Chini, H. Wang, S. D. Khan, S. Chen, and Z. Chang
"Retrieval of satellite pulses of single isolated attosecond pulses" Appl. Phys. Lett. 94, 161112 (2009)

To be used in the following manner:

Reproduced in your doctoral dissertation at the University of Central Florida entitled, "Light Matter Interaction on the Attosecond Timescale".

1. The American Institute of Physics grants you non-exclusive world rights in all languages and media.

2. This permission extends to all subsequent and future editions of the new work.

3. The following copyright notice must appear with the material (please fill in the information indicated by capital letters): "Reprinted with permission from [FULL CITATION]. Copyright [PUBLICATION YEAR], American Institute of Physics."
Full citation format is as follows: Author names, journal title, Vol. #, Page #, (Year of publication).
For an article, the copyright notice must be printed on the first page of the article or book chapter.
For figures, photographs, covers, or tables, the notice may appear with the material, in a footnote, or in the reference list.

4. This permission does not apply to any materials credited to sources other than the copyright holder.

Please let us know if you have any questions.

Sincerely,
Susann Brailey

Manager, Rights and Permissions
American Institute of Physics
Suite 1NO1

2 Huntington Quadrangle
Melville, NY 11747-4502

AIP Publishing

Phone: 1-516-576-2268
Fax: 1-516-576-2450
Email: sbrailey@aip.org

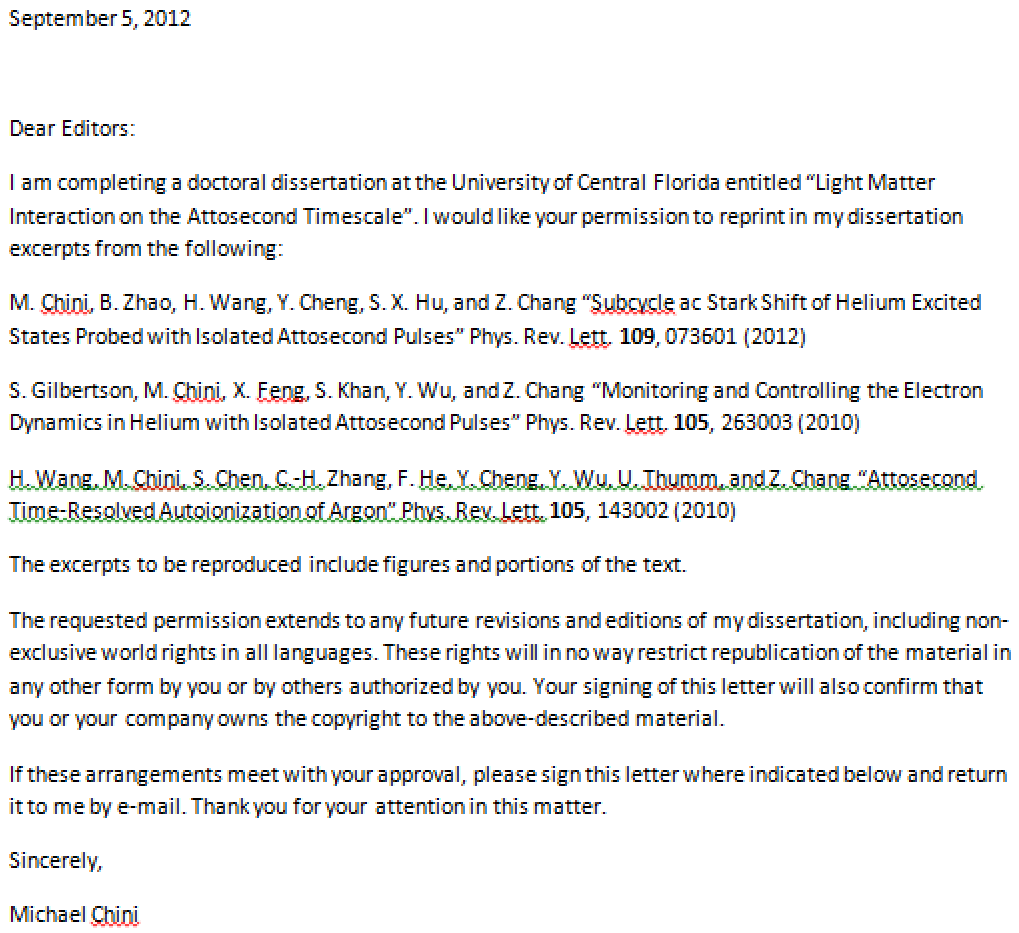

September 5, 2012

Dear Editors:

I am completing a doctoral dissertation at the University of Central Florida entitled “Light Matter Interaction on the Attosecond Timescale”. I would like your permission to reprint in my dissertation excerpts from the following:

M. Chini, B. Zhao, H. Wang, Y. Cheng, S. X. Hu, and Z. Chang “Subcycle ac Stark Shift of Helium Excited States Probed with Isolated Attosecond Pulses” Phys. Rev. Lett. **109**, 073601 (2012)

S. Gilbertson, M. Chini, X. Feng, S. Khan, Y. Wu, and Z. Chang “Monitoring and Controlling the Electron Dynamics in Helium with Isolated Attosecond Pulses” Phys. Rev. Lett. **105**, 263003 (2010)

H. Wang, M. Chini, S. Chen, C.-H. Zhang, F. He, Y. Cheng, Y. Wu, U. Thumm, and Z. Chang “Attosecond Time-Resolved Autoionization of Argon” Phys. Rev. Lett. **105**, 143002 (2010)

The excerpts to be reproduced include figures and portions of the text.

The requested permission extends to any future revisions and editions of my dissertation, including non-exclusive world rights in all languages. These rights will in no way restrict republication of the material in any other form by you or by others authorized by you. Your signing of this letter will also confirm that you or your company owns the copyright to the above-described material.

If these arrangements meet with your approval, please sign this letter where indicated below and return it to me by e-mail. Thank you for your attention in this matter.

Sincerely,

Michael Chini

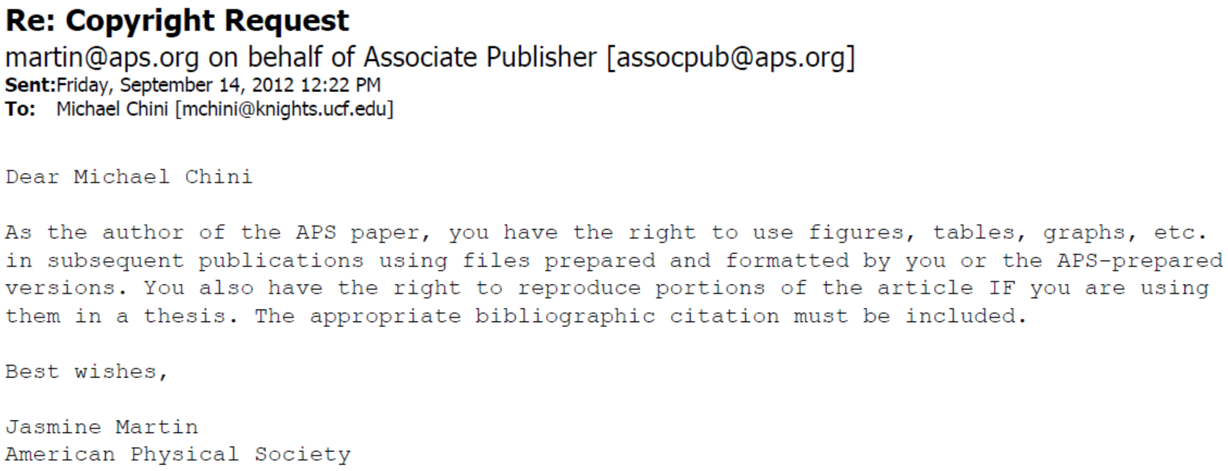

Re: Copyright Request

martin@aps.org on behalf of Associate Publisher [assocpub@aps.org]
Sent: Friday, September 14, 2012 12:22 PM
To: Michael Chini [mchini@knights.ucf.edu]

Dear Michael Chini

As the author of the APS paper, you have the right to use figures, tables, graphs, etc. in subsequent publications using files prepared and formatted by you or the APS-prepared versions. You also have the right to reproduce portions of the article IF you are using them in a thesis. The appropriate bibliographic citation must be included.

Best wishes,

Jasmine Martin
American Physical Society

APPENDIX B: LIST OF PUBLICATIONS

Peer-Reviewed Journal Publications

Chini, M., Wang, X., Cheng, Y., Wu, Y., Zhao, D., Telnov, D. A., Chu, S. I. & Chang, Z. Sub-cycle oscillating dark states brought to light. (submitted) (2012).

Wang, X., Chini, M., Cheng, Y., Wu, Y. & Chang, Z. In Situ Calibration of an Extreme Ultraviolet Spectrometer for Attosecond Transient Absorption Experiments. (submitted) (2012).

Zhao, K., Zhang, Q., Chini, M., Wu, Y., Wang, X. & Chang, Z. Tailoring a 67 attosecond pulse through advantageous phase-mismatch. *Optics Letters* **37**, 3891-3893 (2012).

Chini, M., Zhao, B., Wang, H., Cheng, Y., Hu, S. X. & Chang, Z. Subcycle ac Stark Shift of Helium Excited States Probed with Isolated Attosecond Pulses. *Physical Review Letters* **109**, 073601 (2012).

Wang, X., Chini, M., Zhang, Q., Zhao, K., Wu, Y., Telnov, D. A., Chu, S. I. & Chang, Z. Mechanism of quasi-phase-matching in a dual-gas multijet array. *Physical Review A* **86**, 021802 (2012).

Moller, M., Cheng, Y., Khan, S. D., Zhao, B. Z., Zhao, K., Chini, M., Paulus, G. G. & Chang, Z. Dependence of high-order-harmonic-generation yield on driving-laser ellipticity. *Physical Review A* **86**, 011401 (2012).

Khan, S. D., Cheng, Y., Moller, M., Zhao, K., Zhao, B. Z., Chini, M., Paulus, G. G. & Chang, Z. Ellipticity dependence of 400 nm-driven high harmonic generation. *Applied Physics Letters* **99**, 161106 (2011).

Moller, M., Sayler, A. M., Rathje, T., Chini, M., Chang, Z. & Paulus, G. G. Precise, real-time, single-shot carrier-envelope phase measurement in the multi-cycle regime. *Applied Physics Letters* **99**, 121108 (2011).

Gilbertson, S., Chini, M., Feng, X., Khan, S., Wu, Y. & Chang, Z. Monitoring and Controlling the Electron Dynamics in Helium with Isolated Attosecond Pulses. *Physical Review Letters* **105**, 263003 (2010).

Wang, H., Chini, M., Chen, S., Zhang, C. H., He, F., Cheng, Y., Wu, Y., Thumm, U. & Chang, Z. Attosecond Time-Resolved Autoionization of Argon. *Physical Review Letters* **105**, 143002 (2010).

Gilbertson, S., Khan, S. D., Wu, Y., Chini, M. & Chang, Z. Isolated Attosecond Pulse Generation without the Need to Stabilize the Carrier-Envelope Phase of Driving Lasers. *Physical Review Letters* **105**, 093902 (2010).

Chini, M., Gilbertson, S., Khan, S. D. & Chang, Z. Characterizing ultrabroadband attosecond lasers. *Optics Express* **18**, 13006 (2010).

Gilbertson, S., Wu, Y., Khan, S. D., Chini, M., Zhao, K., Feng, X. & Chang, Z. Isolated attosecond pulse generation using multicycle pulses directly from a laser amplifier. *Physical Review A* **81**, 043810 (2010).

Feng, X., Gilbertson, S., Khan, S. D., Chini, M., Wu, Y., Carnes, K. & Chang, Z. Calibration of electron spectrometer resolution in attosecond streak camera. *Optics Express* **18**, 1316 (2010).

Moon, E., Wang, H., Gilbertson, S., Mashiko, H., Chini, M. & Chang, Z. Advances in carrier-envelope phase stabilization of grating-based chirped-pulse amplifiers. *Laser & Photonics Reviews* **4**, 160 (2010).

Wang, H., Chini, M., Wu, Y., Moon, E., Mashiko, H. & Chang, Z. Carrier–envelope phase stabilization of 5-fs, 0.5-mJ pulses from adaptive phase modulator. *Applied Physics B: Lasers and Optics* **98**, 291 (2010).

Mashiko, H., Gilbertson, S., Chini, M., Feng, X., Yun, C., Wang, H., Khan, S. D., Chen, S. & Chang, Z. Extreme ultraviolet supercontinua supporting pulse durations of less than one atomic unit of time. *Optics Letters* **34**, 3337 (2009).

Yun, C., Chen, S., Wang, H., Chini, M. & Chang, Z. Temperature feedback control for long-term carrier-envelope phase locking. *Applied Optics* **48**, 5127 (2009).

Gilbertson, S., Feng, X., Khan, S., Chini, M., Wang, H., Mashiko, H. & Chang, Z. Direct measurement of an electric field in femtosecond Bessel-Gaussian beams. *Optics Letters* **34**, 2390 (2009).

Wang, H., Chini, M., Khan, S. D., Chen, S., Gilbertson, S., Feng, X., Mashiko, H. & Chang, Z. Practical issues of retrieving isolated attosecond pulses. *Journal of Physics B: Atomic, Molecular and Optical Physics* **42**, 134007 (2009).

Chini, M., Wang, H., Khan, S. D., Chen, S. & Chang, Z. Retrieval of satellite pulses of single isolated attosecond pulses. *Applied Physics Letters* **94**, 161112 (2009).

Chen, S., Chini, M., Wang, H., Yun, C., Mashiko, H., Wu, Y. & Chang, Z. Carrier-envelope phase stabilization and control of 1 kHz, 6 mJ, 30 fs laser pulses from a Ti:sapphire regenerative amplifier. *Applied Optics* **48**, 5692 (2009).

Chini, M., Mashiko, H., Wang, H., Chen, S., Yun, C., Scott, S., Gilbertson, S. & Chang, Z. Delay control in attosecond pump-probe experiments. *Optics Express* **17**, 21459 (2009).

Feng, X., Gilbertson, S., Mashiko, H., Wang, H., Khan, S. D., Chini, M., Wu, Y., Zhao, K. & Chang, Z. Generation of Isolated Attosecond Pulses with 20 to 28 Femtosecond Lasers. *Physical Review Letters* **103**, 183901 (2009).

Wang, H., Chini, M., Moon, E., Mashiko, H., Li, C. & Chang, Z. Coupling between energy and phase in hollow-core fiber based f-to-2f interferometers. *Optics Express* **17**, 12082 (2009).

Invited Book Chapters

Chini, M., Wang, H., Zhao, B., Cheng, Y., Chen, S., Wu, Y. & Chang, Z. Attosecond Absorption Spectroscopy. to be published in *Progress in Ultrafast Intense Laser Science* Vol. 9 (eds. K. Yamanouchi & K. Midorikawa), (Springer).

Zhao, K., Zhang, Q., Chini, M. & Chang, Z. Route to One Atomic Unit of Time – Development of a Broadband Attosecond Streak Camera. in *Multiphoton Processes and Attosecond Physics* Vol. 125 (eds. K. Yamanouchi & K. Midorikawa), Ch. 19, pg. 109 (Springer, 2012).

Chen, S., Gilbertson, S., Wang, H. Chini, M., Zhao, K., Khan, S., Wu, Y. & Chang, Z. Attosecond Pulse Generation, Characterization and Application. in *Advances in Multi-Photon Processes and Spectroscopy* Vol. 20 (eds. S. H. Lin, A. A. Villaeys & Y. Fujimura), Ch. 4 (World Scientific, 2011).

Feng, X., Gilbertson, S., Mashiko, H., Wang, H., Khan, S. D., Chini, M., Wu, Y. & Chang Z. Single Isolated Attosecond Pulses Generation with Double Optical Gating. in *Progress in Ultrafast Intense Laser Science* Vol. 6 (eds. K. Yamanouchi, A. Bandrauk & G. Gerber), Ch. 5, pg. 89 (Springer, 2010).

Conference Presentations

Chini, M., Wang, X., Cheng, Y., Wu, Y., Zhao, K., Zhang, Q., Cunningham, E., Wang, Y., Zang, H. & Chang, Z. Probing Attosecond Electron Dynamics in Atoms (Invited). *IEEE Photonics Conference*, Burlingame CA (2012).

Chini, M., Wang, X., Zhang, Q., Zhao, K., Wu, Y. & Chang, Z. High-order Harmonic Generation from Molecular Hydrogen. *43rd Annual Meeting of the APS Division of Atomic, Molecular and Optical Physics*, Orange County CA (2012).

Chini, M., Zhao, B., Wang, H., Cheng, Y., Hu, S. X. & Chang, Z. Sub-cycle AC Stark Shift. *Conference on Lasers and Electro-Optics*, San Jose CA (2012).

Chini, M., Wang, H., Zhang, C.-H., He, F., Chen, S., Cheng, Y., Zhao, B., Wu, Y., Thumm, U. & Chang Z. Probing Autoionization and AC Stark shift with attosecond transient absorption spectroscopy. *42nd Annual Meeting of the APS Division of Atomic, Molecular and Optical Physics*, Atlanta GA (2011).

Chini, M., Zhao, B. & Chang, Z. Probing AC Stark shift with attosecond transient absorption. *Conference on Lasers and Electro-Optics*, Baltimore MD (2011).

Chini, M., Gilbertson, S., Khan, S. D. & Chang, Z. Characterizing isolated atomic unit attosecond pulses. *Conference on Lasers and Electro-Optics*, Baltimore MD (2011).

Chini, M., Wang, H., Chen, S., Cheng, Y. & Chang, Z. Attosecond-resolved Autoionization in Argon. *37th International Conference on Vacuum UltraViolet and X-ray Physics*, Vancouver BC (2010).

Chini, M., Gilbertson, S., Khan, S. & Chang, Z. OPTICAL: a new method for characterizing ultra-broadband isolated attosecond pulses. *41st Annual meeting of the APS Division of Atomic, Molecular and Optical Physics*, Houston TX (2010).

Chini, M., Gilbertson, S., Khan, S. D., & Chang, Z. Characterizing ultrabroadband attosecond lasers. *Conference on Lasers and Electro-Optics*, San Jose CA (2010).

Chini, M., Gilbertson, S., Feng, X., Khan, S. D., Wang, H. & Chang, Z. Laser-disturbed Electron-electron Interactions Probed by Isolated Attosecond Pulses. *International Workshop on Quantum Dynamic Imaging*, Montreal QC (2009).

Chini, M., Wang, H., Khan, S. D., Chen, S. & Chang, Z. Accurate Retrieval of Satellite Pulses of Isolated Attosecond Pulses. *2nd International Conference on Attosecond Physics*, Manhattan KS (2009).

Chini, M., Wang, H., Mashiko, H., Chen, S., Yun, C., Gilbertson, S. & Chang, Z. Interferometric Delay Control in Attosecond Streaking Experiments. *2nd International Conference on Attosecond Physics*, Manhattan KS (2009).

Chini, M., Wang, H., Khan, S., Chao, W. & Chang, Z. Accurate Retrieval of Satellite Pulses of Isolated Attosecond Pulses. *40th Annual Meeting of the APS Division of Atomic, Molecular and Optical Physics*, Charlottesville, VA (2009).

Chini, M., Wang, H., Moon, E., Mashiko, H. & Chang, Z. Coupling between Energy and Carrier-Envelope Phase in Hollow-Core Fiber Based *f*-to-2*f* Interferometers. *Conference on Lasers and Electro-Optics*, Baltimore MD (2009).

Patents

Chang, Z., Yun, C., Chen, S., Wang, H. & Chini, M. Temperature feedback control for long-term carrier envelope phase locking.

LIST OF REFERENCES

1. Niikura, H. & Corkum, P. B. Attosecond and Angstrom science. *Advances in Atomic Molecular and Optical Physics* **54**, 511-548 (2007).

2. Kirchhoff, M. P. G. *Abhandlungen Über Emission und Absorption: I. Ueber Die Fraunhofer'schen Linien. (1859.) II. Ueber De*. (BiblioBazaar, 2009).

3. Balmer, J. J. Notiz über die Spectrallinien des Wasserstoffs. *Annalen Der Physik* **261**, 80-87 (1885).

4. Lyman, T. *The spectroscopy of the extreme ultra-violet*. (Longmans, Green and Co., 1914).

5. Paschen, F. Zur Kenntnis ultraroter Linienspektra. I. (Normalwellenlängen bis 27000 Å.-E.). *Annalen Der Physik* **332**, 537-570 (1908).

6. Mathies, R., Brito Cruz, C., Pollard, W. & Shank, C. Direct observation of the femtosecond excited-state cis-trans isomerization in bacteriorhodopsin. *Science* **240**, 777-779 (1988).

7. Brabec, T. & Krausz, F. Intense few-cycle laser fields: Frontiers of nonlinear optics. *Reviews of Modern Physics* **72**, 545-591 (2000).

8. Bransden, B. H. & Joachain, C. J. *Physics of atoms and molecules*. 2nd edn, (Prentice Hall, 2003).

9. Phillips, W. D. Laser cooling and trapping of neutral atoms. *Reviews of Modern Physics* **70**, 721-741 (1998).

10. Wieman, C. E., Pritchard, D. E. & Wineland, D. J. Atom cooling, trapping, and quantum manipulation. *Reviews of Modern Physics* **71**, S253-S262 (1999).

11. Stapelfeldt, H. & Seideman, T. Colloquium: Aligning molecules with strong laser pulses. *Reviews of Modern Physics* **75**, 543-557 (2003).

12. Zewail, A. H. Femtochemistry: Atomic-scale dynamics of the chemical bond. *Journal of Physical Chemistry A* **104**, 5660-5694 (2000).

13. Kling, M. F. *et al.* Control of electron localization in molecular dissociation. *Science* **312**, 246-248 (2006).

14. Paulus, G. G. *et al.* Absolute-phase phenomena in photoionization with few-cycle laser pulses. *Nature* **414**, 182-184 (2001).

15. Corkum, P. B., Ivanov, M. Y. & Wright, J. S. Subfemtosecond processes in strong laser fields. *Annual Review of Physical Chemistry* **48**, 387-406 (1997).

16. Corkum, P. B. Plasma Perspective on Strong-Field Multiphoton Ionization. *Physical Review Letters* **71**, 1994-1997 (1993).

17. Hentschel, M. *et al.* Attosecond metrology. *Nature* **414**, 509-513 (2001).

18. Mashiko, H. *et al.* Double optical gating of high-order harmonic generation with carrier-envelope phase stabilized lasers. *Physical Review Letters* **100**, 103906 (2008).

19. Mashiko, H. *et al.* Extreme ultraviolet supercontinua supporting pulse durations of less than one atomic unit of time. *Optics Letters* **34**, 3337-3339 (2009).

20. Mairesse, Y. & Quere, F. Frequency-resolved optical gating for complete reconstruction of attosecond bursts. *Physical Review A* **71**, 011401 (2005).

21. Baltuska, A. *et al.* Attosecond control of electronic processes by intense light fields. *Nature* **421**, 611-615 (2003).

22. Moon, E. *et al.* Advances in carrier-envelope phase stabilization of grating-based chirped-pulse amplifiers. *Laser & Photonics Reviews* **4**, 160-177 (2010).

23. Kim, K. T., Kim, C. M., Baik, M. G., Umesh, G. & Nam, C. H. Compression of harmonic pulses by using material dispersion. *Applied Physics B-Lasers and Optics* **79**, 563-567 (2004).

24. Itatani, J. *et al.* Attosecond streak camera. *Physical Review Letters* **88**, 173903 (2002).

25. Drescher, M. *et al.* X-ray pulses approaching the attosecond frontier. *Science* **291**, 1923-1927 (2001).

26. Sansone, G. *et al.* Isolated single-cycle attosecond pulses. *Science* **314**, 443-446 (2006).

27. Feng, X. *et al.* Generation of Isolated Attosecond Pulses with 20 to 28 Femtosecond Lasers. *Physical Review Letters* **103**, 183901 (2009).

28. Kienberger, R. *et al.* Atomic transient recorder. *Nature* **427**, 817-821 (2004).

29. Gilbertson, S. *et al.* Monitoring and Controlling the Electron Dynamics in Helium with Isolated Attosecond Pulses. *Physical Review Letters* **105**, 263003 (2010).

30. Mauritsson, J. *et al.* Attosecond Electron Spectroscopy Using a Novel Interferometric Pump-Probe Technique. *Physical Review Letters* **105**, 053001 (2010).

31. Cavalieri, A. L. *et al.* Attosecond spectroscopy in condensed matter. *Nature* **449**, 1029-1032 (2007).

32. Schultze, M. *et al.* Delay in Photoemission. *Science* **328**, 1658-1662 (2010).

33. Kitzler, M., Milosevic, N., Scrinzi, A., Krausz, F. & Brabec, T. Quantum theory of attosecond XUV pulse measurement by laser dressed photoionization. *Physical Review Letters* **88**, 173904 (2002).

34. Chini, M., Gilbertson, S., Khan, S. D. & Chang, Z. Characterizing ultrabroadband attosecond lasers. *Optics Express* **18**, 13006-13016 (2010).

35. Wickenhauser, M., Burgdorfer, J., Krausz, F. & Drescher, M. Time resolved Fano resonances. *Physical Review Letters* **94**, 023002 (2005).

36. Zhao, Z. X. & Lin, C. D. Theory of laser-assisted autoionization by attosecond light pulses. *Physical Review A* **71**, 060702 (2005).

37. Pfeifer, T. *et al.* Time-resolved spectroscopy of attosecond quantum dynamics. *Chemical Physics Letters* **463**, 11-24 (2008).

38. Muller, H. G. Reconstruction of attosecond harmonic beating by interference of two-photon transitions. *Applied Physics B-Lasers and Optics* **74**, S17-S21 (2002).

39. Chini, M. *et al.* Subcycle ac Stark Shift of Helium Excited States Probed with Isolated Attosecond Pulses. *Physical Review Letters* **109**, 073601 (2012).

40. Mysyrowicz, A., Hulin, D., Antonetti, A. & Migus, A. Dressed Excitons in a Multiple-Quantum-Well Structure - Evidence for an Optical Stark-Effect with Femtosecond Response-Time. *Physical Review Letters* **56**, 2748-2751 (1986).

41. Becker, P. C., Fork, R. L., Cruz, C. H. B., Gordon, J. P. & Shank, C. V. Optical Stark-Effect in Organic-Dyes Probed with Optical Pulses of 6-Fs Duration. *Physical Review Letters* **60**, 2462-2464 (1988).

42. Normand, D. *et al.* AC Stark Shifts Induced by a Yag Laser in the Np and Nf Rydberg Series in Xenon. *Journal of the Optical Society of America B-Optical Physics* **6**, 1513-1518 (1989).

43. Delone, N. B. & Krainov, V. P. AC-Stark shift of atomic levels. *Uspekhi Fizicheskikh Nauk* **169**, 753-772 (1999).

44. Bayfield, J. E., Gardner, L. D., Gulkok, Y. Z. & Sharma, S. D. Spectroscopic Study of Non-Resonant Photon-Absorption by Highly Excited Hydrogen-Atoms in a Strong Microwave Field. *Physical Review A* **24**, 138-143 (1981).

45. Autler, S. H. & Townes, C. H. Stark Effect in Rapidly Varying Fields. *Physical Review* **100**, 703-722 (1955).

46. Keldysh, L. V. Ionization in Field of a Strong Electromagnetic Wave. *Soviet Physics JETP* **20**, 1307 (1965).

47. Perelomov, A. M., Popov, V. S. & Terentev, M. V. Ionization of Atoms in an Alternating Electric Field. *Soviet Physics JETP* **23**, 924 (1966).

48. Chang, Z. *Fundamentals of Attosecond Optics*. (CRC Press, 2011).

49. Ferray, M. *et al.* Multiple-Harmonic Conversion of 1064-nm Radiation in Rare-Gases. *Journal of Physics B-Atomic Molecular and Optical Physics* **21**, L31-L35 (1988).

50. Mcpherson, A. *et al.* Studies of Multiphoton Production of Vacuum Ultraviolet-Radiation in the Rare-Gases. *Journal of the Optical Society of America B-Optical Physics* **4**, 595-601 (1987).

51. Franken, P. A., Hill, A. E., Peters, C. W. & Weinreich, G. Generation of Optical Harmonics. *Physical Review Letters* **7**, 118-119 (1961).

52. Kulander, K. C., Schafer, K. J. & Krause, J. L. Theoretical Model for Intense Field High-Order Harmonic Generation in Rare Gases. *Laser Physics* **3**, 359-364 (1993).

53. Lewenstein, M., Balcou, P., Ivanov, M. Y., L'Huillier, A. & Corkum, P. B. Theory of High-Harmonic Generation by Low-Frequency Laser Fields. *Physical Review A* **49**, 2117-2132 (1994).

54. L'Huillier, A. *et al.* High-Order Harmonic-Generation Cutoff. *Physical Review A* **48**, R3433-R3436 (1993).

55. Zhou, J., Peatross, J., Murnane, M. M., Kapteyn, H. C. & Christov, I. P. Enhanced High-Harmonic Generation Using 25 fs Laser Pulses. *Physical Review Letters* **76**, 752-755 (1996).

56. Chang, Z. *et al.* Generation of coherent, femtosecond, X-ray pulses in the "water window". *IEEE Journal of Selected Topics in Quantum Electronics* **4**, 266-270 (1998).

57. Paul, P. M. *et al.* Observation of a train of attosecond pulses from high harmonic generation. *Science* **292**, 1689-1692 (2001).

58. Shan, B. & Chang, Z. Dramatic extension of the high-order harmonic cutoff by using a long-wavelength driving field. *Physical Review A* **65**, 011804 (2001).

59. Colosimo, P. *et al.* Scaling strong-field interactions towards the classical limit. *Nature Physics* **4**, 386-389 (2008).

60. Doumy, G. *et al.* Attosecond Synchronization of High-Order Harmonics from Midinfrared Drivers. *Physical Review Letters* **102**, 093002 (2009).

61. Schmidt, B. E. *et al.* High harmonic generation with long-wavelength few-cycle laser pulses. *Journal of Physics B-Atomic Molecular and Optical Physics* **45**, 074008 (2012).

62. Popmintchev, T., Chen, M. C., Arpin, P., Murnane, M. M. & Kapteyn, H. C. The attosecond nonlinear optics of bright coherent X-ray generation. *Nature Photonics* **4**, 822-832 (2010).

63. Popmintchev, T. *et al.* Bright Coherent Ultrahigh Harmonics in the keV X-ray Regime from Mid-Infrared Femtosecond Lasers. *Science* **336**, 1287-1291 (2012).

64. Falcao-Filho, E. L., Gkortsas, V. M., Gordon, A. & Kartner, F. X. Analytic scaling analysis of high harmonic generation conversion efficiency. *Optics Express* **17**, 11217-11229 (2009).

65. Khan, S. D. *et al.* Ellipticity dependence of 400 nm-driven high harmonic generation. *Applied Physics Letters* **99**, 161106 (2011).

66. Corkum, P. B., Burnett, N. H. & Ivanov, M. Y. Subfemtosecond Pulses. *Optics Letters* **19**, 1870-1872 (1994).

67. Moller, M. *et al.* Dependence of high-order-harmonic-generation yield on driving-laser ellipticity. *Physical Review A* **86**, 011401 (2012).

68. Spielmann, C. *et al.* Generation of Coherent X-rays in the Water Window Using 5-Femtosecond Laser Pulses. *Science* **278**, 661-664 (1997).

69. Nisoli, M. *et al.* Toward a terawatt-scale sub-10-fs laser technology. *IEEE Journal of Selected Topics in Quantum Electronics* **4**, 414-420 (2002).

70. Uiberacker, M. *et al.* Attosecond metrology with controlled light waveforms. *Laser Physics* **15**, 195-204 (2005).

71. Goulielmakis, E. *et al.* Single-cycle nonlinear optics. *Science* **320**, 1614-1617 (2008).

72. Abel, M. J. *et al.* Isolated attosecond pulses from ionization gating of high-harmonic emission. *Chemical Physics* **366**, 9-14 (2009).

73. Ferrari, F. *et al.* High-energy isolated attosecond pulses generated by above-saturation few-cycle fields. *Nature Photonics* **4**, 875-879 (2010).

74. Oron, D., Silberberg, Y., Dudovich, N. & Villeneuve, D. M. Efficient polarization gating of high-order harmonic generation by polarization-shaped ultrashort pulses. *Physical Review A* **72**, 063816 (2005).

75. Chang, Z. Single attosecond pulse and xuv supercontinuum in the high-order harmonic plateau. *Physical Review A* **70**, 043802 (2004).

76. Gilbertson, S., Mashiko, H., Li, C., Moon, E. & Chang, Z. Effects of laser pulse duration on extreme ultraviolet spectra from double optical gating. *Applied Physics Letters* **93**, 111105 (2008).

77. Gilbertson, S. *et al.* A low-loss, robust setup for double optical gating of high harmonic generation. *Applied Physics Letters* **92**, 071109 (2008).

78. Mashiko, H., Gilbertson, S., Li, C., Moon, E. & Chang, Z. Optimizing the photon flux of double optical gated high-order harmonic spectra. *Physical Review A* **77**, 063423 (2008).

79. Gilbertson, S. *et al.* Isolated attosecond pulse generation using multicycle pulses directly from a laser amplifier. *Physical Review A* **81**, 043810 (2010).

80. Gilbertson, S., Khan, S. D., Wu, Y., Chini, M. & Chang, Z. Isolated Attosecond Pulse Generation without the Need to Stabilize the Carrier-Envelope Phase of Driving Lasers. *Physical Review Letters* **105**, 093902 (2010).

81. Mauritsson, J. *et al.* Attosecond pulse trains generated using two color laser fields. *Physical Review Letters* **97**, 013001 (2006).

82. Yu, O. S., Kaku, M., Suda, A., Kannari, F. & Midorikawa, K. Generation of extreme ultraviolet continuum radiation driven by a sub-10-fs two-color field. *Optics Express* **14**, 7230-7237 (2006).

83. Budil, K. S., Salieres, P., L'Huillier, A., Ditmire, T. & Perry, M. D. Influence of Ellipticity on Harmonic-Generation. *Physical Review A* **48**, R3437-R3440 (1993).

84. Tzallas, P. *et al.* Generation of intense continuum extreme-ultraviolet radiation by many-cycle laser fields. *Nature Physics* **3**, 846-850 (2007).

85. Thomann, I. *et al.* Characterizing isolated attosecond pulses from hollow-core waveguides using multi-cycle driving pulses. *Optics Express* **17**, 4611-4633 (2009).

86. Kane, D. J. Principal components generalized projections: a review [Invited]. *Journal of the Optical Society of America B-Optical Physics* **25**, A120-A132 (2008).

87. Kane, D. J. & Trebino, R. Single-Shot Measurement of the Intensity and Phase of an Arbitrary Ultrashort Pulse by Using Frequency-Resolved Optical Gating. *Optics Letters* **18**, 823-825 (1993).

88. Delong, K. W., Trebino, R., Hunter, J. & White, W. E. Frequency-Resolved Optical Gating with the Use of 2nd-Harmonic Generation. *Journal of the Optical Society of America B-Optical Physics* **11**, 2206-2215 (1994).

89. Delong, K. W., Fittinghoff, D. N., Trebino, R., Kohler, B. & Wilson, K. Pulse Retrieval in Frequency-Resolved Optical Gating Based on the Method of Generalized Projections. *Optics Letters* **19**, 2152-2154 (1994).

90. Wang, H. *et al.* Practical issues of retrieving isolated attosecond pulses. *Journal of Physics B-Atomic Molecular and Optical Physics* **42**, 134007 (2009).

91. Zhao, K. *et al.* Tailoring a 67 attosecond pulse through advantageous phase-mismatch. *Optics Letters* **37**, 3891-3893 (2012).

92. Lee, P. & Weissler, G. L. Cross Section of the Neon Absorption Continuum. *Journal of the Optical Society of America* **42**, 214-215 (1952).

93. Fittinghoff, D. N., DeLong, K. W., Trebino, R. & Ladera, C. L. Noise sensitivity in frequency-resolved optical-gating measurements of ultrashort pulses. *Journal of the Optical Society of America B-Optical Physics* **12**, 1955-1967 (1995).

94. Chini, M., Wang, H., Khan, S. D., Chen, S. & Chang, Z. Retrieval of satellite pulses of single isolated attosecond pulses. *Applied Physics Letters* **94**, 161112 (2009).

95. Gagnon, J., Goulielmakis, E. & Yakovlev, V. S. The accurate FROG characterization of attosecond pulses from streaking measurements. *Applied Physics B-Lasers and Optics* **92**, 25-32 (2008).

96. Feng, X. *et al.* Calibration of electron spectrometer resolution in attosecond streak camera. *Optics Express* **18**, 1316-1322 (2010).

97. Pfeifer, T. *et al.* Measurement and optimization of isolated attosecond pulse contrast. *Optics Letters* **34**, 1819-1821 (2009).

98. Gilbertson, S. *et al.* Direct measurement of an electric field in femtosecond Bessel-Gaussian beams. *Optics Letters* **34**, 2390-2392 (2009).

99. Bourassin-Bouchet, C., de Rossi, S., Delmotte, F. & Chavel, P. Spatiotemporal distortions of attosecond pulses. *Journal of the Optical Society of America A-Optics Image Science and Vision* **27**, 1395-1403 (2010).

100. Chini, M. *et al.* Delay control in attosecond pump-probe experiments. *Optics Express* **17**, 21459-21464 (2009).

101. Gagnon, J. & Yakovlev, V. S. The robustness of attosecond streaking measurements. *Optics Express* **17**, 17678-17693 (2009).

102. Sansone, G. *et al.* Towards atomic unit pulse duration by polarization-controlled few-cycle pulses. *Journal of Physics B-Atomic Molecular and Optical Physics* **42**, 134005 (2009).

103. Baumert, T., Brixner, T., Seyfried, V., Strehle, M. & Gerber, G. Femtosecond pulse shaping by an evolutionary algorithm with feedback. *Applied Physics B-Lasers and Optics* **65**, 779-782 (1997).

104. Wang, H. *et al.* Attosecond Time-Resolved Autoionization of Argon. *Physical Review Letters* **105**, 143002 (2010).

105. Goulielmakis, E. *et al.* Real-time observation of valence electron motion. *Nature* **466**, 739-743 (2010).

106. Pollard, W. T., Lee, S.-Y. & Mathies, R. A. Wave packet theory of dynamic absorption spectra in femtosecond pump-probe experiments. *The Journal of Chemical Physics* **92**, 4012-4029 (1990).

107. Pollard, W. T. & Mathies, R. A. Analysis of Femtosecond Dynamic Absorption Spectra of Nonstationary States. *Annual Review of Physical Chemistry* **43**, 497-523 (1992).

108. Berera, R., van Grondelle, R. & Kennis, J. Ultrafast transient absorption spectroscopy: principles and application to photosynthetic systems. *Photosynthesis Research* **101**, 105-118 (2009).

109. Loh, Z. H. *et al.* Quantum state-resolved probing of strong-field-ionized xenon atoms using femtosecond high-order harmonic transient absorption spectroscopy. *Physical Review Letters* **98**, 143601 (2007).

110. Loh, Z. H., Khalil, M., Correa, R. E. & Leone, S. R. A tabletop femtosecond time-resolved soft x-ray transient absorption spectrometer. *Review of Scientific Instruments* **79**, 073101 (2008).

111. Loh, Z. H., Greene, C. H. & Leone, S. R. Femtosecond induced transparency and absorption in the extreme ultraviolet by coherent coupling of the He 2s2p (^1P_o) and $2p^2$ (^1S_e) double excitation states with 800 nm light. *Chemical Physics* **350**, 7-13 (2008).

112. Loh, Z. H. & Leone, S. R. Ultrafast strong-field dissociative ionization dynamics of CH_2Br_2 probed by femtosecond soft x-ray transient absorption spectroscopy. *Journal of Chemical Physics* **128**, 204302 (2008).

113. Bressler, C. & Chergui, M. Molecular Structural Dynamics Probed by Ultrafast X-Ray Absorption Spectroscopy. *Annual Review of Physical Chemistry* **61**, 263-282 (2010).

114. Fuji, T. *et al.* Attosecond control of optical waveforms. *New Journal of Physics* **7**, 116 (2005).

115. Fuji, T. *et al.* Monolithic carrier-envelope phase-stabilization scheme. *Optics Letters* **30**, 332-334 (2005).

116. Yun, C., Chen, S., Wang, H., Chini, M. & Chang, Z. Temperature feedback control for long-term carrier-envelope phase locking. *Applied Optics* **48**, 5127-5130 (2009).

117. Chen, S. *et al.* Carrier-envelope phase stabilization and control of 1 kHz, 6 mJ, 30 fs laser pulses from a Ti:sapphire regenerative amplifier. *Applied Optics* **48**, 5692-5695 (2009).

118. Barty, C. P. J. *et al.* Generation of 18-fs, multiterawatt pulses by regenerative pulse shaping and chirped-pulse amplification. *Optics Letters* **21**, 668-670 (1996).

119. Kakehata, M. *et al.* Carrier-envelope-phase stabilized chirped-pulse amplification system scalable to higher pulse energies. *Optics Express* **12**, 2070-2080 (2004).

120. Vaillancourt, G., Norris, T. B., Coe, J. S., Bado, P. & Mourou, G. A. Operation of a 1-Khz Pulse-Pumped Ti-Sapphire Regenerative Amplifier. *Optics Letters* **15**, 317-319 (1990).

121. Li, C. *et al.* Precision control of carrier-envelope phase in grating based chirped pulse amplifiers. *Optics Express* **14**, 11468-11476 (2006).

122. Wang, X., Chini, M., Cheng, Y., Wu, Y. & Chang, Z. *In Situ* Calibration of an Extreme Ultraviolet Spectrometer for Attosecond Transient Absorption Experiments. *(submitted)* (2012).

123. Lopez-Martens, R. *et al.* Amplitude and phase control of attosecond light pulses. *Physical Review Letters* **94**, 033001 (2005).

124. Mashiko, H. *et al.* Tunable frequency-controlled isolated attosecond pulses characterized by either 750 nm or 400 nm wavelength streak fields. *Optics Express* **18**, 25887-25895 (2010).

125. Moon, E. *et al.* Reduction of fast carrier-envelope phase jitter in femtosecond laser amplifiers. *Optics Express* **14**, 9758-9763 (2006).

126. Lepetit, L., Cheriaux, G. & Joffre, M. Linear techniques of phase measurement by femtosecond spectral interferometry for applications in spectroscopy. *Journal of the Optical Society of America B-Optical Physics* **12**, 2467-2474 (1995).

127. Mossessian, D. A. *et al.* Transmission Grating Spectrometer for Characterization of Undulator Radiation. *Nuclear Instruments & Methods in*

Physics Research Section a-Accelerators Spectrometers Detectors and Associated Equipment **347**, 244-248 (1994).

128. Tremsin, A. S. & Siegmund, O. H. W. Spatial distribution of electron cloud footprints from microchannel plates: Measurements and modeling. *Review of Scientific Instruments* **70**, 3282-3288 (1999).

129. Zitnik, M. *et al.* Lifetimes of n P-1 states in helium. *Journal of Physics B-Atomic Molecular and Optical Physics* **36**, 4175-4189 (2003).

130. Madden, R. P. & Codling, K. New Autoionizing Atomic Energy Levels in He, Ne, and Ar. *Physical Review Letters* **10**, 516-518 (1963).

131. Madden, R. P., Ederer, D. L. & Codling, K. Resonances in Photo-Ionization Continuum of Ar I (20-150 eV). *Physical Review* **177**, 136 (1969).

132. Martin, W. C. Energy Levels of Neutral Helium (^{4}He I). *Journal of Physical and Chemical Reference Data* **2**, 257-265 (1973).

133. Drake, G. W. F. *Springer handbook of atomic, molecular, and optical physics*. (Springer, 2006).

134. Tong, X. M. & Toshima, N. Controlling atomic structures and photoabsorption processes by an infrared laser. *Physical Review A* **81**, 063403 (2010).

135. Santra, R., Yakovlev, V. S., Pfeifer, T. & Loh, Z. H. Theory of attosecond transient absorption spectroscopy of strong-field-generated ions. *Physical Review A* **83**, 033405 (2011).

136. Gaarde, M. B., Buth, C., Tate, J. L. & Schafer, K. J. Transient absorption and reshaping of ultrafast XUV light by laser-dressed helium. *Physical Review A* **83**, 013419 (2011).

137. Chen, S., Schafer, K. J. & Gaarde, M. B. Transient absorption of attosecond pulse trains by laser-dressed helium. *Optics Letters* **37**, 2211-2213 (2012).

138. Pfeiffer, A. N. & Leone, S. R. Transmission of an isolated attosecond pulse in a strong-field dressed atom. *Physical Review A* **85**, 053422 (2012).

139. Baggesen, J. C., Lindroth, E. & Madsen, L. B. Theory of attosecond absorption spectroscopy in krypton. *Physical Review A* **85**, 013415 (2012).

140. Chu, W. C. & Lin, C. D. Photoabsorption of attosecond XUV light pulses by two strongly laser-coupled autoionizing states. *Physical Review A* **85**, 013409 (2012).

141. Tarana, M. & Greene, C. H. Femtosecond transparency in the extreme-ultraviolet region. *Physical Review A* **85**, 013411 (2012).

142. Hu, S. X. Optimizing the FEDVR-TDCC code for exploring the quantum dynamics of two-electron systems in intense laser pulses. *Physical Review E* **81**, 056705 (2010).

143. Swoboda, M. *et al.* Phase Measurement of Resonant Two-Photon Ionization in Helium. *Physical Review Letters* **104**, 103003 (2010).

144. Holler, M., Schapper, F., Gallmann, L. & Keller, U. Attosecond Electron Wave-Packet Interference Observed by Transient Absorption. *Physical Review Letters* **106**, 123601 (2011).

145. Johnsson, P. *et al.* Attosecond electron wave packet dynamics in strong laser fields. *Physical Review Letters* **95**, 013001 (2005).

146. Riviere, P., Uhden, O., Saalmann, U. & Rost, J. M. Strong field dynamics with ultrashort electron wave packet replicas. *New Journal of Physics* **11**, 053011 (2009).

147. Ranitovic, P. *et al.* IR-assisted ionization of helium by attosecond extreme ultraviolet radiation. *New Journal of Physics* **12**, 013008 (2010).

148. Tong, X. M., Ranitovic, P., Cocke, C. L. & Toshima, N. Mechanisms of infrared-laser-assisted atomic ionization by attosecond pulses. *Physical Review A* **81**, 021404 (2010).

149. Chini, M. *et al.* Sub-cycle oscillating dark states brought to light. *(submitted)* (2012).

150. Glover, T. E. *et al.* Controlling X-rays with light. *Nature Physics* **6**, 69-U65 (2010).

151. Chu, S. I. & Telnov, D. A. Beyond the Floquet theorem: generalized Floquet formalisms and quasienergy methods for atomic and molecular multiphoton processes in intense laser fields. *Physics Reports-Review Section of Physics Letters* **390**, 1-131 (2004).

152. Ott, C., Raith, P. & Pfeifer, T. Sub-cycle strong-field interferometry. *Optics Express* **18**, 24307-24315 (2010).

153. Fano, U. Effects of Configuration Interaction on Intensities and Phase Shifts. *Physical Review* **124**, 1866-1878 (1961).

154. McConkey, J. W. & Preston, J. A. Autoionizing States in Argon. *Journal of Physics B-Atomic Molecular and Optical Physics* **6**, L138-L141 (1973).

155. Lambropoulos, P. & Zoller, P. Autoionizing States in Strong Laser Fields. *Physical Review A* **24**, 379-397 (1981).

156. Tong, X. M. & Lin, C. D. Empirical formula for static field ionization rates of atoms and molecules by lasers in the barrier-suppression regime. *Journal of Physics B-Atomic Molecular and Optical Physics* **38**, 2593-2600 (2005).

157. Sansone, G., Poletto, L. & Nisoli, M. High-energy attosecond light sources. *Nature Photonics* **5**, 656-664 (2011).

158. Mashiko, H., Suda, A. & Midorikawa, K. Focusing multiple high-order harmonics in the extreme-ultraviolet and soft-x-ray regions by a platinum-coated ellipsoidal mirror. *Applied Optics* **45**, 573-577 (2006).

159. Takahashi, E. J., Lan, P. F., Mucke, O. D., Nabekawa, Y. & Midorikawa, K. Infrared Two-Color Multicycle Laser Field Synthesis for Generating an Intense Attosecond Pulse. *Physical Review Letters* **104**, 233901 (2010).

160. Charalambidis, D. *et al.* Exploring intense attosecond pulses. *New Journal of Physics* **10**, 025018 (2008).

161. Gademann, G., Ple, F., Paul, P. M. & Vrakking, M. J. J. Carrier-envelope phase stabilization of a terawatt level chirped pulse amplifier for generation of intense isolated attosecond pulses. *Optics Express* **19**, 24922-24932 (2011).